Investigations on the role of defects in the thermoelectric properties of the nanostructured bismuth telluride

by

Sinduja. M

Enrollment Number: PHYS02 2016 04 006

Indira Gandhi Centre for Atomic Research, Kalpakkam

A thesis
Submitted to
The Board of Studies in Physical Sciences

In partial fulfillment of requirements for the Degree of
DOCTOR OF PHILOSOPHY

of

Homi Bhabha National Institute

December 2020

Homi Bhabha National Institute

Recommendations of Viva-voce board

As a members of viva-voce board, we certify that we have read the dissertation prepared by **Sinduja M** entitled "**Investigations on the role of defects in the thermoelectric properties of the nanostructured bismuth telluride**" and recommend that it may be accepted as fulfilling the dissertation requirement for the doctor of philosophy.

Chairman: **Dr. B. K. Panigrahi**	Biranya Panigrahi	Date: 29.07.21
Guide and convener: **Dr. S. Amirthapandian**	29/7/21	Date: 29.07.21
Examiner: **Dr. Santanu Ghosh**	Santanu Ghosh 29/7/2021	Date: 29.07.21
Member-1: **Dr. Arup Dasgupta**		Date: 29.07.21
Member-2: **Dr. T. R. Ravindran**	T R Ravindran	Date: 29.07.21
Member-3: **Dr. Anish Kumar**	29/7/21	Date: 29.07.21

Final approval and acceptance of this dissertation is contingent upon the candidate's submission of the final copies of the dissertation to HBNI.

Certificate

I hereby certify that I have read this dissertation prepared under my direction and recommend that it may be accepted as fulfilling the dissertation requirement.

Dr. S. Amirthapandian

Date: 29/7/21

Place: Kalpakkam

Statement by Author

This dissertation has been submitted in partial fulfillment of requirements for an advanced degree at Homi Bhabha National Institute (HBNI) and is deposited in the Library to be made available to borrowers under rules of the HBNI.

Brief quotations from this dissertation are allowable without special permission, provided that accurate acknowledgement of source is made. Requests for permission for extended quotation from or reproduction of this manuscript in whole or in part may be granted by the Competent Authority of HBNI, when in his or her judgment the proposed use of the material is in the interests of scholarship. In all other instances, however, permission must be obtained from the author.

Sinduja. M

Declaration

I, hereby declare that the investigation presented in the thesis has been carried out by me. The work is original and has not been submitted earlier as a whole or in part for a degree / diploma at this or any other Institution / University.

Sinduja. M

List of Publications

(a) Journal

1) **Sinduja M.;** Amirthapandian, S.; P, Jegadeesan. Magudapathy, P. K. Asokan
   Morphological investigations on the growth of defect rich Bi_2Te_3 nanorods and their thermoelectric properties
   CrystEngComm (2018), 20, 4810.
2) **Sinduja M.;** Amirthapandian, S.; Magudapathy, P.; S. K. Srivastva, K. Asokan,
   Tuning of the thermoelectric properties of Bi_2Te_3 nanorods using helium ion irradiation
   ACS Omega (2018), 3, 18411.
3) **Sinduja .M,** S. Amirthapandian, Anha Masarrat, R. Krishnan, S. K. Srivastava, K. Asokan
   Investigations on morphology and thermoelectric transport properties of Cu^+ ion implanted bismuth telluride film
   Thin solid films (2020), 697, 137834.
4) **Sinduja M,** S Amirthapandian, P Magudapathy, Anha Masarrat, R Krishnan, S K Srivastava, K Asokan
   Role of ion irradiation induced defects in thermoelectric transport properties of Bi_2Te_3 films.
   (Under review in *Thin Solid films)*

(b) Conferences:

1) **Sinduja M.;** S. Amirthapandian, B.Sunderavel, B. K. Panigrahi,
   Solid state dewetting on Au tin films: RBS study
   Symposium on 'Two decades on ion beam analysis at 3MV Tandetron' at NCCCM, Hyderabad on March 23-24 2017.
2) **Sinduja M.;** S.Amirthapandian, R.Pandian, K.Ganesan, B. K. Panigrahi,
   Solid state thermal dewetting of gold thin films evaporated on silicon
   International conference on Microscope and XXXVIII Annual meeting of Electron Microscope Society of India (EMSI 2017), IGCAR, Kalpakkam on July 17 to 19, 2017.
3) **Sinduja .M,** S. Amirthapandian, P. Magudapathy, P.Jegadeesan,
   Growth of the Bismuth telluride nanorods by surfactant assisted hydrothermal method

International conference on Microscope and XXXIX Annual meeting of Electron Microscope Society of India (EMSI 2017),International conference on electron microscopy (EMSI 2018), Bhubaneswar on July 18 to 20, 2018.

4) **Sinduja .M,** S. Amirthapandian, Jagnaseni Pradhan, S. K. Srivastava, 'Morphological investigations on the growth of Bi_2Te_3 flakes and their Raman scattering analysis'
National conference on light matter interaction at Nanoscale
LMIN at IGCAR Kalpakkam at July 15- 17, 2019.

5) **Sinduja .M**, S. Amirthapandian, P. Magudapathy, K. Asokan, 'The role of native defects on the thermoelectric transport properties of bismuth telluride films using 120keV He^+ ion irradiations'
5th International conference on Nanostructuring by ion beams (ICNIB-2019), IGCAR, Kalpakkam at Nov 6-8,2019

M Sinduja

Sinduja. M

Acknowledgement

I'm reminded and grateful for many people, who have played a role in helping me to this point in life. Firstly, it is genuinely a privilege to be working under the guidance of my guide Dr. S. Amirthapandian. Thanks and gratitude to be given to him for his open-ended support, insightful opinions, and extremely valuable advices in many occasions. In addition to his help in working on the project, writing the articles, he has always available to encourage and lend perspectives along the way.

I'm extremely delightful to Mr. P. Magudapathy for carrying out number of irradiations and XRD measurements along with necessary technical inputs. I am very much grateful to the dedication and enthusiasm shown by Dr. P Jegadeesan to finish my Ph.D. I thank Dr. Sachin Kumar Srivastava and Ms. Jagnaseni Pradhan for helping me in Raman and AFM experiments and their analysis. I gratefully acknowledge the technical guidance and scientific discussions provided by Dr. C. David and Dr. B. Sundaravel in spite of busy schedule. I sincerely thank Dr. R. Krishnan for assisting me in carrying out the PLD deposition. Also, I acknowledge Dr. C. Sudha and Dr. R. Sundar at assisting thermal diffusivity measurements.

I would like to thank our collaborators from IUAC, Delhi, Dr. K. Asokan and Mrs. Anha Masarat for this wonderful opportunity to work together, which resulted in many publications.

I would also like to recognize and thank the following individuals for their love, support, and care during my PhD: Ms. Balasaritha, Ms. Abhirami, Ms. Jagnaseni Pradhan, Mr. P. Dhilipan, Ms. Rajitha, Ms. Jekathamani, Mr. Velraj. Furthermore, I appreciate the timely assistance provided by lab technicians in our PIF lab, without which this project would be impossible.

Most of all, I would like to gratefully thank my husband, my son, and my parents for their love, support, and inspiration. My husband, Mr. Sivakumar, has always been a good listener at my toughest moments of life. He always there to help unconditionally, support unlimitedly, and inspire me enormously, and I always owe him a special debt of gratitude.

Sinduja M

To my husband

Table of contents

List of Publications ix
Acknowledgement xiii
Abstract xiv
Table of contents xvii
List of Figures xxi
List of tables xxvi

Chapter 1 **Role of defects in thermoelectric materials- A brief review ...1**

1.1. Introduction 1
1.1.1. Seebeck effect 2
1.1.2. Peltier effect 2
1.1.3. Thomson effect 3
1.1.4. Thermoelectric power generator 3
1.2. Thermoelectric transport properties in materials 4
1.2.1. Figure of merit, *ZT* 4
1.2.2. Electrical conductivity (σ) 4
1.2.3. Seebeck Coefficient 5
1.2.4. Thermal conductivity 7
1.2.5. Thermoelectric transport properties – Key issues and challenges 8
1.3. Bismuth telluride (Bi_2Te_3) - semiconducting thermoelectric material 9
1.4. Strategies to improve thermoelectric transport properties in materials 11
1.4.1. Alloying 11
1.4.2. Nanostructure engineering 12
1.4.3. Electronic band structure engineering 13
1.4.4. Defect Engineering 16
1.5. Nanostructured bismuth telluride: synthesis and overview 17
1.5.1. Top-down approach 18
1.5.2. Bottom-up approach 18
1.5.3. Bi_2Te_3 nanostructures- review 19
1.6. Ion implantation 21
1.6.1. Ion-solid interactions and energy loss 22
1.6.2. Ion implantation/irradiation induced defects 23
1.6.3. Overview of ion irradiation effects in Bi_2Te_3 24
1.7. Scope of the thesis 25

Chapter 2 **Experimental methods 26**

2.1. Introduction 26
2.2. Sample preparation methods 26

2.2.1. Hydrothermal method for pellet samples 26
2.2.2. Pulsed laser deposition (PLD) method for thin film samples 27
2.2.3. Ion implantation/irradiation 29
2.2.3.1. 150 kV ion accelerator 29
2.2.3.2. 1.7 MV Tandetron accelerator 30
2.3. Diffraction techniques 31
2.3.1. Gracing incidence X-ray diffraction (GIXRD) 31
2.3.1.1. Scherrer method 32
2.3.1.2. Williamson-Hall (W-H) plot 33
2.3.2. Electron diffraction 33
2.4. Microscopy Techniques 34
2.4.1. Atomic force microscopy (AFM) 34
2.4.2. Scanning electron microscopy (SEM) 34
2.4.3. Transmission electron microscopy (TEM) 36
2.4.3.1. TEM sample preparation 37
2.5. Spectroscopy and spectrometry technique 37
2.5.1. Energy dispersive X-ray (EDX) analysis 37
2.5.2. Raman scattering 38
2.5.3. Rutherford Backscattering spectrometry (RBS) 39
2.6. Thermoelectric (TE) characterization 40
2.6.1. Hall-effect 40
2.6.2. Seebeck coefficients 41
2.6.3. Electrical conductivities 42
2.6.4. Thermal conductivity 43
2.7. Summary 44

***Chapter 3* Growth and thermoelectric properties of the bismuth telluride nanostructures 45**

3.1. Introduction 45
3.2. Experimental methods 46
3.2.1. Sample synthesis 46
3.2.2. Characterization techniques 47
3.3. Results 48
3.3.1. Morphology and structure evolution: the role of surfactant concentration 48
3.3.2. Morphology and structure evolution: a role of reaction temperature 53
3.3.3. Effect of morphology of nanorods on thermoelectric transport properties 55
3.4. Discussion 59
3.4.1. Growth kinetics for the formation of Bi_2Te_3 nanostructures 59

3.4.2. Effect of microstructure on the thermoelectric transport properties. 63
3.5. Conclusion 64

Chapter 4 **Helium ion irradiation effects on the thermoelectric properties of bismuth telluride nanorods. 65**

4.1. Introduction 65
4.2. Experimental methods 66
4.2.1. Sample synthesis 66
4.2.2. Characterization technique 67
4.3. Results 68
4.3.1. GIXRD studies 68
4.3.2. Microstructural studies 69
4.3.3. Monte Carlo simulations on Bi_2Te_3 nanorods 71
4.3.4. Raman scattering studies 74
4.3.5. Thermoelectric transport properties 77
4.4. Discussion 79
4.5. Conclusion 82

Chapter 5 **Copper ion doping effects in bismuth telluride thin films. ...83**

5.1. Introduction 83
5.2. Experimental methods 84
5.2.1. Sample synthesis 84
5.2.2. Characterization techniques 86
5.3. Results 87
5.3.1. Compositional analysis of Cu^+ ion implanted Bi_2Te_3 thin films 87
5.3.2. GIXRD analysis of Cu^+ ion implanted Bi_2Te_3 thin films 89
5.3.3. Raman scattering analysis in Cu^+ ion implanted films 91
5.3.4. Morphological analysis of Cu^+ ion implanted Bi_2Te_3 thin films 93
5.3.5. Thermoelectric transport properties 96
5.4. Discussion 99
5.5. Conclusion 102

Chapter 6 **Role of inert gas ion irradiation effects in thermoelectric properties of bismuth telluride thin films. 103**

6.1. Introduction 103
6.2. Experimental methods 104
6.2.1. Sample synthesis 104
6.2.2. Characterization technique 105
6.3. Results 105
6.3.1. GIXRD studies 105

6.3.2. Morphological analysis 108
6.3.3. Raman scattering analysis 112
6.3.4. Thermoelectric transport properties 115
6.4. Discussion 120
6.5. Conclusion 121

***Chapter 7* Summary and perspectives 122**

7.1. Summary 122
7.2. Future outlook 125

References* *127

List of Figures

Figure 1.1: Schematic of thermocouple circuit formed by two dissimilar metals[9]. 2

Figure 1.2: Schematic of TE module in power generator[10]. 3

Figure 1.3: Carrier concentration dependence on TE transport properties[16]. 8

Figure 1.4: Schematic representation of Bi_2Te_3 hexagonal unit cell[20]. 9

Figure 1.5: Energy dependent g(E) for bulk and nanostructured materials[39,44]. 12

Figure 1.6: Seebeck coefficient (S) and figure of merit (ZT) as a function of temperature for I- and La doped PbTe[49]. 14

Figure 1.7: (a) Schematic representation of enhancement in density of states *via* resonant doping. (b) Temperature dependent Seebeck coefficient values for Sn doped Bi_2Te_3. The symbols are: $Bi_{1.9975}Sn_{0.0025}Te_3$ (red plus), $Bi_{1.9925}Sn_{0.0075}Te_3$ (blue diamond) and $Bi_{1.985}Sn_{0.015}Te_3$ (green dot)[50] 14

Figure 1.8: Schematic representation of the band convergence strategy achieved in Se doped PbTe as a function of temperature[55]. 15

Figure 1.9: Schematic of top-down and bottom-up approach for the preparation of nanostructured TE materials[80]. 18

Figure 1.10: Nuclear and electronic energy loss of He^+ ions in Bi_2Te_3 as a function of ion energy. The data is calculated using SRIM software[130]. 22

Figure 2.1: Schematic of pulsed laser deposition (PLD) technique[152]. 28

Figure 2.2: Photograph (a) and schematic (b) of 150 kV ion accelerator. 29

Figure 2.3: Photograph (a) and schematic (b) of 1.7 MV Tandetron accelerator. 30

Figure 2.4: Scattering geometry of (a) XRD and (b) GIXRD techniques[153] 32

Figure 2.5: Schematic of atomic force microscopy (AFM) 34

Figure 2.6: Schematic representation of various signal obtained in SEM, while the electron interacted with the sample. 35

Figure 2.7: The Crossbeam 340 scanning electron microscope: the photograph (a) and the illustration of the electron path (b). 35

Figure 2.8: Carl Zeiss Libra 200FE Transmission Electron Microscope: the photograph (a) and the illustration of the electron path (b). 36

Figure 2.9: Raman-AFM integrated (WiTec RA 300) system: (a) photograph and (b) schematic diagram of the system for Raman spectra measurements. 39

Figure 2.10: Schematic representation of the experimental setup for Rutherford backscattering analysis. 39

Figure 2.11: Configuration for Hall-effect measurement system. 41

Figure 2.12: Photograph (a) and schematic diagram (b) of the Seebeck coefficient measurement setup. 42

Figure 2.13: Schematic of (a) four-probe method for electrical conductivity measurements and (b) Netzsch LFA 457 laser flash apparatus for thermal diffusivity measurement. 43

Figure 3.1: XRD pattern of the samples (a) 0-SDBS, (b) 3-SDBS, (c) 5-SDBS, (d) 6-SDBS, and (e) 8-SDBS. 49

Figure 3.2: The Williamson-Hall (W-H) plot for the samples: (a) 0-SDBS, (b) 3-SDBS, (c) 5-SDBS, (d) 6-SDBS, and (e) 8-SDBS. (f) show the variation in the crystallite size and lattice strain as a function of surfactant concentration. 50

Figure 3.3: Low magnification (a-e) and high magnification (i-j) FESEM images of (a) 0-SDBS, (b) 3-SDBS, (c) 5-SDBS, (d) 6-SDBS, and (e) 8-SDBS, respectively, Inset shows the diameter distribution of Bi_2Te_3 nanorods. 51

Figure 3.4: TEM bright field image (a, b), HRTEM image(c, d) and the corresponding electron diffraction pattern (e, f) of the sample 6-SDBS and 8-SDBS respectively. 52

Figure 3.5: XRD pattern of the samples synthesized in the presence of 8 mmol SDBS concentration and at different reaction temperatures (a) SBDS-100, (b) SDBS-130, and (c) SDBS-150. 53

Figure 3.6: W-H plot for the samples (a) SDBS-100, (b) SDBS-130, (c)SDBS-150 and (d) shows the variation in the crystallite size and lattice strain as a function of reaction temperature. 54

Figure 3.7: FESEM images of the sample: (a) SDBS-100 and (b) SDBS-150 and the (c) high magnification bright field image of SDBS-150 Bi_2Te_3 nanorods. (d) and (e) are corresponding HRTEM image and indexed electron diffraction pattern. 55

Figure 3.8: XRD pattern of the pressed pellets that composed of (a) flakes-decorated Bi_2Te_3 nanorods, (b) porous Bi_2Te_3 nanorods, and (c) smooth Bi_2Te_3 nanorods. 55

Figure 3.9: FESEM image of the pressed pellets that composed of (a) smooth Bi_2Te_3 nanorods, (b) flake decorated Bi_2Te_3 nanorods, and (c) porous Bi_2Te_3 nanorods. The inset shows the atomic concentrations of Bi and Te (as obtained from EDX analysis). 56

Figure 3.10: Temperature dependent TE transport properties of the pellets made of Bi_2Te_3 nanorods with different surface morphologies: (a) Seebeck coefficient, S, (b) electrical conductivity, σ, (c) power factor, $S^2\sigma$. 58

Figure 3.11: Schematic diagram of Bi_2Te_3 crystals coated with (a) high and (b) intermediate concentration of SDBS. 60

Figure 3.12: Bright field TEM image (a) and (b) demonstrates the oriented attachment (OA) process in the growth of Bi_2Te_3 particles in the 0-SDBS sample. 61

Figure 3.13: Schematic diagram showing the formation of Bi_2Te_3 nanorods by oriented attachment (OA) mechanism. 62

Figure 4.1: GIXRD pattern of (a) the pristine and 100 keV He^+ ion irradiated Bi_2Te_3 pellet with the ion fluences of (b)5×10^{15}, (c)1×10^{16}, (d)5×10^{16}, (e)1×10^{17}, (f)2×10^{17} ions/cm^2. 68

Figure 4.2: FESEM image of the (a) pristine and 100 keV He^+ ion irradiated Bi_2Te_3 pellet with the ion fluences of (b)5×10^{15}, (c)1×10^{16}, (d)5×10^{16}, (e)1×10^{17}, (f)2×10^{17} ions/cm^2. 69

Figure 4.3: HRTEM images (a-d) and the corresponding electron diffraction pattern (e-h) of (a) the pristine and 100 keV He^+ ion irradiated Bi_2Te_3 nanorod with the ion fluence of (b)5×10^{16}, (c)1×10^{17}, (d)2×10^{17} ions/cm^2. Inset shows the bright field TEM image of Bi_2Te_3 nanorod. 70

Figure 4.4: Approximate amorphous volume fraction in Bi_2Te_3 nanorod as a function of 100 keV He^+ ion fluence. 71

Figure 4.5: Vacancy profile of the 100 keV He^+ ion irradiated Bi_2Te_3 bulk target as obtained from TRIM calculations. 72

Figure 4.6: Schematic of the iradina simulation on Bi_2Te_3 nanorod. 73

Figure 4.7: The spatial distribution maps of (a) displaced atoms, (b) vacancies, and (c) interstitials in the Bi_2Te_3 nanorod section (simulated using IRADINA). The total number of displaced atoms, vacancies, and interstitials in the Bi_2Te_3 nanorod at various ion fluences (as calculated from IRADINA) are shown in (d). 74

Figure 4.8: Schematic representation of the atomic vibration corresponding to Raman active and IR active modes. 75

Figure 4.9: Raman spectra of (a) pristine and 100 keV He^+ ion irradiated Bi_2Te_3 pellet for various ion fluences of (b)5×10^{15}, (c)1×10^{16}, (d)5×10^{16}, (e)1×10^{17}, and (f)2×10^{17} ions/cm^2. 75

Figure 4.10: Variation in (a) Raman mode intensity, (b) intensity ratio of in-plane to out-of-plane vibration modes, (c) Raman peak position, and (d) FWHM of the Raman peak as a function of ion fluence. 76

Figure 4.11: Carrier concentration and mobility at room temperature for pristine and 100 keV He^+ ion irradiated Bi_2Te_3 pellets for various ion fluences. 77

Figure 4.12: Temperature dependent TE transport properties of the pristine and 100 keV He^+ ion irradiated Bi_2Te_3 pellets: (a) Seebeck coefficient (S), (b) electrical conductivity (σ), and (c) power factor ($S^2\sigma$). 78

Figure 5.1: The Cu depth profile for the uniform Cu concentration of 0.5 at% in Bi_2Te_3 thin films on quartz substrate using 300 keV and 700 keV Cu^+ ion implantation. The implantation profiles are obtained using SRIM calculations[130]. 85

Figure 5.2: (a) RBS spectrum of pristine Bi_2Te_3 thin film and (b) its expanded view. RBS spectrum of Cu^+ ion implanted Bi2Te3 thin film with Cu concentration of (c) 0.5 at%, (d) 1 at%, (e) 1.5 at%, and (f) 2 at%. 88

Figure 5.3: The depth profile of bismuth, tellurium, and copper in Cu^+ ion implanted Bi_2Te_3 thin films with Cu concentration of (a) 0.5 at%, (b) 1 at%, (c) 1.5 at%, and (d) 2 at%. 89

Figure 5.4: GIXRD pattern of (a) pristine and Cu^+ ion implanted Bi_2Te_3 thin films with Cu concentration of (b) 0.5 at%, (c) 1 at%, (d) 1.5 at%, and (e) 2 at%. 90

Figure 5.5: Average crystallite size of pristine and Cu^+ ion implanted Bi_2Te_3 thin films obtained from GIXRD results. 90

Figure 5.6: GIXRD pattern of annealed Cu^+ ion implanted thin films with Cu concentration of (a) 0.5 at%, (b) 1 at%, (c) 1.5 at%, and (d) 2 at%. 91

Figure 5.7: The Raman spectra of (a) pristine and Cu^+ ion implanted Bi_2Te_3 thin films with Cu concentration of (b) 0.5 at%, (c) 1 at%, (d) 1.5 at%, (e) 2 at% . 92

Figure 5.8: Variation in (a) peak position and (b) FWHM of the pristine and Cu^+ ion implanted Bi_2Te_3 thin films with the Cu concentration. 92

Figure 5.9: Raman spectra for annealed Cu^+ ion implanted Bi_2Te_3 thin films with Cu concentration of (a) 0.5 at%, (b) 1 at%, (c) 1.5 at%, and (d) 2 at%. 93

Figure 5.10: FESEM images of plane view and cross sectional view of the pristine and Cu^+ ion implanted Bi_2Te_3 thin films. 94

Figure 5.11: FESEM images of the annealed Cu^+ ion implanted Bi_2Te_3 thin films with Cu concentration of (a) 0.5 at%, (b) 1 at%, (c) 1.5 at%, and (d) 2 at%. 95

Figure 5.12: AFM (2D) topography of (a) pristine and Cu^+ ion implanted Bi_2Te_3 thin films with Cu concentration of (b) 0.5 at%, (c) 1 at%, (d) 1.5 at%, and (e) 2 at%. The scanned images are area of 1μm×1μm. 96

Figure 5.13: Average grain size and rms roughness values from the AFM images of the pristine and Cu^+ ion implanted Bi_2Te_3 thin films as a function of Cu concentration. 96

Figure 5.14: Carrier concentration (a) and mobility (b) of the Cu^+ ion implanted Bi_2Te_3 thin films before and after the annealing having various Cu concentration. 97

Figure 5.15: (a, d) Seebeck coefficient (S), (b, e) electrical conductivity (σ) and (c, f) power factor ($S^2\sigma$) for Cu^+ ion implanted Bi_2Te_3 thin films before and after the annealing for various Cu concentration. 98

Figure 6.1: GIXRD pattern of (a) the pristine and 120 keV He^+ ion irradiated Bi_2Te_3 thin films for various ion fluences of (b) 5×10^{14}, (c) 1×10^{15}, (d) 5×10^{15},and (e) 1×10^{16} ions/cm^2 respectively. 106

Figure 6.2: Average crystallite size of pristine and 120 keV He^+ ion irradiated Bi_2Te_3 thin films for different ion fluences. 106

Figure 6.3: GIXRD pattern of (a) pristine and 120 keV Ar^+ ion irradiated Bi_2Te_3 thin films for the ion fluences of (b) 5×10^{14}, (c) 1×10^{15}, (d) 5×10^{15}, and (e) 1×10^{16} ions/cm^2 respectively. 107

Figure 6.4: Variation in the average crystallite size as a function of 120 keV Ar^+ ion fluences. 108

Figure 6.5: FESEM image of (a) pristine and 120 keV He^+ ion irradiated Bi_2Te_3 thin films for various ion fluences of (b) 5×10^{14}, (c) 1×10^{15}, (d) 5×10^{15}, and (e) 1×10^{16} ions/cm^2 respectively. 108

Figure 6.6: FESEM image of (a) pristine and 120 keV Ar^+ ion irradiated Bi_2Te_3 thin films for different ion fluences of (b) 5×10^{14}, (c) 1×10^{15}, (d) 5×10^{15}, and (e) 1×10^{16} ions/cm^2 respectively. 109

Figure 6.7: AFM image of (a) pristine and 120 keV Ar^+ ion irradiated Bi_2Te_3 thin films for different ion fluences of (b) 5×10^{14}, (c) 1×10^{15}, (d) 5×10^{15}, and (e) 1×10^{16} ions/cm^2 respectively. 110

Figure 6.8: Variation in grain size and roughness as a function of different 120 keV Ar^+ ion fluences. 112

Figure 6.9: Raman spectra of (a) pristine and 120 keV He^+ ion irradiated Bi_2Te_3 thin films for various ion fluences of (b) 5×10^{14}, (c) 1×10^{15}, (d) 5×10^{15}, and (e) 1×10^{16} ions/cm^2 respectively. 113

Figure 6.10: Variation in (a) peak position and (b) FWHM of the Raman modes of 120 keV He^+ ion irradiated Bi_2Te_3 thin films for various ion fluences. 114

Figure 6.11: Raman spectra of (a) pristine and 120 keV Ar^+ ion irradiated Bi_2Te_3 thin films for various ion fluences of (b) 5×10^{14}, (c) 1×10^{15}, (d) 5×10^{15}, and (e) 1×10^{16} ions/cm^2 respectively. 114

Figure 6.12: Variation in peak position and (b) FWHM of the Raman modes of 120 keV Ar^+ ion irradiated Bi_2Te_3 thin films for various ion fluences. 115

Figure 6.13: Temperature dependent TE transport properties: (a, d) Seebeck coefficient (S), (b, e) electrical conductivity (σ), and (c, f) power factor($S^2\sigma$) of the pristine, 120 keV He^+ and 120 keV Ar^+ ion irradiated Bi_2Te_3 thin films respectively for various ion fluences. 116

Figure 6.14: Variation in the carrier concentration and mobility as a function of peak damages (dpa) and as a function of the corresponding 120 keV He^+ and 120 keV Ar^+ ion fluences. 117

Figure 6.15: TE transport properties at room temperature as a function of peak dpa values and as a function of the corresponding 120 keV He^+ and 120 keV Ar^+ ion fluences. 118

Figure 7.1: Schematic of the morphology evolution of the Bi_2Te_3 products as a function of varying SDBS concentration and reaction temperature. 122

Figure 7.2: Evolution of microstructure of Bi_2Te_3 nanorod and power factor values for the corresponding Bi_2Te_3 pellets as a function of 100 keV He^+ ion fluences.124

Figure 7.3: Variation in power factor values at room temperature for Bi_2Te_3 thin film sample as a function of peak damage values. 125

List of tables

Table 1.1: Formation energy (E_f) for antisite defect (Te_{Bi}, Bi_{Te-1}, Bi_{Te-2}) and vacancies defect (V_{Bi}, V_{Te-1}, V_{Te-2}) in Bi_2Te_3 at Bi rich and Te-rich conditions[28,30]. 10

Table 3.1: Labels for the Bi_2Te_3 samples synthesized under different hydrothermal conditions. 47

Table 3.2: Carrier concentration and mobility of the pellets composed of Bi_2Te_3 nanorods at room temperature with various morphologies. 57

Table 3.3: Room temperature thermal diffusivity, thermal conductivity, power factor and figure of merit values for the pellet composed of Bi_2Te_3 nanorods with different surface morphologies. 59

Table 4.1: Details of ion irradiation in Bi_2Te_3 carried out in present study. 66

Table 5.1: Details of ion irradiation in Bi_2Te_3 carried out in present work. 84

Table 5.2: Estimated 300 keV and 700 keV Cu^+ ion fluences for incorporating Cu concentration of 0.5 at%, 1 at%, 1.5 at%, 2 at% in Bi_2Te_3 thin films. 86

Table 5.3: Elemental compositions of the pristine and Cu implanted thin films. 87

Table 6.1: Details of inert gas ion irradiations in Bi_2Te_3, carried out in the present work. 105

Table 7.1: TE transport characteristics on the various materials presented in the present thesis 123

Chapter 7

Summary and perspectives

7.1. Summary

The present thesis deals with nano-structuring and defect-engineering approaches to improve TE characteristics of Bi_2Te_3 based TE material. Powder samples composed of Bi_2Te_3 nanostructures with different surface morphologies were prepared through surfactant assisted hydrothermal method and the Bi_2Te_3 thin film samples were fabricated using pulsed laser deposition method.

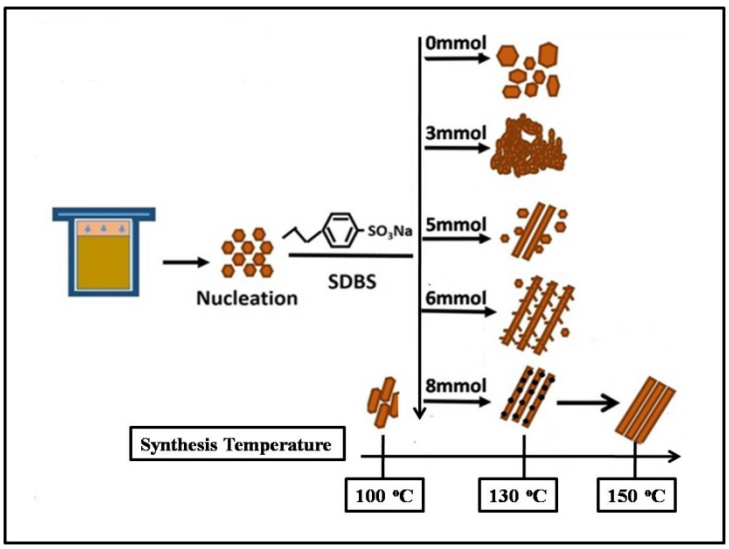

Figure 7.1: Schematic of the morphology evolution of the Bi_2Te_3 products as a function of varying SDBS concentration and reaction temperature.

In the first part of the thesis, the work was focused to optimize the growth conditions of Bi_2Te_3 nanostructures using various factors such as surfactant concentration and reaction temperature, and its effectiveness towards the thermoelectric transport characteristics were investigated. The surfactant SDBS determines the extent of capping effect and also controls the agglomeration of Bi_2Te_3 nuclei. The effective capping or coverage was achieved around the stable Bi_2Te_3 nuclei, when the SDBS concentration is higher than the critical micelle concentration. Therein, imperfect oriented attachment process has been identified as the dominant growth mechanism for the formation of Bi_2Te_3 nanorods. At higher reaction temperature, Oswald ripening process significantly enhances the growth kinetics that modifies the Bi_2Te_3 nanorod growth process and resulted in smooth Bi_2Te_3 nanorods. The overall schematic representation of the Bi_2Te_3 nanorod growth process is given in Figure 7.1.

The major results on the TE transport characteristics on the pellet and thin film samples presented in this thesis have been summarized in Table 7.1. All pellets are exhibiting positive Seebeck coefficient (or *p*-type conductivity), while thin film are demonstrating negative Seebeck coefficient (or *n*-type conductivity). *p*-type conductivity was associated with accepter type Bi_{Te} antisite defects and *n*-type conductivity was associated with donor type V_{Te} defects. The reported values[39,169,170,188] of seebeck coefficient and thermal conductivities of Bi_2Te_3 at 300 K are in the same order as reported in the present work. However, bulk Bi_2Te_3 electrical conductivities[115,188–190] are in the order of 10^4 S/m, whereas all the pellets exhibit the poor electrical conductivity (in the order of 10^2-10^3 S/m) due to low carrier mobility values. Out of all samples, maximum power factor and figure of merit was observed for the pellet that composed of flake decorated Bi_2Te_3 nanorods.

Table 7.1: TE transport characteristics on the various materials presented in the present thesis

Sample	Seebeck coefficient, S (μV/K)	Electrical conductivity, σ (S/m)	Power factor, $S^2\sigma$ (μW/m-K^2)	Thermal conductivity, κ (W/m-K)	Figure of merit, ZT
Smooth Bi_2Te_3 nanorod pellet	215.7	2157	15.7	0.20	0.02
Flake decorated Bi_2Te_3 nanorod pellet	157.4	3603	89.3	0.13	0.20
Porous Bi_2Te_3 nanorod pellet	148.2	779	17.1	0.11	0.04
Bi_2Te_3 thin film	-79.8	7350	46.5	-	-

In the second part of the thesis work, 100 keV He^+ ion irradiation with different ion fluences was performed on Bi_2Te_3 nanorod pellet samples, in an attempt to induce native defects (*i.e.,* defect engineering strategy) with regard to the betterment of TE transport characteristics. GIXRD and FESEM investigations indicate that the polycrystalline nature and surface morphology of Bi_2Te_3 pellets were unaffected upon He^+ ion irradiation. However, HRTEM results showed the presence of amorphous surface layer in the Bi_2Te_3 nanorod, due to the accumulation of migrating point defects and defect clusters at the surface of the nanorod. Figure 7.2 displays the evolution of Bi_2Te_3 nanorod microstructure and power factor as a function of 100 keV He^+ ion fluences. Ionized impurity dominated scattering process significantly enhances the value of S in the irradiated pellets. Bi_2Te_3 pellet irradiated with higher ion fluence (2×10^{17} ions/cm^2) exhibited the maximum value of S (≈184 μV/K) at 390 K, which is 12% higher than that

of the pristine one (≈162 μV/K). Furthermore, Bi_2Te_3 nanostructured pellets irradiated up to a He^+ ion fluence of 1×10^{16} ions/cm^2 improves the thermoelectric transport properties with the highest power factor, 8.2 μW/m-K^2 at 390 K.

Moving from the above observations, the work was then focused to implement defect engineering strategy on Bi_2Te_3 thin film samples using copper doping and inert gas ion irradiations. The results showed the charge carrier type conversion (*i.e., n*-type to *p*-type) in He^+ ion irradiated Bi_2Te_3 thin films. However, upon 120 keV Ar^+ ion irradiation, the material exhibited *p*-type conductivity at lower ion fluence and *n*-type conductivity at higher ion fluences. Being a lighter ion, linear collision cascades are expected for He^+ ion irradiation, which would infuse simple type of point defects in the material. The defects appear to be mobile at room temperature through which most of them annihilate. However, stable V_{Bi} were found to increase hole density and thus expected to be responsible for the *p*-type conductivity and positive value of *S* in He^+ ion irradiated thin films. On the other hand, at higher damage (*i.e.,* in Ar^+ ion irradiated thin films); irradiation induced grain melting aids defect recovery, which would suppresses the defect density and consequently increases the electron concentration.

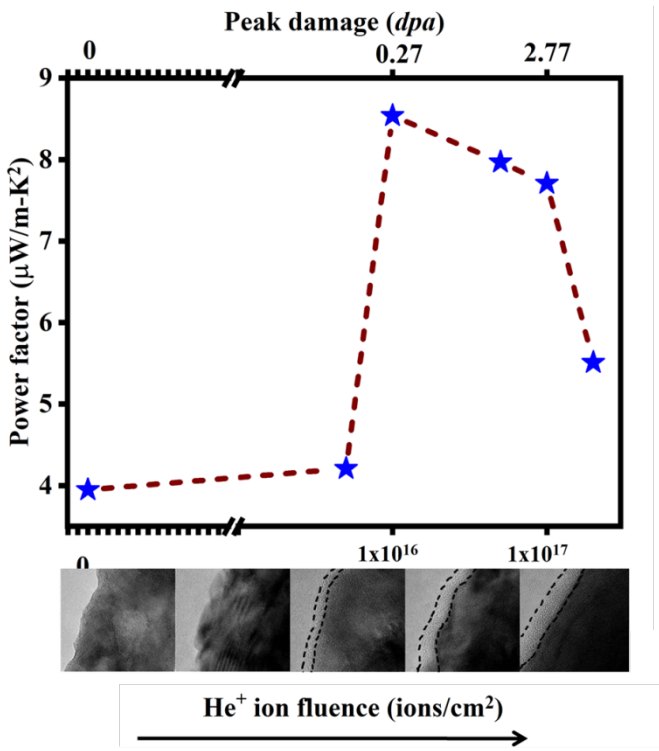

Figure 7.2: Evolution of microstructure of Bi_2Te_3 nanorod and power factor values for the corresponding Bi_2Te_3 pellets as a function of 100 keV He^+ ion fluences. Dotted line is the guide to the eye.

In case of copper doped samples, Hall-effect and Seebeck measurements showed *n*-type to *p*-type charge carrier conversion. Thermal treatment performed after Cu^+ ion implantation suppresses the defects as well as enhances the electron concentration. In other words, Cu^+ ion implanted Bi_2Te_3 thin films after annealing, it exhibits *n*-type conductivity. Significance of this results show the possibility of fabricating TE micro-modules that comprises of *n*- and *p*-type semiconductors. This *n*- to *p*-type charge carrier conversion is attributed to the high density of stable defect complexes in addition to the accepter type V_{Bi} and Cu_{Bi} defects. The amount of peak radiation damage produced by the 120 keV He^+, 120 keV Ar^+ ions, implanted copper ions for various ion fluences were quantified through 'displacements per atom' (*dpa*). Figure 7.3 displays the variation in power factor values at room temperature as a function of peak damage and it has been observed that the maximum power factor was observed in the annealed Cu^+ ion implanted Bi_2Te_3 thin films that correspond to the value of ~106.12 μW/mK^2 at 300 K.

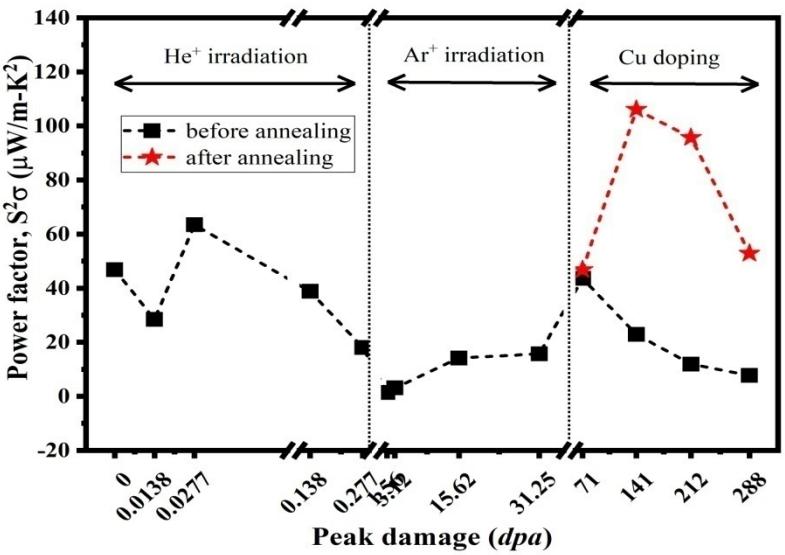

Figure 7.3: Variation in power factor values at room temperature for Bi_2Te_3 thin film sample as a function of peak damage values.

7.2. Future outlook

Nano-structuring and defect engineering are the key aspects presented in the present thesis. The significant finding of this thesis work is the observation of charge carrier type conversions upon damage production. One of the potential studies is to fabricate *p-n* junction TE devices using masked ion implantation/irradiation. However, TE performances reported in this thesis are still far from that needed for commercial applications. Therefore, different implantation conditions such as different energetic ions of various energy ranges need to be explored for the enhancement of TE performances of

materials and devices. For instances, Kennedy *et al.,*[255] achieved the 2- to 4- fold enhancement in TE performance in sulfur ion implanted bismuth antimony telluride thin films. Further, Masarrat *et al.,*[256] reported the power factor of about 700 μW/mK in iron ion implanted $CoSb_3$ thin films.

In addition, instead of focusing single phase Bi_2Te_3 nanostructured materials, the multi-phase/hybrid nanocomposite approach can offer a new way *via* the non-equilibrium transport of charge carriers. The multiphase/hybrid nanocomposite composed of secondary phase nanoparticles embedded in the matrix of other material such as in $Bi_2Te_3/Cu_{2-x}Te$[257], Bi_2Te_3 nanosheet/ MWCNT[258,259], Bi_2Te_3/graphene quantum dot[260] *etc*. The multiphase/hybrid nanocomposites will be prepared through ball milling followed by hot pressing or spark plasma sintering. It is postulated that nanocomposite contain high density of secondary phase inclusion and contains high density of imperfections. This in turn improves TE performances by phonon scattering, energy filtering, and modulation doping. The ability to tune the property of the multi-phase nanocrystalline material by controlling the material composition, crystallite size and its distribution as well as manipulating the interface potential barrier height by alloying without deteriorating the nanocrystalline quality offers extra degrees of freedom for creating material structures with novel electrical properties.

Abstract

Fabrication of highly efficient thermoelectric (TE) devices is necessary to convert waste heat into electrical energy effectively. There has been a continuous strive to achieve, enhance, and optimize the TE materials. Efficient TE materials are obtained by optimizing the value of dimensionless figure of merit (*ZT*), which can be expressed as $ZT = S^2\sigma T/\kappa$, where S, σ, and κ represents the Seebeck coefficient, electrical conductivity, and thermal conductivity respectively. The Seebeck coefficient and electrical conductivity are correlated *via* electronic band structures and often combined into the quantity called power factor ($S^2\sigma$). State-of-the art TE materials need to have high electrical conductivity, high Seebeck coefficient and low thermal conductivity values.

Bismuth telluride (Bi_2Te_3) is one of the intensively studied and commercialized room temperature TE materials that are exhibiting highest values of *ZT* (~1) for very long time. In case of bulk material, improving the *ZT* values beyond the value of 1 is extremely difficult, owing to the interdependency of TE transport properties (*i.e.,* power factor and thermal conductivity). Nanostructuring and defect engineering are the effective strategies to improve and optimize the TE transport properties of materials. In nanomaterials, power factor can be potentially increased by quantum size effects and the thermal conductivity can be decreased due to enhanced scattering. The present thesis aims at optimizing the growth conditions of Bi_2Te_3 nanostructures and further focused to investigate: (i) effectiveness of TE transport properties of nanostructured Bi_2Te_3 materials, (ii) copper doping effects on the TE properties of Bi_2Te_3 thin films, and (iii) the contribution of defects to the TE transport properties of nanostructured bismuth telluride pellets and thin films.

In the first part of the thesis, the growth conditions of Bi_2Te_3 nanostructures were optimized using a surfactant assisted hydrothermal method and a growth mechanism was proposed. The surfactant acts as a template for Bi_2Te_3 nuclei and influences the shape of the Bi_2Te_3 nanoparticles. The concentration of SDBS dictates the degree of capping effect and also ultimately controls the agglomeration of Bi_2Te_3 nuclei through the imperfect oriented attachment (OA) process. Oswald ripening (OR) mechanism plays an additional factor in smoothening of the Bi_2Te_3 nanorods especially at high reaction temperatures. The samples were predominantly composed of Bi_2Te_3 nanorods with different surface morphologies (*i.e.,* flake decorated, porous, and smooth nanorods) and were compressed to form a pellets. The TE transport properties of these samples were subsequently investigated.

In the second part, 100 keV He^+ ion irradiation was employed to induce defects (*i.e.,* defect engineering strategy) in Bi_2Te_3 pellets and the morphological, structural, and TE transport properties were systematically investigated. HRTEM results showed the presence of an amorphous surface layer on the Bi_2Te_3 nanorod, which eventually hinder the out-of-plane atomic displacements (*i.e.,* A_u^2 and A_g^2 mode) in the Raman spectra. The mechanism of the formation of amorphous surface layer was proposed based on thermal spike model. As far as TE transport properties are concerned, He^+ ion irradiation increases the carrier concentration, at the same time preserves the *p*-type conductivity. The defects such as vacancies, interstitials, and defect clusters are the strong perturbation in the lattice sites, which in turn act as charged coulomb scattering centers. It leads to impurity dominated scattering process, which eventually limits the carrier mobility and hence the electrical conductivity. In contrast, the above mechanism aids to improve the Seebeck coefficients and power factor in the irradiated pellets.

Ion implantation was employed on Bi_2Te_3 thin films to incorporate Cu atoms with concentrations of 0.5 *at%*, 1 *at%*, 1.5 *at%*, 2 *at%*. From FESEM results, the grains appeared to be melted and coalesced upon Cu^+ ion implantation. GIXRD results demonstrated that crystallinity was suppressed greatly in Cu^+ ion implanted Bi_2Te_3 thin films. As far as Hall effect and Seebeck measurements are concerned, charge carrier type were change from *n*-type to *p*-type after Cu^+ ion implantation. The complicated counterbalance between acceptor and donor type of ion beam induced stable defect complexes, in addition to implanted Cu atoms, changes the net charge carrier type and is responsible *p*-type conductivity in Cu^+ ion implanted films. The annealing was carried out on Cu^+ ion implanted Bi_2Te_3 thin film at 150 ^oC for 2 hr and the charge carrier type turned back from *p*-type to *n*-type. The annealing process decreases the density of defects that resulted in reduction of hole concentration and subsequent increases in the electron concentration.

Finally, defect engineering strategy was employed in Bi_2Te_3 thin film using inert gas (120 keV He^+ and 120 keV Ar^+) ion irradiation. From FESEM results, one can see that the He^+ ion irradiation did not affected the grainy morphology of the Bi_2Te_3 thin films. In contrast, the grains has appeared to be melted and coalesced upon Ar^+ ion irradiation. Furthermore, from Hall-effect and Seebeck coefficient measurements, charge carrier type conversion (*i.e., n*-type to *p*-type) is observed in He^+ ion irradiated Bi_2Te_3 thin films. However, upon 120 keV Ar^+ ion irradiation, the material exhibited *p*-type conductivity at lower ion fluence and *n*-type conductivity at higher ion fluences. Being a lighter ion, linear collision cascades are expected upon He^+ ion irradiation, which would infuse simple type of

point defects in the material. This could be corroborated with the Raman scattering results, where the activation of the forbidden (*i.e.,* A_u^2) mode is associated with irradiation-induced defects and the intensity of A_u^2 mode is observed to increase with He^+ ion fluence. The V_{Bi} were found to increase hole density and thus expected to be responsible for the *p*-type conductivity and positive value of *S* in He^+ ion irradiated thin films.

On the other hand, at higher damage (*i.e.,* in Ar^+ ion irradiated thin films); the observed irradiation induced grain melting aids defect recovery, which would decreases the defect density and consequently increases the electron concentration (*i.e., n*-type conductivity). In Ar^+ ion irradiated samples, suppression of defects is evidently seen in Raman scattering results, where the intensity of the forbidden mode (*i.e.,* A_u^2) is apparently decreasing with Ar^+ ion fluence. Furthermore, the observed trend in the value of *S* upon Ar^+ ion irradiation is ascribed to the suppression of hole density along with the increase in the electron concentration. Overall, the present thesis work suggests that ion irradiation can be used for conversion of charge carrier (*n*- to *p*-type) which provides a scope of fabricating TE micro modules that comprises of *p*- and *n*-type semiconductors.

Chapter 1

Role of defects in thermoelectric materials- A brief review

1.1. Introduction

Heat and electricity are inseparable and crucial sources of energies, required for the sustainable socio-economic growth of the human race. For the past several decades, fossil fuel plays a significant role in industrial revolution and socio-economic development progresses. Fossil fuel serves the 70% of the requirements of global energy demand. However, there is always urgent need for the alternative sustainable technology, in order to balance the role of energy in socio-economic development, and to overcome the catastrophic impacts of fossil fuel usage.

One of the potential and hopeful techniques to manage the waste thermal energy for global energy crises are the thermoelectric generator (TEG)[1–4]. TEGs are the long-lasting, maintenance-free, eco-friendly, solid-state energy conversion devices with no moving parts. TEG's are used primarily for power generation, refrigeration and sensing purpose, where the cost is not a primary concern[5]. TEGs offer a possibility to utilize the waste heat by creating temperature difference to generate usable electric power. Conversely, electric current induces the temperature gradient, which in turn used for cooling purposes without any hazardous gas emissions.

In general, TEGs are less likely to replace the conventional steam engine for the power generation. This is due to the low conversion efficiency nature of TEG's. However, TEGs are suitable for the applications in the remote areas such as aerospace craft, and satellites, where repairing is difficult[6,7]. For instances, deep space exploring satellites such as Voyager 1 and 2 powered by radioisotope based thermoelectric generator (RTG) that converts the heat released by naturally decaying Pu-238[7,8]. In addition to that, TEGs could play a crucial role in our society for waste heat management to improve the efficiency of the overall system performances, such as in automobile and industry.

The mechanism of direct conversion between thermal energy and electrical energy is termed as thermoelectric effect. In fact, thermoelectric effect comprises of three generic thermodynamically reversible effects such as Seebeck effect, Peltier effect, and Thomson effect.

1.1.1. Seebeck effect

In 1821, German physicist 'Thomas Johann Seebeck' found that, in a thermocouple circuit (Figure 1.1) formed by two dissimilar metals A and B, the electrical potential difference (ΔV) would build up between C and D, when the junctions are maintained at different temperatures (T_c and T_h).

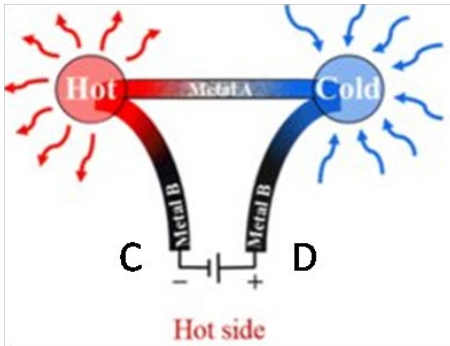

Figure 1.1: Schematic of thermocouple circuit formed by two dissimilar metals[9].

The developed potential difference (or thermoelectric voltage) is proportional to the temperature difference (ΔT) and the constant of proportionality is termed as Seebeck coefficient or thermopower (S) (Eqn. 1.1), which is in the units of $\mu V/K$.

$$S = \frac{\Delta V}{\Delta T} \qquad \textbf{Eqn. 1.1}$$

S dictates the intrinsic property of the material, where the magnitude of S depends on the type of material and the sign is in accordance to the type of majority charge carrier, which can be positive or negative for holes and electrons respectively.

1.1.2. Peltier effect

Peltier effect was discovered by the French physicist 'Jeans Charles Athanase Peltier' in 1834, which is found complimentary to the Seebeck effect. In a circuit consisting of dissimilar metals with self-driving electric current, heat will be generated at one junction as well as heat will be absorbed at other junction. In other words, the junctions will behave as a heater and cooler. The rate of heating or cooling (dQ/dt) is proportional to the applied current (i), and the relation is written as in Eqn. 1.2.

$$\frac{dQ}{dt} = i(\Pi_A - \Pi_B) \qquad \textbf{Eqn. 1.2}$$

where, Π_A and Π_B are the peltier coefficients of material A and B respectively. The Peltier coefficient is defined as the amount of heat is absorbed or evolved at any one of the

junctions when one coulomb of charge passes through it. It is expressed in the units of volts.

1.1.3. Thomson effect

In 1854, British physicist 'William Thomson' observed the correlation between Seebeck and Peltier effects. Thomson effect relates to the emission or absorption of the reversible heat, which results from the passage of current along the material, which there is a temperature gradient. The rate of heat generation or absorption (dQ/dt) is proportional to the applied current (i) and temperature gradient (ΔT) as in Eqn. 1.3.

$$\frac{dQ}{dt} = \tau i \Delta T \qquad \textbf{Eqn. 1.3}$$

where τ is the Thomson coefficient, which is defined as the amount of energy absorbed or released, when one coulomb of charge passes through the unevenly heated material.

1.1.4. Thermoelectric power generator

Figure 1.2 shows the schematic model of the power generator in which heat from any available sources applied at one end of the TE thermocouple, comprised of *p*- and *n*-type semiconductor. In practice, many TE thermocouples are needed to fabricate the practical TE devices. In a TE module, an applied temperature gradient causes the charge carriers (electrons in case) to diffuse from hot side to cold side. Thus, higher density of charge carrier continues to build up at the cold side, until the force due to coulomb repulsion balances the forces of thermal diffusion. This results in the generation of voltage across the material.

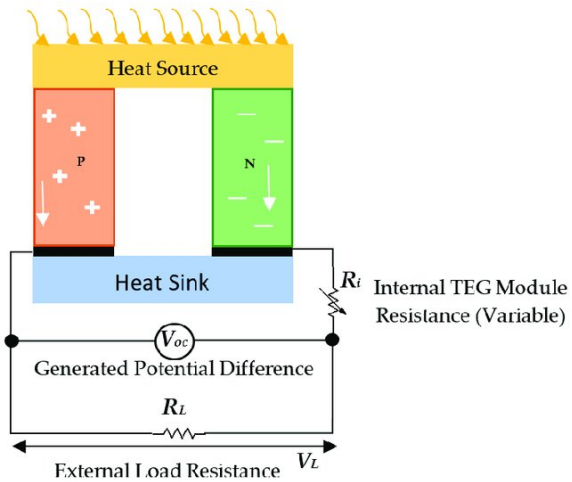

Figure 1.2: Schematic of TE module in power generator[10].

1.2. Thermoelectric transport properties in materials

1.2.1. Figure of merit, *ZT*

Efficiency of the ideal TE power generator is our quantity of interest, which is defined as the ratio of the electrical power delivered to the load to the heat absorbed at the hot junction. In 1910, Altenkirch mathematically obtained the relationship between the properties of TE material and power generator efficiency[11]. However, Ioffe[12] simplified the above relationship to calculate the maximum efficiency of the TE power generator using the complex and material characteristic parameter 'Z'. As given in Eqn. 1.4, the maximum efficiency (η_{max}) is defined as the product of the Carnot efficiency (η_c) (Eqn. 1.5) and γ (Eqn. 1.6) that incorporated the TE materials properties.

$$\eta_{max} = \eta_c \gamma \qquad \textbf{Eqn. 1.4}$$

$$\eta_c = \frac{T_h - T_c}{T_h} \qquad \textbf{Eqn. 1.5}$$

and

$$\gamma = \frac{\sqrt{1+ZT} - 1}{\sqrt{1+ZT} + {}^{T_c}/_{T_h}} \qquad \textbf{Eqn. 1.6}$$

where, T_h, T_c are the respective temperatures at hot and cold side. The parameter '*Z*' is the thermoelectric figure of merit that turned up into dimensionless quantity by multiplying it with absolute temperature *T*. This dimensionless figure of merit '*ZT*' (given in Eqn. 1.7) yields the potential efficiency of the TE effect, and it directly relates the respective electrical and thermal properties of the TE material. The value of *ZT* is given as in,

$$ZT = \frac{S^2 \sigma T}{\kappa} \qquad \textbf{Eqn. 1.7}$$

where, S, σ, κ represents the Seebeck coefficient, electrical conductivity, and thermal conductivity respectively. According to the Eqn. 1.7, the state-of-art thermoelectric materials will have high Seebeck coefficient (S) and electrical conductivity (σ) as in conductors and low thermal conductivity (κ) as in insulators. Moreover, Seebeck coefficient and electrical conductivity are dependent upon electronic transport property and often combined into the quantity called power factor ($S^2\sigma$).

1.2.2. Electrical conductivity (σ)

Electrical conductivity (σ) is the charge current density ($\vec{J}$) per unit electric field ($\vec{E}$) in the absence of temperature gradient ($dT/dx = 0$). In other words, electrical

conductivity quantifies the number of charge carriers (n) that contribute the electrical current (Eqn. 1.8).

$$\sigma = ne\mu \qquad \textbf{Eqn. 1.8}$$

Since carrier mobility (μ) is correlated with carrier relaxation time (τ) and carrier effective mass (m^*), electrical conductivity can be rewritten as in Eqn. 1.9.

$$\sigma = \frac{ne^2\tau}{m^*} \qquad \textbf{Eqn. 1.9}$$

High values of electrical conductivity are desired for any thermoelectric materials for better performances. In other words, thermoelectric material should posses high carrier concentration, high mobility, and low effective mass. Moreover, Ioffe[12] observed that good thermoelectric material are heavily doped semiconductors with optimum carrier concentration of 10^{19}-10^{21} /cm^3.

1.2.3. Seebeck Coefficient

Seebeck coefficient is the measure of electric field ($\vec{E}$) per unit temperature difference (dT/dx) in the absence of charge current density ($\vec{J}=0$). Seebeck coefficient is dependent on the density of states in the band structure and it is more meaningful near the Fermi level. Generally, the changes in the average energy of the carriers from the Fermi energy dictate the behavior of Seebeck coefficient. The most generic form of Seebeck coefficient is given in Eqn. 1.10 and it is directly proportional to difference between the average energy (E) of the electrons in the band weighted by its relaxation time (τ) and its Fermi energy E_F.

$$S = \pm\frac{1}{eT}\left(\frac{\langle\tau E\rangle}{\langle\tau\rangle} - E_F\right) \qquad \textbf{Eqn. 1.10}$$

For example, the increase in temperature leads to increase in carrier concentration and hence the average energy $\langle E\rangle$, resulted in high values of S. Mott established the simple relationship between S and σ using Boltzmann transport distributive functions (Eqn. 1.11).

$$S = \frac{\pi^2 k_B^2 T}{3e}\left[\frac{d(ln\sigma(E))}{dE}\right]_{E=E_F} \qquad \textbf{Eqn. 1.11}$$

using Eqn. 1.9 in Eqn. 1.11, S become,

$$S = \frac{\pi^2 k_B^2 T}{3e}\left[\frac{g(E)}{n(E)} + \frac{1}{\mu(E)}\frac{d\mu(E)}{dE}\right]_{E=E_F} \quad \textbf{Eqn. 1.12}$$

It is thus found from Mott relations (Eqn. 1.12) that *S* measures the variations in *σ(E)* above and below Fermi level, specifically through the logarithmic derivative of electrical conductivity at Fermi energy. It means that, *S* is more sensitive to the changes in the density of states rather than electrical conductivity. In other words, *S* is the measure of asymmetry in the electronic band structures and scattering rate near Fermi level. In the case of single band degenerate semiconductors, there is an energy dependent carrier scattering process ($i.e., \tau(E) \propto E^r$), then Seebeck coefficient can be written as a function of carrier concentration (*n*), density of states effective mass (m_d*), and scattering parameter (*r*) (Eqn. 1.13).

$$S = \frac{8\pi^2 k_B^2 T m_d^*}{3eh^2}\left(\frac{\pi}{3n}\right)^{2/3}\left(\frac{3}{2} + r\right) \quad \textbf{Eqn. 1.13}$$

It is evident from the Eqn. 1.13, that Seebeck coefficient could be enhanced either by increasing energy dependent scattering mechanism or by incorporating asymmetries in the density of states.

For constant relaxation time ($\tau(E) = constant$), *σ(E)* is proportional only to density of states. Therefore, in this case, the Seebeck coefficient for degenerate semiconductors is simply rewritten as in the Eqn. 1.14.

$$S = \frac{8\pi^2 k_B^2}{3eh^2} m_d^* T\left(\frac{\pi}{3n}\right)^{2/3} \quad \textbf{Eqn. 1.14}$$

where, k_B, *h*, *e* represents Boltzmann constant, Planck constant and electric charge respectively. As discussed earlier, the sign of the Seebeck coefficient can be positive or negative in accordance with the type of predominant charge carriers. The Seebeck coefficient of the solid having bipolar conduction or mixed type of charge carriers (*i.e.,* electrons and holes) such as in semimetals and narrow band semiconductors can be expressed by the weighted average value of their respective conductivities (σ_e and σ_h) (Eqn. 1.15).

$$S = \frac{S_e\sigma_e + S_h\sigma_h}{\sigma_e + \sigma_h} \qquad \textbf{Eqn. 1.15}$$

The bipolar effect faces a serious disadvantage especially at high temperature and decreases the overall Seebeck coefficient values. The thermoelectric materials having larger band gap will effectively depress the bipolar effects.

1.2.4. Thermal conductivity

The total thermal conductivity (Eqn. 1.16) is mainly composed of two components: electronic thermal conductivity (κ_e) and lattice thermal conductivity (κ_l).

$$\kappa = \kappa_e + \kappa_l \qquad \textbf{Eqn. 1.16}$$

The electronic thermal conductivity (κ_e) is similar to electrical conductivity (σ). In the former case, the charge carriers transport heat instead of charge. Electronic thermal conductivity is defined as ratio of heat current density (Q) per unit temperature gradient (dT/dx) in the absence of charge current density (J=0). The Wiedemann-Franz law (Eqn. 1.17) relates the electronic thermal conductivity to the electrical conductivity and temperature 'T' through the factor 'L', which is referred as Lorentz number.

$$\kappa_e = L\sigma T \qquad \textbf{Eqn. 1.17}$$

For most metals and degenerate semiconductors, the Lorentz number is fixed to the value of 2.45×10^{-8} $W\Omega K^{-2}$. According to Wiedemann-Franz law, electronic thermal conductivity related directly to electrical conductivity and hence appropriate carrier concentration, and mobility are required. In contrast, the expression for the lattice thermal conductivity due to propagation of phonon is given as in Eqn. 1.18.

$$\kappa_l = \frac{1}{3}C_V l v_s \qquad \textbf{Eqn. 1.18}$$

where, C_V, l, v_s are specific heat at constant volume, phonon mean free path, and velocity of sound waves respectively. The phonon is the quantum of lattice vibrations, which carry most of the thermal energy in the solid, have a wide spectrum of wavelengths and propagate throughout the solid. In general, phonon mean free path has been affected primarily by the phonons scattering with crystal boundary and by lattice imperfections. At sufficiently low temperatures (*i.e.*, below Debye temperatures), number of available phonon would be very less. The phonon mean free path becomes comparable with the geometrical dimensions of the solids and thus lattice thermal conductivity becomes the function of C_V, which varies as T^3. At high temperatures (*i.e.,* above Debye temperature),

the C_V approaches the classical value of *3R*, where R is the gas constant (also refers to Dulong-petit limit). In our case, Debye temperature for *n*-type and *p*-type bulk Bi_2Te_3 is 140 K and 152 K respectively[13]. Therefore, at room temperature, C_v can be approximated by Dulong-petit limit and thus the phonon mean free path is the main factor that determines the lattice thermal conductivity in Bi_2Te_3materials.

1.2.5. Thermoelectric transport properties – Key issues and challenges

In general, all these TE transport parameters (S, σ, κ) coupled with each other through electronic band structure and it will be difficult to manipulate the individual parameters without affecting other[14]. For instances, dependence of '*ZT*' on carrier concentration is shown in Figure 1.3. In order to utilize TE materials for practical applications, the numerical value of *ZT* should reach 3, so that 50% Carnot efficiency would be achieved. Starting point of optimization of any TE material was established *via* carrier concentration optimization. Earlier work on thermoelectrics material focuses only metals, and hence yielded low values of *ZT*[15]. The maximum values of *ZT* are reached in heavily doped semiconductor, where the carrier concentration is around 10^{19} to 10^{21} /cm^3. Meanwhile, further optimizations were done either by selectively improving power factor values or by decreasing lattice thermal conductivity values without affecting other parameters much.

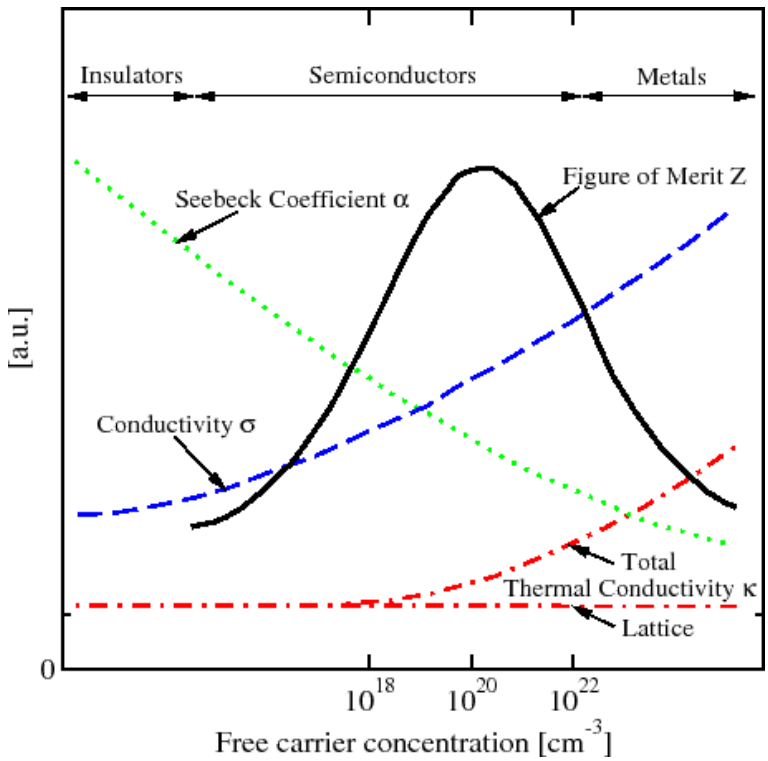

Figure 1.3: Carrier concentration dependence on TE transport properties[16].

1.3. Bismuth telluride (Bi_2Te_3) - semiconducting thermoelectric material

Bismuth telluride (Bi_2Te_3)[17–19] based TE materials have been identified as the important class of TE materials that are exhibiting highest values of ZT (~1) around room temperature for very several decades. Meanwhile, TE devices fabricated using Bi_2Te_3 are widely used in the fabrication of sensors, Peltier cooling devices, and low power TE power generators. In general, Bi_2Te_3-based compounds offer a large number of structural and chemical degree of freedom, which can be utilized to enhance and to optimize TE transport properties effectively.

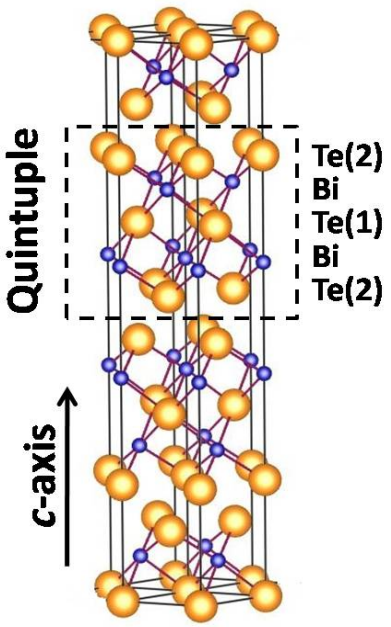

Figure 1.4: Schematic representation of Bi_2Te_3 hexagonal unit cell[20].

Bi_2Te_3 is the narrow band semiconductor with indirect band gap of ~0.12 eV. Crystallization of the Bi_2Te_3 is rhombhohedral with space group of $R\bar{3}m$, while it is often convenient to visualize in hexagonal unit cell. Figure 1.4 displays the schematic representation of Bi_2Te_3 unit cell along *c*-axis. The Bi_2Te_3 crystal structure[21,22] comprised of 3 fundamental blocks namely quintuple layers, while each quintuple layer is made up of isolated five atomic planes, consist of Bi and Te atoms, in a sequence of Te(2)-Bi-Te(1)-Bi-Te(2). Here, Te(1) and Te(2) are used to distinguish two different coordination environment. Te(1) is surrounded by six Bi atoms, while Te(2) is surrounded by three Te atoms and three Bi atoms. The bonds between Bi and Te atoms are strongly covalent, while the adjacent quintuple layers (*i.e.,* between Te(2)-Te(2)) interact *via* Vander-Waals interaction. Layered structure of Bi_2Te_3 and weak Te(2)-Te(2) bonds allow

easy cleaving along quintuple layers and resulted in the establishment of crystallographic directions that are parallel and perpendicular to the *c*-axis.

The anisotropic crystal structure of Bi_2Te_3 also affects the electrical and thermal conductivities as well. For instances, electrical and thermal conductivities in parallel to *c*-axis are always reported to be higher that of in perpendicular to *c*-axis. However, Seebeck coefficient is always isotropic. Over all, Bi_2Te_3 crystal is found to be efficient TE material, when it is oriented in a direction perpendicular *c*-axis despite these anisotropies.

According to earlier reports [23,24], it can be stated that efficient TE materials are likely to have multi-valley semiconductor with several equivalent band (*i.e.,* band degeneracy), high carrier mobility, and highly symmetric crystal structure with many atoms per unit cell. Studies on the band structure of Bi_2Te_3-based TE materials[25–27] have reported that the material possesses complex electronic band structures and thereby has high band degeneracy, low effective mass, high carrier mobility and relatively low thermal conductivity values. Furthermore, Bi_2Te_3 offers a potential freedom to implement various strategies to improve TE efficiency, which explains why this class of material makes best TE material. On the flip side, narrow bandgap of Bi_2Te_3 affects the TE efficiency particularly at higher temperature. The stoichiometric bulk Bi_2Te_3 exhibits *p*-type conductivity. However, conductivity can be tuned by controlling intrinsic point defects in the material. It has to be mentioned that the nature of the carrier type in Bi_2Te_3 materials strongly depended on the intrinsic point defects[28–31], leading to intensive efforts to study the role of point defects on its TE transport properties variation.

Table 1.1: Formation energy (E_f) for antisite defect (Te_{Bi}, Bi_{Te-1}, Bi_{Te-2}) and vacancies defect (V_{Bi}, V_{Te-1}, V_{Te-2}) in Bi_2Te_3 at Bi rich and Te-rich conditions[28,30].

System	E_f (eV)	
	Bi-rich	Te-rich
Te_{Bi}	1.19	0.42
Bi_{Te-1}	0.29	1.06
Bi_{Te-2}	0.72	1.49
V_{Bi}	2.11	1.65
V_{Te-1}	1.18	1.49
V_{Te-2}	1.42	1.73

The most common intrinsic type of point defects in Bi_2Te_3 are (1) Bi vacancy (*i.e.,* V_{Bi}), (2) Te vacancy (*i.e.,* V_{Te}), (3) replacement of Te atoms on Te sub-lattice by Bi atoms (*i.e.,* Bi antisite defect, Bi_{Te}), and (4) replacement of Bi atoms on Bi sub-lattice by Te atoms (*i.e.,* Te antisite defect, Te_{Bi}). The formation energy (Table 1.1) of all these point defects under Bi-rich and Te-rich growth conditions were estimated using DFT

calculations[28,30]. The most dominant point defect are antisite defect on both Bi and Te sub lattice, where acceptor type Bi_{Te} is dominant at Bi-rich condition and donor type Te_{Bi} is dominant at Te-rich condition. In other words, Bi-rich Bi_2Te_3 is *p*-type due to Bi_{Te} defects, while Te-rich Bi_2Te_3 is *n*-type owing to Te_{Bi} defects.

Solids grown from stoichiometric melt will always be Bi-rich and exhibit *p*-type conductivity. However, depending on the growth and processing conditions, material having wide range of Bi:Te stoichiometric ratio can be prepared. For instances, stoichiometric Bi_2Te_3 thin films[32–35] always reported to have *n*-type conductivity, owing to the infusion of doubly ionized donor type V_{Te} defects, resulting from the re-evaporation of TE atoms during thin film fabrication, owing to the higher vapor pressure of Te atoms, when compared to that of Bi atoms. Meanwhile, tuning of charge carrier type and density in Bi_2Te_3 can be established in Bi_2Te_3 *via* various strategies which will be discussed in later sections.

1.4. Strategies to improve thermoelectric transport properties in materials

1.4.1. Alloying

The research on state-of-art TE materials in 1950s was restricted to bulk materials that mainly emphasis the reduction of lattice thermal conductivity without affecting its electrical properties. Early works on TE material, particularly by Ioffe proposed generic strategy for the improvement of TE figure of merit through the process called solid solution alloying[24]. In fact, the solid solution alloying with isomorphous process (*i.e.,* substances with similar crystal structure) would scatter the phonons due to disturbance in the lattice short-range order, while preserving the carrier mobility. In 1950s, Bi_2Te_3 and Sb_2Te_3 alloys were the most widely used TE materials. Yim *et al.,*[18] reported that the alloying of *p*-type Bi_2Te_3 with Sb_2Te_3 or Bi_2Se_3 would increase figure of merit considerably and reported the highest *ZT* value of 0.9 at 273 K for Bi_2Te_3-Sb_2Se_3-Sb_2Te_3 pseudo ternary alloys.

Recently, Powdel *et.al.,*[36] reported the *ZT* value of 1.4 at 334 K for bulk *p*-type BiSbTe alloy, prepared through ball milling and hot pressing. In addition to that, PbTe-PbSe solid solution alloy and SiGe alloy are the good high temperature thermoelectric materials, with ZT values of 1 at 700 K and 1100 K respectively[3]. Nowadays, the search for the state-of-art bulk thermoelectric materials extending to the materials having complex crystal structures such as skutterudites and clathrate, ignited from the concept of PGEC (*i.e.,* phonon glass and electron crystal) as suggested by Slack *et al.*,[37,38]. These

types of materials will lack a long-range order and causes the atoms to rattle. This in turn will enhance the phonon scattering and thus low lattice thermal conductivity, which has been reported to have maximum *ZT* values of around 1 to 1.5 especially at high temperatures (over 700 K).

1.4.2. Nanostructure engineering

Nanostructuring[39] is one of the effective strategies to scale up the figure of merit (*ZT*) of TE materials by simultaneously increase power factor and reduce lattice thermal conductivity. In 1993, Hick and Dresselhaus[40–43] triggered the pioneered research on nanostructured TE materials with the help of theoretically modeled quantum-well structures and one-dimensional conductors. The key concepts of efficiency enhancements in nanostructured TE materials are based on quantum confinement and corresponding changes in the density of states. The density of states for multi-dimensional materials is related to their dimensionality (*D*), ground state energy level (E_o) and its confinement length scale (*a*) and it is given by,

$$g(E) \propto \frac{(E - E_o)^{\left(\frac{D}{2}-1\right)}}{a^{3-D}} \qquad \textbf{Eqn. 1.19}$$

The exponent $D = 3, 2, 1$ refers to the corresponding dimensionality factor for bulk materials, quantum well and nanowires. The energy dependence of density of states ($g(E)$) is changed from $\frac{1}{2}$ for bulk materials to 0 for quantum well to $-\frac{1}{2}$ for nanowires and is schematically represented in the Figure 1.5. In addition to that, there is an inverse correlation between density of states and thickness of the quantum wells or nanowires, which implies that increasing number of density of states as confinement length scale decreases.

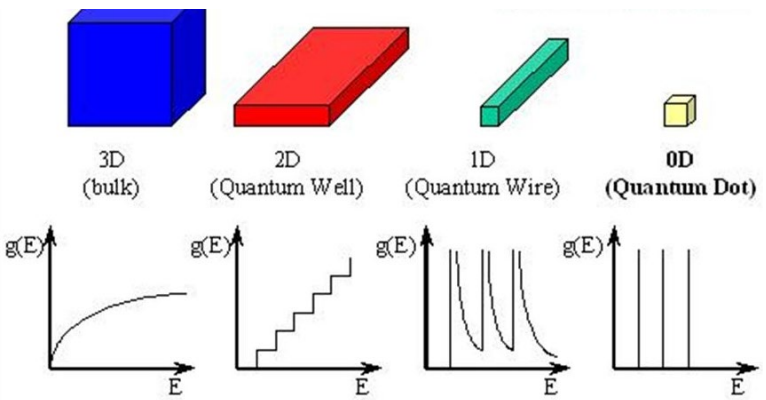

Figure 1.5: Energy dependent g(E) for bulk and nanostructured materials[39,44].

According to Mahan *et al.,* [23] the best thermoelectric material would have sharp features in density of states. Since, the Seebeck coefficient is related to the derivative of electronic density of states at Fermi level (*i.e.,* Mott relation). Therefore, an enhanced value of Seebeck coefficient is expected possibly in these low dimensional materials. For the first time, Venkatasubramanian *et.a.,l*[45] experimentally achieved the high *ZT* values of about 2.4 for *p*-type Bi_2Te_3/Sb_2Te_3 super lattice fabricated by chemical vapour deposition process, which was the benchmark record for Bi_2Te_3 alloys up to date. This extraordinary *ZT* value is explained due to two factors: an extremely low lattice thermal conductivity owing to the phonon back reflection at the Bi_2Te_3/Sb_2Te_3 interfaces and cross-plane and in-plane mobility are equal.

On the other hand, a nanostructured material shows the dramatic reduction in the lattice thermal conductivity. For instances, Zhang *et al.,*[46] reported the ultra thin Bi_2Te_3 wire, which exhibit the enhanced *ZT* of 0.94 (*i.e.*, 13% enhancement) at 380 K, due to the significant reduction of thermal conductivity values. In addition, inclusion of nano-structured grains in the matrix of the bulk thermoelectric materials (*i.e.,* nano-composites) also suppresses the lattice thermal conductivity greatly. For example, Bi_2Te_3 nanotubes embedded nanocomposite possesses holey low dimension structures (like in PEGC) and thereby reported the *ZT* value of ~1 at 420 K[47]. The nano-composites usually fabricated either by hot pressing or by spark plasma sintering of nanostructured powders. In both cases, nano-structured interfaces, grain boundaries, atomic defects will acts as an effective energy filterers and scattering centers. They will effectively scatter the wide range of phonon spectra without affecting the electron mean free path. Particularly, the efficient scattering of mid- to long- wavelength phonons are accomplishing at nano-structured interfaces, and short-wavelength phonons are scattered by the atomic-level point-type defects such as vacancies, interstitials, and extrinsic dopants.

1.4.3. Electronic band structure engineering

Electronic band structure engineering[48,49] offers an immense opportunity to significantly improve the values of *ZT* through the enhancement of thermoelectric material electronic performances (*i.e.,* power factor), which is related to its Seebeck coefficient (S) and electrical conductivity (σ). The Seebeck coefficient of thermoelectric material at any given concentration is directly proportional to the density of states effective mass (m_d^*). Materials having flat bands and multiple degenerate valleys (*i.e.,* N_V) possess high m_d^* and affect the charge carrier mobility and eventually suppress electrical conductivity.

Pei *et al.,*[49] experimentally attempted to correlate m_d^* with thermoelectric performances using I- and La- doped PbTe. The m_d^* of La-doped PbTe near optimal carrier concentration is found to have 20% higher than I-doped PbTe. It may be noted that N_V was four in both cases. As analogues to the higher Seebeck coefficient of La-doped PbTe, the overall power factor and *ZT* values are found to be 20% lower than that of I-doped PbTe as shown in Figure 1.6. This was mainly due to the subsided values of charge carrier mobility in La-doped PbTe.

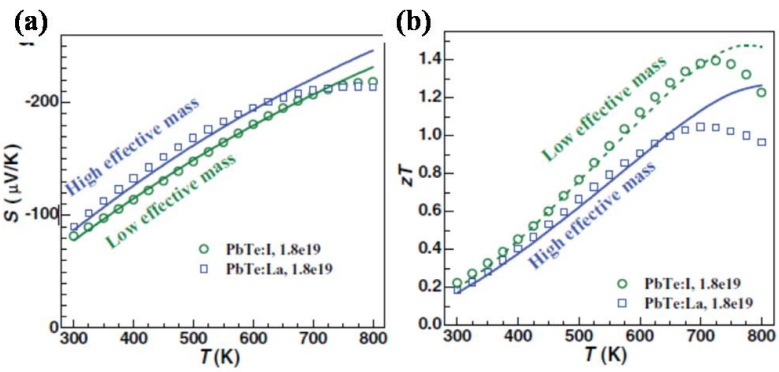

Figure 1.6: Seebeck coefficient (S) and figure of merit (ZT) as a function of temperature for I- and La doped PbTe[49].

It is thus clear that m_d^*enhancement strategy could be applicable to improve *ZT* of any material if and only if the carrier mobility is not affected during the doping processes. Therefore, Jaworski *et al.,*[50] utilized the resonant-doping approach in Bi_2Te_3 to improve the value of *ZT* without affecting carrier mobility much. In general, resonant doping such as Sn, Ge creates an additional energy level (also called resonant level) in Bi_2Te_3 near the valence or conduction band edges and enhances the asymmetry in the density of states near Fermi level (shown in Figure 1.7 (a)).

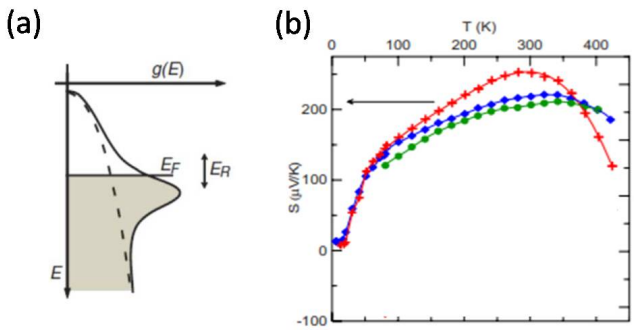

Figure 1.7: (a) Schematic representation of enhancement in density of states via resonant doping. (b) Temperature dependent Seebeck coefficient values for Sn doped Bi_2Te_3. The symbols are: $Bi_{1.9975}Sn_{0.0025}Te_3$ (red plus), $Bi_{1.9925}Sn_{0.0075}Te_3$ (blue diamond) and $Bi_{1.985}Sn_{0.015}Te_3$ (green dot)[50]

This resulted in high m_d^* and Seebeck coefficient values. Resonant doping with Sn provides excess density of states below the valence band edge of Bi_2Te_3, significantly improving electronic density of states near Fermi level and boosting Seebeck coefficient values (Figure 1.7 (b)). In fact, rigorous control on doping and dopants energy levels determines the beneficial applicability of resonant-doping approach for better thermoelectric performances. The resonant doping approach has implemented successfully in many materials like Al-doped PbSe[51], Ge-doped Bi_2Te_3[52,53], In-doped SnTe and GeTe[54] for improved thermoelectric performances.

As analogous to the above strategies, band convergence approach[49] offers a remarkable opportunity by converging valence or conduction band edges, mainly to achieve high valley degeneracy (N_V) in the electronic band structures. This is usually attempted by tuning the energy offset between multiple conduction (or valence band) edges in a properly doped or alloyed high symmetry crystals such as $Si_{1-x}Ge_x$, $PbTe_{1-x}Se_x$[55], $Sn_{1-x-y}In_xMn_yTe$[56], $Mg_2Si_{1-x}Sn_x$[57]. In fact, large valley degeneracy (N_V) have a positive effect on improving m_d^* without its affecting carrier mobility. For instances, Figure 1.8 shows the band structure of *p*-type $PbTe_{0.85}Se_{0.15}$ having primary valance band edge at L point with N_V = 4 and the secondary valence band edge with N_V = 12 along ∑ point[55]. The corresponding energy difference between two valance band edges is 0.2 eV. At 500 K, these two band edges converges, resulting in enhancement of N_V (=16) and thus enables better thermoelectric performances (*i.e., ZT* = 1.8). Similarly, alloying Bi_2Te_3 with Sb_2Te_3 (particularly in $Bi_{0.5}Sb_{1.5}Te_3$ alloy) has been suggested to shift the relative positions of the valence band, which enabling band engineering strategy to achieve band convergence.

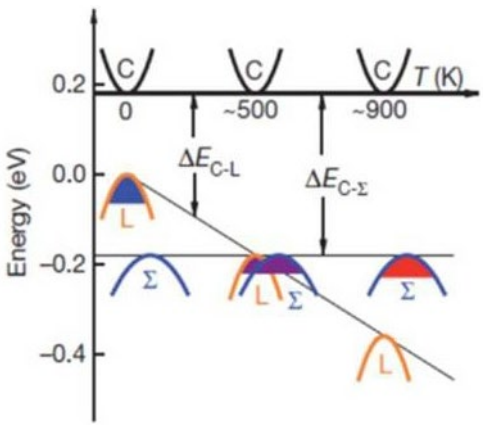

Figure 1.8: Schematic representation of the band convergence strategy achieved in Se doped PbTe as a function of temperature[55].

1.4.4. Defect Engineering

Defect engineering[58–60] strategy is an effective and important method to manipulate carrier and phonon transport behavior as desired. More specifically, inclusion of multi length scale defects, varying from point defects to dislocations, grain boundaries and nano precipitates aid the fine tuning of carrier concentration and band gap in the materials. Defects are often considered as imperfections in the material that are expected to adversely affect the TE transport performances. It is desired to control the nature and extend of the defects in order to achieve better TE performances. However, owing to the limited size scale of nanoparticle, defects could be selectively scatter the phonon and filter low energy carriers. For instances, multi-length scale defects incorporated nanostructures such as holey and hollow nanostructures exhibit poor lattice conductivity than that of its bulk counterpart[61,62]. This is due to the presence of additional phonon scattering at boundaries and interfaces. Therefore, the morphology of the nanostructures along with crystal defects also plays an important role in determining TE transport properties.

From the perspective of point defects[28], the lattice periodicity would be distorted from the normal crystal lattice and become a scattering source for charge carrier and phonon transport process. In addition, point defects causes charge imbalance, which changes the charge carrier concentration and thus have an impact on electric transport process. Enhancement in TE transport properties was reported in many materials, where the point defects were controlled efficiently [63–67]. Point defects in Bi_2Te_3 include intrinsic point defects (or native defects) and extrinsic point defects. The native defects refer to vacancies and antisite defects, while extrinsic point defects refer defects, which are introduced through doping. Zhu *et al.*,[28] reported the formation, control, and evolution of intrinsic point defects in the Bi_2Te_3 based compounds. The conduction type and carrier concentration in undoped Bi_2Te_3 is closely related to its chemical composition and to its intrinsic point defects. Bi–rich Bi_2Te_3 exhibit *p*-type conductivity and Te-rich Bi_2Te_3 demonstrate *n*-type conductivity. Controlling of intrinsic point defects are required to improve the reproducibility of Bi_2Te_3 compounds.

Elemental doping is one of the classical methods to incorporate extrinsic point defects, which could be achieved either by chemical methods or alloying. Sb and Se are the most common acceptor and donor type of dopants in Bi_2Te_3 material respectively. Besides, it is worthwhile to point out that Cu atoms are also known to be one of the potent dopant in Bi_2Te_3 materials[68–71]. Doping of Cu atoms used to suppress the evaporation of Te atoms in Bi_2Te_3 and found to a suitable way to avoid undesirable off-stoichiometry

ratio in Bi_2Te_3[70,72]. Furthermore, dual electronic nature[69,72–74] was exhibited by transition metals (Au, Ag, Cu) doped Bi_2Te_3. It has been reported that the transition metals act as either donor or acceptors that depends on the dopant concentration and their locations in Bi_2Te_3 crystal. For instances, Cu doped Bi_2Te_3 exhibited *p*-type conductivity at low Cu concentration (<1 *at%*) and *n*-type conductivity at high Cu concentration (>1 *at%*)[72,75].

Furthermore, various processing methods at various stages of material synthesis have also been observed to manipulate the electrically active intrinsic defects in the material. For instances, processing methods such as grinding, high energy ball milling, electro deposition induce donor-like effects. Most importantly, using hot deformation method, antisite defects and donor type defects were successfully tuned in $(Bi, Sb)_2(Te, Se)_3$ solid solutions[59] and high *ZT* value of around ~1.3 were achieved at 380 K. Using spark plasma sintering, Wang *et al.,*[76] effectively suppresses Te vacancies and thereby achieves better TE characteristics in *n*-type Bi_2Te_3 nanostructured pellets. Recently, the evolution of intrinsic point defects in *n*-type Bi_2Te_3 based TE materials were systematically investigated using sintering process and reported by Zhang *et al.,*[29]. Sintering aided the formation of donor type vacancies in the Bi_2Te_3 and eventually increased the electron concentration. It is important to note that the above reports use equilibrium processes (*i.e.*, sintering and hot deformation technique) to tune the amount of point defects in the material.

In few reports, intrinsic point defects were introduced through thermally non-equilibrium process[77] *viz* ion irradiation to tune the TE transport properties. During ion implantation, intrinsic point defects and possibly extended defects might infuse in the material that may subsequently evolve or anneal out during the course of experiment. The implantation induced defects and defect clusters aid to decouple and evidently enhances TE transport characteristics[78].

1.5. Nanostructured bismuth telluride: synthesis and overview

As discussed above, nano structuring strategy aid to decouple the interdependency of TE transport parameters, ultimately become a key strategy to improve TE efficiency, both by boosting power factor and reducing thermal conductivity values. Material synthesis method is very crucial for the improvement of TE properties of material, since different fabrication method offers a various physical properties. Two approaches namely, top-down and bottom-up methods, are usually adopted to synthesize bulk nanostructured

TE materials (Figure 1.9). The present section aims to present the different techniques to synthesize the nanostructured materials.

1.5.1. Top-down approach

In the top-down approach, nanostructured powders are obtained from bulk material through structural deformations such as in high energy ball milling method and melt-spinning method. For instances, powders are constantly cold-welded and fractured to form nanostructured powders during 'high-energy ball milling' method, due to the severe impact collisions between powder samples and ball bearing. Recently, nanostructured Bi_2Te_3 pellets are reported to exhibit maximum *ZT* value of 1.22 at 473 K, where the samples are prepared through high energy ball milling followed by spark plasma sintering[79]. Apart from ball-milling, melt spinning method can also able to produce nanostructured bulk TE materials with enhanced *ZT* values. Fan *et al.,*[47] synthesized the *p*-type $Bi_{0.4}Sb_{1.6}Te_3$ nanocomposites *via* melt-spinning method and the samples exhibit maximum *ZT* of 1.8 (56% increment over bulk), due to effective scattering of phonon over wide range of spectrum. Large scale production and cost effectiveness are the major advantage of this approach. However, control over reproducibility on size of the nanoparticles and carrier concentration is difficult to achieve.

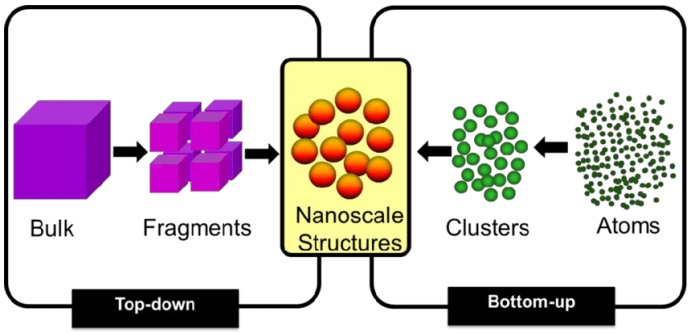

Figure 1.9: Schematic of top-down and bottom-up approach for the preparation of nanostructured TE materials[80].

1.5.2. Bottom-up approach

In the bottom-up approaches, synthesis of nanostructures was established through the direct manipulation of atoms or molecules. In other words, bottom-up method involves atom-by-atom, molecule-by-molecule, nanoparticle-by-nanoparticle manipulations *via* chemical reactions. This approach includes preparation of thin film and nanostructured bulk pellet. In case of thin film fabrication techniques, atom-by-atom manipulations will be achieved at high vacuum conditions and some of the techniques include molecular-beam epitaxy (MBE)[81], physical or chemical vapor deposition (PVD or

CVD)[45,82,83]. Particularly among the PVD techniques, pulsed laser deposition (PLD) method has been focused in the present thesis; since it offers great versatility in fabricating high quality polycrystalline thin film with multi element stoichiometry (like in Bi_2Te_3) along with high growth rates, where diverse and complex nano structural morphologies with desired properties for TE applications can be obtained.

For the synthesis of nanostructured pellets, nanostructured powders were synthesized first and then compressed into highly dense pellets *via* cold-pressing/hot-pressing technique. Chemical synthesis method such as solvothermal[84], hydrothermal[85], and colloidal synthesis[86] are widely used for the synthesis of nanostructured powder, where building blocks will be ions and nanoparticles in the solution. Out of all chemical synthesis method, hydrothermal method is preferred in the present thesis. Because, hydrothermal method are easy to perform at low cost efficiency, due to low reaction temperature and processing time. Further, these methods exhibit great control over crystallinity, morphology, and particle size distribution of nanostructured powders. This method has been used to grow various nanostructured TE materials such as Bi_2Te_3, PbTe, $CoSb_3$ with various complex morphologies and particle size distributions[87–90]. A significant advantage of using hydrothermal method is that morphology of the nanoparticle could be controlled using suitable surfactants. Regardless of all these advantages, hydrothermal method experience serious drawback such as (1) to remove impurities such as surfactants, solvents *etc* in the final powders, (2) low yield, and (3) to control exact stoichiometry.

1.5.3. Bi_2Te_3 nanostructures- review

Experiments with nanostructured Bi_2Te_3 materials show that highly efficient TE energy conversion could be prospective. The first attempt to grow Bi_2Te_3/Sb_2Te_3 superlattices on GaAs substrate was done by Venkadasubramian *et al.,*[45,91]. The maximum *ZT* value of ~2.4 and thermal conductivity value as low as 0.22 W/m-K was reported. Meanwhile, Yamasaki *et al.,*[92,93] prepared Bi_2Te_3/Sb_2Te_3 superlattices on Si substrates through PLD method and the authors reported the minimum thermal conductivity value of 0.11 W/m-K around room temperature, which is mainly due to the phonon scattering effects at the interfaces and boundaries. Recently, Park *et al.,*[94] fabricated $Bi_2Te_3/Bi_{0.5}Sb_{1.5}Te_3$ superlattices film and TE transport properties were found to be remarkably enhanced, which is owing to energy filtering effect in addition to low interfacial resistance of the superlattice structure. Up to date, in the reports of the TE

transport properties on Bi_2Te_3 bulk nanostructured and thin films[32,33,76,95–98], there exist a wide variation of *ZT* values, varying from 0.4 to 1.7 around room temperature. Recently, Newbrook *et al.,*[99] reported the improved TE performances, where 3-fold improvement in power factor and 5-fold improvement in *ZT* values are observed in Bi_2Se_3 alloyed Bi_2Te_3 thin films.

Several groups have fabricated Bi_2Te_3-based thin films using PLD method. Various studies have optimized and obtained the relationship between several experimental conditions (such as substrate type, deposition temperature, laser fluence, background inert gas type and pressure), crystallinity and the stoichiometry of thin films[32,100–104]. For instances, it was found that films with improved crystallinity and TE characteristics could be deposited at the substrate temperature between 250 ºC to 300 ºC. Meanwhile, substrate type has found to have no effect on the film stoichiometry and crystallinity. However, highly oriented growth could be achieved on the substrate such as mica and silicon. Effects of various dopant atoms such as Se, Sb, Gd, Cu, Ag, Au, Pb, Sn in TE characteristics of Bi_2Te_3 also studied[81,105–108]. In most cases, dopant atom found to exhibit phonon scattering and carrier filtering effect, thereby optimize TE characteristics by remarkably enhances Seebeck coefficient and reduces thermal conductivity values.

Annealing effects on TE properties of Bi_2Te_3 thin films are studied by many authors[98,101,109]. It has been found that both structural and electrical properties were affected by annealing treatment. Crystalline nature was enhanced remarkably in Bi_2Te_3 thin films with annealing temperature. However, maintaining exact stoichiometric composition would be difficult due to high vapor pressure of Te atoms, which in turn reduce the carrier concentration values. Zeng *et al.,*[110] studied the thickness dependent TE transport properties of Bi_2Te_3 thin films. It was found that thickness affect the TE characteristics considerably. On contrary with the Seebeck coefficient, carrier mobility was observed to improve with film thickness. In addition, Nguyen *et al.,*[111] studied the TE properties of Bi_2Te_3 thin films at ultra-thin film limit. The authors reported the maximum *S* value of 1 *mV/K* and high electrical conductivity in the ultra-thin film limit. Wudil *et al.,*[112] reported highest *ZT* value of 0.92 at 250 ºC for Se doped Bi_2Te_3 thin films. High quality Bi_2Te_3 thin films were fabricated on polymide substrate using PLD method and high Seebeck coefficient value of ~220 μV/K are reported[113].

A variety of simple, complex, hierarchical nanostructures of Bi_2Te_3 have been synthesized using hydrothermal method, including nanowires[114], nanotubes[89],

nanoflowers[115], ultra thin nanorods[116], Bi_2Te_3/Te hetero-nanojunctions[117], Te/Bi_2Te_3 nanostring cluster hierarchical nanostructure[118], hexagonal nanoplates[119]. Feng *et al.,*[120] used Te nanorods as template for the synthesis of Bi_2Te_3 nanowires in high yield. In addition, Soni *et al.,*[121] synthesized $Bi_2Te_{3-x}Se_x$ nanoplatelet, exhibiting high *ZT* value of 0.54 at 300 K. On considering complex and hierarchical structures, Bi_2Te_3/Bi core-shell nanostructures were prepared using Bi_2S_3 nanorods as template[122]. Wang *et al.,*[123] reported the preparation of Bi_2Te_3 nanotubes through hydrothermal synthesis process. At the same time, time dependent morphological evolution of Bi_2Te_3 nanotubes and the possible growth mechanism during hydrothermal growth conditions was also reported by Shyni *et al.,*[124].

Surfactants are the growth-directing agents that are generally used to control the morphology in the synthesis of nanostructures. Effect of various surfactants on the nanostructures of Bi_2Te_3 and the dependence of the nanostructure morphology on the TE characteristics was studied by several authors[85,125,126]. Dharmaiah *et al.,*[127] prepared Bi_2Te_3 nanobelts, nanoflowers in the presence of surfactant, EDTA (ethylenediaminetetraacetic acid). It was found that the pellet prepared form nanoflowers exhibit better TE characteristics with ZT value of 1.4 at 300 K. However, residuals of surfactants at the final product affect the TE transport properties. Zhang *et al.,*[128] reported the surfactant-free synthesis of hetero phase Bi_2Te_3-Te nanostructures and the unique structure exhibits the maximum *ZT* value of 0.4 at 300 K. In all these nanostructured powders, enhancements in Seebeck coefficient values are due to carrier-energy filtering effect, established at the grain boundaries, and while poor lattice thermal conductivity are due to phonon scattering.

1.6. Ion implantation

Ion implantation or ion irradiation[129] is the powerful tool for the modification of structural and electric properties of the materials, by means of bombarding solids with energetic ions from particle accelerator. Ion beam methods offer a precise control over the ion fluences, ion profile, and temperature. This technique can be used either to create nano patterned surface of materials by ion beam erosion, or to introduce impurities (or dopant atoms) by ion implantation, or to investigate novel properties resulting from impurity defect interactions by inert gas ion irradiation. The basic aspect of ion-solid interactions that produces various radiation effects in materials are discussed in later sections.

1.6.1. Ion-solid interactions and energy loss

During ion implantation, energetic ion interacts with a target solid and forms the collision cascade by undergoing series of collisions with nuclei and electrons in the target. Fast ions in target solid lose their energy predominantly *via* two mechanisms; (1) elastic collisions (or nuclear energy loss, denoted by S_n), in which energy is transmitted from moving particle to the target atom, (2) in-elastic collisions (or electronic energy loss, denoted by S_e), in which incoming particle causes excitation of target electron and ionization of target atoms. In general, nuclear stopping results in displacement of lattice atoms and electronic stopping leads to heating up of the target material.

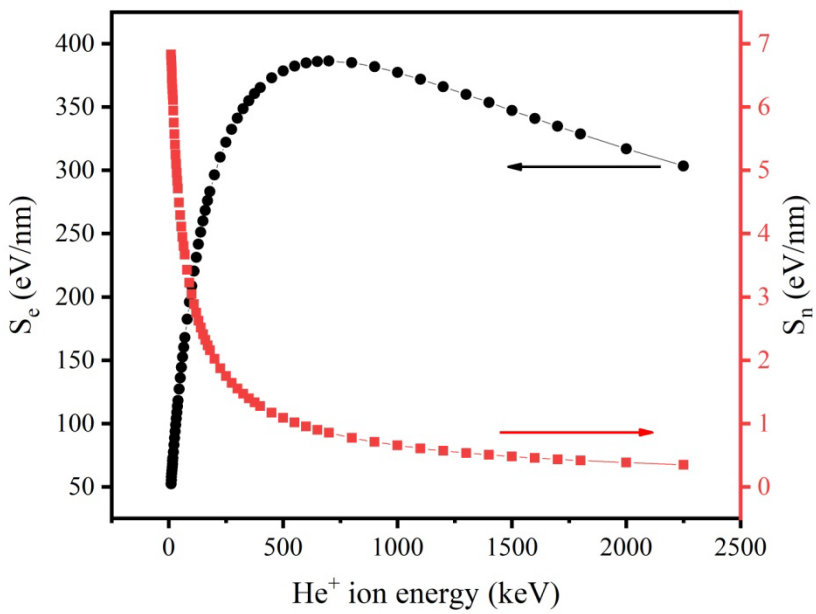

Figure 1.10: Nuclear and electronic energy loss of He^+ ions in Bi_2Te_3 as a function of ion energy. The data is calculated using SRIM software[130].

The electronic energy loss dominates when the incident ion beam bears high energies, whereas nuclear stopping becomes prominent as the ion slows down. The relative contribution of these energy loss mechanism depend on energy of incoming ion and mass of the target solid that can be calculated using simulation software, such as Monte-Carlo simulation SRIM (Stopping and Range of Ions in Matter)[130]. For instances, the schematic of energy loss phenomena in He^+ ion irradiated Bi_2Te_3 as a function of He^+ ion are shown in Figure 1.10. Moreover, it has to be noted that the total energy loss (S_{total}) is the sum of nuclear energy loss (S_n) and electronic energy (S_e) loss, which can be expressed as below.

$$S_{total} = S_n + S_e \qquad \textbf{Eqn. 1.19}$$

1.6.2. Ion implantation/irradiation induced defects

The transfer of ion energy (projectile) to the target atoms could lead to formation of structural defects, which in turn resulted in the modification of material properties. The type, number, distribution of defects induced depends on the number of interactions and on the quantity of energy transferred. For instances, if the energy transferred to the lattice atom exceeds 'displacement threshold energy' E_d, atom will be ejected from the lattice position. Meanwhile, displacement of atom from the lattice leads to the formation of Frenkel pair defect (*i.e.,* interstitials and vacancy). In general, ion implantation induced defects can be comprised of following processes.

1) Interaction of energetic ion resulted in the transfer of its kinetic energy to the lattice atom, which gives rise to atom displacements (*i.e.,* primary knock on atom, PKA).
2) The PKA atom might carry enough kinetic energy to secondary displacements. The secondary displaced atoms (or recoil atom) in turn induce other displacements. The process continues and highly disordered region (known as collision cascade) might form along the path of the energetic ion.
3) The termination of displaced atoms gives rise to the formation of vacancies and interstitials. However, implantation induced point defects will migrate throughout the lattice and most of them will recombine subsequently. In general, the radiation damage is the collection of stable point defects (*i.e.,* vacancies and interstitials) and the defect clusters. The ion fluence could be converted in to equivalent peak radiation damage, in the units of displacements per atom (*dpa*), which is given by Eqn. 1.20.

$$dpa = \frac{N^*}{N}\phi \qquad \textbf{Eqn. 1.20}$$

where N^* is atomic displacements per ion-angstrom at peak damage, N is the atomic density of Bi_2Te_3 (atoms/cm^3), and ϕ is the ion fluence (ions/cm^2). The atomic displacements per ion-angstrom can be estimated using the SRIM damage profile.

For a given target material, low energy-light ion tends to create a binary or linear collision cascade, where the atomic motion of the incident ion would immediately stop after a few collisions. The high energy-heavier ion creates a dense collision cascade and thereby generates large number of recoil atoms. Electronic energy loss is the dominant

energy loss mechanism in the high energy-heavy ion irradiation, where the projectile ion deposits its energy in the electronic sub system through electronic excitation and ionization. According to the thermal spike model[131,132], the highly excited electron rapidly distributes their energy through electron-electron interaction until electrons are thermalized to dissipate their energy through electron-phonon coupling to the atoms in the target material. The local temperature during thermal spike phase will increase up to ~10^4 K that spreads and quenches subsequently within ~10^{-12} s. The resulting liquid-like non-equilibrium state induces the various thermally activated processes such as atom migration, evaporation of atom, and atomic jumps across grain boundaries. This resulted in permanent structural modifications that include phase transitions (crystalline to amorphous or amorphous to crystalline)[133,134], damage production[135–137], such as defects or an ion track or the recovery of pre existing damage.

1.6.3. Overview of ion irradiation effects in Bi_2Te_3

The ion implantation/irradiation of Bi_2Te_3 can be used as an effective tool to decouple as well as to enhance and optimize the TE transport characteristics. For instance, in the case of 3 MeV He^{2+} ion irradiated Bi_2Te_3 thin films[77], irradiation induced defects drastically enhance the TE properties by decoupling all the three TE transport parameters. The authors pointed-out the multiple functions of point defects in Bi_2Te_3, which acts electron donors, charge scattering centers, and phonon blockers at the same time. Fu *et al.,*[78] had employed 400 keV Ne^+ ions to infuse defects in Bi_2Te_3 thin films. Ionization induced defect recovery and enhanced crystallinity was observed in the ion irradiated films, which increases the power factor by 208%. Proton irradiation[138] was employed to induce defects in Bi_2Te_3 and flexible Bi_2Te_3/PEDOT:PSS composite films, where the films exhibited maximum *ZT* value of 0.18 and 0.28 at 300 K respectively. Wang *et al.,*[139] synthesized Bi_2Te_3 nanosheets using solvothermal method and Fe^+ ion irradiation was carried out to infuse defects in the sample. It was shown that conductivity of Fe^+ ion implanted Bi_2Te_3 nanosheets improved remarkably. In addition, Fe^+ ion irradiation changed the characteristic Bi_2Te_3 surface from hydrophobic to hydrophilic in nature.

In recent report, diameter dependence of TE characteristics for $Bi_{0.8}Sb_{1.2}Te_{2.9}$ nanowires was studied using FIB trimming process[140]. The authors showed that both electrical and thermal conductivity exhibited dramatic reduction in accordance with nanowires diameter, which is attributed to the phonon scattering of defects created by Ga^+

ion irradiation. Guerra *et al.,*[141] exposed Bi nanowires of different diameter to a beam of 400 keV and 1 MeV Au^+ ions until complete degradation. The authors proposed the complete mechanism of morphological modifications by considering sputtering and radiation induced surface diffusion effects. Chang *et al.,*[27] reported proton irradiation effects on single crystalline Bi nanowires. Seebeck coefficient remains stable at various irradiation energy, while the electrical conductivity significantly declined with proton energies. Moreover, the authors[143] found that the thermal conductivity reduced by half after proton irradiation. There are several works in the literature on the synthesis of Bi_2Te_3 nanostructures and its morphology dependent TE transport properties. Various attempts were done by several authors to improve the TE transport efficiency. However, the role of defects in the defect incorporated Bi_2Te_3 nanostructures on the TE transport properties has not been well established.

1.7. Scope of the thesis

The present thesis is an attempt to systematically investigate (1) Bi_2Te_3 nanostructures and the role of defect incorporated morphology in TE transport properties, (2) copper doping effects in Bi_2Te_3 thin films and (3) the role of defects in the TE transport properties of nanostructured pellets and thin film.

Chapter 2

Experimental methods

2.1. Introduction

This chapter presents details of sample preparation methods employed for the preparation of Bi_2Te_3 nanostructured pellets and thin film. The technical details about the ion irradiation facilities are discussed in this chapter.

The characterization methods employed in the present thesis are also discussed. They can be divided in to three sections: diffraction techniques, spectroscopic and spectrometry techniques, and thermoelectric (TE) characterization technique. Grazing incidence X-ray diffraction (GIXRD) and electron diffraction techniques were used to characterize the crystal structure of the samples. Atomic force microscopy (AFM), scanning electron microscopy (SEM) and high resolution transmission electron microscopy (HRTEM) were applied to investigate the morphology and microstructure of the samples. Under the section 'spectroscopic and spectrometry techniques', energy-dispersive X-ray spectrometry (EDS), Rutherford back-scattering spectrometry (RBS), and Raman scattering will be discussed. Furthermore, various measurement techniques were applied for TE characterization, including Hall-effect, Seebeck coefficient, electrical conductivity and thermal conductivity in the section 'TE characterization techniques'.

2.2. Sample preparation methods

2.2.1. Hydrothermal method for pellet samples

Hydrothermal method is solution reaction-based approach for the synthesis of Bi_2Te_3 nanoparticles, which can be carried out in a wide temperature range from room temperature to very high temperature. It has to be mentioned that the hydrothermal synthesis offer significant advantages over others methods[19,89,103,144–147]. For instances, nanomaterials with very high vapour pressure can be synthesized with a minimum loss of materials.

In general, hydrothermal synthesis will be carried out in a sealed reactor (known as autoclave). In most cases, the stainless steel autoclave was coated with teflon lining in order to protect the autoclave body from the corrosive solvent, which is held at high temperature and high pressure. Material synthesis by the hydrothermal method follows two steps, namely crystal nucleation and subsequent growth. The composition and the

morphology of the nanoparticles can be well controlled by adjusting several parameters such as reaction temperature, pH value, and reactant and surfactant concentration.

Following steps were applied in this work for the synthesis of Bi_2Te_3 nanoparticles:

1. Bismuth chloride ($BiCl_3$) and sodium telluride (Na_2TeO_3) were used as the Bi and Te precursors respectively. 2 mmol of $BiCl_3$ and 3 mmol of Na_2TeO_3 were dissolved in 100 ml distilled water.
2. 2 M NaOH was added drop by drop to the prepared solution.
3. Eventually, different concentration of surfactant was added to the above-mixed solution and the resultant solution was continuously stirred for several hours.
4. Subsequently, reducing agent (*i.e.,* sodium borohydrite, $NaBH_4$) was added and the final solution was transferred to a 200 ml teflon-lined stainless steel autoclave. The autoclave was made to fill up to 80% of its volume using distilled water.
5. The autoclave was sealed and maintained at different temperatures for several hours. Upon natural cooling, the final black precipitates were filtered and washed several times with ethanol, acetone and distilled water.
6. The nanostructured Bi_2Te_3 powder was pelletized using circular and rectangular shape mechanical pelletizer with a pressure of 10 MPa for 10 min and subsequently sintered at 150 ^{o}C for 2 hr. The diameter and thickness of circular pellets are 14 mm and 2 mm respectively, while the dimensions of rectangular pellets are 10 mm × 5 mm × 1 mm.

2.2.2. Pulsed laser deposition (PLD) method for thin film samples

Pulsed laser deposition (PLD) is a thin film growth technique, which offers several advantages over other growth methods [32,99,148–151]. Due to pulsed nature of laser, this technique has an ability of stoichiometric transferability of materials from target to the substrate[32,92,152]. Also, the laser source is outside the vacuum chamber, which is useful for easy and clean operation with less complexity of thin film fabrication processes.

The deposition of thin films by PLD can be divided into four stages

1. Laser-target interaction
2. Plasma plume formation
3. Deposition of ablated material on substrate
4. Nucleation and growth of the thin film on the substrate surface.

Each of these steps will have a significant impact on the crystallinity, uniformity, and stoichiometry of the thin film. Schematic of PLD technique is shown in Figure 2.1. It can be seen that a very high intense laser pulse is focused on the target material, where it is partially absorbed. Above the threshold power density, which depends on target material, material ejects out as luminous plasma. Vacuum chamber is filled with the controlled atmosphere of gas (such as Ar, O, Ne) to enable chemical reactions to make desired stoichiometry. Plasma material re condenses on to the substrate, which allows thin film growth *via* crystallization process. The PLD system mainly consists of two parts, a laser system to evaporate materials, and a deposition chamber, where the actual deposition takes place.

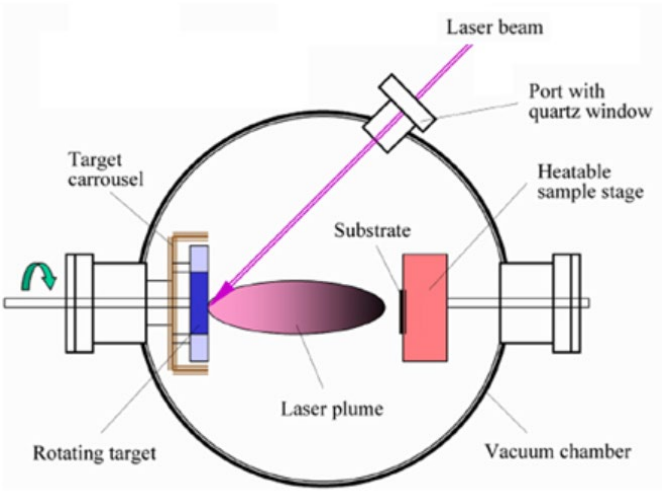

Figure 2.1: Schematic of pulsed laser deposition (PLD) technique[152].

It has to be mentioned that the PLD deposition involves the complex interplay between several parameters such as laser parameters (laser fluence and laser energy), pressure of background gas, substrate temperature, target-substrate distance. All these parameters determine film quality, stoichiometry, and rate of deposition.

In the present thesis, Bi_2Te_3 thin films were deposited using PLD method and quartz was used as the substrate. The target pellet was made by using hydrothermally synthesized Bi_2Te_3 nanoparticles, for which the synthesis procedure was explained in previous section. Prior to the deposition, the chamber was evacuated to a base pressure of ~3×10^{-5} mbar and then purged with argon gas. The deposition was carried at the pressure of ~8×10^{-1} mbar under Ar gas atmosphere. The KrF excimer laser (M/s Coherent Inc.) of wavelength 248 nm with pulse duration of 20 ns was used to ablate the target. The energy of each laser pulse used was maintained at 250 mJ with 5 Hz frequency and 3000 laser

shots were used. During ablation, PLD target was rotated at a speed of 3 rpm to continuously expose the fresh surface for ablation and to avoid crater formation. All films were grown at the substrate temperature of 250 ºC and the target-substrate distance was kept as ~5 cm.

2.2.3. Ion implantation/irradiation

In the present thesis, ion implantation/irradiation experiments were carried out using a 1.7 MV Tandetron accelerator and a 150 kV ion accelerator. The details of the accelerators are explained below.

2.2.3.1. 150 kV ion accelerator

Figure 2.2 shows a photograph and a schematic representation of 150 kV ion accelerator at the IGCAR, used in this work. A RF plasma source at a pressure of 10^{-2} mbar produces desired gaseous ions, which are extracted and accelerated to desired voltage. The ions are mass analyzed by a 45° electromagnetic mass analyzer. Finally, the analyzed ion beam is collimated using quadruple lens and allowed to hit on the sample in the ion irradiation chamber.

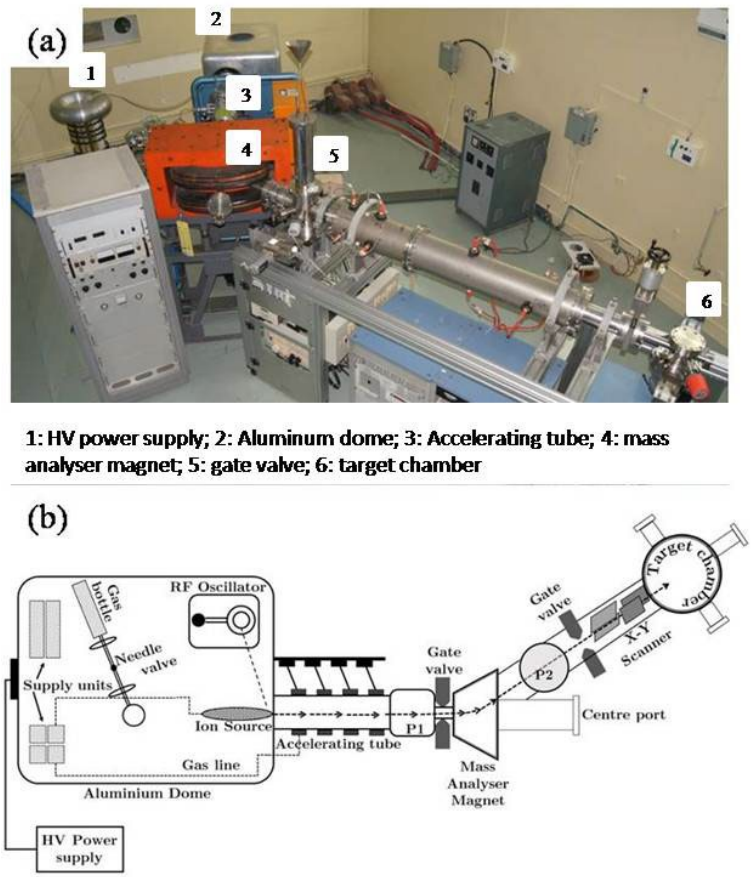

Figure 2.2: Photograph (a) and schematic (b) of a 150 kV ion accelerator.

The irradiation chamber is maintained at high vacuum of 10^{-7} to 10^{-8} mbar using a turbomolecular pump. A liquid nitrogen trap was fixed to trap the organic contaminants to maintain clean vacuum. The sample is mounted on a copper block in the sample manipulator and is electrically isolated from the rest of the chamber, to facilitate beam current measurement. The beam current and the ion fluence (ions/cm^2) are measured using a current integrator. A secondary electron trap is used to eliminate the error in the beam current measurement caused by the emission of secondary electrons from the target. The ion beam current density was maintained less than 1μA/cm^2 during ion irradiation to avoid the beam heating of the target material. In the present thesis, inert gas ion irradiations at room temperature were carried out using this accelerator.

2.2.3.2. 1.7 MV Tandetron accelerator

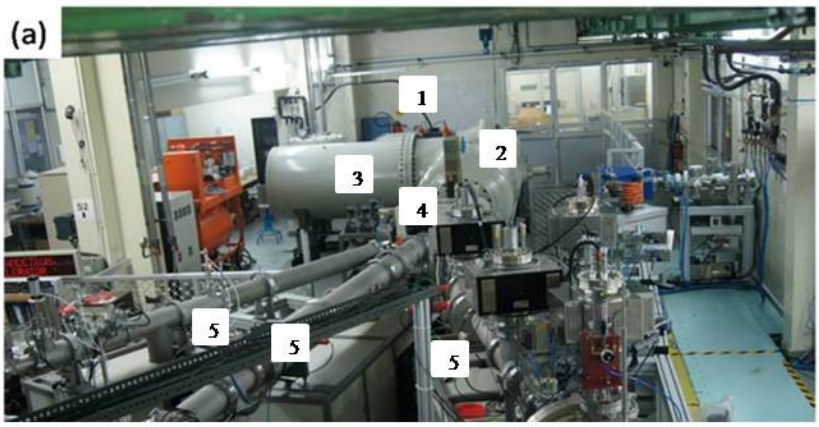

1: SNICS; 2: Accelerator tank; 3: Power supply tank; 4: mass analyser magnet; 5: beam line

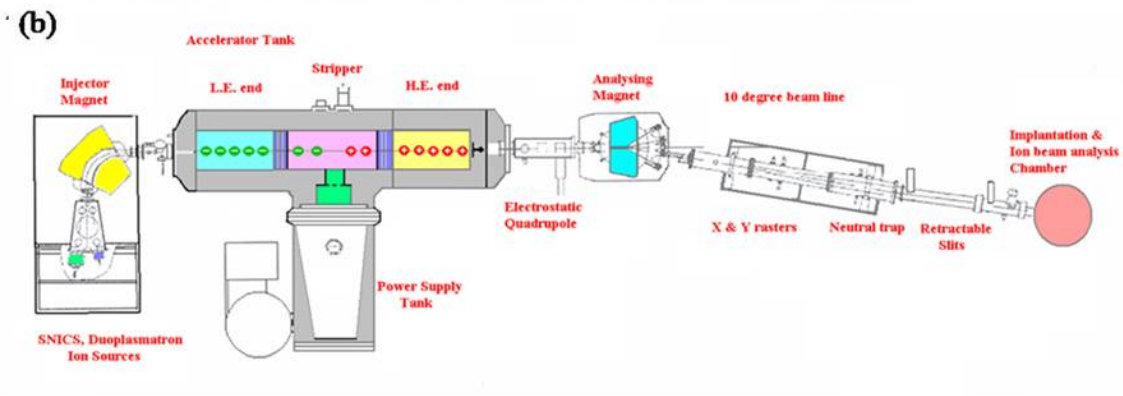

Figure 2.3: Photograph (a) and schematic (b) of 1.7 MV Tandetron accelerator.

The accelerator is the tandem type ion accelerator, with 1.7 MV terminal voltage. Figure 2.3 shows the photograph and schematic of 1.7 MV tandetron accelerator. The beam injection system of the accelerator is capable of producing negative ions of almost all elements. The negative ions are extracted from the ion source (Source of Negative Ion

by Cesium Sputtering, SNICS), analyzed using 90º mass analyzing magnet, and then injected in to the accelerator. The injected ions are then accelerated in two steps. First the injected negative ion accelerated towards the positive high voltage, which is at the center of the terminal tank. The positive high voltage is maintained at the center of the terminal by Cockcraft-Walton type cascade generator consisting of identical stages of capacitor and diodes.

At the terminal, the negative ions are stripped of one or more electrons through charge transfer process. The stripping of ions is obtained by using nitrogen gas stripper. The beam is now composed of positive ions with distribution of charges and these ions are accelerated towards ground potential.

The high energy switching magnet select the ion beam according to the mass and energy of the ions, which switches the beam to the experimental ports located at ±10° and ±30° angular ports. An implantation beam line with the beam sweep system, neutral trap, beam profile monitor and retractable slits for beam collimation has been installed at the 10°port of the switching magnet. The maximum energy achievable, is decided by the charge state (q) of the ions at the terminal after stripping and the terminal voltage (V), for $E=V(1+q)$. A UHV compatible irradiation cum ion beam analysis chamber has been installed at the end of the 10° beam line. In the present thesis, Cu^+ ion irradiation and RBS spectrometry was carried out using 1.7 MV Tandetron accelerator.

2.3. Diffraction techniques

2.3.1. Gracing incidence X-ray diffraction (GIXRD)

X-ray diffraction (XRD) is a non-destructive technique for characterizing crystalline material. It provides detailed information regarding phases, crystalline structure and other structural parameters such as average grain size, crystallinity, strain, and crystal defects. In XRD experiment, a crystal is irradiated with monochromatic X-rays of a wavelength comparable to the spacing between crystal lattice planes. Under certain incident angles, the wavelength of the scattered X-rays interferes constructively and intense reflected X-rays are produced. In order for the waves to interfere constructively, differences in the travel path must be equal to the integer multiple of wavelength. When this constructive interference occurs, a diffracted beam of X-rays will leave the crystal at an angle equal to that of incident beam. The Bragg's law (Eqn. 2.1) calculates the angles under which constructive interference from X-rays scattered by parallel planes of atoms in a crystal will produce a diffraction peak.

$$n\lambda = 2dsin(\theta) \qquad \textbf{Eqn. 2.1}$$

where n, λ, d, and θ are the diffraction order (n= 1,2,3,..), wavelength of the X-ray, inter-planar distance and glancing angle respectively.

In case of thin films, XRD measurement generates weak signal from film and strong signal from the substrate. On the other hand, ion implantation induced damage is observed near the surface of the samples. Therefore to enhance the signal from the film as well as to probe the near sample surfaces, grazing incidence XRD (GIXRD) is used. The scattering geometry of XRD and GIXRD technique is displayed in Figure 2.4. It is seen that in GIXRD scattering geometry, the incident X-ray beam impinges onto the surface of a thin film, at an incident angle less than 5°. This provides advantage over other diffraction schemes in the studies of thin surface layers, since the penetration depth of X-ray is reduced by three orders of magnitude typically from few µm to few nm.

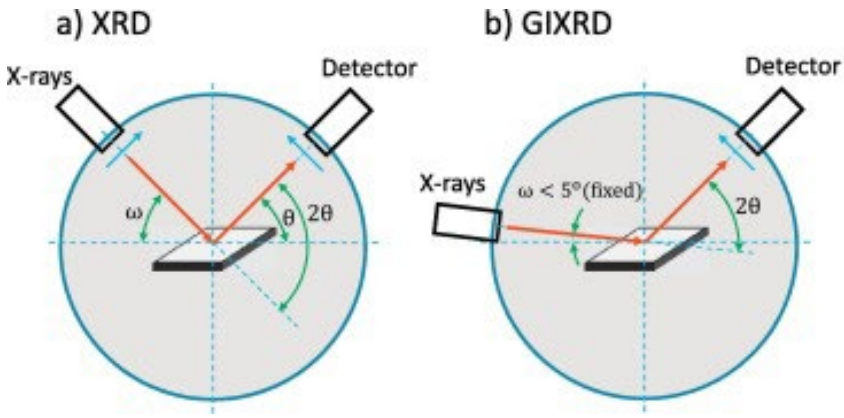

Figure 2.4: Scattering geometry of (a) XRD and (b) GIXRD techniques[153]

In the present thesis, Inel Equinox 2000 X-Ray Diffractometer was used for characterization of the all the samples. The diffraction peaks were fitted using pseudo-Voigt function and the estimated full width at half maximum (FWHM) was used to calculate parameters such as crystallite size and strain in the sample using various methods.

2.3.1.1. Scherrer method

Scherrer formula (Eqn. 2.2) can be used to estimate the average crystallite size from XRD peak broadening. It is seen that the average crystallite size L depends on the FWHM *(β)* of the diffraction peak, wavelength *(λ)* of the X-rays, the Scherrer constant *(K)*, the diffraction angle θ. The *FWHM (β)* varies inversely with size (D) and θ.

$$\beta = \frac{K\lambda}{Dcos\theta} \qquad \textbf{Eqn. 2.2}$$

The Scherrer constant is affected by the factors like the crystallite size, crystal shape and size distribution.

2.3.1.2. Williamson-Hall (W-H) plot

The XRD peak broadening is associated to the combined effects of crystallite size and lattice strain in the samples[154]. The lattice strain induced broadening is attributed to the crystal imperfections and lattice distortions. These combined effects of average crystallite size (D) and lattice strain (ε) values could be decoupled using Williamson-Hall (W-H) relation, which is given as in Eqn. 2.3.

$$\beta cos\theta = \frac{k\lambda}{D} + 4\varepsilon sin\theta \qquad \textbf{Eqn. 2.3}$$

where β is FWHM of the XRD peak, θ is the peak position, κ is the structure factor, λ is the X-ray wavelength, D is the crystallite size, and ε is the lattice strain.

By plotting $\beta cos\theta$ against $sin\theta$, strain component could be obtained from the slope (4ε) and crystallite size component could be obtained from the intercept ($^{\kappa\lambda}/_{D}$). The W-H method assumes isotropic strain in all crystallographic directions come from the fact that the individual peak width has to be accessible, which means the method will fail at intensive peak overlap.

2.3.2. Electron diffraction

Electron diffraction is similar to X-ray diffraction (XRD), except it uses a beam of electrons to obtain a diffraction pattern from the sample of interest. In other words, electron diffraction is a result of the wave nature of the electrons and the periodic lattice of the crystal. The electron diffraction patterns can be used for the identification of: phases and crystal structure types, crystal symmetry and crystal space group determinations, identifying defects, determining the ordering behavior of crystal structures and the site occupancy preferences, *etc*.

The single crystalline materials show spot pattern or Kikuchi line pattern, while the polycrystalline materials exhibit ring pattern. When the grain size of the specimen is extremely fine or completely amorphous, the feature of concentric rings in the pattern disappears and a halo is left around the bright center spot, which shows that the electrons are scattered randomly by the amorphous structure of specimen. The amorphous and

glassy materials are identified by this method. In the present thesis, electron diffraction pattern were obtained using HRTEM (LIBRA 200 FE, Carl Zeiss) system.

2.4. Microscopy Techniques

2.4.1. Atomic force microscopy (AFM)

The atomic force microscope (AFM) is an important tool to study the surface topography of thin films. In this technique, the probe is a small sharp tip, which is scanned across the sample surface (Figure 2.5). The distance between the tip and the sample is so small, so that the atomic range of forces acts between them. In order to measure these forces, the tip is attached to the end of the cantilever. The deflection of the cantilever depends on the atomic range of forces, which can be measured using laser beam deflection system. AFM can be used in contact or tapping mode.

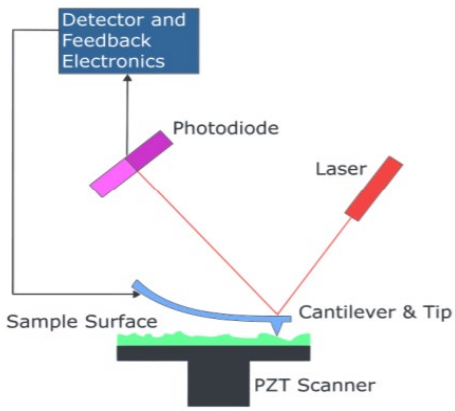

Figure 2.5: Schematic of atomic force microscopy (AFM)

In the tapping mode, the cantilever is made to oscillate near its resonance frequency. When the tip comes closer to the surface, the amplitude of the cantilever oscillation will decrease. The vibration of the cantilever is detected using laser beam deflection system. The measured laser beam deflection can be used as an input for feedback loop mechanism that keeps constant tip-sample interaction by changing the tip height over the scanned area. In the present thesis, AFM measurements were carried out in tapping mode under ambient conditions using Raman-AFM integrated (WiTec alpha RA 300) system. All the AFM images were analyzed using Wsxm software[155] to obtain various parameters such as root mean square (rms) roughness and grain size.

2.4.2. Scanning electron microscopy (SEM)

A scanning electron microscope (SEM) collects wide ranges of signal from the sample by scanning the surface with a focused beam of electrons. As the electrons interact

with the sample, they produce various signals (as shown in Figure 2.6), that come from the various depths of the sample. The signals include secondary electrons (SE), back scattered electrons (BSE), Auger electrons, and characteristic X-rays.

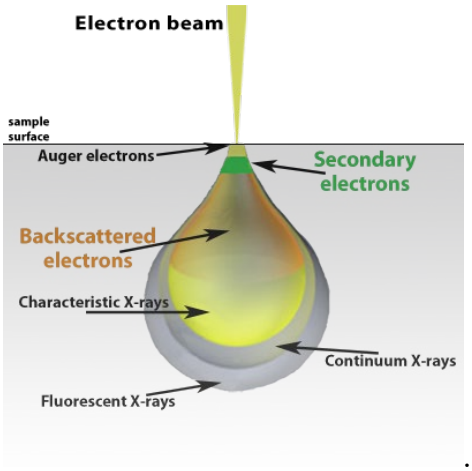

Figure 2.6: Schematic representation of various signal obtained in SEM, while the electron interacted with the sample.

The signals reveal the information about the sample including morphology, chemical composition, and crystalline structure and orientation of the sample. Secondary electrons and backscattered electrons are commonly used for imaging the samples, where secondary electrons gives topography contrast and backscattered electrons gives composition (*i.e., Z* contrast).

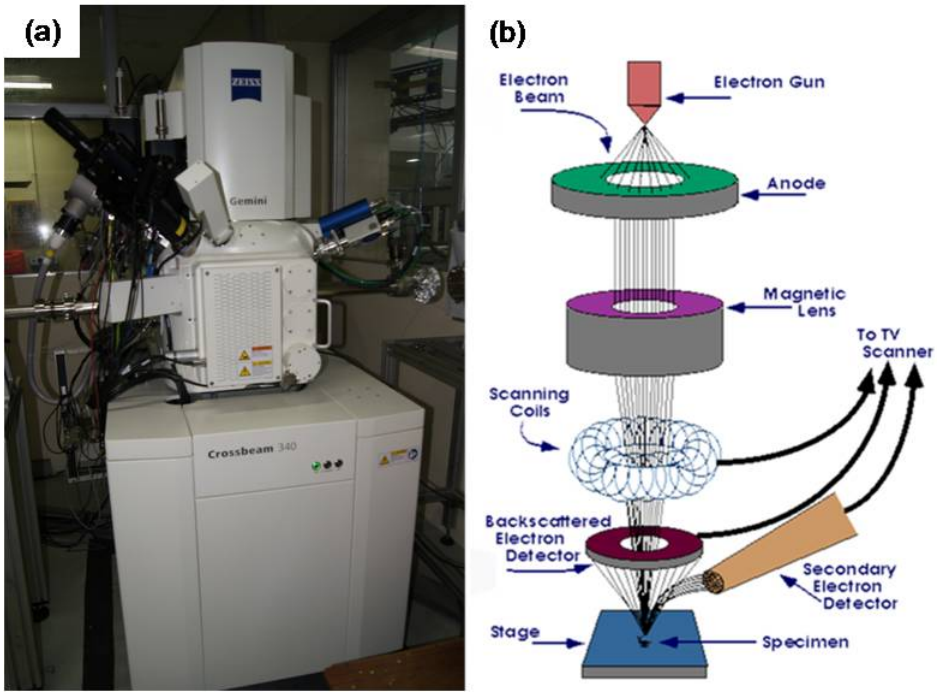

Figure 2.7: The Crossbeam 340 scanning electron microscope: the photograph (a) and schematic of the electron path (b).

The microscope used for the studies in the present thesis is Crossbeam 340 (Carl Zeiss). Figure 2.7 shows the photograph (a) and schematic illustration of the electron microscope. It consists of field emission gun (electron source), 5 axis stage manipulator, SESI (secondary electron secondary ion) detector and in-lens duo detector. Electrons are produced at the top of the column, accelerated down and passed through a combination of lenses and apertures to produce a focused beam of electrons which hits the surface of the sample. The sample is mounted on a stage in the chamber area and, unless the microscope is designed to operate at low vacuums, both the column and the chamber are evacuated by a combination of vacuum pumps.

2.4.3. Transmission electron microscopy (TEM)

The transmission electron microscope (TEM) is the characterization tool for structural and chemical characterization at the nanoscale.

In TEM microscopy, an electron transparent sample is bombarded by a beam of high energy coherent electrons. The beam has enough energy for the electrons to be transmitted through the sample, and the transmitted or scattered electron signal is greatly magnified by a series of electromagnetic lenses. The magnified signal may be observed in terms of electron diffraction, mass-thickness contrast imaging, amplitude-contrast imaging such as diffraction contrast, or phase-contrast imaging such as high resolution TEM.

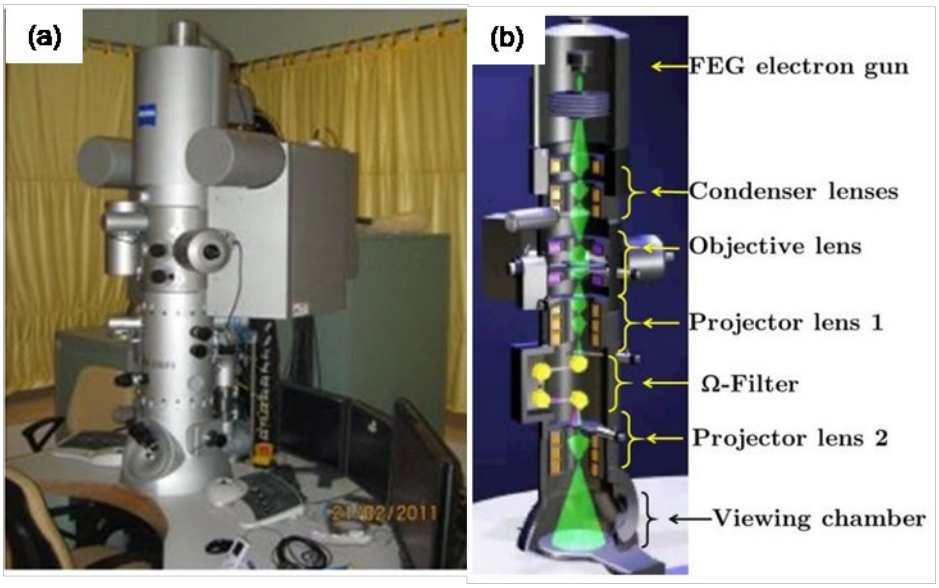

Figure 2.8: Carl Zeiss Libra 200FE Transmission Electron Microscope: the photograph (a) and schematic of the electron path (b).

Transmission electron diffraction patterns help to determine the crystallographic structure of a material. Amplitude-contrast images yield information about the chemistry

and microstructure of a material and its defects. Phase-contrast imaging or high-resolution (HR) TEM imaging gives information about the microstructure of a material and its defects at an atomic resolution. In the present thesis, TEM characterization was done using HRTEM (LIBRA 200 FE, Carl Zeiss) system. It is a high resolution TEM (HRTEM), equipped with field emission gun (FEG) electron source and an in column omega filter. Figure 2.8 shows the photograph of the high resolution transmission electron microscope and the illustration of electron path. HRTEM is operated at 200 kV. The information limit of the microscope is 1.3 Å. The essential components of TEM consist of illumination system, objective lens system, and imaging system.

The illumination system consists of the electron gun and one or two condenser lenses. In the objective lens system, the electrons encounter the specimen and one of three things can happen. They may pass through it unimpeded. They may be scattered without loss of energy (elastic scattering), or they may be inelastically scattered; this involves an exchange of energy between the electron beam and the specimen, and may cause the emission from the specimen of secondary electrons or X-rays. In the Imaging system, several lenses are used to magnify and focus the images on the viewing screen or on the charged couple detector (CCD) device.

2.4.3.1. TEM sample preparation

The sample should be ultimately electron beam transparent (less than 100 nm) for TEM sample characterization. Different methods exist for sample preparation, for different types of materials (metals/glass/ceramics) and different sample geometries (bulk/thin films/powders). In the present thesis, TEM samples were prepared by dispersing few microgram of Bi_2Te_3 powder in ethanol and are ultrasonicated for few minutes. Above liquid mixture drawn by a micro pipette, it is dispersed carefully on a carbon coated TEM copper grid and are dried. Furthermore, in order to study the ion irradiation induced defects, ion irradiation was carried out separately on Bi_2Te_3 dispersed TEM grids and were investigated accordingly. The above method is entirely used for TEM observations over ion milling and FIB milling method in order to avoid the artifacts produced during the process of TEM sample preparation.

2.5. Spectroscopy and spectrometry technique

2.5.1. Energy dispersive X-ray (EDX) analysis

Energy dispersive X-ray (EDX) analysis is a technique that can be used to identify and quantify the elemental composition of the sample. It is generally coupled with SEM or

TEM instrument. This technique relies on the excitation of atoms on the surface by electron beam. Upon excitation, the electrons in the inner shell may eject out, while creating hole. An electron from an outer, higher-energy shell then fills the hole, and the difference in energy between the higher-energy outer shell and the lower energy inner shell may be released in the form of X-ray. It is the characteristic of the atomic structure of the elements. Thereby, it allows the identification of the particular elements and the relative proportion of the sample. This works best for the element with atomic number greater than 3. The output of the EDX is spectrum, where the peaks reveal the elements that have been identified in the sample.

Accuracy of the EDX analysis can be affected by various factors including the nature of the sample. There is no special sample preparation for EDX analysis, except that the sample should be flat and polished. In the present thesis, EDX spectra were obtained using FESEM (SUPRA 55, Carl Zeiss) instrument equipped with X-ray detector.

2.5.2. Raman scattering

Raman scattering is a type of non-destructive vibrational spectroscopy, which is used to probe and study the dynamics of vibrations and rotations of the molecules in the sample. Raman spectroscopic technique uses a monochromatic light (*i.e.,* laser) source, which is used to excite the material sample. When light is scattered by matter, most fraction of light elastically scattered without any change in energy and this process is called Rayleigh scattering. At the same time, a very small fraction of light undergoes inelastic scattering, where it loses energy in modifying the vibrational level of the molecule.

In the present thesis, Raman spectra were obtained using Raman-AFM integrated (WiTec alpha RA 300) system. The photograph and schematic diagram of the system are shown in Figure 2.9. The instrument consists of a laser source, filter, objective lens, beam splitter, notch filter, spectrometer and CCD camera. The excitation is produced by the Nd-YAG laser source with the wavelength of 532 nm. The elastically scattered Rayleigh signal is filtered using dichroic beam splitter along with notch filter, while the unwanted wavelength is removed by the laser line filter. The laser spot size was fixed to ~1μm. The Raman spectra were recorded through 100X objective lens and dispersed through 1800 g/mm grating, which provide the spectral resolution of 1 cm^{-1}. To avoid sample heating during Raman measurements, laser excitation power was optimized and fixed to the value of 0.5 mW. In case of Bi_2Te_3 materials, the above laser excitation power is consistent with

the previous literature[156,157] and gives good signal to noise ratio without damaging the samples.

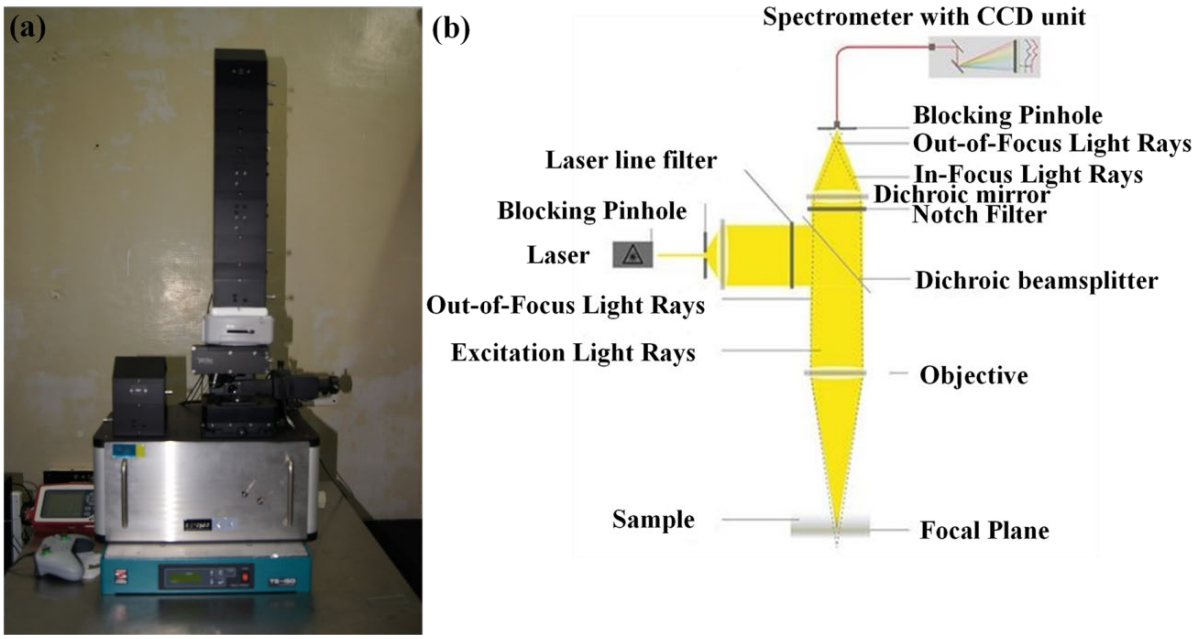

Figure 2.9: Raman-AFM integrated (WiTec RA 300) system: (a) photograph and (b) schematic diagram of the system for Raman spectra measurements.

2.5.3. Rutherford Backscattering spectrometry (RBS)

The Rutherford backscattering spectrometry (RBS) is a non-destructive ion-scattering technique used for the depth profiling of elements present in the sample, atomic mass identification, and stoichiometric determination. In RBS, the sample is bombarded with He^+ ions of very high energy, particularly around MeV range using 1.7 MV tandetron accelerator. The back-scattered ions energy depends on the mass and depth of the target sample, which interacts. A simplified layout of backscattering experiment is shown in Figure 2.10. The energy of the backscattered ions is detected by solid state surface barrier detector.

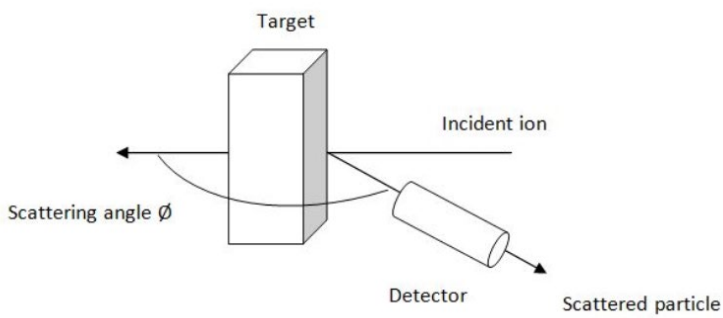

Figure 2.10: Schematic representation of the experimental setup for Rutherford backscattering analysis.

The surface barrier detector is a thin layer of *p*-type silicon on the *n*-type substrate resulting *p-n* junction. When the scattered ions create electron-hole pairs in the detector, the energy of scattered ions is detected by simply counting the number of electron-hole pairs. The energy resolution of the surface barrier detector is 12 keV to 15 keV. The surface barrier detector is generally set between the scattering angle of 90° and 170° to the incident beam. Films are usually set normal to the incident ion beam.

Basic description of RBS can be expressed by the following equations.

$$E_1 = kE_0 \qquad \textbf{Eqn. 2.4}$$

$$k = \left(\frac{m_1 cos\theta_1 + \sqrt[2]{(m_2^2 - m_1^2(cos\theta_1)^2)}}{m_1 + m_2}\right)^2 \qquad \textbf{Eqn. 2.5}$$

where E_1 is the energy of the back-scattered ion, E_o is the energy of the incident ion, k is the kinematic factor, which is actually the energy ratio of the particle before and after the collision. Since k depends on the masses of the incident particle (m_1) and target atom (m_2) and the scattering angle (θ_1), the energy of the scattered particle is also determined by these three parameters. The RBS spectra can be simulated using SIMNRA software[158] and compared with the experimental RBS spectra to obtain the various parameters such as film thickness and stoichiometry. The peak position in the RBS spectrum gives elemental information, while thin film thickness values could be determined from the peak width and height. In the present thesis, RBS spectrometry was carried out in Bi_2Te_3 thin films using 1.7 MV Tandetron accelerator.

2.6. Thermoelectric (TE) characterization

2.6.1. Hall-effect

Hall-effect measurement is performed to determine various material parameters such as Hall coefficient, sheet resistivity, charge carrier type, concentration and carrier mobility of the sample. The underlying principle for Hall-effect measurement is Lorentz force. Under Vander-pauw configuration, the Hall voltage (V_H) is determined by placing the sample perpendicular to magnetic field, applying DC current diagonally across the sample, and measuring voltage across the other diagonal connection as given in Figure 2.11.

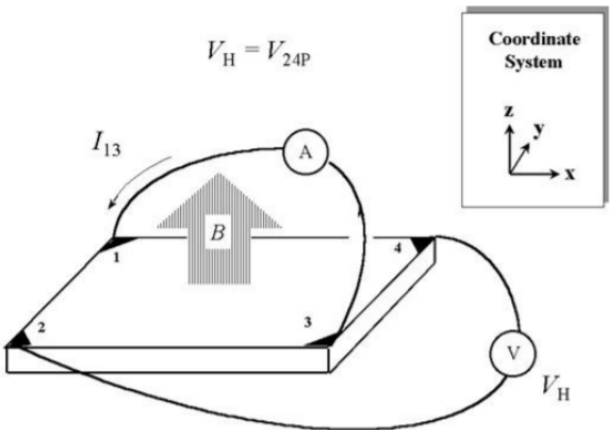

Figure 2.11: Configuration for Hall-effect measurement system.

When magnetic field is applied perpendicular to the direction of current flow, electrons will accumulated at the one edge of the sample. This in turn leads to potential difference across the sample, known as Hall voltage. The accuracy can be improved by reversing the current and repeating the measurements. The magnetic field is reversed and the entire procedure is repeated to remove any bias due to sample geometry.

In the present thesis, room temperature Hall-effect measurements were carried out using Ecopia HMS 5000 system. The measurements were done under the magnetic field of 0.57 T to measure carrier concentration and carrier mobility of the sample.

2.6.2. Seebeck coefficients

Seebeck coefficient (*S*) is the important parameter for TE characterization, which is defined as the ratio of voltage drop induced by a small temperature difference in the material. In the present thesis, home-made setup at Inter university accelerator center (IUAC) was used to perform Seebeck coefficient measurements[159]. The photograph and the schematic diagram of the Seebeck coefficient measurement setup is shown in Figure 2.12. In the setup, *S* can be measured in the temperature range of 77 K to 500 K by using differential method under vacuum environment. The setup consists of two rectangular copper bars like a bridge arrangement for sample mounting, a pair of surface mount chip resister for creating temperature difference, and a type E thermocouple for measuring temperature gradient across the sample. Keithly 2182A nanovoltmeter is used to measure the Seebeck voltage and all the equipment and measurements are controlled by Labview program in a PC which makes the system automated one.

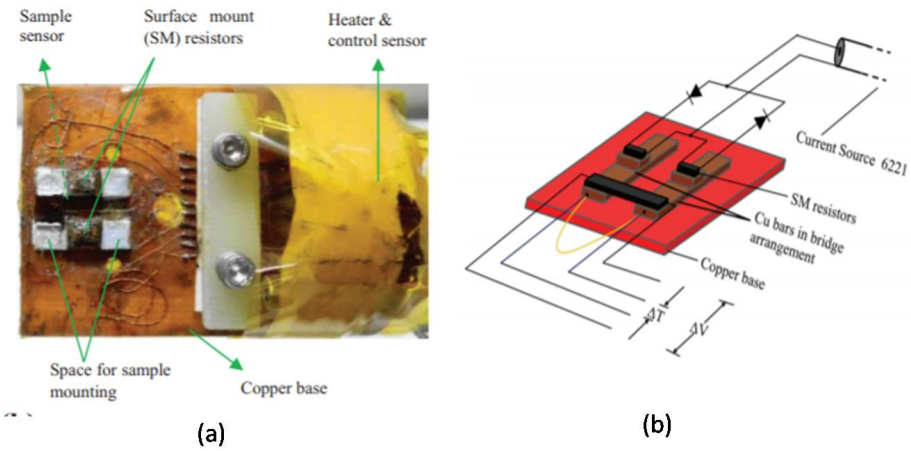

Figure 2.12: Photograph (a) and schematic diagram (b) of the Seebeck coefficient measurement setup.

2.6.3. Electrical conductivities

Electrical conductivity (σ) was measured using in-built standard four probe method at Inter university accelerator center (IUAC). In the four probe setup, outer probes are used to pass constant current through the sample. Inner probes are used to measure the potential drop on the section of the sample, generated by passing the current, I. In this way, the effect of contact resistance is suppressed and the only the contribution from the sample is obtained. Figure 2.13 (a) illustrates the linear four probe configuration used in this work. Sheet resistance (R_s) can be calculated using the following equation:

$$R_s = \frac{\pi}{ln(2)} \frac{\Delta V}{I} \qquad \textbf{Eqn. 2.6}$$

where, ΔV, I is the voltage measured between probe 2 and 3, electric current applied between the probe 1 and 4. $\pi/\ln(2)$ is the geometric correction factor. If the thickness of the material is known, electrical conductivity (σ) can be calculated from the sheet resistance (Eqn. 2.6).

$$\sigma = \frac{1}{R} = \frac{1}{R_S t} \qquad \textbf{Eqn. 2.7}$$

Here, R is the resistivity and t is the thickness of the sample. length, width, and thickness of the film. The contacts were made using silver paste, since silver paste offers an ohmic contact and the probe wires are attached to the sample using silver epoxy solder. All the measurements were performed at rotary vacuum in the temperature ranges from 300 K to 420 K. All the equipment and measurements was automated using Labview program.

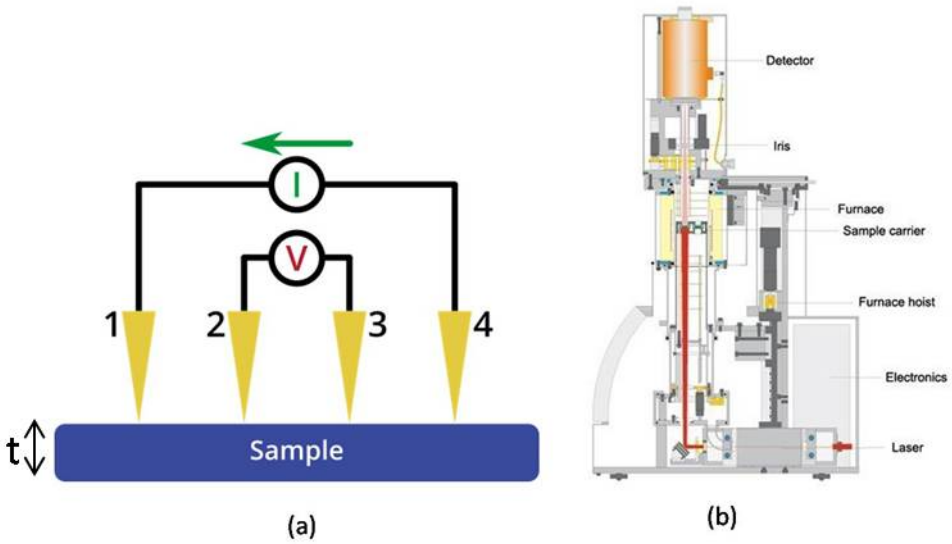

Figure 2.13: Schematic of (a) four-probe method for electrical conductivity measurements and (b) Netzsch LFA 457 laser flash apparatus for thermal diffusivity measurement.

2.6.4. Thermal conductivity

Room temperature thermal conductivity (κ) can be calculated from $\kappa = DC_p d$, where D, C_p, d are thermal diffusivity, specific heat capacity, and density respectively. A c_p value[151] for bulk Bi_2Te_3 as 0.155 J/g-K was considered. In this thesis, thermal diffusivity was measured on the pellet samples (dimension: 14 mm and thickness: 2 mm) using Netzsch LFA 457 Microflash laser flash apparatus (Figure 2.13 (b)). In laser flash measurement system, the one side of the pellet sample is first heated by a short energy laser pulse. The resulting time dependent temperature change on the upper surface of the sample is then measured with an infrared detector. Thermal diffusivity can be calculated from its temperature rise. In other words, thermal diffusivity is the measure of speed at which the body can change its temperature and the values can be calculated using the Eqn. 2.8.

$$D = 0.1388\frac{d^2}{t_{1/2}} \qquad \textbf{Eqn. 2.8}$$

where, d is the thickness of the pellet in cm and $t_{1/2}$ is the time to reach half maximum of temperature in sec. In addition, the density of the pellets was measured in water using Archimedes principle.

2.7. Summary

The experimental procedures followed for the Bi_2Te_3 sample synthesis and the ion irradiation experiments have been discussed. The ion irradiation facility (150 kV and 1.7 MV Tandem accelerator) used in the work is explained. The details of various characterization tools used in the present work are discussed briefly.

Chapter 3

Growth and thermoelectric properties of the bismuth telluride nanostructures

3.1. Introduction

The fabrication of the highly efficient thermoelectric (TE) devices is essential to convert waste heat into electrical energy effectively. Bismuth telluride[17,160] (Bi_2Te_3) is our material of interest, since Bi_2Te_3-based TE materials are exhibiting highest values of *ZT* (~1) at room temperature since 1950s. Improving the *ZT* values beyond 1 are extremely difficult in bulk materials, owing to the interdependency of TE transport properties (*i.e.,* power factor and electronic thermal conductivity) *via* electronic band structures.

As discussed in Chapter 1, nano-structuring strategy has been successfully employed during last two decades to improve and optimize the *ZT* value of some materials. A particularly interesting class of nanomaterials is defect incorporated nanostructures[61,62,89,161] that containing several phonon scattering centers and interfaces, which may boost the phonon scattering and eventually suppress the lattice thermal conductivity more strongly than the electrical conductivity. Meanwhile, another potential advantage of these nanostructures is the possibility to tune the TE characteristics such as Seebeck coefficient and electrical conductivity. In that regard, enhancement in density of states near Fermi level due to quantum confinement has been predicted to enhance the TE transport parameters[40,42,43]. Additionally, energy filtering at nanostructured interfaces may further enhance Seebeck coefficient by selectively scattering low energy carriers[39]. Therefore, the morphology of the nanostructures along with crystal defects also plays an important role in determining TE transport properties.

The morphology control of nanomaterials has been considered as a crucial role in synthesis procedure due to their structure-dependent TE transport properties. Among various synthesis techniques, hydrothermal method is adopted in the present work, aiming at attaining good control on the morphology of the fabricated materials. This can be achieved by the proper choice of the appropriate surfactant and reaction temperature that enables rapid, high yield products with desired chemical compositions, at relatively low synthesis temperatures. Surfactant-assisted hydrothermal methods[86,125,162] have been widely used in the preparation of nanoparticles with different morphologies such as nanorods, hexagonal sheets, nanotubes *etc*.

Typically, it has been demonstrated that surfactants can be used as templates during the growth process. Surfactant-assisted hydrothermal method offers a flexibility to control the nucleation and the growth of nanoparticles, hence the morphology control of the synthesized products are achieved.

It is important to note that the Bohr radius[163] of the Bi_2Te_3 for electron and hole is 57 nm and 45 nm respectively, which are three orders of magnitude higher than the Bohr radius of hydrogen. This is due to the small values of hole (electron) effective mass and large values of its dielectric constant. Thus, Bi_2Te_3 nanorods with a diameter less than Bohr radius (*i.e.,* < 57 nm) will exhibit a strong quantum confinement effects and are expected to have enhanced TE transport properties. Until now, Bi_2Te_3 nanorods has diameter ranging between 50 nm and 100 nm have been fabricated by the hydrothermal method[85,86,125,164,165], whereas narrower Bi_2Te_3 nanorods (diameter < 50 nm) have been fabricated, by employing Te nanorods as the Te precursor[46,166]. In general, the Bi_2Te_3 nanorod samples were made in to pellet and have been characterized for TE transport properties. For example, sintered pellet composed of Bi_2Te_3 nanorods bundles[167] with an average diameter of ~ 60 nm demonstrated peak *ZT* value (~ 0.43) at 473 K. Rashad *et.al* [168]., showed that hot pressed Bi_2Te_3 nanorods (diameter of 50 to 100 nm) pellets exhibited *ZT* of 0.14.

In this chapter, result on the growth of Bi_2Te_3 nanostructures using surfactant assisted hydrothermal method and are presented. Furthermore, the Bi_2Te_3 nanostructures are grown under wide range of conditions and the morphology of the resulting Bi_2Te_3 nanostructures were investigated as a function of surfactant concentration and reaction temperature. These systematic investigations enable to explore the growth kinetics and growth mechanism of Bi_2Te_3 nanostructures. The TE properties of these nanostructures is also investigated and discussed.

3.2. Experimental methods

3.2.1. Sample synthesis

The starting materials for the synthesis of nanostructured Bi_2Te_3 powder samples are bismuth chloride ($BiCl_3$, 99.99%) and sodium tellurite (Na_2TeO_3, 99%). Sodium borohydride ($NaBH_4$, 99%) and sodium dodecylbenzenesulphonate (SDBS, 98%) were used as the reducing agent and surfactant respectively. All the chemicals were of analytical grade and are used without further purification.

Table 3.1: Labels for the Bi_2Te_3 samples synthesized under different hydrothermal conditions.

Sample label	Growth conditions	
	SDBS concentration	Reaction temperature
0-SDBS	0 mmol	130 ºC
3-SDBS	3 mmol	
5-SDBS	5 mmol	
7-SDBS	7 mmol	
8-SDBS	8 mmol	
SDBS-100	8 mmol	100 ºC
SDBS-130		130 ºC
SDBS-150		150 ºC

2 mmol of $BiCl_3$ was dissolved in 100 ml distilled water to prepare milky white bismuth chloride solution. 20 ml of 2 M NaOH (2 M and 20 ml) was added drop by drop to the prepared bismuth chloride solution. Eventually, Na_2TeO_3 (3 mmol) and SDBS of different concentrations (0 to 8 mmol) were added to the above-mixed solution and the resultant solution was continuously stirred for 2 h. Then, 10 mM $NaBH_4$ was added dropwise to the above milky white solution. Subsequently, the solution turned milky white to dark grey. The final solution was transferred to a 200 ml Teflon-lined stainless steel autoclave. The autoclave was made to fill up to 80% of its volume using distilled water.

The autoclave was sealed and kept in a hot-air oven at different temperatures (100 ºC, 130 ºC, and 150 ºC) for 24 h. Upon natural cooling, the final black precipitates were filtered, washed several times with ethanol, acetone and distilled water. The final precipitates were dried at 80 ºC for 4 h in vacuum. Finally, the resultant products are labeled accordingly in Table 3.1.

The powder samples of Bi_2Te_3 with different morphology were pelletized in the form of rectangular shape (dimension: 10 mm × 5 mm × 1 mm) for Seebeck coefficient, electrical conductivity measurements and circular shape (diameter: 14 mm and thickness: 2 mm) for thermal diffusivity measurements, respectively. During the pelletizing process, the Bi_2Te_3 powders were kept under a pressure of about 10 MPa for 10 min and the relative density of the each pellet was measured in water using the Archimedes principle.

3.2.2. Characterization techniques

As mentioned in Chapter 2, samples were investigated with X-ray diffraction (Inel, Equinox 2000) by using Cu K_α radiation (1.541 Å) to ensure the formation of the Bi_2Te_3 crystalline phases. The morphology and the microstructure of the synthesized Bi_2Te_3 samples were obtained using focused ion beam field emission scanning electron

microscopy (FIB-FESEM, Zeiss, Cross beam 340) and high resolution transmission electron microscopy (HRTEM, Zeiss, LIBRA 200 FE). The FIB-FESEM was operated with an accelerating voltage of 5 KV at a working distance of ~3 mm and the images were recorded using in-lens detector. The HRTEM was operated with an accelerating voltage of 200 kV. The HRTEM samples were prepared by dispersing few microgram of Bi_2Te_3 powder in isopropyl alcohol and drop casting it on carbon coated Cu grids. Energy dispersive X-ray (EDX) analysis was employed to analyze the chemical composition of the samples.

The TE properties were measured in the temperature range of 300-410 K. The Seebeck coefficient was carried out by using in-house developed measurement setup having bridge arrangement of two copper bars[159]. Electrical conductivity was measured using standard four probe method and the room temperature hall-effect measurements was carried out by using 4 probes under Vander-pauw configuration (Ecopia HMS-2000) for carrier concentration and mobility measurements. Furthermore, the room temperature thermal conductivity was calculated from thermal diffusivity values, which in turn were determined using laser flash apparatus (Netzsch LFA 457). The Seebeck coefficient and electrical conductivity were measured in-plane, while thermal diffusivity was measured across the pellets.

3.3. Results

3.3.1. Morphology and structure evolution: the role of surfactant concentration

The XRD pattern of Bi_2Te_3 samples synthesized in the presence of different surfactant (SDBS) concentration at 130 ºC, are shown in Figure 3.1. Evidently, all the diffraction peaks of the XRD patterns are indexed to the rhombohedral crystal structure of Bi_2Te_3. The diffraction peaks are in line with the planes of [1 0 1], [0 1 5], [0 1 8], [1 0 10] *etc,* as reported in the standard reference data JCPDS 01-080-6959. The space group is identified as $R\bar{3}m$ with lattice constant of $a = b = 4.345$ Å and $c = 30.483$ Å. Diffraction peaks corresponding to the precursor material and/or impurity phases are not observed. Furthermore, it has been observed that Bi_2Te_3 sample synthesized in the absence of surfactant (0-SDBS) contains all possible orientation of Bi_2Te_3 crystal as compared to other samples and the addition of SDBS surfactant decreases the relative intensities of various planes such as [1 0 1], [0 2 10].

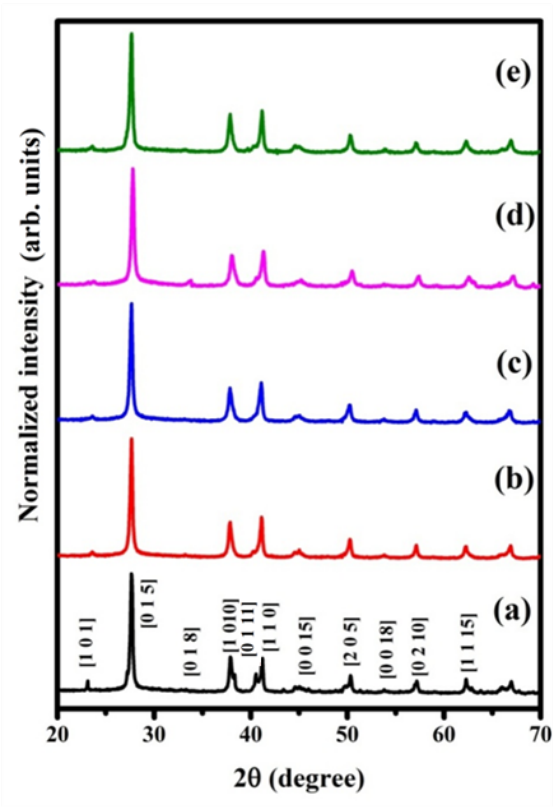

Figure 3.1: XRD pattern of the samples (a) 0-SDBS, (b) 3-SDBS, (c) 5-SDBS, (d) 6-SDBS, and (e) 8-SDBS.

The W-H plots for Bi_2Te_3 samples synthesized under different concentrations of SDBS surfactant and the corresponding deconvolute values of average crystallite size and strain are presented in Figure 3.2. When adding the surfactant, the crystallite size decreases remarkably from ~40 nm to ~28 nm. In contrast, the lattice strain increases and reached maximum value (~15×10^{-4}) until SBDS concentration (6-SDBS), and then the strain value steadily decreases. The increase in lattice strain is ascribed to the increase in lattice imperfections in the crystal.

Figure 3.3 shows the morphology of Bi_2Te_3 nanostructures synthesized at 130 ºC in the presence of varying SDBS concentration. The low magnification FESEM images are presented in Figure 3.3 (a) to Figure 3.3 (e), while the corresponding high magnification FESEM images are displayed in Figure 3.3 (f) to Figure 3.3 (j) and the insets show the diameter distribution of Bi_2Te_3 nanorods. The morphology of Bi_2Te_3 grown in the absence of surfactant (0-SDBS) consists of hexagonal platelets (size varying from 20 nm to 200 nm), thick nanorods, and agglomerated particles (Figure 3.3 (a)). 3-SDBS sample consist of nanostructures, which exhibit web-like morphology (Figure 3.3 (b)). The corresponding high magnification image (Figure 3.3 (g)) of these filamentous

morphology revealed the interweaving and interconnection of 50 nm to 100 nm sized elongated nanoparticles.

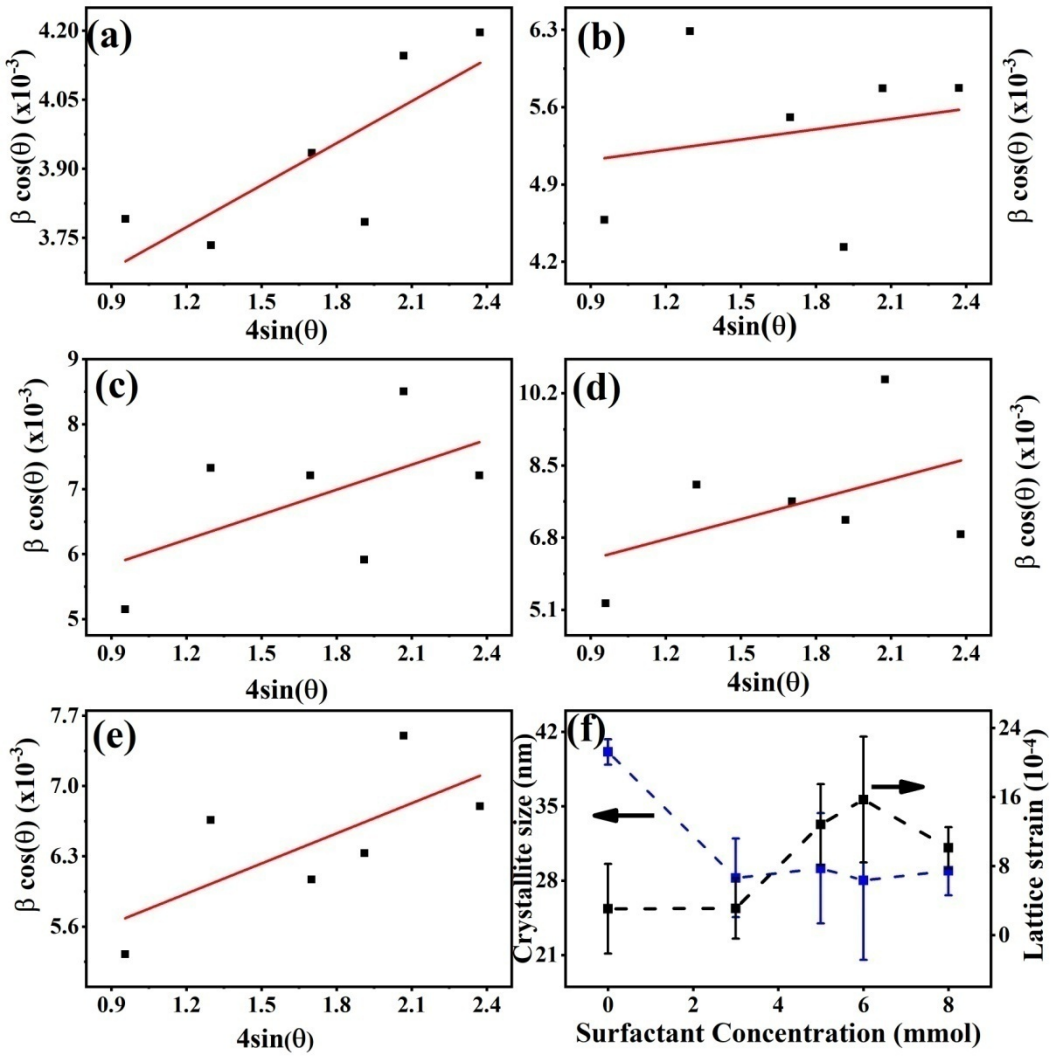

Figure 3.2: The Williamson-Hall (W-H) plot for the samples: (a) 0-SDBS, (b) 3-SDBS, (c) 5-SDBS, (d) 6-SDBS, and (e) 8-SDBS. (f) show the variation in the crystallite size and lattice strain as a function of surfactant concentration.

Further, 5-SDBS (Figure 3.3 (c)) sample composed of Bi_2Te_3 nanorods (mean diameter- 75 nm) along with the agglomerated particles. The enlarged FESEM image (Figure 3.3 (h)) of the typical Bi_2Te_3 nanorod shows that the rods are rough and that most of them are composed of nanoparticles. The sample 6-SDBS predominantly consist of Bi_2Te_3 nanorods with a mean diameter of 70 nm (Figure 3.3 (d)) and the associated magnified image shows the faceted and smooth Bi_2Te_3 nanorods (Figure 3.3 (i)).

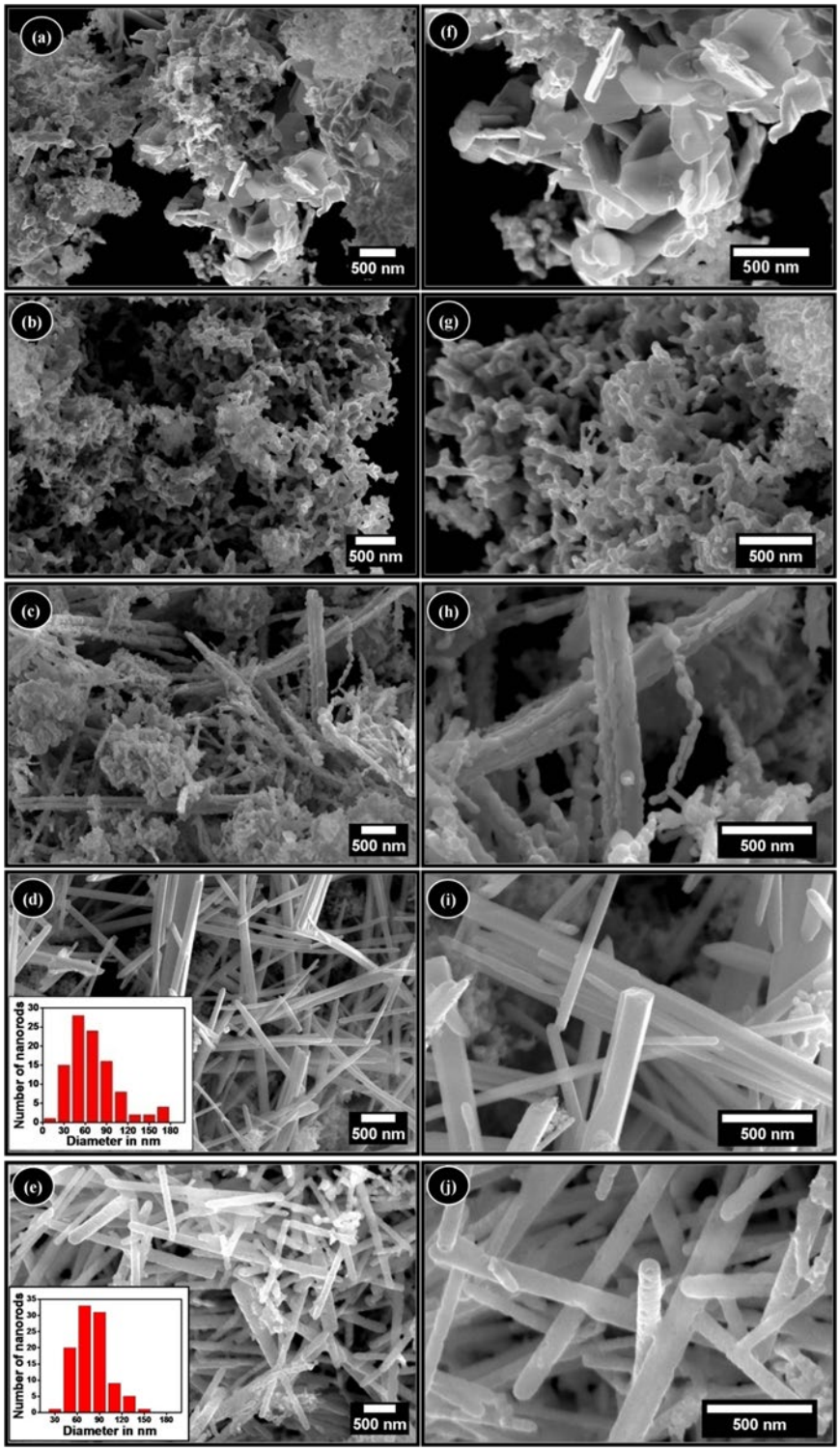

Figure 3.3: Low magnification (a-e) and high magnification (i-j) FESEM images of (a) 0-SDBS, (b) 3-SDBS, (c) 5-SDBS, (d) 6-SDBS, and (e) 8-SDBS, respectively, Inset shows the diameter distribution of Bi_2Te_3 nanorods.

As seen clearly in Figure 3.3 (e), sample 8-SDBS is composed of rough Bi_2Te_3 nanorods and the pores are seen distinctly on the surface of the nanorods (Figure 3.3 (j)). Moreover, the inset of Figure 3.3 (e) presents the diameter distribution of Bi_2Te_3 porous nanorods and the mean diameter is found to be 78 nm. It has to be noted that all these

Bi_2Te_3 samples are synthesized under same reaction conditions such as solvent concentration, reaction time, and reaction temperature, except SDBS concentration. Therefore, one can conclude that the amount of SDBS plays an important role in the formation of Bi_2Te_3 nanorods and significantly influences the morphology of the sample and the surface morphology of Bi_2Te_3 nanorods.

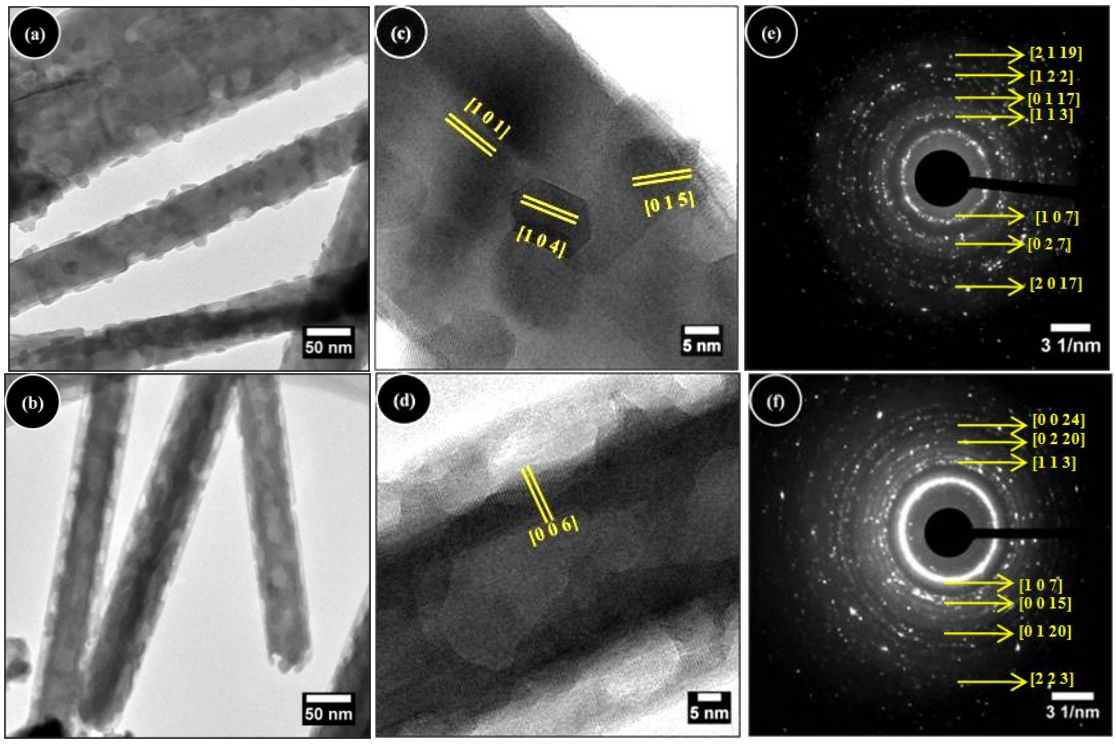

Figure 3.4: TEM bright field image (a, b), HRTEM image(c, d) and the corresponding electron diffraction pattern (e, f) of the sample 6-SDBS and 8-SDBS respectively.

Detailed investigations have been carried out on the samples 6-SDBS and 8-SDBS using HRTEM (Figure 3.4). The bright field image (Figure 3.4 (a), Figure 3.4 (b)), HRTEM image (Figure 3.4 (c), Figure 3.4 (d)) and corresponding electron diffraction pattern (Figure 3.4 (e), Figure 3.4 (f)) have been analyzed to reveal the detailed microstructural features present in the synthesized Bi_2Te_3 nanorods. For the sample 6-SDBS (Figure 3.4 (a)), the Bi_2Te_3 crystallizes in the form of nanorods, having mean diameter of 70 nm. In contrast to their corresponding FESEM image (Figure 3.3 (i)), one can see that Bi_2Te_3 flakes were apparently cemented on the surface of these nanorods. Furthermore, Figure 3.4 (c) confirms the polycrystalline nature of flakes decorated Bi_2Te_3 nanorods and the average size of these Bi_2Te_3 flakes were observed to be about 20 nm. It has to be noted that the lattice fringes of the flakes decorated Bi_2Te_3 nanorods were corresponding to [1 0 1], [1 0 4], and [0 1 5] planes of Bi_2Te_3 crystal respectively.

Figure 3.4 (b) displays the bright field image of the porous Bi_2Te_3 nanorods (Sample 8-SDBS). The pores are distinctly recognized from the variation in the contrast in the corresponding bright field and HRTEM images. Most importantly, this variation in the contrast is observed in the outer rim of the Bi_2Te_3 nanorods. The differences in contrast are due to the variation in the nanorod thickness. These pores are irregular in shape and the sizes are varied from 20 nm to 30 nm. HRTEM image (Figure 3.4 (d)) further confirms the highly crystalline nature of porous nanorod, with lattice spacing of ~0.34 nm, corresponding to [0 0 6] planes of Bi_2Te_3 crystal. All the electron diffraction patterns (Figure 3.4 (e), Figure 3.4 (f)) obtained on the group of these flakes decorated and porous Bi_2Te_3 nanorods confirm the polycrystalline nature and the diffraction rings are indexed to the various planes of Bi_2Te_3 crystal.

3.3.2. Morphology and structure evolution: a role of reaction temperature

The XRD pattern of Bi_2Te_3 samples synthesized at different reaction temperatures (Figure 3.5) is correlated well with the standard reference data JCPDS 01-080-6959. The W-H plots for the samples prepared under different reaction temperature are presented in the Figure 3.6 (a) to Figure 3.6 (c).

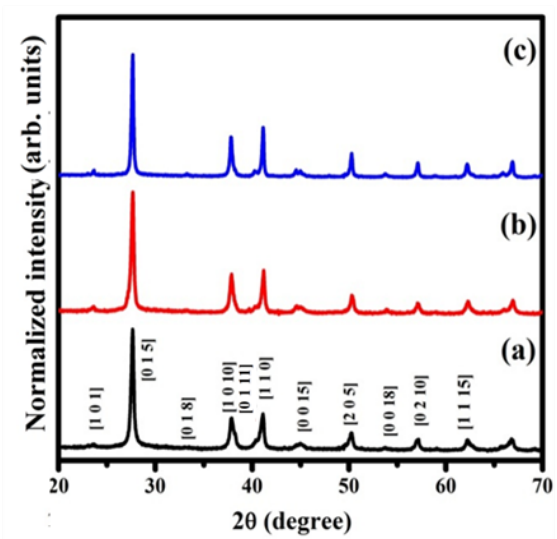

Figure 3.5: XRD pattern of the samples synthesized in the presence of 8 mmol SDBS concentration and at different reaction temperatures (a) SBDS-100, (b) SDBS-130, and (c) SDBS-150.

Furthermore, it has been concluded from Figure 3.6 (d) that the increase in reaction temperature resulted in samples with slightly higher crystallite size and significantly lower strain. Figure 3.7 presents the morphology and microstructure of the Bi_2Te_3 prepared at the reaction temperatures of 100 °C and 150 °C, while SDBS concentration was fixed at

8 mmol. Bi_2Te_3 products prepared at low reaction temperature (SDBS-100) result in thick and short Bi_2Te_3 nanorods (Figure 3.7 (a)), while Bi_2Te_3 flakes were apparently cemented and decorated the surface of the short nanorods. In contrast, when the reaction temperature is high (SDBS-150), smooth Bi_2Te_3 nanorods with mean diameter of 80 nm are formed.

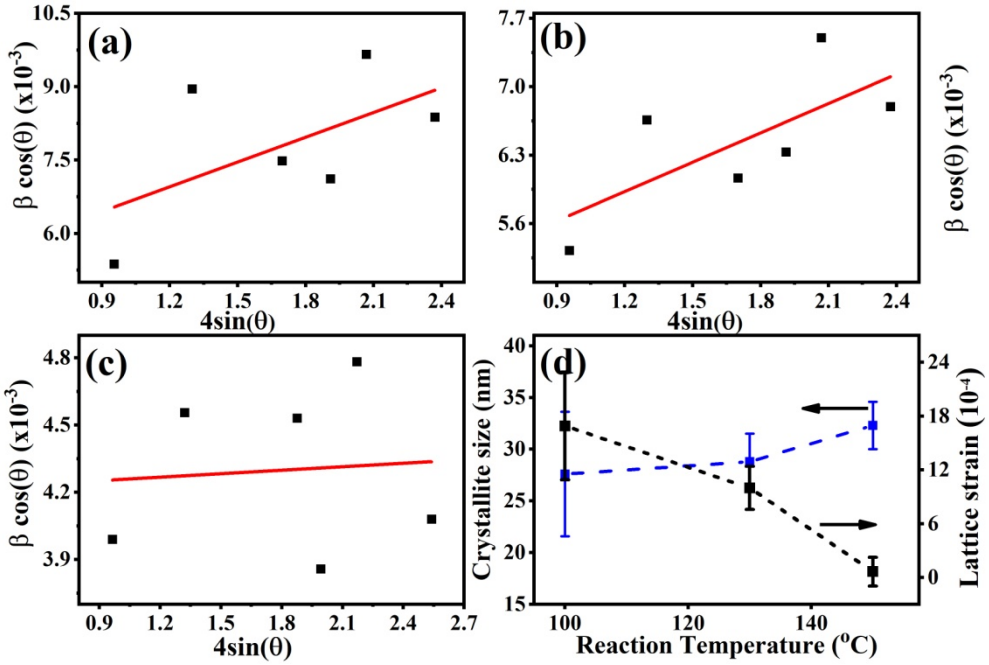

Figure 3.6: W-H plot for the samples (a) SDBS-100, (b) SDBS-130, (c)SDBS-150 and (d) shows the variation in the crystallite size and lattice strain as a function of reaction temperature.

Further insight into the Bi_2Te_3 nanorods synthesized at higher temperature is provided by TEM results and it is presented in Figure 3.7 (c). Figure 3.7 (c) shows a typical bright field image of a Bi_2Te_3 nanorod with a diameter of about 70 nm. The corresponding HRTEM image (Figure 3.7 (d)) confirms the single crystalline nature of nanorods. In addition, the lattice fringes with *d* spacing of 0.58 nm and 0.32 nm are corresponding to [0 0 6] and [0 1 5] planes of Bi_2Te_3 are shown in Figure 3.7 (d). The electron diffraction patterns (Figure 3.7 (e)) obtained on the smooth Bi_2Te_3 nanorods demonstrate their poly crystalline nature and the corresponding diffraction patterns are indexed to the various planes of Bi_2Te_3 crystals.

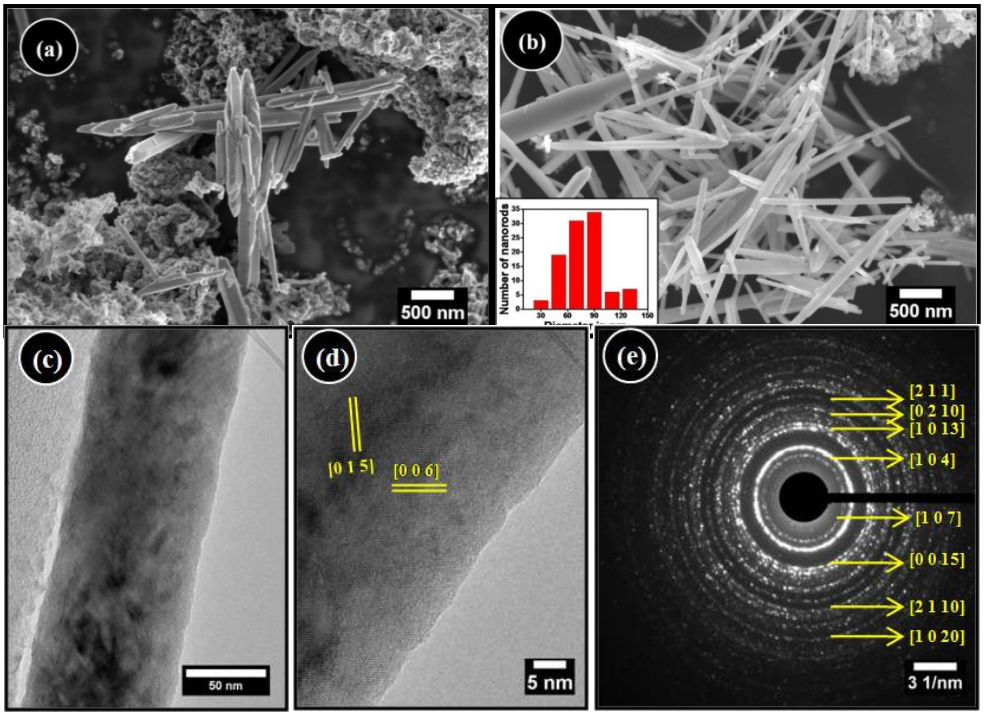

Figure 3.7: FESEM images of the sample: (a) SDBS-100 and (b) SDBS-150 and the (c) high magnification bright field image of SDBS-150 Bi_2Te_3 nanorods. (d) and (e) are corresponding HRTEM image and indexed electron diffraction pattern.

3.3.3. Effect of morphology of nanorods on thermoelectric transport properties

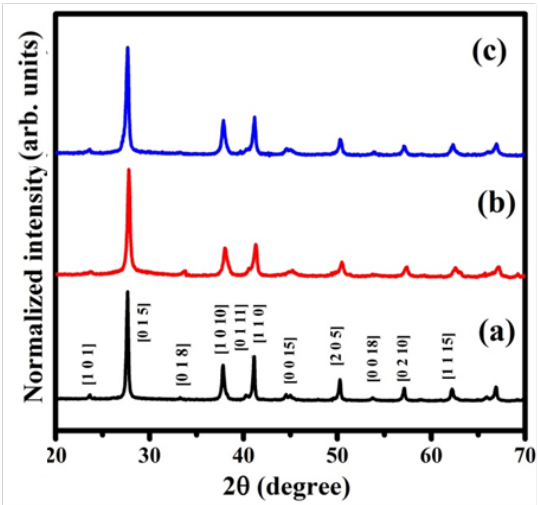

Figure 3.8: XRD pattern of the pressed pellets that composed of (a) flakes-decorated Bi_2Te_3 nanorods, (b) porous Bi_2Te_3 nanorods, and (c) smooth Bi_2Te_3 nanorods.

The samples 6-SDBS, SDBS-130, SDBS-150 are composed of powders containing high yield of Bi_2Te_3 nanorods with different microstructures such as flake-decorated, porous, and smooth nanorods respectively. All three samples were prepared to form

pellets. The relative density of the smooth, flakes decorated, porous Bi_2Te_3 nanorods pellet with respect to the bulk are ~6.73 g/cm^3 (85.7%), ~6.49 g/cm^3 (83.4%), and ~5.87 g/cm^3 (75.4%) respectively. The XRD patterns of the pressed pellets are illustrated in Figure 3.8. The observed XRD patterns were indexed to the rhombohedral structure of Bi_2Te_3 without the signature of impurity phases as reported in the standard PDF card (JCPDS 01-080-6959). Further, Figure 3.9 displays the FESEM image of the pressed pellets, composed of flakes decorated, porous, and smooth Bi_2Te_3 nanorods. The atomic concentrations of Bi and Te atoms (as obtained from EDX analysis) in the pressed pellets are included in the corresponding insets. The atomic concentrations of Bi and Te atoms in the pressed pellets deviated slightly from the exact Bi:Te stoichiometric values.

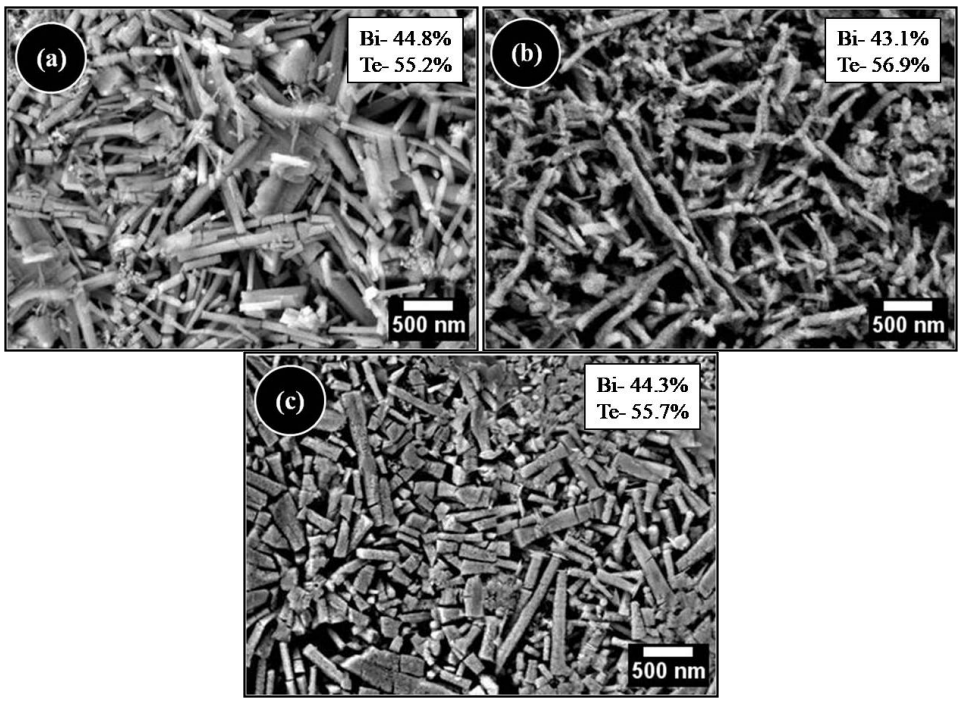

Figure 3.9: FESEM image of the pressed pellets that composed of (a) smooth Bi_2Te_3 nanorods, (b) flake decorated Bi_2Te_3 nanorods, and (c) porous Bi_2Te_3 nanorods. The inset shows the atomic concentrations of Bi and Te (as obtained from EDX analysis).

The TE properties of these samples were investigated. Firstly, Hall-effect measurements confirm the *p*-type conductivity for all pellets. Further, room temperature carrier concentration and carrier mobility of the Bi_2Te_3 pellets are obtained using Hall Effect measurements and are given in the Table 3.2. One can see that the carrier concentration for the pellet made from flakes decorated (~58.2×10^{20} /cm^3) and porous nanorods (~60.9×10^{20} /cm^3) are of an order of magnitude higher than that of smooth nanorods (~3.9×10^{20} /cm^3). On the other hand, carrier mobility for the Bi_2Te_3 pellets made

of smooth, flake-decorated, and porous nanorods is ~4.18×10^{-2} cm^2/Vs, ~3.86×10^{-2} cm^2/Vs, and ~0.79×10^{-2} cm^2/Vs respectively. In general, optimum carrier concentration and carrier mobility of bulk Bi_2Te_3 is in the order of 10^{19} -10^{20} $/cm^3$ and 10- 10^2 cm^2/V-s respectively[28,169,170]. The poor carrier mobility in the present work is ascribed to the pellet roughness. The surface roughness acts as an effective scattering potential[171] and charge carriers would possibly scatter out from the surface of the Bi_2Te_3 nanorods that subsequently degrade the carrier mobility values.

Table 3.2: Carrier concentration and mobility of the pellets composed of Bi_2Te_3 nanorods at room temperature with various morphologies.

Sample	Carrier type	Carrier concentration ($\times10^{20}$ $/cm^3$)	Mobility ($\times10^{-2}$ cm^2/V-s)
Smooth Bi_2Te_3 nanorods pellet	*p*-type	3.9	4.18
Flakes decorated Bi_2Te_3 nanorods pellet	*p*-type	58.2	3.86
Porous Bi_2Te_3 nanorods pellet	*p*-type	60.9	0.79

The variations in seebeck coefficient (S), electrical conductivity (σ), and power factor ($S^2\sigma$) were characterized in the temperature range of 300 to 410 K and are displayed in Figure 3.10. The Figure 3.10 (a) shows the temperature dependent Seebeck coefficient (S) of the Bi_2Te_3 pellets. The positive values of S values again confirm the *p*-type conductivity of the samples, as expected from the Bi-rich composition. Variations in the value of S with temperature is owing to the effect arises from bipolar conductivity[85,172]. Based on two conduction band model, the emergence of opposite type carriers (*i.e.*, holes and electrons) with temperature suppresses the net S value and the commencement temperatures for the bipolar conductivity are different for different pellets.

For the pellets prepared from smooth and porous Bi_2Te_3 nanorods, S has a highest value of ~215 μV/K and ~148 μV/K respectively at 300 K, while the flakes decorated Bi_2Te_3 nanorod pellet has its peak at ~167 μV/K at 410 K. Temperature dependent electrical conductivity of the Bi_2Te_3 pellets (Figure 3.10 (b)) shows typical semiconductor behavior. The electrical conductivity of flakes decorated nanorod pellet is around 36.02×10^2 S/m at 300 K and gradually increased to the value of 47.36×10^2 S/m at 410 K, approximately an order of magnitude higher than that of porous and smooth Bi_2Te_3 nanorods pellets. On the basis of above results, the variation in power factor ($S^2\sigma$) as a function of temperature was calculated and presented in Figure 3.10 (c). The maximum

power factor was achieved by flakes decorated Bi_2Te_3 nanorods pellet and corresponds to the value of about ~132.1 μW/mK^2 at 410 K, which is higher than that of smooth Bi_2Te_3 nanorods pellet (~11.7 μW/mK^2) and porous Bi_2Te_3 nanorods pellet (~17.1 μW/mK^2).

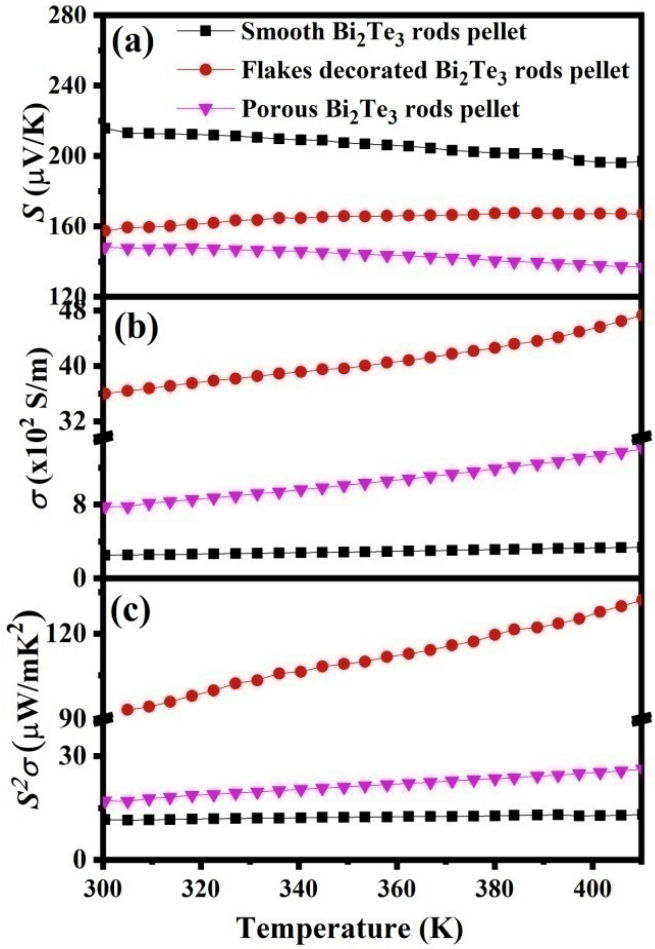

Figure 3.10: Temperature dependent TE transport properties of the pellets made of Bi_2Te_3 nanorods with different surface morphologies: (a) Seebeck coefficient, S, (b) electrical conductivity, σ, (c) power factor, $S^2\sigma$.

The values of thermal diffusivity (α), thermal conductivity (κ), power factor ($S^2\sigma$) and figure of merit (ZT) for the pellet composed of Bi_2Te_3 with different surface morphologies at 300 K are tabulated in Table 3.3. It can be seen that the thermal conductivity (κ) obtained for the pellet made of smooth nanorod (~-0.2 W/mK) is higher than that of flake decorated (~0.13 W/mK) and porous nanorods (~0.1 W/mK). Finally, the room temperature TE figure of merit (ZT) was calculated and is found to be 0.02, 0.2, and 0.04 for the pellet consisting of smooth, flake decorated, and porous nanorods respectively.

Table 3.3: Room temperature thermal diffusivity, thermal conductivity, power factor and figure of merit values for the pellet composed of Bi_2Te_3 nanorods with different surface morphologies.

Sample	Thermal diffusivity, α ($\times 10^{-7}$ m^2/s)	Thermal conductivity, κ (W/m-K)	Power factor, $S^2\sigma$ ($\mu W/m\text{-}K^2$)	Figure of merit, ZT
Smooth Bi_2Te_3 nanorods pellet	1.98	0.20	15.7	0.02
Flakes decorated Bi_2Te_3 nanorods pellet	1.3	0.13	89.3	0.20
Porous Bi_2Te_3 nanorods pellet	1.37	0.11	17.1	0.04

3.4. Discussion

3.4.1. Growth kinetics for the formation of Bi_2Te_3 nanostructures

It is well established that the growth of nanoparticles by the hydrothermal method involves two main processes, namely nucleation and crystal growth self assembly process. The first stage of nanoparticles growth, the nucleation process, accompanies the formation of precursors (or nuclei) having finite and stable size, which will acts as a template for nanoparticles growth. Nucleation stage mainly depends on the type of chemical reagents and their chemical reaction.

The chemical reactions for the growth of Bi_2Te_3 nanostructures can be summarized in the following steps. In a typical chemical reaction, $BiCl_3$ was hydrolyzed to form BiOCl and HCl (Eqn. 3.1). In a high temperature sealed system[173], the standard redox potential corresponding to Bi^{3+} / Bi (~0.2 V) is very low as compared to that of Te^{4+} / Te(~0.568 V). Therefore, it is concluded that Bi^{3+} could be reduced to its metallic form (metallic Bi) rapidly in the presence of $NaBH_4$ and NaOH (Eqn. 3.2).

On the other hand, in the presence of strong reducing agent, Na_2TeO_3 (*i.e.,* Te source) could be reduced to the form of polytelluride colloids (Te^{2-}_{a+1}) (Eqn. 3.3)[88]. The polytelluride colloids (Te^{2-}_{a+1}) contain both metallic Te and Te^{2-} ions. It can be concluded that the Te^{2}_{a+1} will act as an effective Te source as compared to the metallic Te powder. Therefore, two independent reactions *viz.,* ionic (Eqn. 3.4) and elemental (Eqn. 3.5) combinations that results in the formation of Bi_2Te_3 nuclei as proposed[174,175]. The chemical reactions for the typical hydrothermal synthesis of Bi_2Te_3 nuclei could be as follows:

$$BiCl_3 + H_2O \rightarrow BiOCl + 2HCl \quad \textbf{Eqn. 3.1}$$

$$Bi_3^+ + 2BH_4^- + 6OH^- \rightarrow Bi + 2H_2BO_3^- + 5H_2 \uparrow \quad \textbf{Eqn. 3.2}$$

$$TeO_3^{2-} + BH_4^- \rightarrow Te_{a+1}^{2-} + H_2BO^{3-} + H_2 \uparrow \quad \textbf{Eqn. 3.3}$$

$$2Bi^{3+} + 3Te^{2-} \rightarrow Bi_2Te_3 \quad \textbf{Eqn. 3.4}$$

$$2Bi + 3Te \rightarrow Bi_2Te_3 \quad \textbf{Eqn. 3.5}$$

After a stable nuclei formed, nanoparticles may start to grow. It is well established that the surface free energy plays a key role in determining the shape of nanoparticles. Owing to the anisotropic nature of Bi_2Te_3 crystal structure, the surface free energy of the Bi_2Te_3 crystal along edge layer (*i.e., a* and *b* axis) will be high. Hence, Bi_2Te_3 crystals always tend to grow along edge layer and crystallize in the form of layered structure[97,119,176]. The surfactants are surface active agents[177], preferably adsorbed on the specific crystal facets to reduce their surface free energy and subsides the further growth of the corresponding facets. Therefore, the growth of the nanoparticles along any direction and the shape of nanoparticles could be controlled by providing appropriate surface active agents or surfactants.

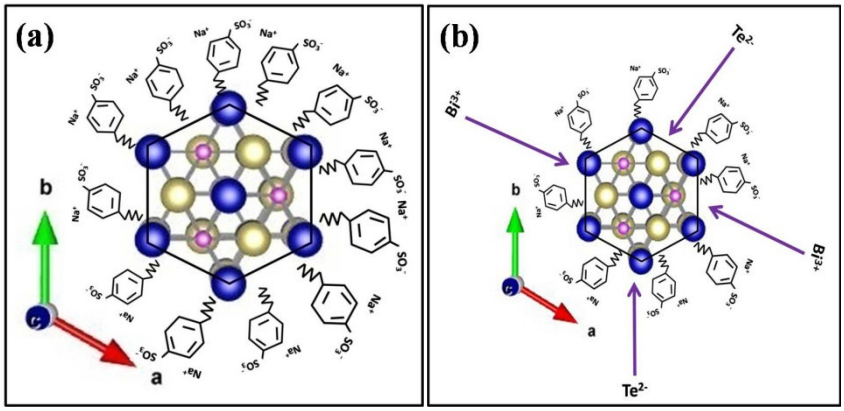

Figure 3.11: Schematic diagram of Bi_2Te_3 crystals coated with (a) high and (b) intermediate concentration of SDBS.

The SDBS[86] is an anionic surfactant, which exhibits amphiphilic nature. The structure of SDBS is composed of hydrophilic polar head (high affinity for water) carrying the negative charge ($ROSO_3^-$) and long hydrophobic tail. At low surfactant concentrations, SDBS molecules are dispersed as individual molecules throughout the aqueous media. Therefore, low surfactant concentrations will not effectively cap the Bi_2Te_3 nuclei. This leads to the formation of thermodynamically unstable and aggregated Bi_2Te_3 nanoparticles. Beyond critical micelle concentration (*i.e.,* CMC), SDBS molecules begun

to aggregate themselves to form a complex molecular structure called micelles, with hydrophobic tail attached to the Bi_2Te_3 edge layer (due to the high surface free energy) and hydrophilic polar head facing outwards. Thereafter, the number and size of the micelles increases with SDBS concentration (especially above CMC). The CMC of the SDBS in water at 25 ºC is approximately 1.6 mM [178]. However, the hindrance of the ordered SDBS micelles structure is always attributed to the enhanced thermal motions of the surfactant and the solvent molecule at the elevated temperature[179]. Thus, the SDBS micelle aggregation number is found to decrease with the increase in the temperature of the system.

Figure 3.11 displays the schematic of the Bi_2Te_3 nuclei coated with different concentration of SDBS. A high SDBS concentration facilitates the effective coverage of the stable Bi_2Te_3 nuclei (Figure 3.11 (a)) by SDBS micelles and favors the formation of stable Bi_2Te_3 primary particles having narrow size distribution. In contrast, the intermediate SDBS concentration (Figure 3.11 (b)) will also promotes the coverage of sufficient number of SDBS micelles around the Bi_2Te_3 nuclei. The intercalation of Bi^{3+} and Te^{2-} ions may also possibly attached to the edge layer of the Bi_2Te_3 nuclei. This resulted in broader distribution of stable Bi_2Te_3 primary particles. In this manner, the concentration of the surfactant SDBS added during the hydrothermal synthesis determines the extent of capping effect as well as the size distribution of the Bi_2Te_3 primary particles[180].

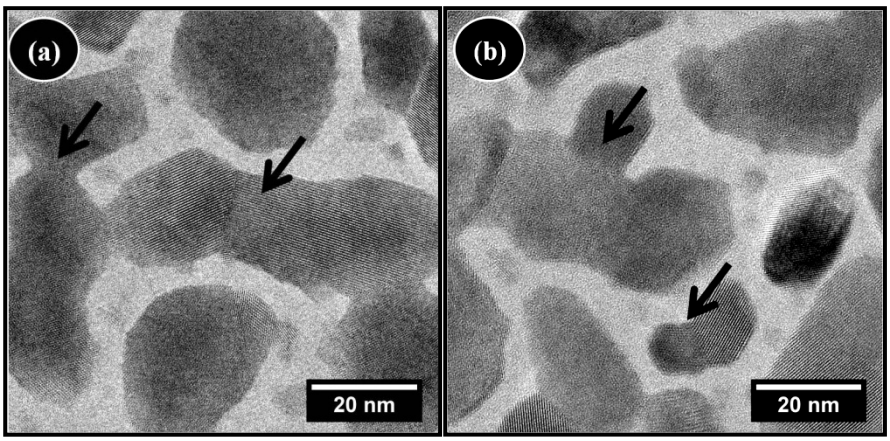

Figure 3.12: Bright field TEM image (a) and (b) demonstrates the oriented attachment (OA) process in the growth of Bi_2Te_3 particles in the 0-SDBS sample.

The growth of nanoparticles after the formation of stable Bi_2Te_3 primary particles involves two different mechanisms *viz*. Oswald ripening (*i.e.,* OR) and oriented attachment (*i.e.,* OA) mechanism. The OR mechanism entails dissolution and the re-precipitation of

the smaller particles (*i.e.,* Gibbs-Thomson effect) on the surface of the larger particles, tending to form defects free crystalline nanoparticles. The Figure 3.12 shows the OA processes, where the arrow indicates the attachment of two Bi_2Te_3 flakes. Due to the effect of the surfactant adsorption of the Bi_2Te_3 nuclei along different facets, which thermodynamically hinder the OR process in the initial stages of the reaction.

The OA mechanism involves the minimization of surface energy of the high-energy facets through particles collisions and coalescence. The particle collisions are the statistical process and control the kinetics of the nanoparticles growth process. Thereby, the Bi_2Te_3 nanorods grow when structurally similar and atomically rough Bi_2Te_3 primary particles collide with each other. The imperfect attachments of nanoparticles are due to Van der Waals interactions and simultaneously enhance the aggregation and coalescence of the Bi_2Te_3 primary particles particularly along *c* axis[181,182].

The imperfect attachment leads to the wide range of lattice imperfections and these lattice imperfections are considered as the high-energy defect sites that act as a spot for secondary nucleation[90]. Figure 3.13 presents the schematic diagram of the growth of Bi_2Te_3 nanorods. Based on the above-illustrated OA mechanism, the formation of high energy defect sites at the intermediate SDBS concentration (*i.e.,* 6 mmol) is also presented in Figure 3.13. Due to its anisotropic layered nature of Bi_2Te_3 crystal, the growth of the hexagonal Bi_2Te_3 platelets are expected to grow from the defect sites (*i.e.,* secondary nucleation sites).

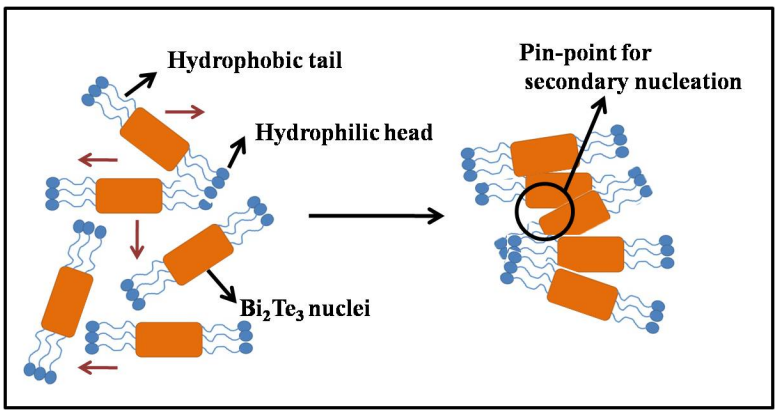

Figure 3.13: Schematic diagram showing the formation of Bi_2Te_3 nanorods by oriented attachment (OA) mechanism.

In case of high SDBS concentration (*i.e.,* 8 mmol), the smaller sized primary particles are involved. Hence, upon effective collisions followed by the aggregation and coalescence, one can expect a higher number of defects such as stacking faults and twining boundaries in the particle[183]. The diffusion of Bi_2Te_3 could be triggered near the defect

sites in order to release the excess strain. Formation of porous rod could be attributable to the inconsistency of in and out diffusion of Bi_2Te_3 through the interface between the defect regions.

The reaction rate is affected by the reaction temperature. Hence, high reaction temperature (*i.e.,* 150 ºC) promotes the collision frequency and nanoparticles mobility in the system, which eventually improve the degree of coalescence[184,185]. Furthermore, at high reaction temperature, diffusion motion of atoms and small nanoparticles could also be activated, leading to OR process and subsequently smoothen the Bi_2Te_3 nanorods.

3.4.2. Effect of microstructure on the thermoelectric transport properties

The Hall-effect and temperature dependent Seebeck coefficient measurements indicate the *p*-type conductivity of all pellets. Zhao *et al*.,[186] reported the formation energy of various types of defects in Bi_2Te_3 crystal, when the synthesis is carried out in Bi-rich and Te-rich conditions. The formation energy of Bi_{Te} antisite defects is very low (*i.e.,* 0.2 eV) in Bi-rich conditions. Hence, the observed *p*-type conductivity could be attributable to the generation of Bi_{Te} antisite defects in Bi_2Te_3. Similarly, Zu *et al.,*[187]., also observed the presence of Bi_{Te} antisite defects on the pellets composed of Bi_2Te_3 nanotubes. The extent and magnitude of the intrinsic lattice defects in Bi_2Te_3 are responsible for the variation in the carrier concentration and carrier mobility in different pellets. It has been observed that the pellet made of smooth nanorods is having suppressed carrier concentration. This is because, smooth nanorods are synthesized at high reaction temperature (*i.e.,* 150 ºC), where the lattice defects are greatly reduced *via* recombination of vacancies with Bi_{Te} antisite defects.

As seen from the Figure 3.10 (a), the S of the smooth Bi_2Te_3 nanorods pellet is found to be more prominent than that of other pellets. It is known that S is inversely proportional to the carrier concentration (n) through the relation given in Eqn. 3.6.

$$S = \frac{8\Pi^2 k_B^2}{3eh^2} m^* T \left(\frac{\Pi}{3n}\right)^{2/3} \qquad \textbf{Eqn. 3.6}$$

where k_B, h, m^*, T denotes the Boltzmann constant, Planck constant, effective mass of the carrier, and temperature respectively. Thus, the observed high value of S in smooth Bi_2Te_3 nanorods pellet is associated to its low carrier concentration values. The reported values[39,169,170,188] of seebeck coefficient and thermal conductivities of Bi_2Te_3 at 300 K are in the same order as reported in the present work. Furthermore, Eqn. 3.7 relates the σ with carrier concentration (n) and its mobility (μ).

$$\sigma = ne\mu \qquad \textbf{Eqn. 3.7}$$

In the present work, flakes decorated Bi_2Te_3 nanorods pellet (~3602 S/m) is reported to have higher electrical conductivity than that of smooth Bi_2Te_3 nanorods pellet (~251.4 S/m) and porous Bi_2Te_3 nanorods pellet (~779 S/m). However, bulk Bi_2Te_3 electrical conductivities[115,188–190] are in the order of 10^4 S/m, whereas all these pellets exhibit the poor electrical conductivity that is (in the order of 10^2-10^3 S/m), which was mainly due to low carrier mobility values. The carrier mobility values were suppressed in the present work due to pellet surface roughness and low pellet density. When compared to other pellets, flakes decorated nanorod pellet are exhibiting enhanced power factor, which arises from its improved *S* values. As a whole, the maximum value of room temperature TE figure of merit (*ZT*) is found in pellet consisting of flake decorated (~0.2) nanorods. The observed poor *ZT* values are accountable to the lower values of electrical conductivity, which was due to the pellet roughness and nanostructure morphology.

3.5. Conclusion

Bi_2Te_3 nanorods (*p*-type) with different surface morphology were synthesized and optimized successfully by a one-step hydrothermal method with the help of surfactant (SDBS). The SDBS concentration dictates the degree of capping effect and also ultimately controls the agglomeration of Bi_2Te_3 nuclei through the imperfect OA process. The OR mechanism plays an additional factor in smoothening the preformed Bi_2Te_3 nanorods at high reaction temperature. Furthermore, the nanowires samples were compacted into pellets and the pellet's transport properties were investigated. It was found that an outstanding power factor (132 μW/m-K^2) was achieved by flakes decorated nanorod pellet at 410 K. The TE figure of merit (*ZT*) was reached up to 0.20 for the flakes decorated Bi_2Te_3 nanorods pellet at room temperature, which exhibits the excellent *ZT* value taking in to account that no extrinsic doping was intentionally included in these materials.

Chapter 4

Helium ion irradiation effects on the thermoelectric properties of bismuth telluride nanorods.

4.1. Introduction

In the previous chapter, lattice defects in the flake decorated nanorods were found to be responsible for their highest figure of merit values. It is known that the microstructural defects can greatly impact materials thermoelectric (TE) properties. Hence, it is possible to tailor the TE transport properties by effectively manipulating defects in the materials. The intentional manipulation of the type, concentration, and extend of spatial distribution of the defects in the material were used to optimize as well as enhance the TE transport properties.

Thereby, 'defect engineering'[31,59,60,191] strategy was suggested as possibility to decouple the tradeoff relationship between TE transport properties by effectively tuning electronic band structures and at the same time enhance phonon scattering. It is worth noting that the traditional strategies of introducing defects can be realized by tuning the stoichiometry or alloying with a defect compound and were witnessed to obtain high performance TE material[69,161,192]. For instances, Hu *et. al.,*[59] demonstrated the top-down hot deformation approach to enhance the TE performance of Bi_2Te_3 based solid solutions through point defect engineering mechanism. Besides, Guo *et al.,*[193] reported that the high pressure sintering technique significantly improved the TE transport properties of $(Bi_{1-x}Sb_x)_2Te_3$ alloys. The influence of high pressure influences the point defects and finally modulates the carrier concentration.

Recently, Suh *et al.*[77] demonstrated the alternative and effective atomic scale defect engineering mechanism to improve the TE performances by employing 3 MeV He^{2+} ion irradiation. Dating back to 1960s, the effect of various irradiation *viz.,* thermal neutrons, reactor radiations, protons and inert gas ions on TE transport properties of Bi_2Te_3 were extensively studied[78,194–196]. The formation of defect clusters and dislocations in Bi_2Te_3 by 7.5 MeV proton irradiation were observed. In all the cases, it has been observed that TE transport properties are extremely sensitive to the defects generated during the ion irradiation and have both positive and negative impacts on the TE properties. More recently, Fu *et.al.*[78], reported that 400 keV Ne^+ ion irradiation on Bi_2Te_3 and Sb_2Te_3 thin films leads to 208% and 337% enhancement in its power factor.

Such an enhancement was due to ionization-induced enhanced crystallinity. However, the enhancement of the TE transport properties are suppressed at high ion fluences.

Thus, the controlled adjustment of the TE transport properties could be evidently accomplished in TE materials *via* ion irradiation. This helps to increase their applicability in the different fields. On the other hand, the detailed investigation of the properties of the TE material under extreme environment is also important to rate the potential of TEG for energy harvesting in extra-terrestrial areas. In this chapter, 100 keV He^+ ion irradiation was carried out on Bi_2Te_3 pellets. Pellet composed of smooth Bi_2Te_3 nanorods were chosen. When compared to the other samples (*i.e.,* flake-decorated and porous nanorod), smooth Bi_2Te_3 nanorods are exhibiting less defective. Therefore, one can able to study and tailor the ion irradiation induced defects in the morphology, structural, and TE transport properties of the Bi_2Te_3 nanorods as a function of 100 keV He^+ ion fluences.

4.2. Experimental methods

4.2.1. Sample synthesis

The sample composed of smooth Bi_2Te_3 nanorods were synthesized through surfactant assisted hydrothermal method [20] following the synthesis procedure explained in the chapter 3. Powder comprised of smooth Bi_2Te_3 nanorods were pelletized (dimension: 10 mm × 5 mm × 1 mm) for the present study and the relative density of the pellet is measured using Archimedes principle, which is estimated to be ~6.73 g/cm^3 (*i.e.,* 85.7% of the theoretical density).

Table 4.1: Details of ion irradiation in Bi_2Te_3 carried out in present study.

Ion	Mean projected range ± straggling (nm)	S_e (eV/nm)	S_n (eV/nm)	Sputtering yield (atoms/ion)	Ion fluence (ions/cm^2)	Peak damage (*dpa*)
100 keV He^+	441 ±160	208.5	3.963	0.021	5×10^{15}	0.13
					1×10^{16}	0.27
					5×10^{16}	1.38
					1×10^{17}	2.77
					2×10^{17}	5.55

The pellets of Bi_2Te_3 nanorods were irradiated with 100 keV He^+ ions at room temperature under normal incidence with ion fluences ranging from 5×10^{15} ions/cm^2 to 2×10^{17} ions/cm^2 using the 150 kV ion accelerator facility. The base pressure of the implantation chamber was better than 1×10^{-6} mbar and the beam current density was maintained at ~1 μA/cm^2 to avoid beam heating. The relevant parameters such as mean

projected ion range, electronic energy loss (S_e), nuclear energy loss (S_n), sputtering yield, ion fluences and the corresponding peak damage were calculated using Monte Carlo-based SRIM 2006 code[130]. For SRIM calculations, displacement energy was fixed to 25 eV for all elements in Bi_2Te_3 thin films as given in the report[78].

4.2.2. Characterization technique

The crystalline phases of the Bi_2Te_3 were identified with grazing incident X-ray diffraction (GIXRD, Inel, Equinox 2000) by using Cu-K_α radiation (1.541 Å). The incidence angle was kept at 1° to probe the ion beam irradiated region. The X-rays penetration depth corresponding to the chosen incident angle is estimated to be ~800 nm. The microstructure of the pristine Bi_2Te_3 and the ion-induced structural modifications were observed by using focused ion beam field emission scanning electron microscopy (FIB-FESEM, Zeiss, cross beam 340) and high-resolution transmission electron microscopy (HRTEM, Zeiss, LIBRA 200FE). The FIB-FESEM was operated with an accelerating voltage of 5 kV at the working distance of ≈ 3.2 mm and the images were recorded using in-lens detector. The HRTEM was operated with an accelerating voltage of 200 kV.

Bi_2Te_3 nanorods were dispersed in iso-propanol solution and then drop casted on the carbon coated copper grids, which is used for TEM investigations. Furthermore, in order to study the irradiation induced structural modifications, 100 keV He^+ ion irradiation was carried out separately on Bi_2Te_3 nanorods dispersed TEM grids. Further, the evolution of the vibrational modes of the Bi_2Te_3 pellets under 100 keV He^+ ion irradiation were performed by micro-raman spectrometer (WiTec Alpha RA-300), using Nd:YAG laser with an excitation wavelength of 532 nm. To avoid sample heating during Raman measurements, laser excitation power was optimized and fixed to the value of 0.5 mW. The above laser excitation power gives good signal to noise ratio without damaging the samples.

The room temperature Hall-Effect measurements were carried out under Van der Pauw configuration using magnetic field of 0.57 T (ECOPIA, HMS 5000). Temperature dependent Seebeck coefficient (S) measurements were carried out by using the bridge arrangement of two copper bars maintained at the temperature gradient of 2 K under vacuum[197]. The temperature dependent electrical conductivity of the Bi_2Te_3 pellets was measured using a standard four-probe technique.

4.3. Results

4.3.1. GIXRD studies

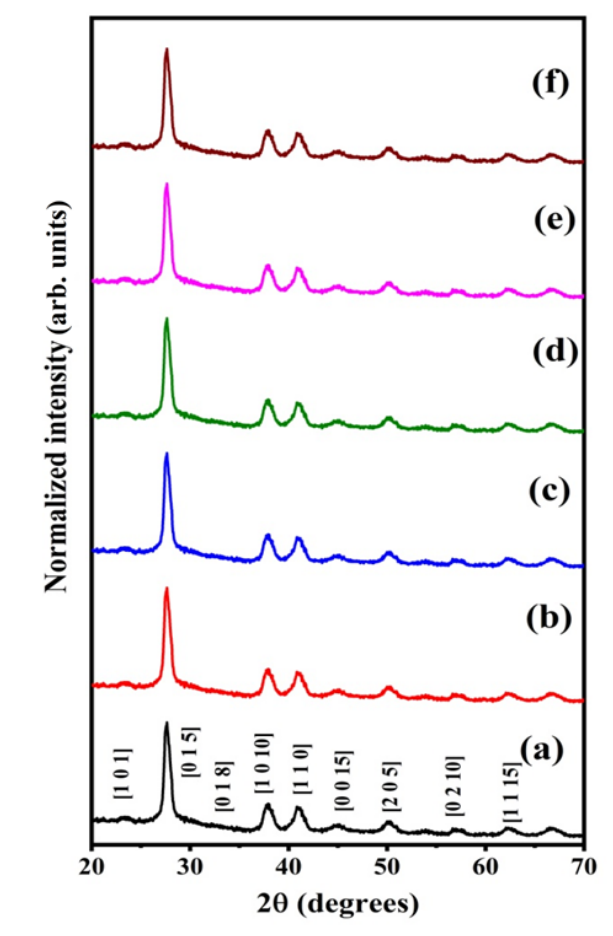

Figure 4.1: GIXRD pattern of (a) the pristine and 100 keV He^+ ion irradiated Bi_2Te_3 pellet with the ion fluences of (b)5×10^{15}, (c)1×10^{16}, (d)5×10^{16}, (e)1×10^{17}, (f)2×10^{17} ions/cm^2.

Figure 4.1 depicts the GIXRD patterns of the pristine and 100 keV He^+ ion irradiated Bi_2Te_3 pellet with various ion fluences. The XRD peaks in the Figure 4.1 are found match with the rhombohedral structure of Bi_2Te_3 crystal (JCPDS 01-080-6959) with lattice parameters of $a = b = 4.39$ Å and $c = 30.15$ Å. The diffraction peaks corresponding to the precursor material/impurity phases are not observed. Further, the XRD peaks are indexed and labeled according to their Miller indices. The pristine Bi_2Te_3 pellet exhibited polycrystalline nature that was not altered by the 100 keV He^+ ion irradiation. Furthermore, within the range of ion fluences used, it is also observed that the absence of XRD peak broadening, and the signature of grain growth, phase segregations, and amorphization in the irradiated Bi_2Te_3 pellets.

4.3.2. Microstructural studies

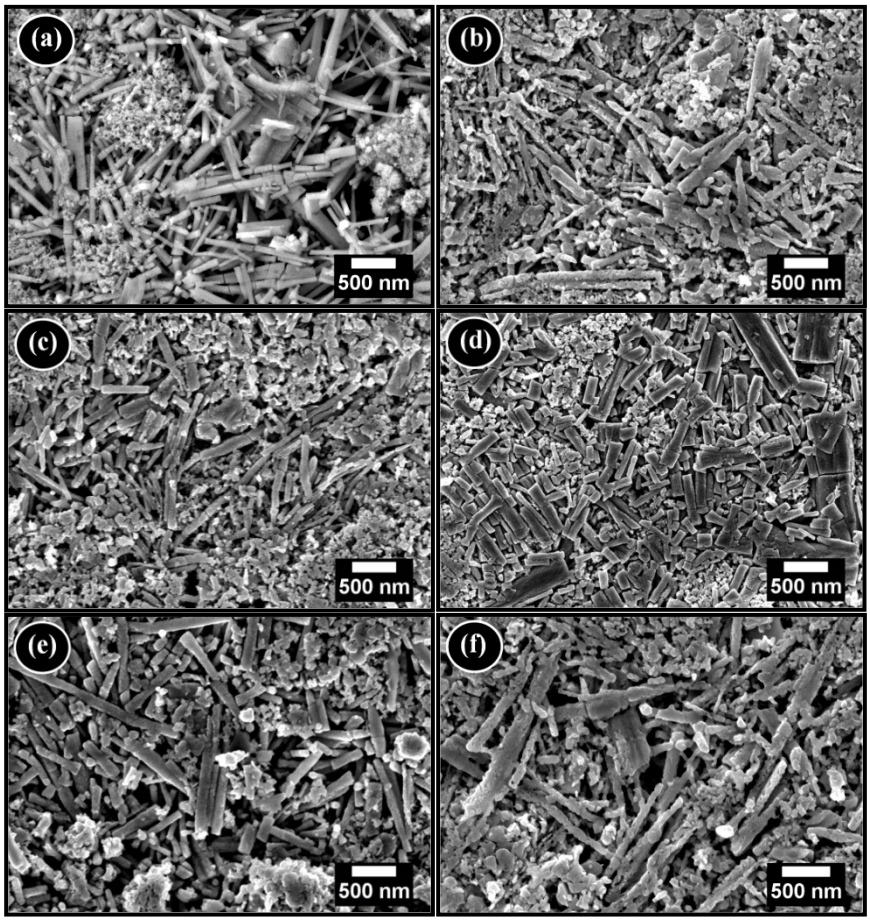

Figure 4.2: FESEM image of the (a) pristine and 100 keV He^+ ion irradiated Bi_2Te_3 pellet with the ion fluences of (b) 5×10^{15}, (c) 1×10^{16}, (d) 5×10^{16}, (e) 1×10^{17}, (f) 2×10^{17} ions/cm^2.

The surface morphology of the pristine and 100 keV He^+ ion irradiated Bi_2Te_3 pellets has been investigated using FESEM and is displayed in Figure 4.2. The FESEM image of the Bi_2Te_3 pellets before and after 100 keV He^+ ion irradiation visibly shows the presence of Bi_2Te_3 nanorods in the pellets. In addition, no significant change in the surface morphologies is observed upon He^+ ion irradiation (Figure 4.2 (b) to Figure 4.2 (f)).

Therefore, 100 keV He^+ ion irradiation induced microstructural changes was investigated further using HRTEM and the images are presented in Figure 4.3. The HRTEM images (Figure 4.3 (a) to Figure 4.3 (d)) and the corresponding electron diffraction patterns (Figure 4.3 (e) to Figure 4.3 (f)) of the pristine and 100 keV He^+ ion irradiated Bi_2Te_3 nanorods were analyzed using ImageJ software [198] and are displayed accordingly. The insets of Figure 4.3 (a) to Figure 4.3 (d) shows the bright field TEM image of the Bi_2Te_3 nanorod for various ion fluences.

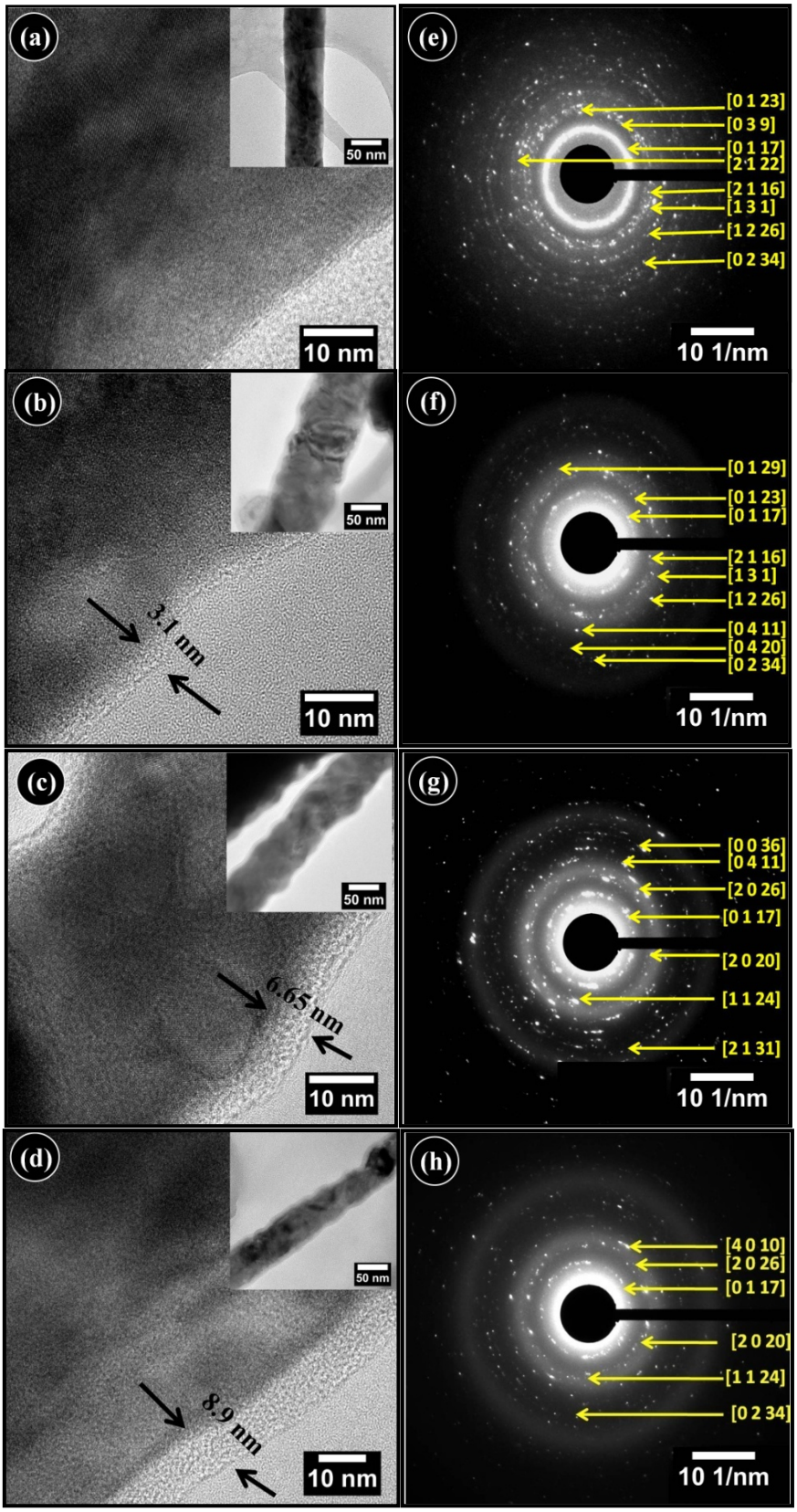

Figure 4.3: HRTEM images (a-d) and the corresponding electron diffraction pattern (e-h) of (a) the pristine and 100 keV He^+ ion irradiated Bi_2Te_3 nanorod with the ion fluence of (b)5×10^{16}, (c)1×10^{17}, (d)2×10^{17} ions/cm^2. Inset shows the bright field TEM image of Bi_2Te_3 nanorod.

Crystalline nature was exhibited by pristine Bi_2Te_3 nanorod, which in turn confirmed from the bright spots in the electron diffraction pattern (Figure 4.3 (e)). Up to the ion fluence of 1×10^{16} ions/cm^2, crystalline nature and the microstructure of the Bi_2Te_3 nanorods remained unaffected. However, He^+ ion fluence of 5×10^{16} ions/cm^{2}onwards, presence of the damage layer was identified at the outer rim of the Bi_2Te_3 nanorods (Figure 4.3 (b)).

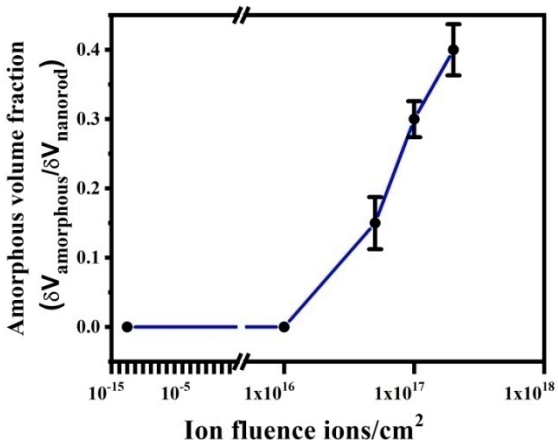

Figure 4.4: Approximate amorphous volume fraction in Bi_2Te_3 nanorod as a function of 100 keV He^+ ion fluence.

Thereafter, starting from the surface of the nanorods, thickness of disordered layer had been extended up to ~6 nm, especially for the ion fluence of 1×10^{17} ions/cm^2 (Figure 4.3 (c)). In addition, the appearance of the halo rings along with diffraction spots (Figure 4.3 (f) to Figure 4.3 (h)) in the irradiated nanorods signifies the coexistence of crystalline and amorphous phases. The thickness of the amorphous layer is observed to increase gradually with ion fluences. Particularly, the thickness of the amorphous layer was ~9 nm (Figure 4.3 (d)) for the highest ion fluence (2×10^{17} ions/cm^2). The similar type of layered damage accumulations are reported in ion implanted GaN, Si, Ge, *etc*[199–201]. Figure 4.4 displays the systematic and gradual evolution of the amorphous volume fraction in the Bi_2Te_3 nanorods as a function of 100 keV He^+ ion fluence.

4.3.3. Monte Carlo simulations on Bi_2Te_3 nanorods

Irradiation of Bi_2Te_3 nanorods with 100 keV He^+ ions was simulated using SRIM2006 code[130]. For the calculations, 80 nm wide bulk Bi_2Te_3 target (*i.e.,* the average diameter of Bi_2Te_3 nanorods is considered) was chosen. Table 4.1 shows the derived parameters calculated with SRIM simulations.

Figure 4.5 shows the vacancy depth profile of the 100 keV He^+ ion irradiated 80 nm thick Bi_2Te_3 target, which were created by the incident ions (black curve) and by

the recoiling atom (red curve). It is important to note that the SRIM simulations considered the layered and flat target geometry. In reality, it is expected that the fraction of ions would likely leave from the sides of the nanostructured targets such as nanorods and nanoparticles during ion irradiation. In other words, one can say that the SRIM code was used to estimate various parameters such as ion ranges, electronic and nuclear energy loss, but it is not adequate to estimate the defect densities in the nanostructures. Therefore, Iradina simulations were employed in the present work.

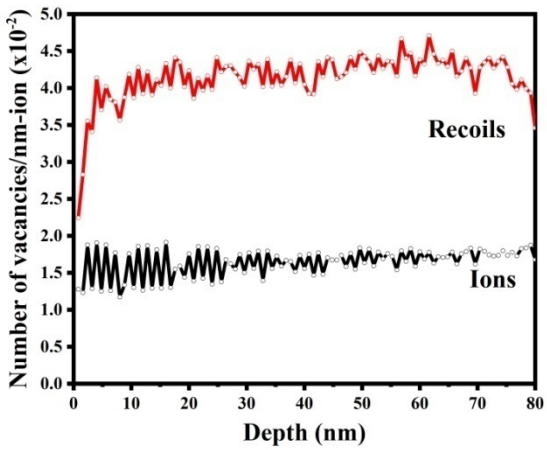

Figure 4.5: Vacancy profile of the 100 keV He^+ ion irradiated Bi_2Te_3 bulk target created by incident ions (black curve) and by recoiling target atoms (red curve) as obtained from SRIM calculations.

Iradina (ion range and damage in nanostructures)[202] is a simulation software that is similar to the SRIM simulation. Iradina works on 3 dimensional target geometries such as nanorods and nanoparticles. The input data required for iradina simulations are similar to the SRIM simulation such as target density, energy and mass of the projectile ions. The output data of the iradina simulation consists of the profile of displaced atoms, vacancies, and interstitials. The iradina simulation on the typical nanorod geometry at normal incidence is illustrated in Figure 4.6.

The target was chosen as cylinder of Bi_2Te_3 (*i.e.,* nanorod) with 80 nm in diameter. The section of the nanorod was defined by periodic boundary condition (PBC) having translation symmetry along *z* axis and hence suggested to have infinite length along *z* axis. The 100 keV He^+ ion beam was projected along *x* axis. In addition, the section of the nanorod was embodied of 1600 cells, where each cell acted as the counter and records the He^+ ion interaction events.

Figure 4.7 (a) to Figure 4.7 (c) show the spatial distribution maps of displaced atoms, vacancies and interstitials in the simulated section of the Bi_2Te_3 nanorod. It is

estimated that each 100 keV He^+ ion displace 3 and thereby create 2.8 vacancies and 2.7 interstitials. A representative cylindrical nanorod of diameter 80 nm and length 2 μm encompasses 5×10^7 atoms. However, especially at the highest ion fluence (*i.e.,* 2×10^{17} ions/cm^2), ion beam exposed region in the nanorod would maximally receive 5×10^8 number of energetic ions that displaces the atoms in the Bi_2Te_3 lattice target and creates a large number of vacancies and interstitials (*i.e.,* Frenkel pair). The total number of displaced atoms, vacancies and interstitials in a simulated Bi_2Te_3 nanorod for different ion fluence are calculated and are shown in Figure 4.7 (d). The total number of displaced atoms, vacancies, and interstitials in the typical nanorod is estimated to have a very high values (*i.e.,* around 10^8 to 10^9 atoms).

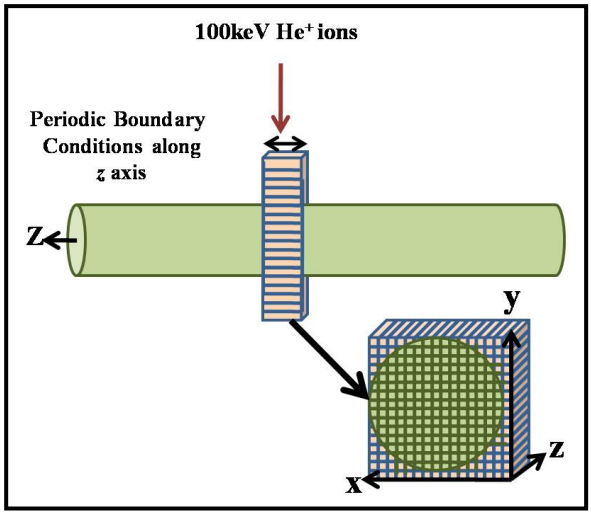

Figure 4.6: Schematic of the iradina simulation on Bi_2Te_3 nanorod.

In reality, these ion irradiation induced Frenkel pairs will not stay at definite place but will migrate throughout the lattice even at liquid nitrogen temperatures[200]. As a consequence, most of these Frenkel pairs may anneal out through direct and indirect defect recombination. In general, the complex dynamic annealing processes [203] are prominently experienced in nanorods, where vacancies (interstitials) are most likely to recombine with interstitial (vacancy) complexes and resulted in large number of antisite defects and defect complexes. In fact, the surface of the nanorod acts as an effective trap for migrating defects[204]. The accumulation of more number of defect complexes at the surface of the nanorods increases the free energy of the surfaces, which acts as the nucleation site for amorphization, collapses into an energetically favorable amorphous state. Hence, the thickness of the amorphous layer continuously increases with increase in defect concentration (*i.e.,* ion fluence).

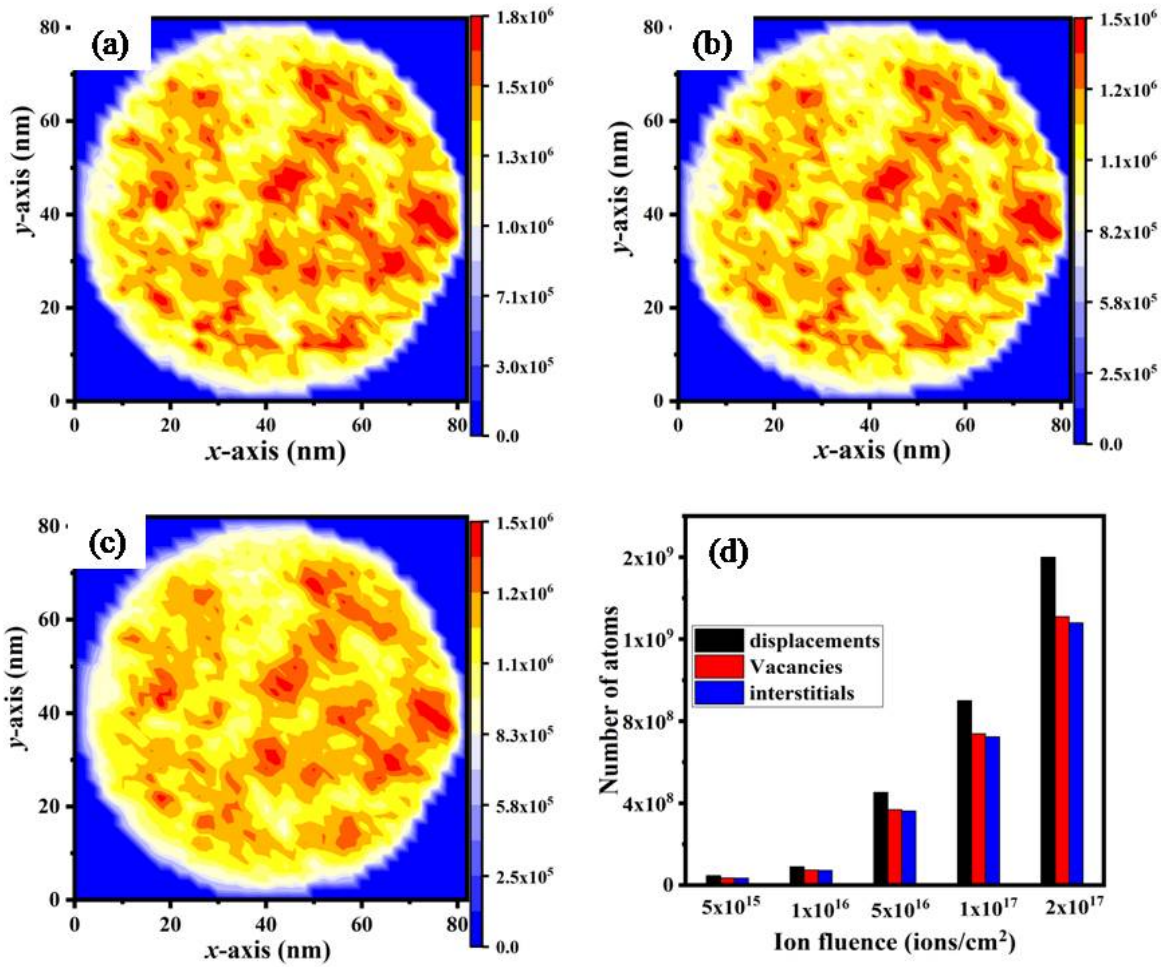

Figure 4.7: The spatial distribution maps of (a) displaced atoms, (b) vacancies, and (c) interstitials in the Bi_2Te_3 nanorod section (simulated using IRADINA). The total number of displaced atoms, vacancies, and interstitials in the Bi_2Te_3 nanorod at various ion fluences (as calculated from IRADINA) are shown in (d).

4.3.4. Raman scattering studies

The unit cell of Bi_2Te_3 crystal with inversion symmetry contains 5 atoms. Accordingly, one could expect 15 lattice vibration modes, out of which 12 are optical modes and 3 are acoustic modes [22,156,205]. The optical modes are inclusively classified in to Raman active modes ($2E_g$ and $2A_g$) and IR active/Raman inactive modes ($2E_u$ and $2A_u$). The schematic of the atomic vibrations corresponding to the Raman active and IR active/Raman inactive modes are displayed in Figure 4.8. The E_g and E_u mode represents in-plane lattice vibrations, while A_g and A_u represent out-of-plane lattice vibrations. It has to be noted that the superscript '1' and '2'on the vibrational mode notation represents low and high frequency vibrational modes respectively.

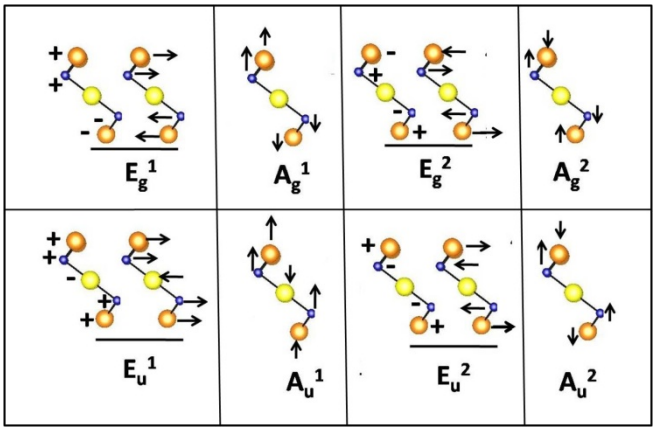

Figure 4.8: Schematic representation of the atomic vibration corresponding to Raman active and IR active modes.

The changes in the vibrational modes of the Bi_2Te_3 pellets under 100 keV He^+ ion irradiation for different ion fluences are shown in Figure 4.9. It is seen that pristine and He^+ ion irradiated pellets are showing two Raman active modes (*i.e.,* E_g^2 and A_g^2) and one Raman inactive/IR active mode (*i.e.,* A_u^2). The peaks corresponding to E_g^2, A_u^2, and A_g^2 modes were assigned at ~99, ~118, ~136 cm^{-1} in the Raman spectra.

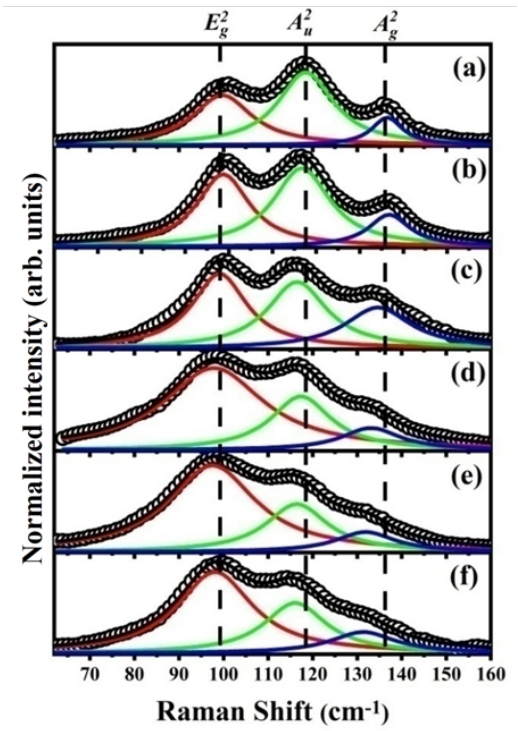

Figure 4.9: Raman spectra of (a) pristine and 100 keV He^+ ion irradiated Bi_2Te_3 pellet for various ion fluences of (b)5×10^{15}, (c)1×10^{16}, (d)5×10^{16}, (e)1×10^{17}, and (f)2×10^{17} ions/cm^2.

The activation of Raman inactive vibration mode (A_u^2) in the pristine Bi_2Te_3 pellet (Figure 4.9 (a)) is owing to the effects of crystal symmetry breaking that has been reported

earlier[206–209]. The loss of translational symmetry may be due to the presence of confinement along with lattice disorder. Therefore, atoms on the surface of the nanorods acquire higher energies and are about to move out of the plane. Additinally, the third order symmetry breaking provoked by the Bi_{Te} antisite defects in the pristine sample (Bi-rich growth conditions), would also contribute to the forbidden (*i.e.*, IR active/Raman inactive) mode of vibration.

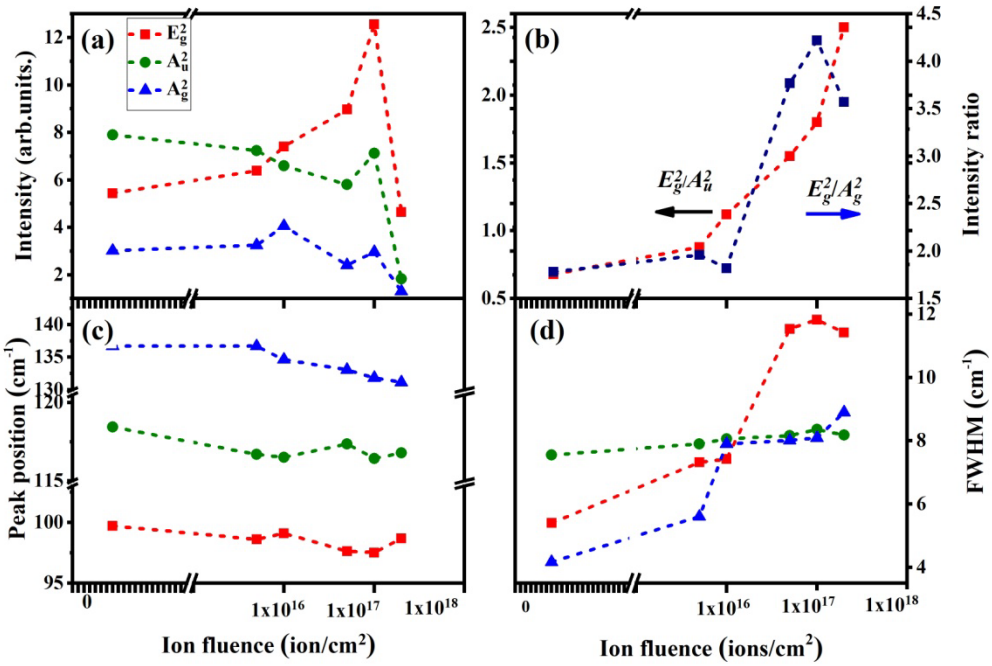

Figure 4.10: Variation in (a) Raman mode intensity, (b) intensity ratio of in-plane to out-of-plane vibration modes, (c) Raman peak position, and (d) FWHM of the Raman peak as a function of ion fluence. Dotted lines are the guide to the eye.

Three major changes are spotted in the Raman spectra of Bi_2Te_3 pellets upon 100 keV He^+ ion irradiation. In the first instance, upon ion irradiation, one could observe the gradual changes in the intensities of the in-plane (E_g^2) and out-of-plane vibrations (A_u^2 and A_g^2). Figure 4.10 (a) displays the variation in the intensity of in-plane and out-of-plane vibrations. The progressive reduction in the intensity of out-of-plane vibrations upon ion irradiation is observed. However, in-plane vibration intensity is sequentially improved until the ion fluence of 1×10^{17} ions/cm^2 and subsequently phases out for highest ion fluence (2×10^{17} ions/cm^2). Furthermore, it is clearly seen from Figure 4.10 (b) that the intensity ratio (E_g^2/A_u^2 and E_g^2/A_g^2) of the vibration modes increases with He^+ ion fluence and this signifies the hindrance of the out-of-plane vibrations in the ion irradiated Bi_2Te_3 nanorods.

A notable feature of the above effect clearly indicates that the accumulation of defects and lattice disorder at the surface of nanorods (as confirmed by the TEM results) restricted the longitudinal atom displacements (out-of-plane vibrations). On the other hand, it has been observed that the shifting of vibration modes towards lower wave number with ion fluence (Figure 4.10 (c)). This could be ascribed to introduction of strain due to lattice displacements from its equilibrium position[209,210]. Furthermore, in the ion irradiated Bi_2Te_3 pellets, high defect concentration relaxes the zone-center phonon selection rule and resulted in broad Raman peak (Figure 4.10 (d)).

4.3.5. Thermoelectric transport properties

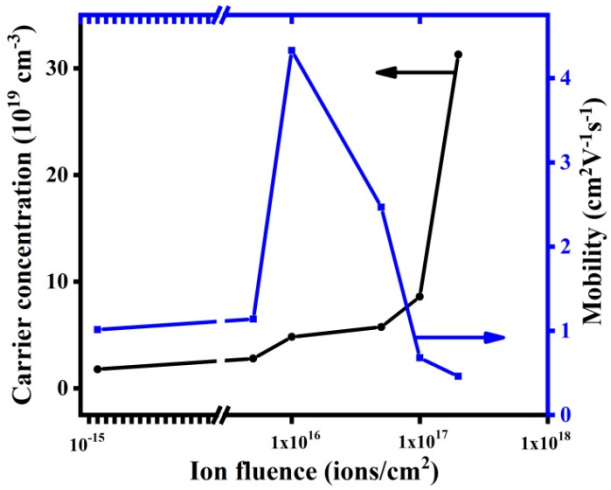

Figure 4.11: Carrier concentration and mobility at room temperature for pristine and 100 keV He^+ ion irradiated Bi_2Te_3 pellets for various ion fluences.

It has been noted that the range of the 100 keV He^+ ion is smaller than the thickness of the pellet. However, changes in the carrier concentration, mobility, and TE properties are due to the consequence of the damage produced by the He^+ ion irradiation. Besides, the contributions from the undamaged regions cannot be neglected.

From room temperature Hall-effect measurements (Figure 4.11), it was concluded that the majority charge carriers in the pristine and 100 keV He^+ ion irradiated Bi_2Te_3 pellets are holes, as all samples are exhibiting *p*-type conductivity. It is recapitulated that formation energy of acceptor type Bi_{Te} antisite defects is very low (~0.2 eV) in Bi-rich growth conditions, which could be the reason for *p*-type conductivity nature of the pristine Bi_2Te_3 pellet. As shown in Figure 4.11, carrier concentration and the mobility of the Bi_2Te_3 pellets are sensitive to the 100 keV He^+ ion irradiation. The pristine Bi_2Te_3 pellet has carrier concentration of 1.8×10^{19} /cm^3 and the value improved gradually up to the value of 31.3×10^{19} /cm^3 for ion fluence of 2×10^{17} ions/cm^2. The consistent *p*-type

conductivity and gradual improvement in carrier concentration indicates that the He^+ ion irradiation infuse acceptor type defects (*i.e.,* Bi_{Te} antisite defects), which increases with ion fluences.

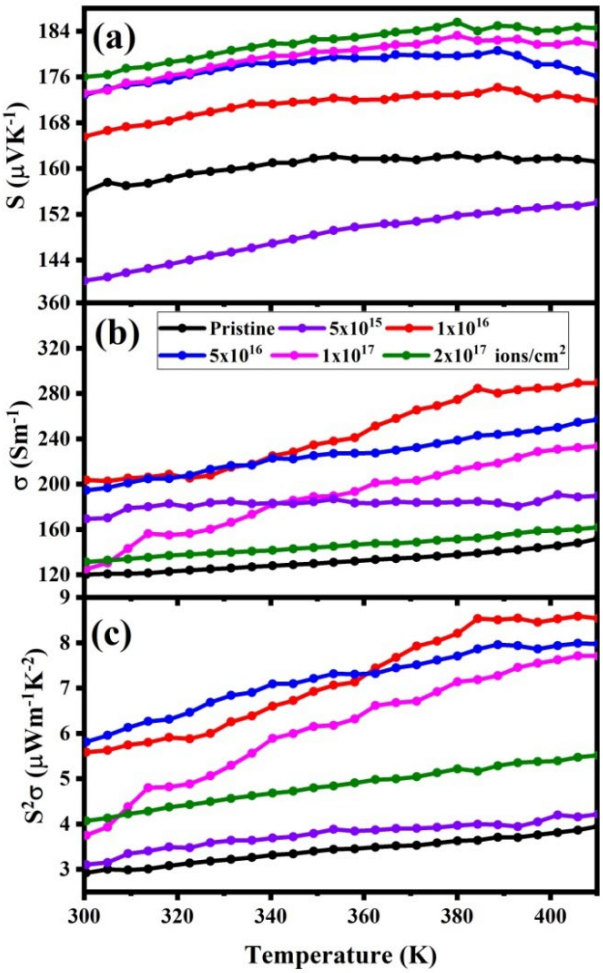

Figure 4.12: Temperature dependent TE transport properties of the pristine and 100 keV He^+ ion irradiated Bi_2Te_3 pellets: (a) Seebeck coefficient (S), (b) electrical conductivity (σ), and (c) power factor ($S^2\sigma$).

On the other hand, the mobility of the Bi_2Te_3 is observed to improve until the He^+ ion fluence of 1×10^{16} ions/cm^2. In general, defects will act as scattering center and reduce the carrier relaxation time and thus the mobility. However, the above contrasting behavior of the carrier mobility was reported previously on 3 MeV He^{2+} ion irradiated Bi_2Te_3 thin films[77]. It is proposed that the surface conductivity (*i.e.,* grain boundary) plays a dominant role in the pristine Bi_2Te_3. In contrast, the ion irradiation induces more charge carriers in the bulk. Consequently, the contribution of the bulk conductivity leads to the improved mobility values at the intermediate ion fluence. Thereafter, due to the

accumulation of more defects under higher ion fluence, the mobility starts to decrease accordingly.

The temperature dependent Seebeck coefficient (S) of the pristine and ion irradiated Bi_2Te_3 pellets are shown in Figure 4.12 (a). The S of the pristine and irradiated Bi_2Te_3 exhibited positive values and once again confirms the *p*-type conduction. The pristine pellet are demonstrating the value of S for at 300 K is ~155.9 μV/K, while it is observed that the values of S were reduced significantly at lower ion fluence (*i.e.,* 5×10^{15} ions/cm^2) and were subsequently improved to the value of ~176 μV/K at higher ion fluence.

As shown in Figure 4.12 (b), the temperature dependent electrical conductivity (σ) of the Bi_2Te_3 has improved to a peak value (~289.1 S/m and 254 S/m at 410 K) after irradiation at lower ion fluence (5×10^{15} and 1×10^{16} ions/cm^2), then decreases with subsequent ion fluence. Based on the above results, the power factor ($S^2\sigma$) was calculated and presented in Figure 4.12 (c). The maximum power factor (~ 8.2 μW/mK^2) was observed for the Bi_2Te_3 pellet irradiated up to ion fluence of 1×10^{16} ions/cm^2.

4.4. Discussion

GIXRD and FESEM investigations indicate that the polycrystalline nature and surface morphology of the Bi_2Te_3 pellets were unaffected after He^+ ion irradiations. However, HRTEM results evidenced the presence of amorphous surface layer in the Bi_2Te_3 nanorod, which eventually hinder the out-of-plane atomic displacements (*i.e.,* A_u^2 and A_g^2 mode) in the Raman spectra.

It is well-established that an incidence of energetic ion during ion irradiation dissipates its energy *via* elastic collisions (*i.e.,* nuclear energy loss, S_n) and inelastic electronic excitations (*i.e.,* electronic energy loss, S_e). It may be noted from Table 4.1 that the energy loss due to inelastic electronic excitation (S_e = 0.208 keV/nm) is predominant with high electronic to nuclear energy loss ratio (S_e/S_n) of ≈53. The thermal spike model is the adopted model to explain the inelastic energy loss predominant ion-beam interactions such as swift heavy ion (SHI) interactions with matter. The above model outlined the physics of the latent track formation, amorphous pockets and amorphous zones in materials[131,211–215].

According to thermal spike model, 100 keV He^+ ion will be deposit its energy to the electronic sub-system of Bi_2Te_3 within 10^{-17} s. After that, thermalization of the electronic system would last for 10^{-15} s. The consecutive transfer of energy from electronic

system to lattice (in 10^{-14} s) through electron-phonon and electron-electron interactions will increase the local lattice temperature and resulted in local melting. The local melting and subsequent quenching (*i.e.*, thermal spike) occur as the local lattice temperature exceeds the lattice melting point. The mathematical description of time dependent thermal spike process is expressed as two coupled differential equations in cylindrical geometry[216] and given as,

$$C_e \frac{\partial T_e}{\partial t} = \frac{1}{r}\frac{\partial}{\partial r}\left(rK_e \frac{\partial T_e}{\partial x}\right) - g(T_e - T_a) + A(r,t) \qquad \textbf{Eqn. 4.1}$$

$$C_a \frac{\partial T_a}{\partial t} = \frac{1}{r}\frac{\partial}{\partial r}\left(rK_a \frac{\partial T_a}{\partial x}\right) - g(T_e - T_a) + B(r,t) \qquad \textbf{Eqn. 4.2}$$

where T_e, T_a, C_e, C_a, K_e, and K_a are the temperature, the specific heat and the thermal conductivity for the electronic and atomic lattice system respectively. *A(r, t)* and *B(r, t)* are the radial energy density per unit time supplied by the incident ion to the electronic system from S_e and to the atomic lattice system from S_n respectively.

It is important to note that the factor '*g*' (electron-phonon coupling strength) describes the ability of the electrons to transfer its heat/energy to the atomic lattice system and subsequently dictates the extent of lattice heating due to energy transfer. The value of g $(= \frac{K_e}{\lambda^2})$ can be estimated from the values of electron mean free path and electronic thermal conductivity. Electron mean free path in bulk Bi_2Te_3 is 61 nm[217], while the value was suppressed in nanostructures due to partial diffuse scattering of electrons by the surfaces of the nanostructures and grain boundary scattering in the polycrystalline sample. For instances, in the case of 52 nm Bi_2Te_3 nanowire, the electron mean free path value is 40 nm only[217]. Using Wiedemann-Franz relation, $K_e = \sigma LT$, the electronic thermal conductivity was estimated to be $K_e = 8.9\times10^{-4}$ W/m-K. Here, σ (=120 S/m) is the electrical conductivity of Bi_2Te_3 pellet at 300 K and L is the Lorentz constant. Henceforth, the value of g for bulk Bi_2Te_3 and 52 nm Bi_2Te_3 nanowire is evaluated to be 2.35×10^{11} W/m^3-K and 5.5×10^{11} W/m^3-K respectively, which are several orders of magnitude lower than the reported values[131,218] for effective energy transfer.

Thus the weak electron-phonon interactions will allow the electronic heat/energy to spreads out more quickly (*i.e.,* before 10^{-12} s) throughout the material. This result in the shorter time for lattice to heat up and consequently could induce rearrangement of atoms which gives rise to the production of large number of point defects (*i.e.,* vacancies and interstitials). However, irradiation induced point defects would migrate throughout the

lattice and most of these point defects would disappear through complex dynamic annealing process. This creates stable defects and defect complexes that are expected to accumulate at the outer rim of the nanorods. This resulted in the lattice disorder or amorphization at the surface of the Bi_2Te_3 nanorods.

As far as TE transport properties are concerned, He^+ ion irradiation increases the carrier concentration, at the same time preserves the *p*-type conductivity. On the other hand, Bi_2Te_3 pellet irradiated with higher ion fluence (2×10^{17} ions/cm^2) exhibited the maximum value of *S* (≈184 μV/K) at 390 K, which is 12% higher than that of pristine one (≈162 μV/K). Conversely, electrical conductivity values were deteriorated at higher ion fluences. The defects,[26]such as vacancies and interstitials and defect clusters are the strong perturbation in the lattice sites, which in turn act as charged coulomb scattering centers. It leads to impurity dominated scattering process, which eventually limited the carrier mobility and hence electrical conductivity. In contrast, the above mechanism aids to improve the Seebeck coefficients in the irradiated pellets. Pan *et al.,*[219] investigated the mechanism of the ionized impurity scattering process of charge carriers behind the improvement of the value of *S* in polycrystalline $AgPb_mSnSe_{2+m}$ samples.

The low energy charge carriers are extremely scattered by these charged coulomb scattering centers (*i.e.,* defects) and leads to increase in the average carrier energy, resulting in improved *S* value at the higher ion fluence. However, at lower ion fluence, the ionized impurity dominant scattering could be inconsiderable. This could be due to the generation of feeble number of antisite defects (especially at 5×10^{15} ions/cm^2) which in turn acts as the effective charge carriers (as evidenced from Hall-effect measurements). Therefore, it is believed that the lower values of *S* at 5×10^{15} ions/cm^2 could be ascribed primarily due to its improved carrier concentration. Furthermore, the emergence of bipolar effect due to the emanation of opposite type charge carriers deteriorated the value of *S* significantly at higher temperatures.

Additionally, the effect of ion induced amorphous surface layer of the Bi_2Te_3 nanorods (up to 9 nm at 2×10^{17} ions/cm^2) on thermoelectric transport properties should also be considered. Because, hopping conduction is activated in the amorphous materials between the high densities of localized states. This results in the high values of *S* and σ and increases with temperature. However, the hopping conductivity trends were not observed in nanostructured bulk Si containing nanograins of crystalline Si (70%) and amorphous SiO_x (30%)[220]. In present case, the estimated maximum volume fraction of the amorphous region is around 4% for ion fluence of 2×10^{17} ions/cm^2. Thus, the effects of

the amorphous region on the thermoelectric transport properties and Raman scattering experiment are insignificant.

4.5. Conclusion

Bi_2Te_3 nanorods were compacted to thin pellets, which were subsequently irradiated with 100 keV He^+ ions from 150 kV accelerator. The influence of ion irradiation on the structure, morphology, and TE properties, was investigated systematically as a function of ion fluence for 100 keV He^+ ions. TEM images evidenced the formation of an amorphous layer on the surface of the nanorods, which could be due to the accumulation of migrating/diffusing defect complexes favored by the high temperatures (due to dynamic annealing process). Raman scattering experiments on pellets provided further insight to the ion-induced structural modifications by enhancing the in-plane to out-of-plane atom displacements. Ionized impurity (*i.e.,* defects) dominated scattering process significantly enhances the value of S in the irradiated pellets (especially at higher ion fluence). However, at lower ion fluence, the ionized impurity scattering process is insignificant. For higher ion fluence, σ is lower due to more ionized impurity scatterings, resulting in lower power factors.

Chapter 5

Copper ion doping effects in bismuth telluride thin films.

5.1. Introduction

Nanostructured materials are expected to have enhanced *ZT* values, mainly because of phonon blocking effect along with density of states enhancement[39,41,43]. In addition, devices based on thin films can play a tremendous role in large-scale practical applications like in micro-module Peltier cooling devices, micro-generators, miniature low power microelectronics systems[3,4,221]. In the literature, many deposition methods such as chemical vapour deposition[45], co-evaporation[33], sputtering[102], electrodeposition[222], and pulsed laser deposition (PLD)[100]were employed for the deposition of Bi_2Te_3 thin films. However, the fabrication of Bi_2Te_3 thin films with exact stoichiometry is still a challenging task. Because, slight changes in the Bi:Te stoichiometry ratio result in the Bi_2Te_3 thin films either being *p*-type or *n*-type semiconductors and decrease *ZT*[223].

The PLD deposition method employed in this work has remarkable controllability and reproducibility over the thin film stoichiometry[92,151,224]. The bulk stoichiometric Bi_2Te_3 exhibits *p*-type conductivity. However, stoichiometric Bi_2Te_3 thin films have always reported to exhibit *n*-type conductivity. The high vapour pressure of Te atoms causes the evaporation of Te atoms during the deposition of the films, when compared to that of Bi atoms. Hence, *n*-type conductivity is attributed to the large number of Te vacancies[33,83,102,109] in the films. The difficulty in fabricating *p*-type Bi_2Te_3 thin films could be resolved through doping strategy.

For example, Ge and Sb were used as a *p*-type dopant, which will substitute at Bi site[225,226]. In contrast, *n*-type conductivity was exhibited by rare earth elements (La, Ce, Y, Er, Sm)[227,228] and halogens (I, Br)[229] doped Bi_2Te_3. For instances, the maximum *ZT* value of ~1.29 was reported by Ce doped Bi_2Te_3 nanostructured pellet at 300 K[230]. On the other hand, dual dopant behavior[69,72–74] was exhibited by transition metals (Au, Ag, Cu) doped Bi_2Te_3. It has been reported that the transition metals act as either donor or acceptor that depends on the dopant concentration and their locations in Bi_2Te_3 crystal. Therefore, choosing the appropriate dopant in addition to its concentration is needed to improve TE properties and for designing TE modules. For example, Ag doped $Bi_2(Se,Te)_3$ was exhibiting dual electronic nature[73] and is reported

to have 10% enhancement of TE figure-of-merit at room temperature for Ag-doped $Bi_2(Se,Te)_3$ as compared to that of pristine $Bi_2(Se,Te)_3$. Most importantly, copper has been found to be one of the potential dopants to enhance TE property of Bi_2Te_3. For long time, ambiguity in the occupancy of Cu atoms in the Bi_2Te_3 crystal is still a debate. Chen *et al.*,[72] reported that the Cu act as a *p*-type acceptors in Bi_2Te_3 at low concentration (<1 *at%*) and *n*-type donor at high concentration (>1 *at%*). This is attributed to the occupancy of Cu atoms, either it intercalates between Bi_2Te_3 layers or replaces Bi atoms at Bi site of Bi_2Te_3, which increase the electron and hole concentration respectively. The above observations are as well supported by several reports[68–71].

Unlike the other conventional doping technique, ion implantation[129] provides indispensable doping process in semiconductor device fabrication industry for past 50 years. Its advantage over other conventional doping techniques includes their control over the doping level, uniform dopant concentration, reproducibility of the dopant profile, lower processing temperature, and to tailor the miniature micro-fabricated devices[231]. In the present chapter, Bi_2Te_3 thin films were fabricated using PLD method and ion implantation was employed to incorporate Cu atoms with concentration of 0.5 *at%*, 1 *at%*, 1.5 *at%*, 2 *at%*. Further, the morphological, structural, vibrational, and TE properties of Cu-doped Bi_2Te_3 films are systematically investigated.

5.2. Experimental methods

5.2.1. Sample synthesis

Table 5.1: Details of ion irradiation in Bi_2Te_3 carried out in present work obtained by Monte Carlo based SRIM 2006 code.

Cu^+ ion energies	Mean projected range ± straggling (nm)	S_e (eV/nm)	S_n (eV/nm)	Sputtering yield (atoms/ion)
300 keV	156 ±100.8	244.7	875	7.312
700 keV	356 ±171.8	484.2	710	5.45

Bi_2Te_3 thin films of 400 nm thickness were deposited using pulsed laser deposition (PLD) method and quartz substrates were used. The target pellet for PLD deposition was made by using hydrothermally synthesized Bi_2Te_3 smooth nanorods and the synthesis procedure was explained in chapter 3. Prior to the deposition, the chamber was evacuated to a base pressure of ~3×10^{-5} mbar and then purged with argon gas. The deposition was carried out at a pressure of ~8×10^{-1} mbar. The KrF excimer laser (M/s Coherent Inc.) of wavelength 248 nm with pulse duration of 20 ns was used to ablate the target. The energy

of each laser pulse was ~250 mJ with 5 Hz frequency and 3000 laser shots were used. During ablation, PLD target was rotated at a speed of 3 rpm to continuously expose the fresh surface for ablation and to avoid crater formation. All films were grown at the substrate temperature of 250 ºC and the target-substrate distance was fixed to 5 cm.

The Cu^+ ions were implanted on Bi_2Te_3 thin films at room temperature using a 1.7 MV Tandetron accelerator. The implantation chamber was evacuated to a base pressure of ~3×10^{-7} mbar. For Cu^+ ion implantation, the energy of the Cu^+ ions was chosen 300 keV and 700 keV, such a way that one can obtain uniform copper concentration across the 500 nm thick film. The beam current density was maintained ~1 μA/cm^2, to avoid beam heating. Monte Carlo simulations were performed for 300 keV and 700 keV Cu^+ ion irradiation in Bi_2Te_3 using SRIM2006 code[130] and estimated mean projected range, straggling, electronic energy loss (S_e), nuclear energy loss (S_n), and sputtering yield are listed in Table 5.1. For SRIM calculations, displacement energy (E_d) was fixed to 25 eV for both the elements in Bi_2Te_3 thin films[78].

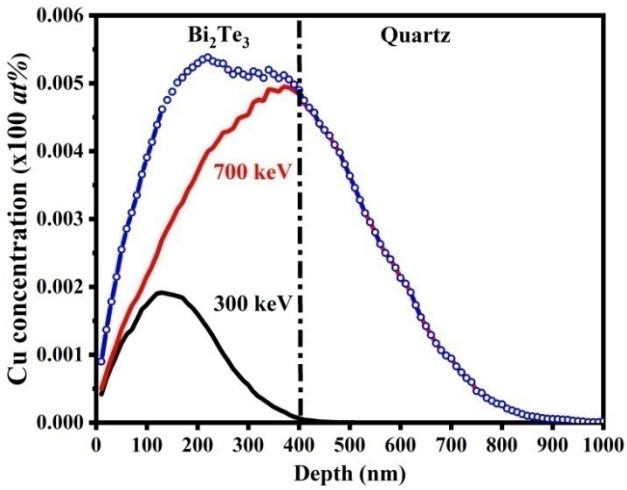

Figure 5.1: The expected depth profile (denoted by blue circles) for the uniform Cu concentration of 0.5 at% in Bi_2Te_3 thin films on quartz substrate using 300 keV (denoted by black line) and 700 keV (denoted by red line) Cu^+ ion implantation. The implantation profiles are obtained using SRIM calculations[130].

From Table 5.1, one can note that the mean projected range of 300 keV and 700 keV Cu^+ ions in Bi_2Te_3 are ~156 and ~356 nm respectively. The implanted Cu concentration was varied from 0.5 *at%* to 2 *at%* in Bi_2Te_3 thin films. 300 keV and 700 keV Cu^+ ion fluences are accordingly adjusted to get the uniform Cu atom concentration throughout the Bi_2Te_3 thin films. Figure 5.1 shows the expected Cu depth profile for the uniform Cu concentration of 0.5 *at%* in Bi_2Te_3 thin films. The required Cu^+

ion fluences are calculated for the above-mentioned Cu concentration in Bi_2Te_3 thin film and are tabulated in Table 5.2. In order to decouple effects of the ion beam induced defects and implanted Cu atoms, another set of Cu^+ ion implanted Bi_2Te_3 thin film samples were annealed at 150 ºC for 2 hrs and characterized accordingly.

Table 5.2: Estimated 300 keV and 700 keV Cu^+ ion fluences for incorporating Cu concentration of 0.5 at%, 1 at%, 1.5 at%, 2 at% in Bi_2Te_3 thin films.

Cu (*at%*)	Ion fluence (ions/cm^2)	
	300 keV	**700 keV**
0.5	1.3×10^{15}	6.65×10^{15}
1	2.6×10^{15}	1.33×10^{16}
1.5	3.9×10^{15}	2×10^{16}
2	5.2×10^{15}	2.7×10^{16}

5.2.2. Characterization techniques

The structural characterization of the pristine and Cu doped Bi_2Te_3 thin films before and after annealing was carried out using grazing incidence X-ray diffractometer (GIXRD, Inel, equinox 2000) with Cu-K_α (1.541 Å) radiation. The incidence angle was kept 1°. The morphology of the Bi_2Te_3 thin films was obtained using focused ion beam field emission scanning electron microscope (FIB-FESEM, Zeiss, Crossbeam 340), while operating at an accelerating voltage of 5 kV and the working distance of ~3 mm. The images were recorded using in-lens detector. Energy dispersive X-ray (EDX) analysis was carried out in FESEM (Carl Zeiss, SUPRA55) equipped with X-ray detector, while operating with the accelerating voltage of 20 kV.

Furthermore, the surface topography of the Bi_2Te_3 thin films were studied using atomic force microscopy (WiTec Alpha RA 300). The Raman spectra of the pristine and Cu-doped Bi_2Te_3 thin films before and after annealing were examined by micro Raman spectrometer (WiTec Alpha RA 300) using excitation wavelength of 532 nm with the laser power of 0.5 mW. Using 3 MeV α particles, Rutherford backscattering spectrometry (RBS) was carried out at normal incidence and the backscattered particles were detected using surface barrier detector. The experimental RBS spectra were compared with simulated RBS spectra using SIMNRA tool[158] for its composition analysis.

The Hall-effect measurements (Ecopia HMS 5000) were carried out using magnetic field of 0.5 Tesla at room temperature under Van der pauw configuration to evaluate charge carrier concentration and mobility. The temperature dependent in-plane Seebeck coefficient and electrical conductivity of the films were measured using bridge method[159] and DC four probe method respectively.

5.3. Results

5.3.1. Compositional analysis of Cu^+ ion implanted Bi_2Te_3 thin films

The elemental composition of pristine and Cu^+ ion implanted Bi_2Te_3 thin films were investigated using EDX spectra and the atomic percentage of the elements Bi, Te, and Cu in the samples (pristine and Cu^+ ion implanted thin films) are given in Table 5.3. One can see that the elemental composition in the samples were in agreement to the Bi_2Te_3 stoichiometry and the observed Cu concentration in Cu^+ ion implanted Bi_2Te_3 films are closely matched with the estimated Cu^+ ion fluences (see Table 5.2).

Table 5.3: Elemental compositions of the pristine and Cu implanted thin films.

Sample	Bi (*at%*)	Te (*at%*)	Cu (*at%*)
Pristine	41	59	-
Cu-0.5	42	58	-
Cu-1	41	58	1
Cu-1.5	42	57	1
Cu-2	41	57	2

The experimental and simulated RBS spectra of pristine and Cu^+ ion implanted Bi_2Te_3 thin films are displayed in Figure 5.2. The peak position in the RBS energy spectrum gives elemental information, while thin film thickness values could be determined from the peak width and height. The arrow pointed at 2.8 MeV, 2.62 MeV, 2.3 MeV, 1.5 MeV, and 0.9 MeV in the Figure 5.2(a) represents the backscattered α particle energies that are corresponding to the Bi, Te, Cu, Si, and O atoms respectively. The edges in the RBS spectra correspond to Si and O atoms, which represent the quartz substrate. From simulated RBS profile, film thickness was estimated to be around 400 nm. The overlapping profiles of Bi and Te in RBS spectra are attributed to the thick Bi_2Te_3 films. Expanded view of RBS spectra for the pristine and the Cu^+ ion implanted Bi_2Te_3 thin films are shown in Figure 5.2 (b) to Figure 5.2 (f).

In addition to that, simulated backscattering yield of Bi and Te as function energy for all films are also plotted. Signature of the implanted Cu atoms has not been observed in RBS spectra of Cu^+ ion implanted Bi_2Te_3 thin films due to small concentration of Cu, which is below to the limitation of the RBS experiment. However, the profile of the Bi (Figure 5.2 (c) to Figure 5.2 (f)) displays the gradual reduction in the Bi yield across the Cu^+ ion implanted Bi_2Te_3 thin films.

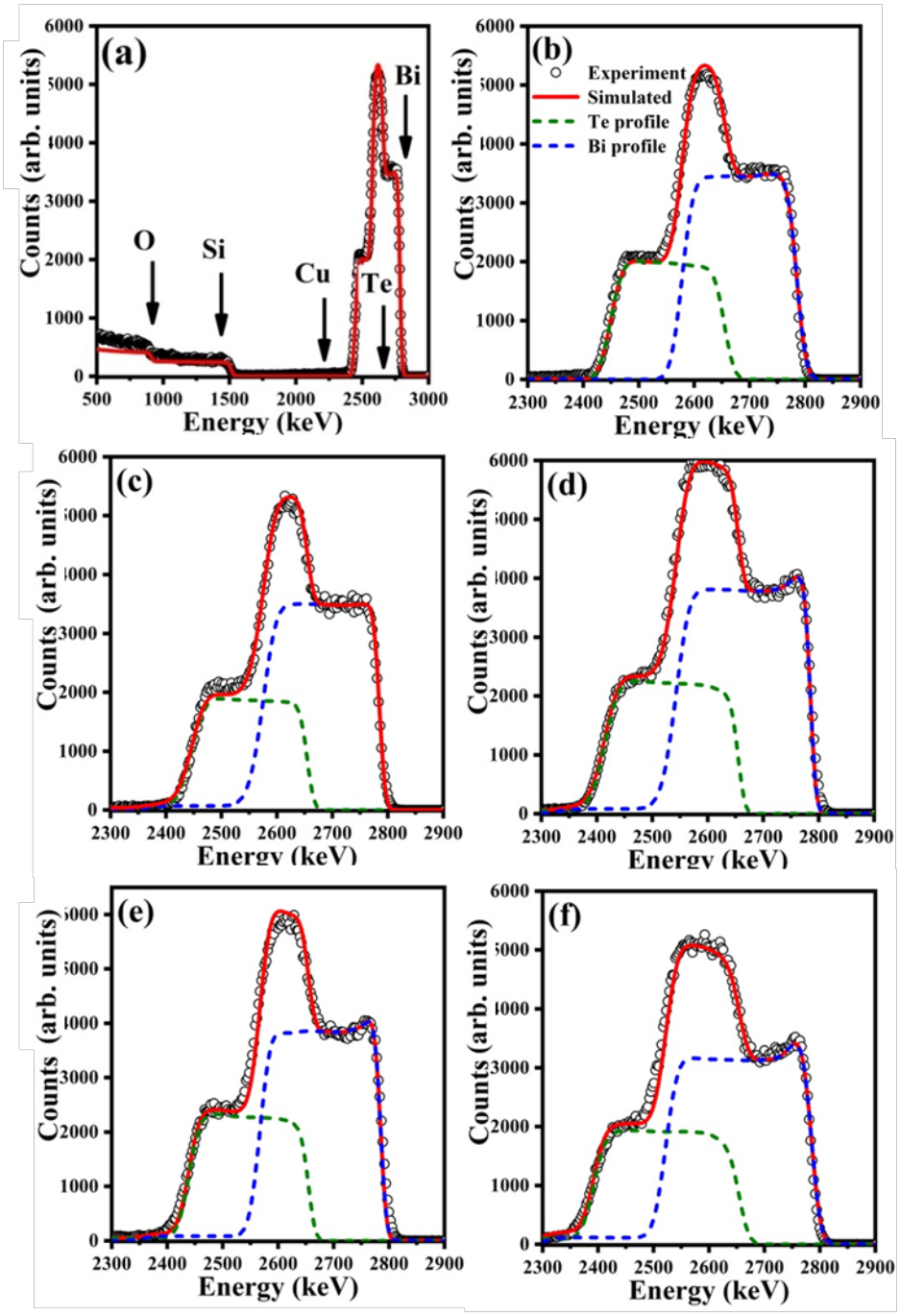

Figure 5.2: (a) RBS spectrum of pristine Bi_2Te_3 thin film and (b) its expanded view. RBS spectrum of Cu^+ ion implanted Bi_2Te_3 thin film with Cu concentration of (c) 0.5 at%, (d) 1 at%, (e) 1.5 at%, and (f) 2 at%.

To obtain depth distribution profile of Bi, Te, and Cu across the film, quantitative investigation on the RBS spectra was carried out using SIMNRA simulations. This was done by segmenting thin films in to 10 sub-layers, each of having 40 nm thick with different Bi, Te, and Cu concentration. The depth profile of Bi, Te, and Cu atoms in Cu^+ ion implanted Bi_2Te_3 films (Figure 5.3) show the presence of nearly uniform Cu concentration across the thin film (more explicitly beyond the thickness of ~150 nm) and

is consistent with SRIM profile (see Figure 5.1). The concentration of Bi and Te at the surface of the pristine thin film is ~43.5% and ~56.5% respectively. However, gradual reduction in the atomic concentration of Bi from ~43.5% to ~42%, ~40%, ~39%, ~38% are observed in the Cu^+ ion implanted films having Cu concentration of 0.5 *at%*, 1 *at%*, 1.5 *at%*, and 2 *at%* respectively.

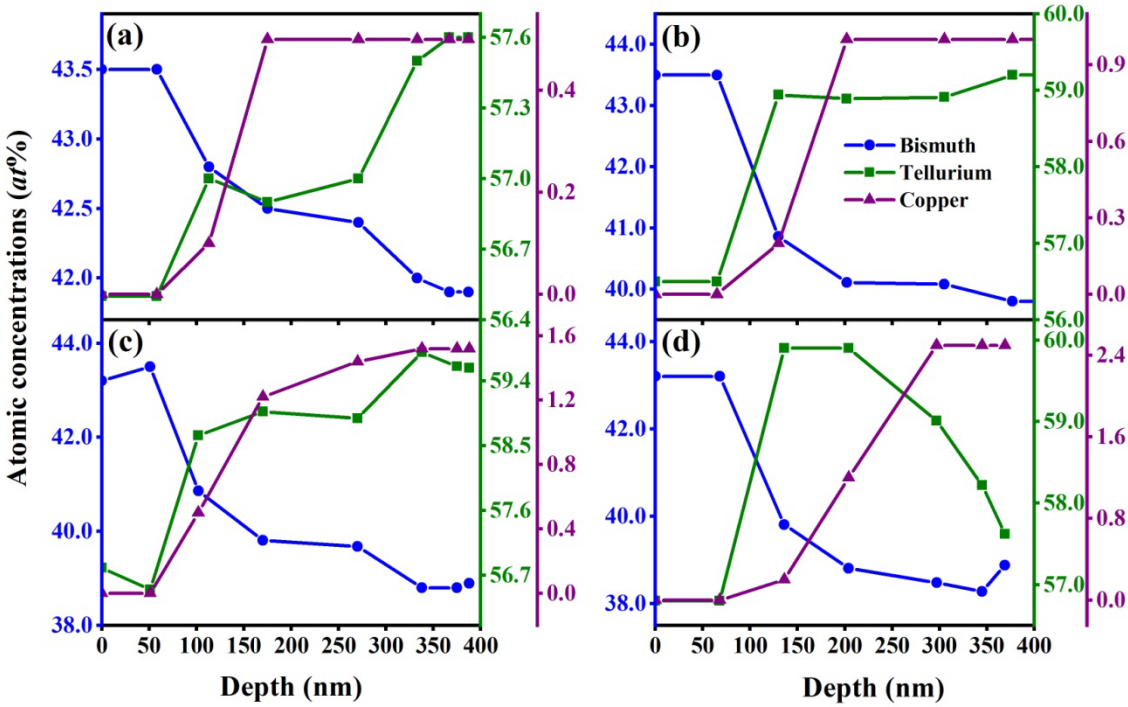

Figure 5.3: The depth profile of bismuth, tellurium, and copper in Cu^+ ion implanted Bi_2Te_3 thin films with Cu concentration of (a) 0.5 at%, (b) 1 at%, (c) 1.5 at%, and (d) 2 at%.

5.3.2. GIXRD analysis of Cu^+ ion implanted Bi_2Te_3 thin films

Figure 5.4 display the GIXRD patterns of pristine and Cu^+ ion implanted Bi_2Te_3 thin films. The diffraction peaks were confirming with the rhombohedral structure of the Bi_2Te_3 crystal and the diffraction peaks were indexed, labeled accordingly as in JCPDS 01-080-6959. It has been observed that all thin films are exhibiting polycrystalline nature and no trace of impurities and phase transformation were seen. The peaks corresponding to the Cu and Cu-Bi_2Te_3 phases are not seen in Cu^+ ion implanted films and this could be ascribed to the small concentration of Cu in Bi_2Te_3 films.

As seen from the Figure 5.4, the relative intensities of the diffraction peaks in Cu^+ ion implanted films with respect to the most prominent [0 1 5] peak are reduced considerably and the poor crystallinity was seen in 2 *at%* Cu^+ ion implanted Bi_2Te_3 thin film.

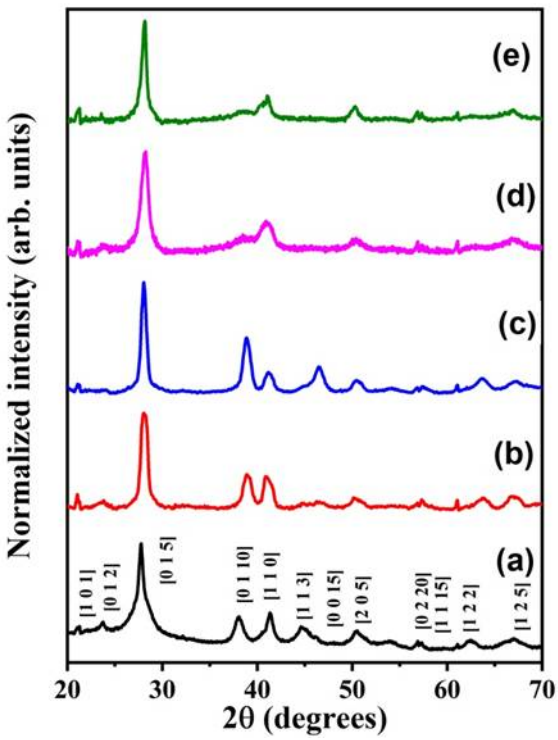

Figure 5.4: GIXRD pattern of (a) pristine and Cu^+ ion implanted Bi_2Te_3 thin films with Cu concentration of (b) 0.5 at%, (c) 1 at%, (d) 1.5 at%, and (e) 2 at%.

The average crystallite size was measured using Scherrer formula and the average crystallite size as a function of Cu concentration in Cu^+ ion implanted sample is shown in Figure 5.5. The average crystallites in pristine Bi_2Te_3 film is ~11 nm and the value increases up to Cu concentration of 1 *at%* in the films (~18 nm), due to grain growth and then subsequently decreased to ~15 nm at higher Cu concentration.

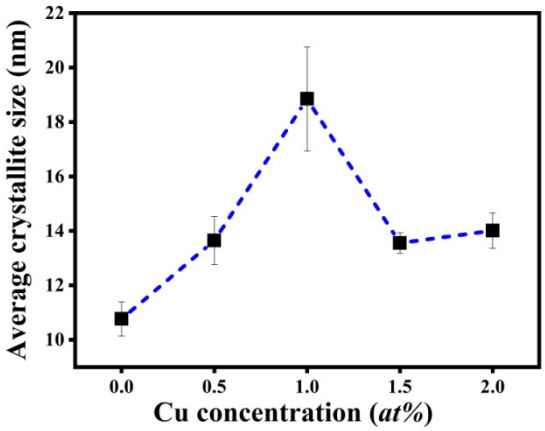

Figure 5.5: Average crystallite size of pristine and Cu^+ ion implanted Bi_2Te_3 thin films obtained from GIXRD results.

The changes observed in the relative peak intensity diffracted with increasing ion fluence depict the modification in the crystallinity and orientation in the planes of Bi_2Te_3

upon Cu ion implantation. From the diffraction pattern, it is observed that the relative intensity for the planes [1 0 10], [1 1 3], [0 0 15] increase up to 1 at% Cu doped Bi_2Te_3 and then substantially. This suggests that amorphization process occurs after 1 at% of Cu and crystallinity decrease at these planes as high temperature zones are generated due to Cu ion implantation. On the other hand, Figure 5.6 shows GIXRD pattern of annealed Cu^+ ion implanted thin films.

It has been observed that the Cu^+ ion implanted Bi_2Te_3 thin films are exhibiting polycrystalline nature even after annealing. There are no traces for phase transformations and phase segregations. Furthermore, from the sharp GIXRD peaks, one can say that the defect annealing enhances the crystallinity of Cu^+ ion implanted Bi_2Te_3 thin films.

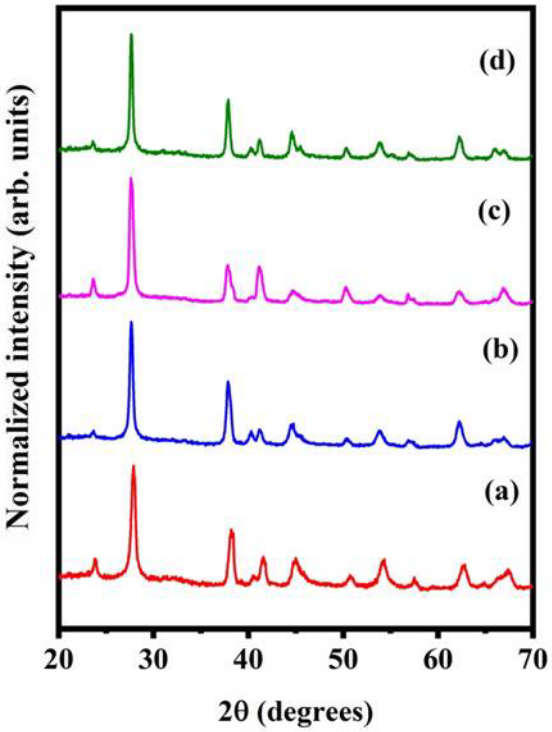

Figure 5.6: GIXRD pattern of annealed Cu^+ ion implanted thin films with Cu concentration of (a) 0.5 at%, (b) 1 at%, (c) 1.5 at%, and (d) 2 at%.

5.3.3. Raman scattering analysis in Cu^+ ion implanted films

The Raman spectra of pristine and Cu^+ ion implanted Bi_2Te_3 thin films are displayed in Figure 5.7. The high frequency vibrational modes ($E_g^2$and A_g^2) are observed at ~100, ~135 cm^{-1}, while the low frequency vibrational modes (E_g^1 and A_u^1) were not observed in the spectra. In addition, the peak at ~125 cm^{-1} was assigned to Raman inactive/IR active/forbidden mode (*i.e.,* A_u^2) [156,232]. In the pristine thin films, the activation of forbidden mode (*i.e.,* A_u^2) were ascribed to the loss of Bi_2Te_3 crystal

inversion symmetry due to presence of disorder at grain boundaries and thin film surface.It has been observed that the intensity of A_u^2 increases progressively with Cu concentration (or Cu^+ ion fluence) and it is associated with implantation induced defects and damage accumulation.

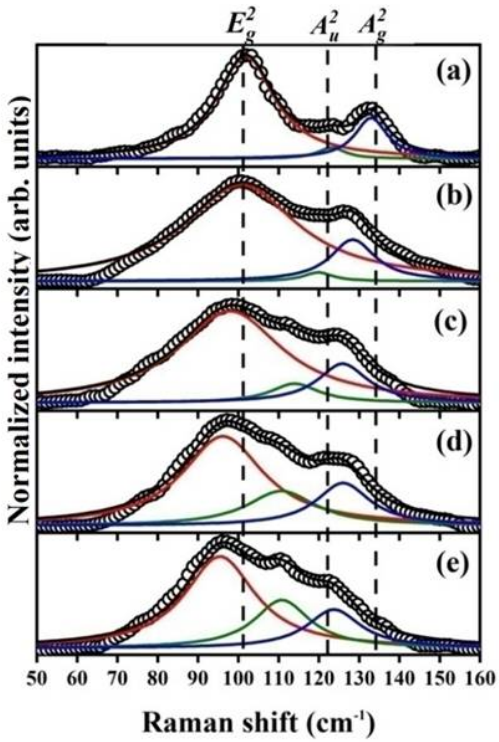

Figure 5.7: The Raman spectra of (a) pristine and Cu^+ ion implanted Bi_2Te_3 thin films with Cu concentration of (b) 0.5 at%, (c) 1 at%, (d) 1.5 at%, (e) 2 at% .

Figure 5.8 shows the variation in the Raman peak position and FWHM of the pristine and Cu^+ ion implanted Bi_2Te_3 thin films with the Cu concentration. The consistent shifting of the Raman peak position (Figure 5.8 (a)) towards lower wavenumber was observed in all Cu^+ ion implanted Bi_2Te_3 thin films.

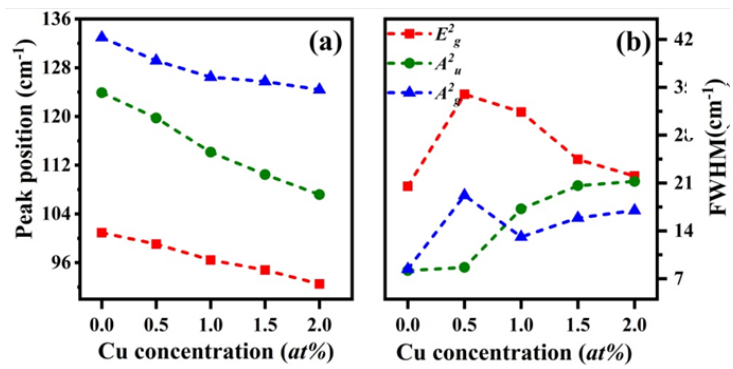

Figure 5.8: Variation in (a) peak position and (b) FWHM of the pristine and Cu^+ ion implanted Bi_2Te_3 thin films with the Cu concentration. Dotted lines are the guide to the eye.

The Cu^+ ion implantation induces short-range lattice disorder and the lattice strain in the Bi_2Te_3 thin film, which was consistent with the earlier report on Au^+ ion implanted Si[210]. On the other hand, it may be noted that the increase in FWHM of the Raman mode with Cu concentration. Raman peak broadening was directly correlating to the ion beam induced damage and its accumulation. The zone center selection rule is relaxed owing to the presence of defects and damage accumulation. Therefore, the optical phonons of momentum around Brillouin zone along with zone center can participate in Raman scattering that increases the FWHM of Raman peak.

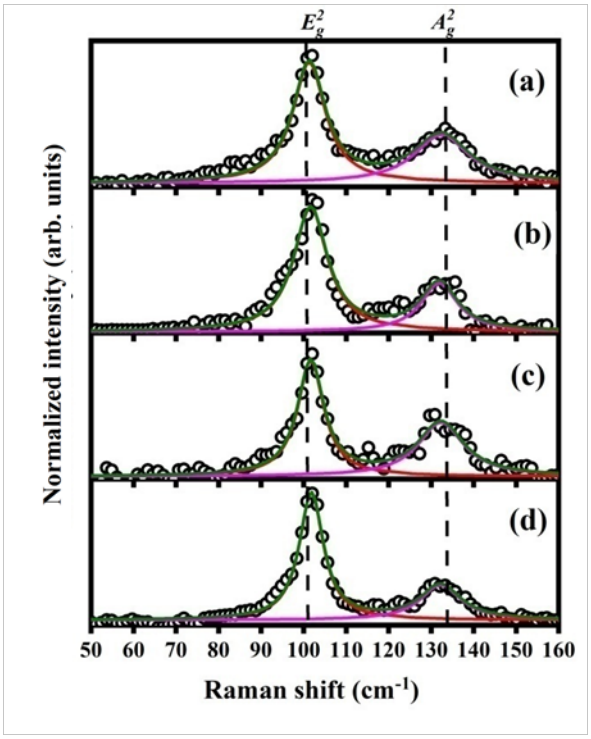

Figure 5.9: Raman spectra for annealed Cu^+ ion implanted Bi_2Te_3 thin films with Cu concentration of (a) 0.5 at%, (b) 1 at%, (c) 1.5 at%, and (d) 2 at%.

On the other hand, absence of forbidden mode (*i.e.,* A_u^2) in the Raman spectra of annealed Cu^+ ion implanted Bi_2Te_3 thin films (Figure 5.9) signifies the suppression of implantation induced defects and damage accumulation.

5.3.4. Morphological analysis of Cu^+ ion implanted Bi_2Te_3 thin films

The plane view and cross-sectional FESEM images of the pristine and Cu^+ ion implanted Bi_2Te_3 films are displayed in Figure 5.10. Irregularly shaped faceted crystallites with the different grain sizes are seen in the pristine Bi_2Te_3 thin film and the grain boundaries along with irregular pores are clearly visible. The grain sizes in the pristine Bi_2Te_3 thin film were estimated using imageJ software[198]. The mean grain size is calculated from the grain size distribution plot and the value is evaluated to be ~85±34 nm.

On the other hand, morphology of the Cu^+ ion implanted Bi_2Te_3 films lack definite features and imperceptible with nano-size pinholes. It is suggested that the pinhole formation in the Cu^+ ion implanted thin films could be a consequences of grain coalescence.

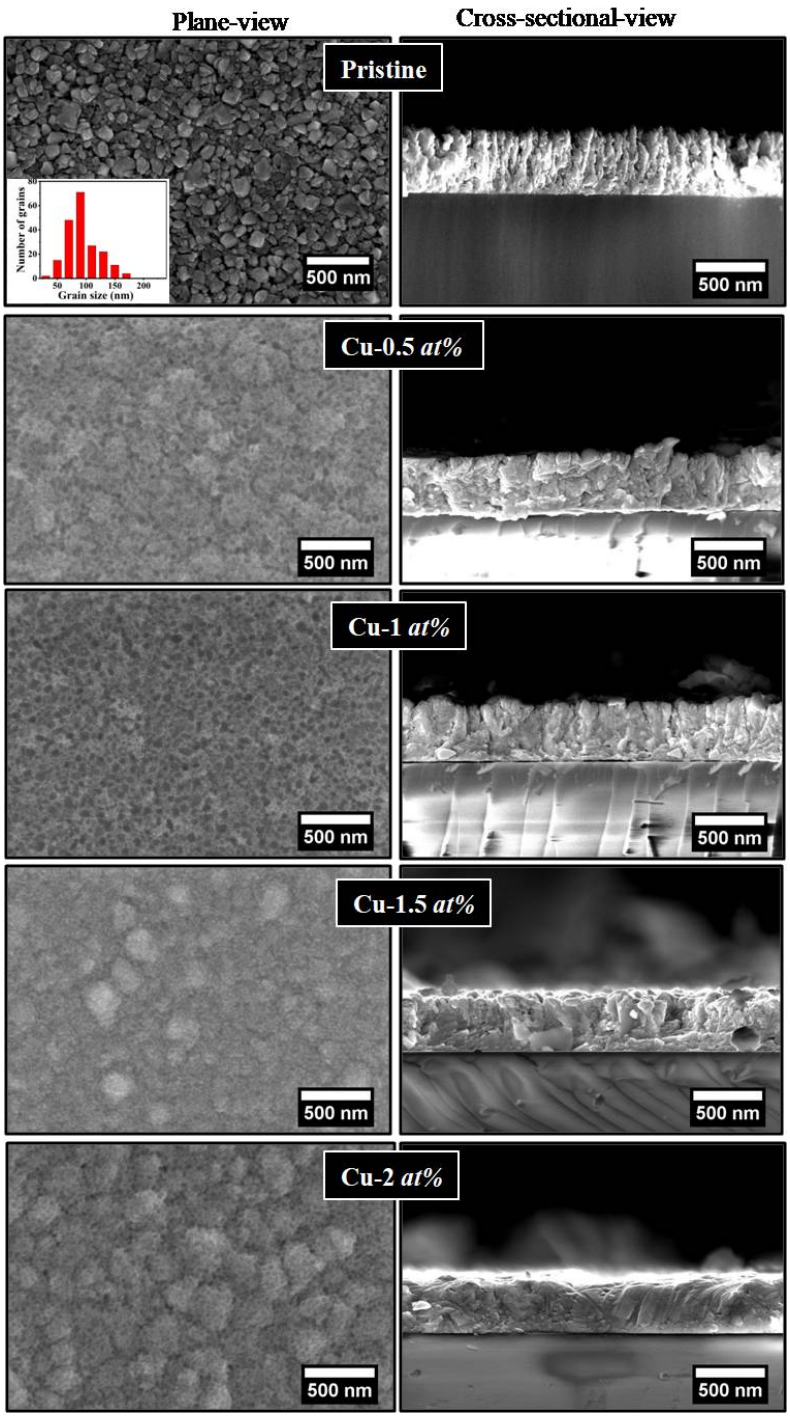

Figure 5.10: FESEM images of plane view and cross sectional view of the pristine and Cu^+ ion implanted Bi_2Te_3 thin films.

The cross-sectional FESEM images approximately estimate the thickness of all films to be ~400 nm. The pristine thin film confirms the densely packed columnar structures, where the structures were evidently grown perpendicular to the quartz substrate, while Cu^+ ion implanted films visibly displays the merged, coalesced columnar structures, which is consistent with its corresponding FESEM planar view. From Figure 5.11, it has been observed that the morphology of the Cu^+ ion implanted Bi_2Te_3 thin films remained same even after annealing.

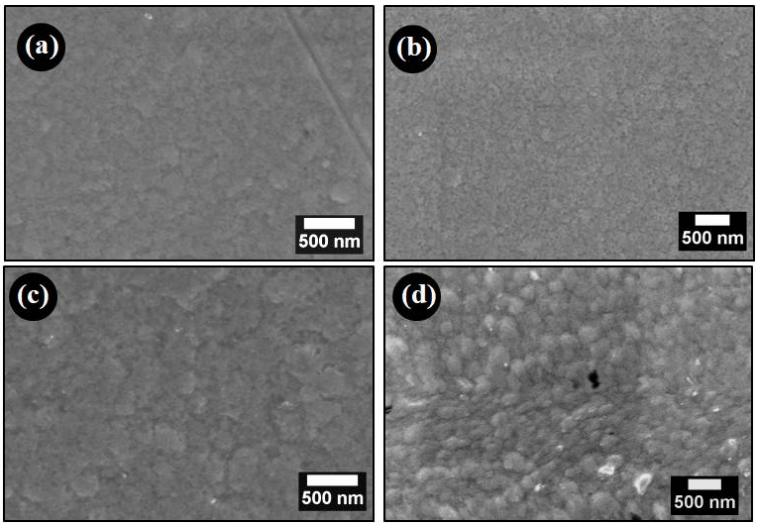

Figure 5.11: FESEM images of the annealed Cu^+ ion implanted Bi_2Te_3 thin films with Cu concentration of (a) 0.5 at%, (b) 1 at%, (c) 1.5 at%, and (d) 2 at%.

The surface topography of the thin films was investigated further using AFM and Figure 5.12 displays the AFM topography (2D view) of the pristine and Cu^+ ion implanted Bi_2Te_3 thin films. The topography of the pristine Bi_2Te_3 thin film (Figure 5.12 (a)) has well-defined, narrow sized grains, while Cu^+ ion implanted Bi_2Te_3 thin films (Figure 5.12 (b) to Figure 5.12 (e)) has diffusive grain boundaries. The AFM images were analyzed using Wsxm tool [155] and the systematic evolution of the surface topography in terms of grain size and roughness of the Bi_2Te_3 thin films upon Cu^+ ion implantation are shown in Figure 5.13.

The average grain size and rms roughness values for the pristine Bi_2Te_3 thin film are ~174.4±21 nm and ~13.6 nm respectively. Until the Cu concentration of 1 *at%*, the average grain size was not varied much, while rms roughness value decreases from ~13.6 nm to ~3.7 nm. Further, increase in the Cu concentration led to increase in the average grain size (~363±6 nm) and rms roughness. The grain coalescence (during Cu^+ ion implantation) could increase the average grain size and rms roughness until smaller Cu^+ ion fluences. However, at high Cu^+ ion fluences, sputtering process could be dominant

which would increase rms roughness in Bi_2Te_3 thin films. Furthermore, ion-beam induced strain[233] will also acts as the additional surface roughening mechanism for the high Cu^+ ion fluences.

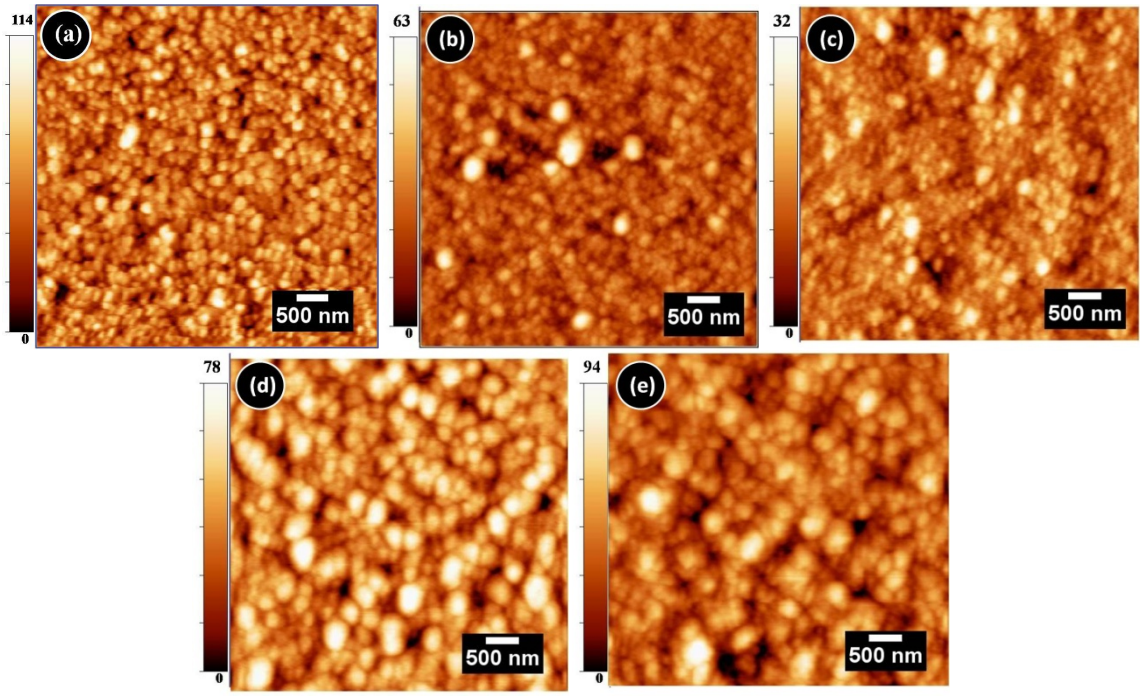

Figure 5.12: AFM (2D) topography of (a) pristine and Cu^+ ion implanted Bi_2Te_3 thin films with Cu concentration of (b) 0.5 at%, (c) 1 at%, (d) 1.5 at%, and (e) 2 at%. The area of the scanned images are 5μm×5μm.

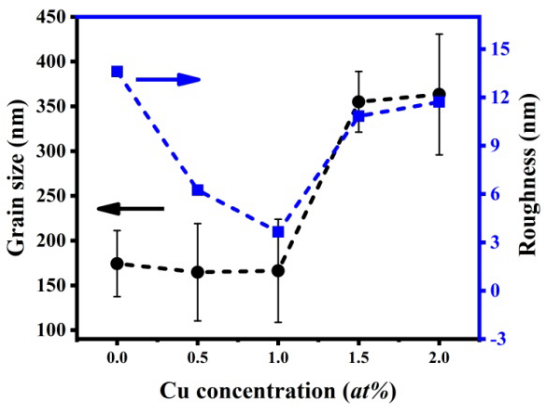

Figure 5.13: Average grain size and rms roughness values from the AFM images of the pristine and Cu^+ ion implanted Bi_2Te_3 thin films as a function of Cu concentration. Dotted lines are the guide to the eye.

5.3.5. Thermoelectric transport properties

Hall-effect measurements at room temperature confirm the *n*-type conductivity of pristine Bi_2Te_3 thin film, indicating electrons as their majority charge carriers. On the other hand, *p*-type conductivity was demonstrated by Cu^+ ion implanted Bi_2Te_3 thin films.

After annealing, Cu^+ ion implanted Bi_2Te_3 thin films exhibited *n*-type conductivity. It is recapitulated from the previous chapters that Bi_2Te_3 target pellet that were used to fabricate thin films had *p*-type charge carriers. In Bi_2Te_3, donor-type defects in Bi_2Te_3 are Te vacancies (V_{Te}) and Bi antisite defects (Te_{Bi}), while acceptor type defects are Te antisite defects (Bi_{Te}) and Bi vacancies (V_{Bi}). Hashibon *et al.,*[30] reported the formation energy of the above-mentioned types of defects in Bi-rich and Te-rich growth conditions using first principle calculations. The *n*-type conductivity of the pristine Bi_2Te_3 thin films is associated with V_{Te} that donates two electrons per defect. The earlier reports[33,83,102,151,234] on Bi_2Te_3 thin films mostly had *n*-type charge carriers and the authors were attributed the *n*-type conductivity with the generation of donor type, doubly ionized V_{Te}. It is suggested that the Te atom has higher vapour pressure than Bi atoms, which resulted in the re-evaporation of Te atoms from the substrate during Bi_2Te_3 deposition process.

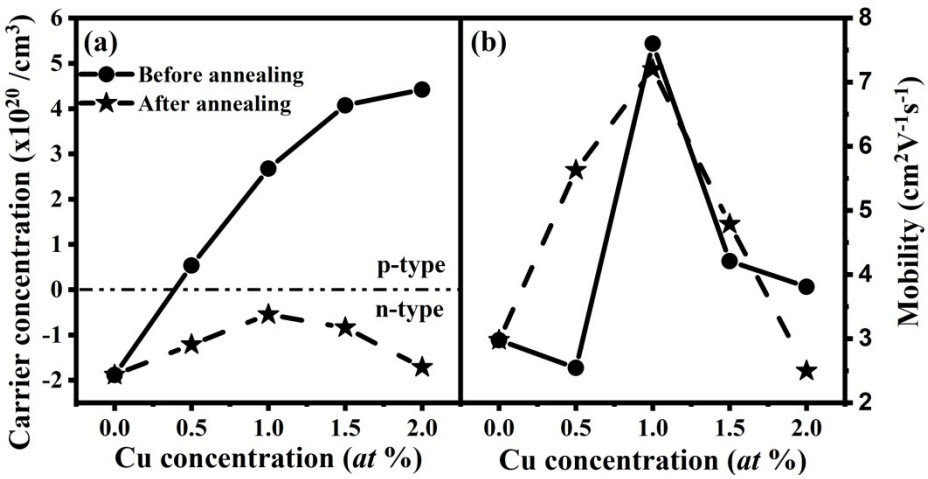

Figure 5.14: Carrier concentration (a) and mobility (b) of the Cu^+ ion implanted Bi_2Te_3 thin films before and after the annealing having various Cu concentration.

The carrier concentration and mobility values for the Cu^+ ion implanted Bi_2Te_3 thin films before and after annealing are displayed in Figure 5.14. As far as carrier type and carrier concentration are concerned, the electron carrier concentration in the pristine film is ~1.88×10^{20} /cm^3 and the hole carrier concentration are estimated to ~0.538×10^{20} /cm^3 in 0.5 *at%* Cu^+ ion implanted film, which were sequentially improved up to ~4.42×10^{20} /cm^3 with Cu dopant concentration. However, the annealed Cu^+ ion implanted Bi_2Te_3 thin films does not exhibit any charge carrier type conversion and at the same time, the electron concentration was observed to be reduced in the annealed Bi_2Te_3 thin films, up to the Cu concentration of 1 *at%* that enhances slightly to the value of

~1.71×10^{20} /cm^3. The mobility of the pristine Bi_2Te_3 thin film is ~2.4 cm^2/V-s and was enhanced up to ~10.76 cm^2/V-s in case of 0.5 *at%* Cu^+ ion implanted Bi_2Te_3 thin film. The enhancement in the mobility values could correspond to ion beam induced grain coalescence processes. Furthermore, the mobility of the Cu^+ ion implanted thin films with the Cu concentration of 1 *at%*, 1.5 *at%*, 2 *at%* are consistently suppressed to the values of ~6.29, ~3.12, ~2.62 cm^2/V-s respectively, which could be ascribed to the ion beam induced defect accumulation. It has to be noted that the annealed Cu^+ ion implanted Bi_2Te_3 thin films also exhibit the similar trend.

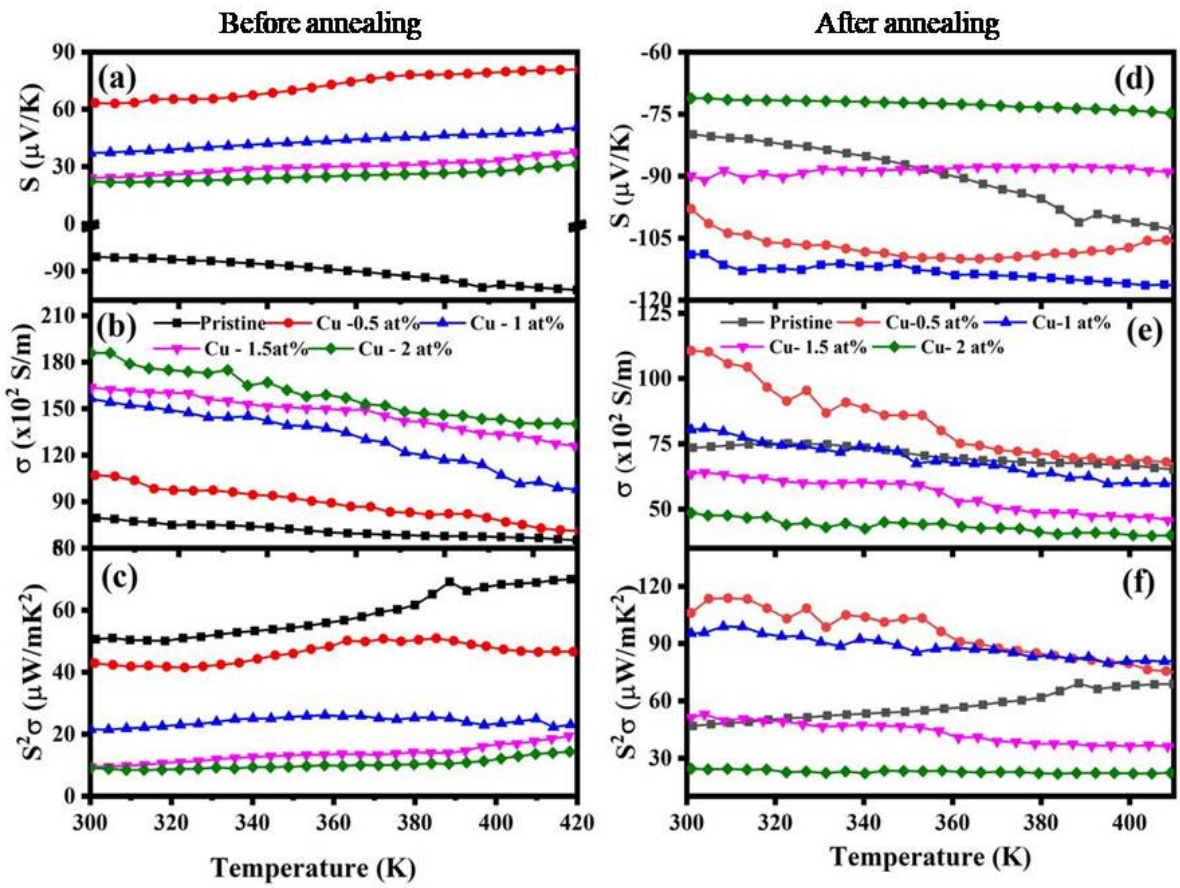

Figure 5.15: (a, d) Seebeck coefficient (S), (b, e) electrical conductivity (σ) and (c, f) power factor ($S^2\sigma$) for Cu^+ ion implanted Bi_2Te_3 thin films before and after the annealing for various Cu concentration.

Temperature dependent Seebeck coefficient (*S*) of pristine, Cu^+ ion implanted and annealed Cu^+ ion implanted Bi_2Te_3 thin films are presented in Figure 5.15 (a, d). The pristine and annealed Cu^+ ion implanted Bi_2Te_3 thin films demonstrates the negative *S* values, while Cu^+ ion implanted films possess positive *S* values. The results once again confirm that the pristine and annealed Cu^+ ion implanted Bi_2Te_3 thin films has electrons as the majority charge carriers, while Cu^+ ion implanted Bi_2Te_3 thin films are dominated by

holes. According to two conduction band model, the relative contribution of electrons and holes results suppresses the net *S* values, where the values are ranging from positive to negative values. In addition to that, this bipolar effect suppresses the net *S* value at high temperature. In the case of pristine Bi_2Te_3 thin film, *S* value at 300 K is around -79.8 μV/K, while, trend with increasing Cu concentration decreases the absolute value of *S* from ~65.32 μV/K to ~37.12, ~30.16, ~22.25 μV/K respectively. In the case of annealed Cu^+ ion implanted thin films, it is observed that the value of *S* significantly increases at lower Cu concentration (<1 *at%*) and subsequently decreases at higher Cu concentration (>1 *at%*) at near room temperature.

The electrical conductivity (σ) for the pristine, Cu^+ ion implanted and annealed Cu^+ ion implanted Bi_2Te_3 thin films (Figure 5.15 (b, e)) decreases with increase in temperature. This trend portrays the highly degenerate semiconductor behavior. In the case of Cu^+ ion implanted Bi_2Te_3 thin films, at 300 K, the value of the σ abruptly increases from ~73.5×10^2 S/m (for the pristine Bi_2Te_3 film) to ~112.16×10^2, ~166.6×10^2, ~174.5×10^2, ~186×10^2 S/m for Cu^+ ion implanted Bi_2Te_3 films with Cu concentration of 0.5 *at%*, 1 *at%*, 1.5 *at%*, 2 *at%* respectively. On the other hand, in the case of annealed Cu^+ ion implanted thin films, the value of σ enhanced to the value of 110.72×10^2 S/m for the Cu concentration of 0.5 *at%* and the value subsequently decreases. Based on the above results, the power factor ($S^2\sigma$) was calculated and presented in Figure 5.15 (c, f). The maximum $S^2\sigma$ was achieved in the annealed Cu^+ ion implanted Bi_2Te_3 thin films and corresponds to the value of ~106.12 μW/mK^2 at 300 K, which is higher than that of pristine and Cu^+ ion implanted Bi_2Te_3 thin films.

5.4. Discussion

From FESEM and AFM analysis, one can see that the grainy and polycrystalline nature of pristine Bi_2Te_3 thin film, more planar and less grainy upon Cu^+ ion implantation. The activation of the forbidden Raman mode (*i.e.,* A_u^2) in the Cu^+ ion implanted Bi_2Te_3 thin films was correlated with the implantation-induced defects and the intensity of A_u^2 mode is observed to increase upon Cu^+ implantation. As far as Hall effect and Seebeck measurements are concerned, charge carrier type were converted from *n*-type to *p*-type upon Cu^+ ion implantation, while charge carrier type turned back to *n*-type after annealing. Furthermore, density of ion implantation induced defects was suppressed greatly after annealing, where the results were corroborated with Raman scattering analysis (*i.e.,* reduction in the intensity of A_u^2 mode).

During Cu^+ ion implantation, the energetic Cu^+ ions displace atoms from their lattice site and create large number of atomic scale electrically active displaced atoms. It is recapitulated that the incoming energetic ion loses its energy in a target material through elastic collisions (*i.e.,* nuclear energy loss, S_n) and inelastic electronic excitations (*i.e.,* electronic energy loss, S_e). One can see from the Table 5.1 that the elastic collisions (*i.e.,* nuclear energy loss) were dominating during 300 keV and 700 keV Cu^+ ion irradiation. In the nuclear stopping regime, the materials having low *Z* numbers will exhibit simple binary collisions, where the atomic motion of the incident ion would immediately stop after a few collisions. In contrast, complex many body collisions are seen in the materials having high *Z* number (especially Z > 20), where higher number of recoils atoms will be generated owing to dense collision cascade.

According to the Cheng *et al.,*[235,236], collision cascade comprises of spatially separated localized recoil sub-cascades, where recoil atoms transfer some of their energy to other atoms in the target material that causes the other atoms to move rapidly in a small volume. This create localized short-lived high temperature spike in the target material. Local or spherical thermal spike will be expected in the material, when recoil energy (E_R) is lesser than critical kinetic energy (E_C), which in turn related to the properties of the target (Eqn. 5.1).

$$E_C = 0.03923 \times Z^{2.23} \text{ (eV)} \qquad \textbf{Eqn. 5.1}$$

The local thermal spike will be in spherical shape and termed as spherical thermal spike. In contrast, when the recoil atom satisfies the critical energy (E_{SC}) conditions (Eqn. 5.2), the spherical thermal spikes would overlap and forms cylindrical (or global) thermal spike.

$$E_{SC} = 0.5 \times Z^{2.23} \text{ (eV)} \qquad \textbf{Eqn. 5.2}$$

The values of E_C, E_{SC} for Bi_2Te_3 are evaluated to be 424 eV and 5.4 keV respectively; while E_R values for 300 keV and 700 keV Cu^+ ion implantation in Bi_2Te_3 are estimated to be ~120 eV and ~200 eV respectively. In the present case, one can note that the E_R values are found to be lesser than E_C. Therefore, the spherical thermal spikes are expected to be initiated by 300 and 700 keV Cu^+ ion implantation.

The local temperature during thermal spike will increase up to ~10^4 K that spreads and quenches subsequently within few picoseconds. The resulting liquid-like non-equilibrium state induces the various thermally activated processes[237]. In general,

during ion beam interaction, the spherical thermal spike would initiate throughout the polycrystalline grains. However, spike that occurs in the close proximity of grain boundaries activates the atoms to jump and diffuse across the grain boundary. This causes the grain boundary to coalescence upon Cu^+ ion implantation.

Moreover, the electrically active displaced atoms in Bi_2Te_3 are vacancies (*i.e.,* V_{Bi} and V_{Te}), interstitials (*i.e.,* I_{Bi}, and I_{Te}), and vacancy-interstitial pairs, along with implanted Cu ions. However, vacancies and interstitials were expected to annihilate during the ion implantation, which in turn create high density of defect complexes. The survived stable point defects and defect complexes in addition to implanted Cu atoms are responsible for the observed charge carrier type conversion. It has to be noted that the peak ion damage due to Cu^+ ion implantation were 71 *dpa*, 141 *dpa*, 212 *dpa*, 288 *dpa* for the Cu concentration of 0.5 *at%*, 1 *at%*, 1.5 *at%*, 2 *at%* in Cu^+ ion implanted Bi_2Te_3 thin films respectively. As inferred from Raman scattering analysis, the infusion of a high density of implantation-induced damages would result in the partial formation of amorphous pockets in Cu^+ ion implanted Bi_2Te_3 thin films.

The experimental results indicate that the activation energy for vacancy migration for Te atoms (~0.16 eV)[238] are sufficiently low as compared to that of Bi atoms (~0.3 eV)[239]. Therefore, it is expected that the ion beam implantation may activate the vacancy migration during ion implantation, where migration of V_{Te} may occur promptly than V_{Bi}. Further the recovery of defects may occur *via* recombination. The above mechanism significantly reduces the number of V_{Te}. In addition to that, the interstitials (I_{Bi} and I_{Te}) that produced along with vacancies (V_{Bi} and V_{Te}) are highly mobile, even at liquid nitrogen temperature and interstitials have low migration energy as compared to that of vacancies. The grain boundaries act as an effective trap for these migrating interstitials and hence the fraction of these defects would disappear subsequently.

Hence, Cu^+ ion implantation on Bi_2Te_3 thin films would likely generate high densities of stable V_{Bi}, Cu_{Bi}, in addition to defect complexes. Both V_{Bi} and Cu_{Bi} are acceptor type defects, contributing three and one holes per defect respectively and will increase the density of hole concentration. Hence, the complicated counterbalance between these ion beam induced donor and acceptor type native defects in addition to the implanted atoms and high density of defect complexes altered the type and magnitude of charge carriers, which is responsible for the positive Seebeck coefficient values. The annealing process suppresses the density of defects greatly, which resulted in reduction of hole concentration and subsequently increases the electron concentration.

It is well known that the presence of inverse relationship between *S* and carrier concentration and hence, the observed trend in the values of *S* in the case of Cu^+ ion implanted and annealed Cu^+ ion implanted thin films could be ascribed to their variations in the carrier concentration. Moreover, high σ of the Cu^+ ion implanted films is primarily due to its enhanced carrier concentration and mobility values. The downturns of power factor are mainly due to diminished absolute *S* values in Cu^+ ion implanted Bi_2Te_3 thin films. Hence, the above results suggested that the ion beam assisted Cu^+ ion doping in to Bi_2Te_3 thin films did not enhance the power factor ($S^2\sigma$) due to trade-off relationship between its Seebeck coefficient and electrical conductivity. However, the charge-carrier type conversion is successively achieved in Bi_2Te_3 thin films using Cu^+ ion implantation. This is attributable to the high density of defect complexes. The present experiments suggests that ion implantation can be used for conversion of charge carrier (*n*- to *p*-type) which provide a scope of fabricating TE micro modules that comprises of *p*- and *n*-type semiconductors.

5.5. Conclusion

Bi_2Te_3 thin films were fabricated using PLD deposition method. It is found that the pristine Bi_2Te_3 thin films exhibit *n*-type conductivity due to the abundance of V_{Te}. The Cu^+ ion implantation was carried out to incorporate Cu concentration of 0.5 *at%*, 1 *at%*, 1.5 *at%*, 2 *at%*. The RBS experiment reveals the gradual changes in the elemental composition across the Cu^+ ion implanted Bi_2Te_3 thin films. On the other hand, the power factor was observed to decrease as a function of Cu concentration due to low values of absolute Seebeck coefficient, in contrast to the electrical conductivity values. However, the Hall-effect and Seebeck coefficient measurements help to obtain the interesting result of *n*-type to *p*-type charge carrier conversion as a function of Cu concentration. The *p*-type conductivity of Cu-doped Bi_2Te_3 is ascribed to high density of acceptor type V_{Bi} and Cu_{Bi} defects, in addition to the defect complexes. In contrast to that, the *n*-type to *p*-type carrier inversions are not observed in annealed Cu^+ ion implanted Bi_2Te_3 thin films. This observation indicates the possibility of fabricating TE micro modules and micro devices by manipulating the charge carrier type with Cu concentration.

Chapter 6

Role of inert gas ion irradiation effects in thermoelectric properties of bismuth telluride thin films.

6.1. Introduction

As mentioned in the previous chapter, *n*- to *p*- type charge carrier conversion was observed in Cu^+ ion implanted Bi_2Te_3 thin films and these charge carrier conversion was attributable to the implanted Cu atoms along with defects and defect complexes. However, followed by defect annealing, these Bi_2Te_3 thin films no longer exhibit above-observed charge carrier conversion. Therefore, it is essential to understand the contribution of defects in TE transport properties of Bi_2Te_3 thin films. In that regard, inert gas ions irradiation was employed to include substantial amount of defects in the Bi_2Te_3 thin films.

Depending on the mass and energy of the implanted ions[201,240], different amount of energy will be deposited in the material and this generates wide range of damage in the material. In case of light ions, the displacement cascades will be linear and thus have only isolated point defects such as vacancies and interstitials. In contrast, for heavy ions, displacement cascade consist of extended defects such as defect clusters and dislocation loops. Enhanced TE materials were reported in materials by effectively manipulating intrinsic point defects [63–67]. Intrinsic point defects such as vacancies and interstitials play an important role in optimizing TE transport properties. Zhu *et al.*,[28] reported the formation, control, and evolution of intrinsic point defects in the Bi_2Te_3 based compounds. The above report pointed out that the intrinsic defects could be actively controlled *via* doping and also through composition, mechanical, and thermal treatment at various stages of material synthesis.

Most importantly, using hot deformation method, antisite and donor like effects were successfully tuned in $(Bi, Sb)_2(Te, Se)_3$ solid solutions[59] and high *ZT* value of around ~1.3 were achieved at 380 K. Wang *et al.,*[76] controlled and achieved better TE transport properties of nanostructured Bi_2Te_3 using intrinsic defects *via* spark plasma sintering technique. Recently, the evolution of intrinsic point defects in *n*-type Bi_2Te_3 based TE materials were systematically investigated using sintering process and reported by Zhang *et al.,*[29]. Sintering aided the formation of donor type vacancies in the Bi_2Te_3 and eventually increases the electron concentration. It is important to point out that the

above reports use equilibrium processes (*i.e.*, sintering and hot deformation technique) to tune the amount of point defects in the material.

Out of few reports, intrinsic point defects that were introduced through non-equilibrium process by Suh *et al.*,[77] to enhance both seebeck coefficient and electrical conductivity values simultaneously. It has to be noted that these native point defects were generated in Bi_2Te_3 thin films using 3 MeV He^{2+} ion irradiation. The above technique helps to decouple the trade off relationship between above mentioned TE transport parameters, since the defects act as electron donor and energy filters at the same time. In addition, the 400 keV Ne^+ ion radiation effects in TE transport properties of Bi_2Te_3 and Sb_2Te_3 thin films were investigated by Fu *et al.,*[78]. While comparing with the former study, Ne^+ ions were heavier than He^{2+} ions and were known to create more damage, which eventually induced defect recovery. This process enhances the crystallization and causes reorientation in Bi_2Te_3 thin films. Furthermore, the above reports reported the positive impacts on the TE transport properties of Bi_2Te_3 thin films.

In the present chapter, low energy inert gas (such as He^+ and Ar^+ ion) irradiation were carried out in Bi_2Te_3 thin films to understand the role of defects in TE transport properties. In addition to that, the morphological, structural, vibrational, and TE transport properties are investigated systematically.

6.2. Experimental methods

6.2.1. Sample synthesis

Bi_2Te_3 thin films were deposited on the quartz substrate using pulsed laser deposition method. The details of the deposition procedure were explained in the chapter 5. Ion irradiation experiments were carried out using 150 kV ion accelerator. The base pressure in the irradiation chamber was maintained at $\sim 1\times10^{-7}$ mbar. In order to avoid ion beam heating, the beam current density was kept ~1 μA/cm^2 on the sample. Bi_2Te_3 thin film samples were irradiated 120 keV He^+ and Ar^+ ions. The sample temperature during ion irradiation was room temperature and the ion fluences were varying from 5×10^{14} ions/cm^2 to 1×10^{16} ions/cm^2.

SRIM2006 code[130] was performed to obtain ion irradiation parameters and the values are tabulated in Table 6.1. For SRIM calculations, displacement energy was fixed to 25 eV for all elements in Bi_2Te_3 thin films as given in the report[78].

Table 6.1: Details of inert gas ion irradiations in Bi_2Te_3, carried out in the present work.

Ion	Mean projected range ± straggling (nm)	S_e (eV/nm)	S_n(eV/nm)	Sputtering yield (atoms/ion)	Ion fluence (ions/cm^2)	Peak damage (*dpa*)
120 keV He^+	507 ±175	232.3	2.759	0.013	5×10^{14}	0.013
					1×10^{15}	0.027
					5×10^{15}	0.13
					1×10^{16}	0.27
120 keV Ar^+	94 ±50	304.6	421.2	4.907	5×10^{14}	1.56
					1×10^{15}	3.12
					5×10^{15}	15.62
					1×10^{16}	31.27

6.2.2. Characterization technique

The phase composition of the pristine and ion irradiated Bi_2Te_3 thin films were characterized using grazing incidence X-ray diffraction (GIXRD, Inel Equinox 2000) using Cu K_α radiation. The angle of incidence was kept at 1° and the depth probed by X-rays in Bi_2Te_3 at this angle is 800 nm. The morphology of all ion irradiated samples were characterized using focused ion beam field emission scanning electron microscope (FIB-FESEM, zeiss, crossbeam 340). FIB-FESEM was operating at an accelerating voltage of 5 kV with the working distance of ~3 mm. The images were recorded using in-lens detector. In addition, the surface topography of the pristine and irradiated Bi_2Te_3 thin films were examined further by atomic force microscopy (WiTec Alpha RA 300) under tapping mode. The changes in the vibrational modes of the thin films upon ion irradiation were investigated using micro Raman spectrometer (WiTec Alpha RA 300) using Nd-YAG laser having excitation wavelength of 532 nm and laser power of 0.5 mW.

The room temperature Hall-effect measurements (Ecopia HMS 5000) were measured under Vander-pauw configuration at the magnetic field of 0.57 Tesla. The temperature dependent in-plane Seebeck coefficient and electrical conductivity of the films were carried out using bridge method[159] and DC four probe method respectively.

6.3. Results

6.3.1. GIXRD studies

Figure 6.1 shows the GIXRD pattern of pristine and 120 keV He^+ ion irradiated Bi_2Te_3 thin films for different ion fluences. All the diffraction peaks were found match with rhombohedral structure of Bi_2Te_3 crystal (JCPDS 01-080-6959) and are labeled

accordingly. It has been observed that all samples are exhibiting polycrystalline nature and there were no significant changes in the diffraction pattern upon He^+ ion irradiation.

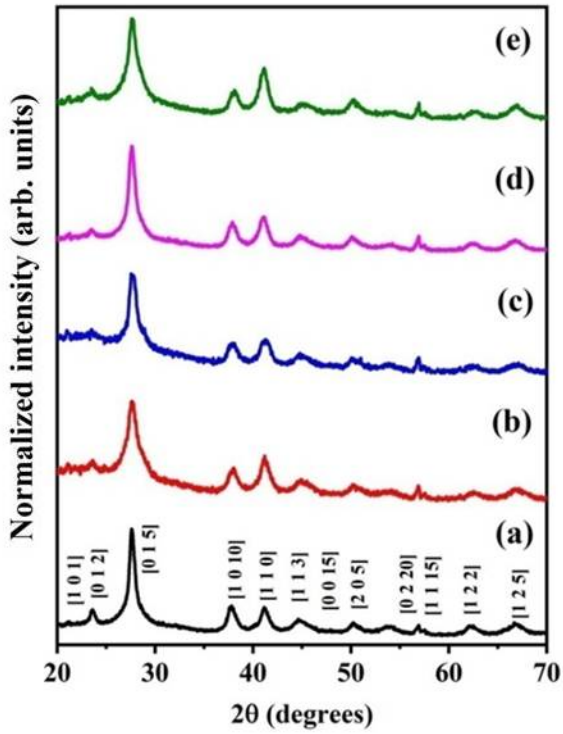

Figure 6.1: GIXRD pattern of (a) the pristine and 120 keV He^+ ion irradiated Bi_2Te_3 thin films for various ion fluences of (b) 5×10^{14}, (c) 1×10^{15}, (d) 5×10^{15},and (e) 1×10^{16} ions/cm^2 respectively.

The average crystallite size was estimated using Scherrer formula and the value is estimated to ~10.6 nm for pristine Bi_2Te_3 thin film. As far as He^+ ion irradiation is concerned, average crystallite size was varied between ~11 nm to ~9 nm in the irradiated thin films (Figure 6.2).

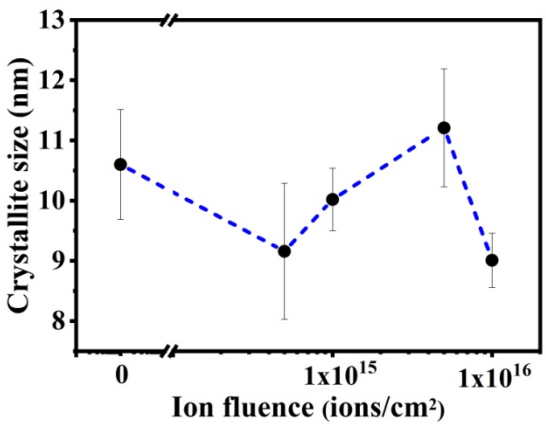

Figure 6.2: Average crystallite size of pristine and 120 keV He^+ ion irradiated Bi_2Te_3 thin films for different ion fluences .Dotted line is guide to the eye.

It has to be pointed out that the variation in the average crystallite size did not have any trend. Because, these inconsistencies in the average crystallite size is assignable to the inherent nature of Bi_2Te_3 thin films during deposition process and they are not ascribed to the He^+ ion irradiation process.

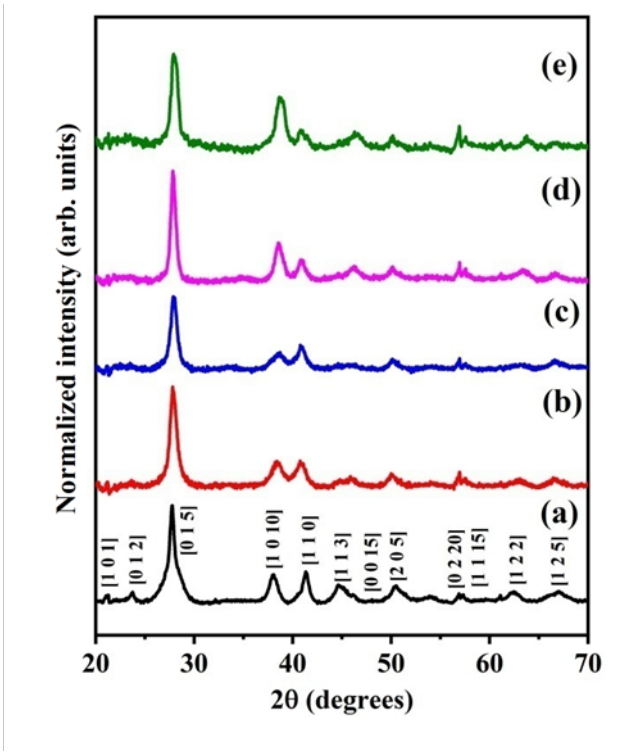

Figure 6.3: GIXRD pattern of (a) pristine and 120 keV Ar^+ ion irradiated Bi_2Te_3 thin films for the ion fluences of (b) 5×10^{14}, (c) 1×10^{15}, (d) 5×10^{15}, and (e) 1×10^{16} ions/cm^2 respectively.

Figure 6.3 displays the GIXRD pattern of the pristine and 120 keV Ar^+ ion irradiated Bi_2Te_3 thin films. From the Figure 6.3 (b) - Figure 6.3 (e), it is observed that the diffraction peaks corresponding to the irradiated thin films remain consistent with that of the pristine Bi_2Te_3 thin films (Figure 6.3 (a)). In addition to that, the signatures of phase segregation and amorphization were not identified in the ion irradiated Bi_2Te_3 thin films. However, upon Ar^+ ion irradiation, the relative intensity of various planes such as [1 0 1], [0 1 2], [1 1 0], [2 0 5], [1 2 2], and [1 2 5] with respect to that of most prominent plane [0 1 5] had been reduced considerably.

Figure 6.4 shows the variation in the average crystallite size of Bi_2Te_3 thin films as a function of 120 keV Ar^+ ion fluences. The average crystallite size in the pristine Bi_2Te_3 thin film is ~10.6 nm. It is clear that the average crystallite value decreases significantly to ~6.8 nm until the ion fluence of about 1×10^{15} ions/cm^2 and then improved eventually to the value of ~8.7 nm.

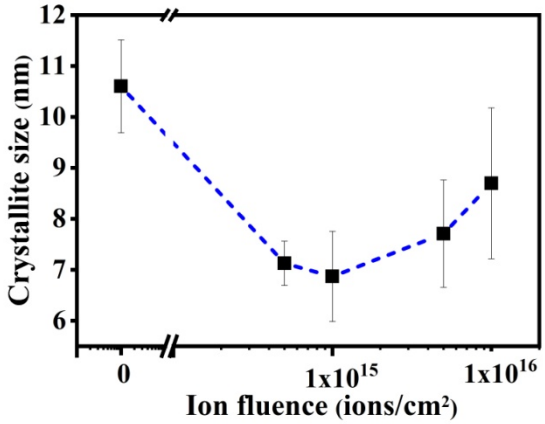

Figure 6.4: Variation in the average crystallite size as a function of 120 keV Ar^+ ion fluences. The dotted line is the guide to the eye.

6.3.2. Morphological analysis

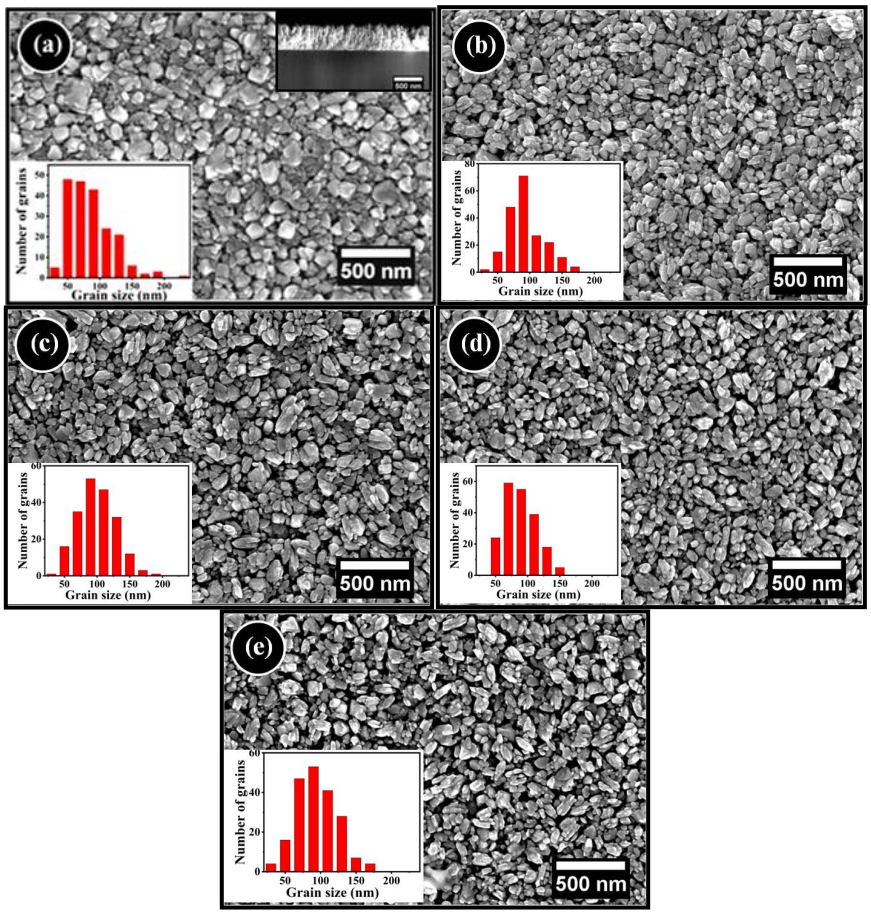

Figure 6.5: FESEM image of (a) pristine and 120 keV He^+ ion irradiated Bi_2Te_3 thin films for various ion fluences of (b) 5×10^{14}, (c) 1×10^{15}, (d) 5×10^{15}, and (e) 1×10^{16} ions/cm^2 respectively.

FESEM images obtained from the pristine and 120 keV He^+ ion irradiated Bi_2Te_3 thin films are displayed in Figure 6.5. As shown in the inset of Figure 6.5 (a), cross-sectional FESEM image of pristine Bi_2Te_3 films estimate that the thickness of the

deposited films are around ~400 nm. Further, grains sizes were analyzed using ImageJ software[198]. The grain size distribution is plotted and is shown in the inset of Figure 6.5. Figure 6.5 (a) clearly shows that the pristine Bi_2Te_3 thin films contain widely varying oddly shaped multi-faceted grains, where the grain sizes were varying from 30 nm to 230 nm. The mean grain size in the pristine thin film is estimated to be 85±34 nm (inset of Figure 6.5 (a)).

Figure 6.5 (b) to Figure 6.5 (e) shows the corresponding morphology of Bi_2Te_3 thin films irradiated for He^+ ion fluences of 5×10^{14} ions/cm^2, 1×10^{15} ions/cm^2, 5×10^{15} ions/cm^2, 1×10^{16} ions/cm^2 and the mean grain sizes were found to be 92.3±28 nm, 93.1±29 nm, 88.4±25.2 nm, and 92.2±28 nm (inset of Figure 6.5 (b) to Figure 6.5 (e)) respectively. It is clear that the He^+ ion irradiation did not affect the morphology of Bi_2Te_3 thin films significantly, since there were no noteworthy changes in the shape and sizes of multi-faceted grains after ion irradiation.

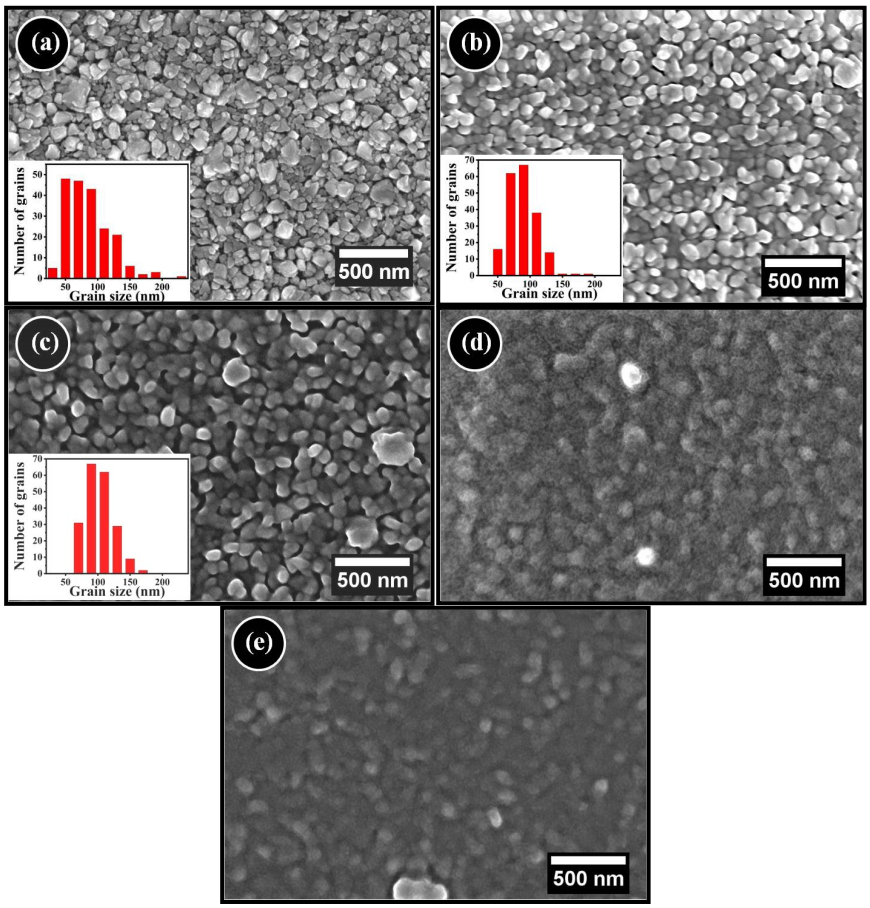

Figure 6.6: FESEM image of (a) pristine and 120 keV Ar^+ ion irradiated Bi_2Te_3 thin films for different ion fluences of (b) 5×10^{14}, (c) 1×10^{15}, (d) 5×10^{15}, and (e) 1×10^{16} ions/cm^2 respectively.

This is because, during 120 keV He^+ ion irradiation, energy loss due to inelastic electronic excitations (S_e = 232.3 eV/nm) is dominated over the elastic collisions (S_n = 2.759 eV/nm) (refer Table 6.1). According to the thermal spike model[131,241–243], incoming energetic ion deposits its huge amount of energy to the electronic sub system, which in turn transferred to the lattice through electron-phonon interaction. This will increase the local lattice temperature and subsequently resulted in local lattice melting. However, in this case, being a lighter ion, the energy deposited by He^+ ion is not sufficient for local lattice melting, which would resulted in non-melting thermal spikes[244]. It has to be mentioned that non-melting thermal spikes would create only simple point defects such as vacancies and interstitials, which would left the morphology of the Bi_2Te_3 thin films unaffected.

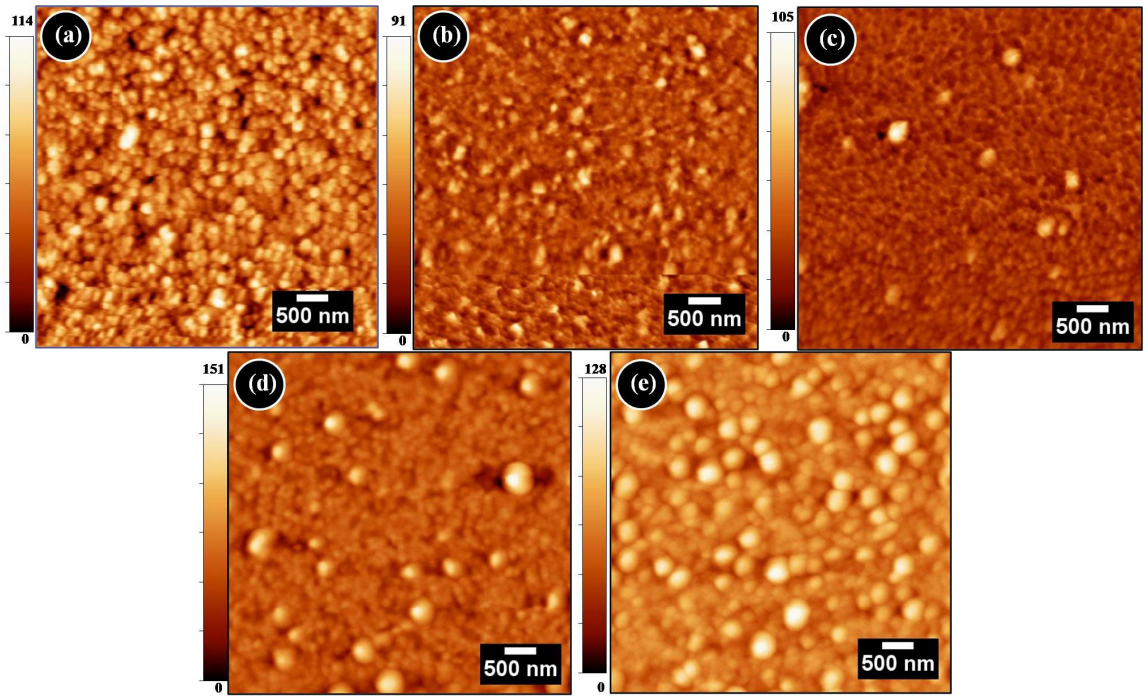

Figure 6.7: AFM image of (a) pristine and 120 keV Ar^+ ion irradiated Bi_2Te_3 thin films for different ion fluences of (b) 5×10^{14}, (c) 1×10^{15}, (d) 5×10^{15}, and (e) 1×10^{16} ions/cm^2 respectively. The area of the scanned images are 5μm×5μm.

Figure 6.6 shows the evolution of surface morphology of Bi_2Te_3 thin a film upon 120 keV Ar^+ ion irradiation and the inset shows the grain size distributions. Unlike the case of He^+ ion irradiation, there are changes in the grain size of Bi_2Te_3 thin films upon 120 keV Ar^+ ion irradiation. The mean grain size in the pristine thin film is 85±34 nm, while the mean grain size of Bi_2Te_3 thin films irradiated for Ar^+ ion fluences of 5×10^{14} ions/cm^2 and 1×10^{15} ions/cm^2 were estimated to be 88.6±22.5 nm, and 102.3±21 nm respectively.

Furthermore, at higher ion fluences, the grains have lost the contrast and could not able to find the grain size distribution. One could conclude from the grain size distributions that the smaller size grains were disappeared after Ar^+ ion irradiation. In addition to that, as compared with the pristine thin films, grains were observed to be melted and fused after irradiation. This result suggested the increase in mean grain size upon irradiation, which could be attributed to the grain coalescence.

The AFM images predict the clear picture of surface topography in nanoscale dimensions. Figure 6.7 shows the AFM images (2D view) of the pristine and 120 keV Ar^+ ion irradiated Bi_2Te_3 thin films. The pristine Bi_2Te_3 thin film exhibits granular and dense grain structures (Figure 6.7 (a)), while coalesced grain as well as grain growth are observed in 120 keV Ar^+ ion irradiated Bi_2Te_3 thin films (Figure 6.7 (b) to Figure 6.7 (e)). Furthermore, AFM images were analyzed using Wsxm software[155] and the systematic variation in the grain size and surface roughness is displayed in Figure 6.8.

As far as grain size is concerned, the average grain size of the pristine Bi_2Te_3 thin film is ~174.4±21 nm, while slight variation in the average grain size is observed until the ion fluence of 1×10^{15} ions/cm^2. Moreover at higher ion fluences, grain size is observed to increase to the value of ~277.2±58 nm (at the ion fluence of 1×10^{16} ions/cm^2). It has to be noted that in case of Ar^+ ion irradiation, the values of S_e and S_n are estimated to be 304 eV/nm and 421 eV/nm respectively (refer Table 6.1). Both atomic collisions and electronic excitations are expected to contribute to the above-mentioned morphological deformations. Momir *et al.,*[245] pointed out the difference between the contribution of nuclear energy loss and electronic energy loss effects in Ar^+ ion and Xe^+ ion irradiated AlN/TiN system. Further, it has to be mentioned that model of grain growth under ion irradiation was shown by Kaoumi *et al.*[237].

Electronic excitations thermalize the target lattice through electron-phonon interactions. Therefore, the thermal spikes are expected to increase the local lattice temperature over the target melting point and subsequently induce the local melting. Being a heavier ion, temperature induced by the Ar^+ ion is much higher and the thermal spike would last longer than that of He^+ ions, eventually leads to grain melting. The thermal spike would last for few pico-seconds and annealed rapidly. Meanwhile atomic collisions are suggested to improve atomic mobility and atomic jumps across the grain boundaries. The above processes lead grain growth at the expense of others[246–249]. Overall, grain melting and grain coalescences are the combined processes during Ar^+ ion irradiation, which concurrently increases the mean grain size and eventually resulted in fused grains.

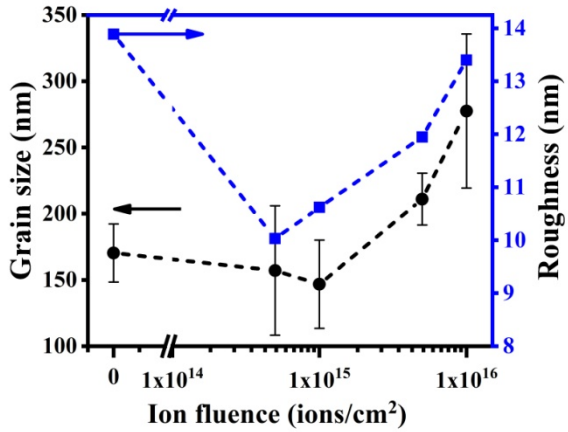

Figure 6.8: Variation in grain size and roughness as a function of different 120 keV Ar^+ ion fluences.Dotted lines are the guide to the eye.

Moreover, from Figure 6.8, the rms roughness of the pristine Bi_2Te_3 thin film is estimated to be ~13.8 nm, while the value significantly decreases to ~10 nm until the ion fluence of 5×10^{14} ions/cm^2 and then eventually increased to ~13.4 nm at higher ion fluences. According to the reports[250–252], irradiation induced smoothening and roughening are two competing factors during ion irradiation. At low ion fluences, smoothening or decrease in roughness value was ascribed to grain melting and grain coalescences. Using SRIM, the sputtering yield is estimated to the value of ~4.9 atoms/ion. Hence, one can expect that the sputtering process could play the dominant role to roughen the thin films especially at higher ion fluences.

6.3.3. Raman scattering analysis

Figure 6.9 shows the Raman spectra of pristine and 120 keV He^+ ion irradiated Bi_2Te_3 thin films. From Figure 6.9, it is seen that all samples are showing two Raman active modes (*i.e.,* E_g^2 and A_g^2) and one Raman inactive/IR active mode (*i.e.,* A_u^2). It has to be recapitulated that E_g^2 mode is in-plane vibrational mode, while A_g^2 and $A_u^2$are out-of-plane vibrational modes. In the pristine Bi_2Te_3 thin film (Figure 6.9(a)), E_g^2 and A_g^2mode were identified at ~101.3 cm^{-1} and ~132.2 cm^{-1} respectively, while A_u^2 mode was assigned at ~121.3 cm^{-1}.

As pointed out in the previous chapters, the activation of out-of-plane Raman inactive/IR active vibrational mode (*i.e.,* A_u^2) in the pristine Bi_2Te_3 thin films is attributed to the breakdown of translational symmetry in the sample, due to presence of intrinsic lattice disorder in the grain boundaries and thin film surfaces, created during deposition processes[156,157]. Furthermore, from Figure 6.9, the intensities, peak position, and

FWHM (Full width at half maximum) of Raman vibrational modes were found to be change with He^+ ion fluences.

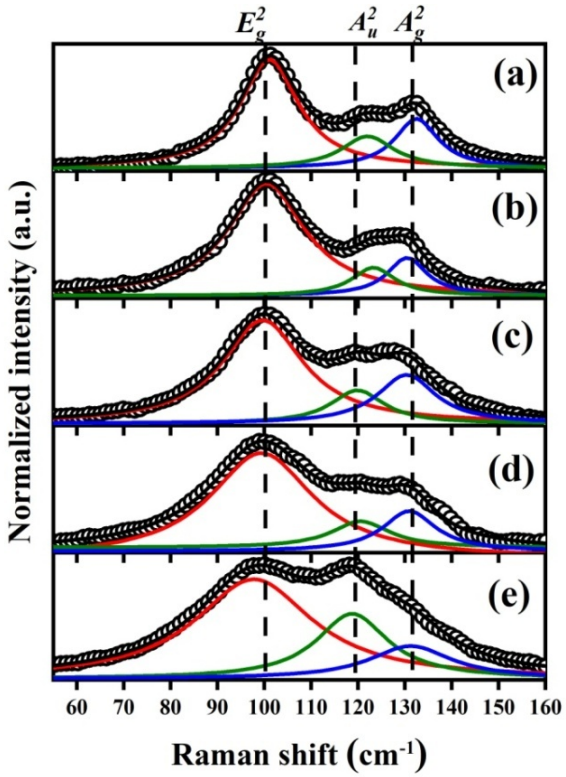

Figure 6.9: Raman spectra of (a) pristine and 120 keV He^+ ion irradiated Bi_2Te_3 thin films for various ion fluences of (b) 5×10^{14}, (c) 1×10^{15}, (d) 5×10^{15}, and (e) 1×10^{16} ions/cm^2 respectively.

Compared to the pristine Bi_2Te_3 thin film, intensity of the A_u^2 mode was seen to increase gradually upon He^+ ion irradiation. The increase in the intensity of A_u^2 mode is associated with introduction of He^+ ion irradiation induced defects. The ion irradiation induced defects create the local lattice disorders in the Bi_2Te_3 crystal. Because of this, the zone centre selection rule will be relaxed and the Raman inactive/IR active vibrational mode will get activated[209].

Figure 6.10 (a) and Figure 6.10 (b) show the variation in the peak position and FWHM of Raman modes of Bi_2Te_3 thin films upon He^+ ion irradiation. The red shift in Raman modes is observed (Figure 6.10 (a)). This indicates the generation of strain in the Bi_2Te_3 crystal lattices during ion irradiation, which arises due to displacement of atoms from its equilibrium positions. In addition to that, FWHM of the Raman vibrational modes (Figure 6.10 (b)) were observed to be increase upon He^+ ion fluences. This is directly correlated to the irradiation induced defect accumulation in the He^+ ion irradiated Bi_2Te_3 thin films.

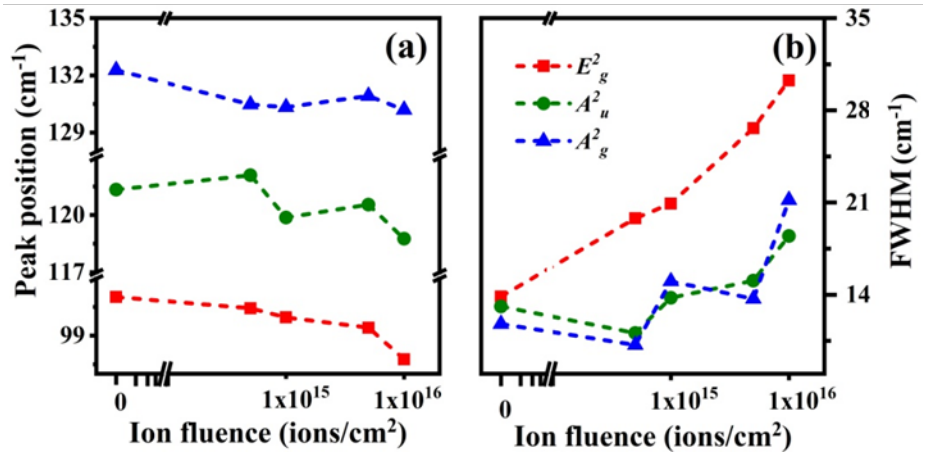

Figure 6.10: Variation in (a) peak position and (b) FWHM of the Raman modes of 120 keV He^+ ion irradiated Bi_2Te_3 thin films for various ion fluences.

Figure 6.11 shows the Raman spectra of the pristine and 120 keV Ar^+ ion irradiated Bi_2Te_3 thin films for various ion fluences. As compared with the pristine Bi_2Te_3 thin film, Raman active (E_g^2 and A_g^2) and Raman inactive/IR active (A_u^2) vibrational modes peak position, intensity, and FWHM were varied upon 120 keV Ar^+ ion irradiation.

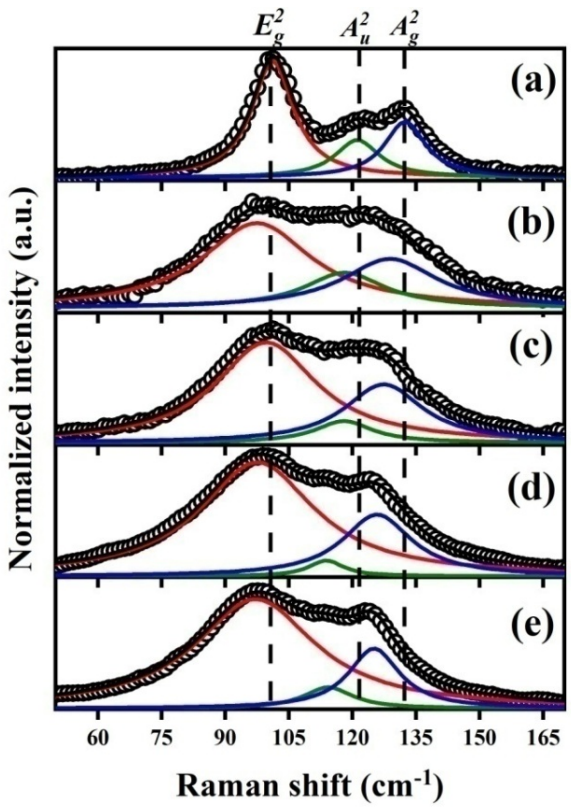

Figure 6.11: Raman spectra of (a) pristine and 120 keV Ar^+ ion irradiated Bi_2Te_3 thin films for various ion fluences of (b) 5×10^{14}, (c) 1×10^{15}, (d) 5×10^{15}, and (e) 1×10^{16} ions/cm^2 respectively.

From Figure 6.11, one can see the gradual decrease in the intensity of Raman inactive/IR active vibrational mode (A_u^2) in accordance with Ar^+ ion fluences. As discussed above, irradiation induced melting and annealing effect were observed in Ar^+ ion irradiated Bi_2Te_3 thin films, which were suggested to reduce defects in the thin film considerably and in turn resulted in the diminished intensity of forbidden mode (*i.e.,* A_u^2) in the Raman spectra. The systematic variation in the peak position and FWHM of Raman modes as a function of Ar^+ ion fluences are displayed in Figure 6.12.

It is observed that in Ar^+ ion irradiated thin films, Raman peaks shift towards lower wavenumber in accordance with Ar^+ ion fluences (Figure 6.12 (a)). One could associate red shift in Raman mode with irradiation induced strain in the samples.

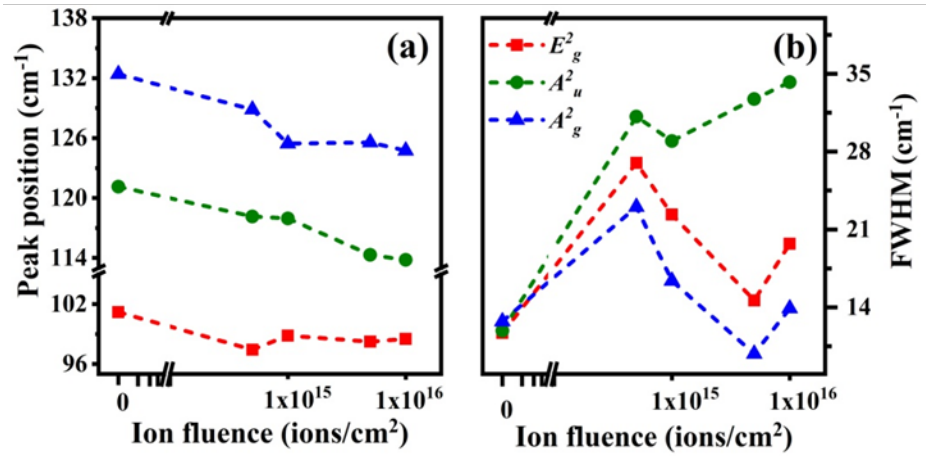

Figure 6.12: Variation in peak position and (b) FWHM of the Raman modes of 120 keV Ar^+ ion irradiated Bi_2Te_3 thin films for various ion fluences.

In addition to that, Figure 6.12 (b) shows the broadening of Raman peaks at low ion fluences, while FWHM of Raman peaks were found to decrease at high ion fluence. At higher ion fluences, reduction in FWHM of Raman peak are ascribed to irradiation induced melting and annealing effect, where ion irradiation induced defects are expected to anneal out at grain boundaries

6.3.4. Thermoelectric transport properties

Temperature dependent Seebeck coefficient (*S*) for pristine, 120 keV He^+ and 120 keV Ar^+ ion irradiated Bi_2Te_3 thin films for various ion fluences are presented in Figure 6.13 (a, d).

Pristine and Ar^+ ion irradiated Bi_2Te_3 thin films are exhibiting negative *S* values in the measured temperature range (300 K to 410 K) as they indicate *n*-type conductivity, while He^+ irradiated Bi_2Te_3 thin films are showing positive *S* values. The results suggest

that the majority carriers in the pristine and Ar^+ ion irradiated thin film are dominated by electrons, whereas majority carriers in the He^+ ion irradiated thin films are holes.

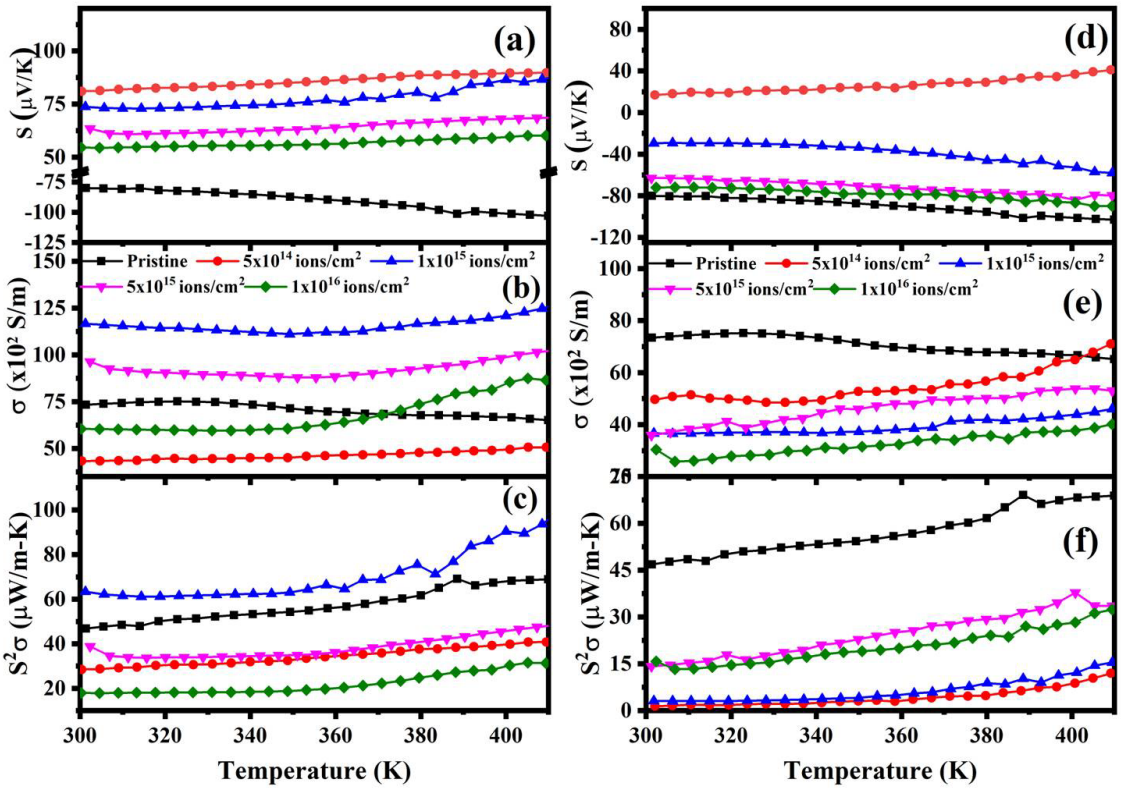

Figure 6.13: Temperature dependent TE transport properties: (a, d) Seebeck coefficient (S), (b, e) electrical conductivity (σ), and (c, f) power factor($S^2\sigma$) of the pristine, 120 keV He^+ and 120 keV Ar^+ ion irradiated Bi_2Te_3 thin films respectively for various ion fluences.

As mentioned in the previous chapters, the crossover behavior on the sign of S is ascribed to the bipolar conductivity, where the contribution of electron and hole conductivity is indulged separately. The net value of the S for the solid having bipolar conduction can be written as the weighted average of electron and hole Seebeck coefficient (S_{el} and S_{ho}) along with their electrical conductivities (σ_{el} and σ_{ho}). Therefore, one can expect that the complicated counterbalance of the electron and hole charge carrier density in the sample gives the net S values, which are varying from positive and negative values.

Temperature dependent variation in electrical conductivity (σ) of pristine, 120 keV He^+ and 120 keV Ar^+ ion irradiated Bi_2Te_3 thin films for various ion fluences are displayed in Figure 6.13 (b, e). The trend shows that the σ value increases with temperature and portrays typical semiconductor behavior. Using the above results, temperature dependent power factor ($S^2\sigma$) for pristine, 120 keV He^+ and 120 keV Ar^+ ion

irradiated Bi_2Te_3 thin films for various ion fluences are calculated and are presented in Figure 6.13 (c, f). It is shown that the maximum value of power factor was exhibited in He^+ ion irradiated Bi_2Te_3 thin film irradiated to an ion fluence of 1×10^{15} ions/cm^{2}and the value is found to be ~6.3 μW/m-K^2. The variation in TE transport properties can be understood in terms of carrier concentration and Hall mobility.

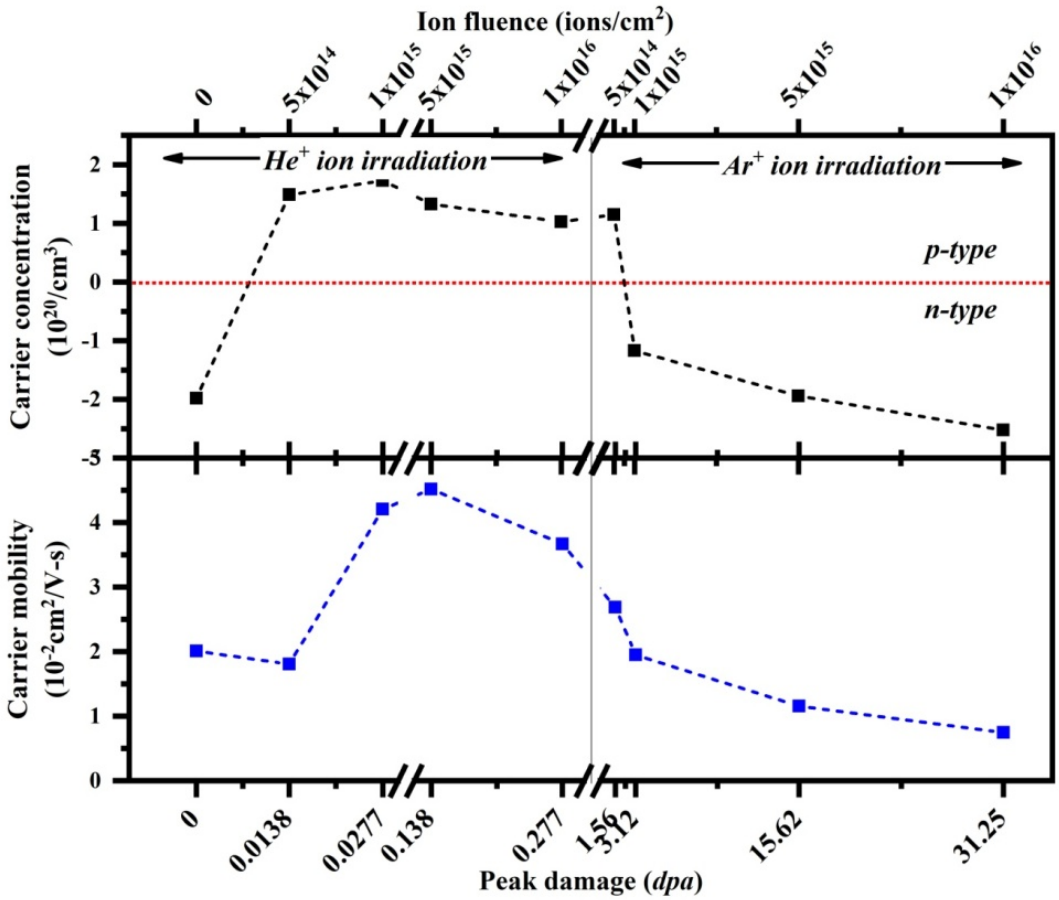

Figure 6.14: Variation in the carrier concentration and mobility as a function of peak damages (dpa) and as a function of the corresponding 120 keV He^+ and 120 keV Ar^+ ion fluences. The dotted lines are the guide to the eye.

Hall-effect measurements (Figure 6.144) at room temperature confirm the *n*-type conductivity of pristine Bi_2Te_3 thin film, indicating majority charge carriers are electrons. The charge carrier type conversion (*n*-type to *p*-type) is observed upon 120 keV He^+ ion irradiation. Furthermore, charge carrier type again turned back to *n*-type after 120 keV Ar^+ ion irradiation, which is in concordant with the above results. It is recapitulated that the *n*-type conductivity of pristine Bi_2Te_3 thin film[165,253] was ascribed to the presence of doubly ionized donor type V_{Te}. The V_{Te} were generated during thin film deposition processes owing to the low vapour pressure of Te atoms. The charge carrier type

conversion and changes in the charge carrier concentration were associated with the type and amount of defects that were created during the course of ion irradiation.

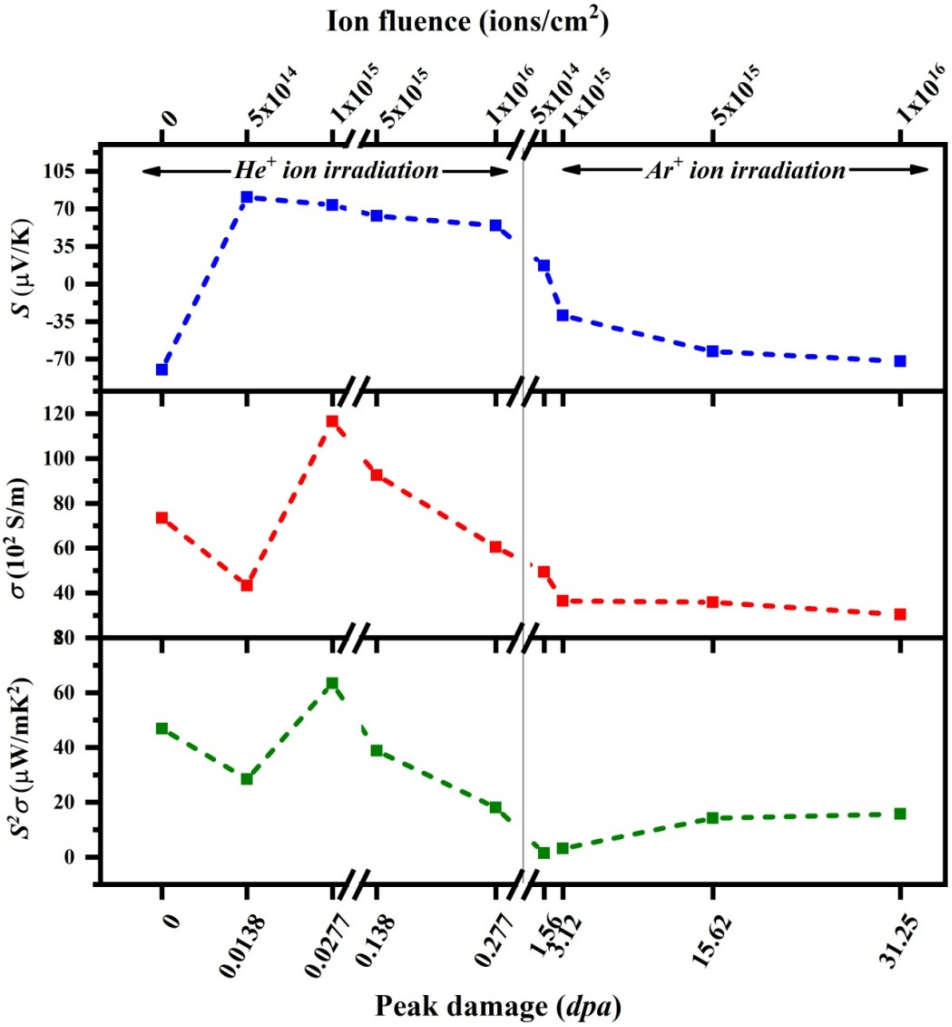

Figure 6.15: TE transport properties at room temperature as a function of peak dpa values and as a function of the corresponding 120 keV He^+ and 120 keV Ar^+ ion fluences. The dotted lines are the guide to the eye.

As inferred from Table 6.1, the amount of peak radiation damage produced by the 120 keV He^+ and 120 keV Ar^+ ions for various ion fluences were quantified through 'displacements per atom' (*dpa*). For He^+ ion irradiation, the peak damage was varied from 0.013 *dpa* to 0.27 *dpa*, whereas in case of Ar^+ ion irradiation, peak damage was varied from 1.56 *dpa* to 31.27 *dpa*. The carrier concentration and mobility values (see Figure 6.14) at room temperature were plotted against peak damage (*dpa*) as well as against He^+ and Ar^+ ion fluences. The carrier concentration at room temperature for pristine Bi_2Te_3 thin film is ~1.8×10^{20} /cm^3. The charge carrier type was observed to be switches from *n*-type to *p*-type upon He^+ ion irradiation. At the same time, carrier concentration improved

from ~1.5×10^{20} /cm^3 to ~1.7×10^{20} /cm^3 at low He^+ ion fluences and subsequently decreased at higher He^+ ion fluences. The results indicate that the acceptor type of defects could be infused during He^+ ion irradiation, which ultimately resulted in the charge carrier type conversion and their variation in concentration in the Bi_2Te_3 thin films. In addition, as discussed above, during Ar^+ ion irradiation, defect recovery due to grain melting and rapid annealing are expected, which resulted in upturning of charge carrier type (*i.e.,* to *n*-type) especially at the Ar^+ ion fluence of 1×10^{15} ions/cm^2 and the electron concentration was observed to improve sequentially up to ~2.5×10^{20} /cm^3 during the course of ion irradiation.

On the other hand, the mobility of the pristine Bi_2Te_3 thin film is ~2.0 cm^2/Vs and the values are observed to increase remarkably until intermediate damage (*i.e.,* at 0.14 *dpa*) and then steadily decreases. The surface conduction plays a significant role in conductivity and hence mobility of the pristine thin film. In case of ion irradiated samples, ion irradiation introduce more charge carriers (or defects) in the bulk and contribution of bulk conductivity would come into play that consequently improves the mobility of the thin films especially at low damage range (*i.e.*, low *dpa* values)[77]. On contrary, at high damage (*i.e.,* at high *dpa* values), irradiation-induced roughness (as inferred from AFM experiment) affected the mobility of the Bi_2Te_3 thin films negatively.

The variation in room temperature S, σ, and $S^2\sigma$ values were plotted against peak damage (*dpa*) as well as against He^+ and Ar^+ ion fluences and is displayed in Figure 6.15. In case of pristine thin film, S value at 300 K is around -79.8 μV/K. Further, the S values for the doses of 0.013 *dpa*, 0.027 *dpa*, 0.13 *dpa*, 0.27 *dpa* (in case of He^+ ion irradiation) are found to be ~81 μV/K, ~73.7 μV/K, ~63.4 μV/K, and ~54.5 μV/K respectively. It is well-known that the existence of inverse relationship between S values and carrier concentration values. Hence, the down turn of S values upon He^+ ion irradiation might be ascribing to the increase in the hole concentration.

On the other hand, for Ar^+ ion irradiation, the room temperature S values for the doses of 1.5 *dpa*, 3.1 *dpa*, 15.6 *dpa*, 31.2 *dpa* are found to be around -17 μV/K, -29.3 μV/K, -62.8 μV/K, and -72 μV/K respectively. The observed trend may be arises from suppression of hole concentration due to irradiation induced defect recovery upon Ar^+ ion irradiation. The room temperature σ values increases from ~63.6×10^2 S/m (for pristine sample) to ~116.6×10^2 S/m until the peak damage of 0.023 *dpa* and then eventually decreases to the value of ~30.4×10^2 S/m at 31.2 *dpa*. The observed high σ values of the films are attributed to the enhanced carrier concentration and mobility values. This is because σ values are directly proportional to carrier concentration and

mobility values. Therefore, the downturns of σ values are corresponding to the diminished carrier concentration and mobility values. Furthermore, the maximum power factor (~6.3 μW/m-K^2) at room temperature was achieved in Bi_2Te_3 thin films having peak damage of 0.023 *dpa* values (or ion fluence of 1×10^{15} ions/cm^2), which were irradiated using 120 keV He^+ ions.

6.4. Discussion

From FESEM investigations, the grainy and polycrystalline nature of the Bi_2Te_3 thin films was seen to be preserved upon the He^+ ion irradiation. In contrast, melted and coalesced grains were observed upon Ar^+ ion irradiation. On the other hand, Hall-effect and Seebeck coefficient measurements confirmed the charge carrier type conversion (*n*-type to *p*-type) upon He^+ ion irradiation and maximum value of *S* (~81 μV/K) and power factor (~6.3 μW/m-K^2) were achieved for the He^+ ion fluence of 1×10^{15} ions/cm^2. Furthermore, charge carrier type again turned back to *n*-type after 120 keV Ar^+ ion irradiation. In order to explain the observed charge carrier type conversion, it is necessary to understand the mechanism of defect generation during ion irradiation.

Mechanism underlying irradiation induced damage is solely ascribed to energy transfer of incoming energetic ion to the atomic structure, which results in the displacement of target atoms from their lattice sites and defects being produced *via* atomic or displacement collision cascades. The atomic collision cascade create large number of electrically active point defects such as vacancies (*i.e.,* V_{Bi}, V_{Te}), interstitials (*i.e.,* I_{Bi}, I_{Te}), and defect clusters in the material. However, the probability of annihilation of vacancies and interstitials is large and hence the survived point defects and defect cluster in the material is expected to alter the TE transport properties. Being a lighter ion, linear collision cascade are expected in case of He^+ ion irradiation, which would infuse simple type of point defects in the material. This could be corroborated with the Raman scattering results, where the activation of the forbidden (*i.e.,* A_u^2) mode is associated with irradiation-induced defects and the intensity of A_u^2 mode is observed to be increase upon He^+ ion fluences in He^+ ion irradiated Bi_2Te_3 thin films.

Furthermore, it is important to recapitulate that the interstitials (*i.e.,* I_{Bi}, and I_{Te}) and tellurium vacancies (*i.e.,* V_{Te}) are having low migration energy[238,239], migrate faster than the bismuth vacancies (*i.e.,* V_{Bi}) towards grain boundaries and get annihilated. The bismuth vacancies (*i.e.,* V_{Bi}) are acceptor type defect which would contribute three holes per defect[254]. The V_{Bi} were found to increase hole density and thus expected to be

responsible for the positive value of *S*. Accordingly, increase in hole concentration upon He^+ ion fluences affected the *S* values negatively.

On the other hand, at higher damages (*i.e.,* in Ar^+ ion irradiated thin films); the observed irradiation induced grain melting, rapid annealing, and grain coalescence (as inferred from FESEM and AFM studies) aids defect recovery and thus expected to suppress the defect density. In other words, number of defects produced is expected to be linearly dependent on ion fluences only at lower ion fluences (at lower *dpa*) and as the *dpa* increases the defects start to annihilate. This will increases the electron concentration and consequently resulted in negative *S* values. The suppression of defects is evidently seen in Raman scattering results, where the intensity of the forbidden mode is apparently decreases with Ar^+ ion fluences in Ar^+ ion irradiated samples. Furthermore, observed trend in the value of *S* upon Ar^+ ion irradiation is ascribed to the suppression of hole density along with increase in the electron concentration.

6.5. Conclusion

Bi_2Te_3 thin films were irradiated using 120 keV He^+ and Ar^+ ions for various ion fluences using 150 kV accelerator and the modifications in the structural, optical, and TE transport properties are investigated systematically. The *n*- to *p*-type charge carrier type conversion is observed in He^+ ion irradiated samples, while the charge carrier type conversion revert back to *n*-type upon Ar^+ ion irradiation. The result suggests that the number of defects produced is dependent linearly at low *dpa,* which resulted in increase in hole concentration. The increase in hole concentration are attributed to the generation of bismuth vacancies (*i.e.,* V_{Bi}). Furthermore, the defects start to annihilate and recovered at high *dpa* that eventually suppress the hole concentration and thereby increase the electron concentration. The maximum value of power factor (~ 6.3 μW/m-K^2) is observed in He^+ ion irradiated thin films, with the ion fluence of 1×10^{15} ions/cm^2.

References

[1] Yang B., Ahuja H., Tran T.N., Review Article: Thermoelectric Technology Assessment: Application to Air Conditioning and Refrigeration, *HVAC&R Res.*, (2008), **14**, 635–653

[2] Bell L.E., Cooling, Heating, Generating Power, and Recovering Waste Heat with Thermoelectric Systems, *Science*, (2008)

[3] Tan G., Ohta M., Kanatzidis M.G., Thermoelectric power generation: from new materials to devices, *Philos. Trans. R. Soc. A Math. Phys. Eng. Sci.*, (2019), **377**, 20180450

[4] Zoui M.A., Bentouba S., Stocholm J.G., Bourouis M., A Review on Thermoelectric Generators: Progress and Applications, *Energies*, (2020), **13**

[5] Champier D., Thermoelectric generators: A review of applications, *Energy Convers. Manag.*, (2017), **140**, 167–181

[6] Rowe D.M., Applications of nuclear-powered thermoelectric generators in space, *Appl. Energy*, (1991), **40**, 241–271

[7] Lange R.G., Carroll W.P., Review of recent advances of radioisotope power systems, *Energy Convers. Manag.*, (2008), **49**, 393–401

[8] O'Brien R.C., Ambrosi R.M., Bannister N.P., Howe S.D., Atkinson H. V, Safe radioisotope thermoelectric generators and heat sources for space applications, *J. Nucl. Mater.*, (2008), **377**, 506–521

[9] Bogala M.R., Reddy R.G., Reaction kinetic studies of metal-doped magnesium silicides, *J. Mater. Sci.*, (2017), **52**, 11962–11976

[10] Memon S., Tahir K.N., Experimental and Analytical Simulation Analyses on the Electrical Performance of Thermoelectric Generator Modules for Direct and Concentrated Quartz-Halogen Heat Harvesting, *Energies*, (2018), **11**

[11] Feldhoff A., Power Conversion and Its Efficiency in Thermoelectric Materials, *Entropy*, (2020), **22**

[12] Vedernikov M. V, Iordanishvili E.K., A.F. Ioffe and origin of modern semiconductor thermoelectric energy conversion, In: Seventeenth International Conference on Thermoelectrics. Proceedings ICT98 (Cat. No.98TH8365), *(1998)*, 37–42

[13] Wang H., Porter W.D., Böttner H., König J., Chen L., Bai S., *et al.*, Transport Properties of Bulk Thermoelectrics: An International Round-Robin Study, Part II: Thermal Diffusivity, Specific Heat, and Thermal Conductivity, *J. Electron. Mater.*, (2013), **42**, 1073–1084

[14] Hamid Elsheikh M., Shnawah D.A., Sabri M.F.M., Said S.B.M., Haji Hassan M., Ali Bashir M.B., Mohamad M., A review on thermoelectric renewable energy: Principle parameters that affect their performance, *Renew. Sustain. Energy Rev.*, (2014), **30**, 337–355

[15] Gaultois M.W., Sparks T.D., Borg C.K.H., Seshadri R., Bonificio W.D., Clarke D.R., Data-Driven Review of Thermoelectric Materials: Performance and Resource Considerations, *Chem. Mater.*, (2013), **25**, 2911–2920

[16] Dughaish Z. ~H., Lead telluride as a thermoelectric material for thermoelectric power generation, *Phys. B Condens. Matter*, (2002), **322**, 205–223

[17] Shi Y., Sturm C., Kleinke H., Chalcogenides as thermoelectric materials, *J. Solid State Chem.*, (2019), **270**, 273–279

[18] Yim W.M., Rosi F.D., Compound tellurides and their alloys for peltier cooling—A review, *Solid. State. Electron.*, (1972), **15**, 1121–1140

[19] Mamur H., Bhuiyan M.R.A., Korkmaz F., Nil M., A review on bismuth telluride (Bi2Te3) nanostructure for thermoelectric applications, *Renew. Sustain. Energy Rev.*, (2018), **82**, 4159–4169

[20] M S., Amirthapandian S., Jegadeesan P., Magudapathy P., Asokan K., Morphological investigations on the growth of defect-rich Bi2Te3 nanorods and their thermoelectric properties, *CrystEngComm*, (2018), **20**, 4810–4822

[21] Chen Y.L., Analytis J.G., Chu J.-H., Liu Z.K., Mo S.-K., Qi X.L., Zhang H.J., Lu D.H., Dai X., Fang Z., Zhang S.C., Fisher I.R., Hussain Z., Shen Z.-X., Experimental Realization of a Three-Dimensional Topological Insulator, Bi2Te3, *Science*, (2009), **325**, 178–181

[22] Nakajima S., The crystal structure of Bi2Te3−xSex, *J. Phys. Chem. Solids*, (1963), **24**, 479–485

[23] Mahan G.D., Sofo J.O., The best thermoelectric, *Proc. Natl. Acad. Sci.*, (1996), **93**, 7436–7439

[24] Sootsman J.R., Chung D.Y., Kanatzidis M.G., New and Old Concepts in Thermoelectric Materials, *Angew. Chemie Int. Ed.*, (2009), **48**, 8616–8639

[25] Fang T., Li X., Hu C., Zhang Q., Yang J., Zhang W., Zhao X., Singh D.J., Zhu T., Complex Band Structures and Lattice Dynamics of Bi2Te3-Based Compounds and Solid Solutions, *Adv. Funct. Mater.*, (2019), **29**, 1900677

[26] Pecheur P., Toussaint G., Tight-binding studies of crystal stability and defects in Bi2Te3, *J. Phys. Chem. Solids*, (1994), **55**, 327–338

[27] Mishra S.K., Satpathy S., Jepsen O., Electronic structure and thermoelectric properties of bismuth telluride and bismuth selenide, *J. Phys. Condens. Matter*, (1997), **9**, 461–470

[28] Zhu T., Hu L., Zhao X., He J., New Insights into Intrinsic Point Defects in V2VI3 Thermoelectric Materials, *Adv. Sci.*, (2016), **3**, 1600004

[29] Zhang Q., Gu B., Wu Y., Zhu T., Fang T., Yang Y., Liu J., Ye B., Zhao X., Evolution of the Intrinsic Point Defects in Bismuth Telluride-Based Thermoelectric Materials, *ACS Appl. Mater. Interfaces*, (2019), **11**, 41424–41431

[30] Hashibon A., Els C., First-principles density functional theory study of native point defects in Bi 2 Te 3, (2011), **144117**, 14–16

[31] An T.-H., Lim Y.S., Choi H.-S., Seo W.-S., Park C.-H., Kim G.-R., Park C., Lee C.H., Shim J.H., Point defect-assisted doping mechanism and related thermoelectric transport properties in Pb-doped BiCuOTe, *J. Mater. Chem. A*, (2014), **2**, 19759–19764

[32] Le P.H., Liao C.-N., Luo C.W., Leu J., Thermoelectric properties of nanostructured bismuth–telluride thin films grown using pulsed laser deposition, *J. Alloys Compd.*,

(2014), **615**, 546–552

[33] Zou H., Rowe D.M., Min G., Growth of p- and n-type bismuth telluride thin films by co-evaporation, *J. Cryst. Growth*, (2001), **222**, 82–87

[34] Peranio N., Eibl O., Nurnus J., Structural and thermoelectric properties of epitaxially grown Bi2Te3 thin films and superlattices, *J. Appl. Phys.*, (2006), **100**, 114306

[35] Makala R.S., Jagannadham K., Sales B.C., Pulsed laser deposition of Bi2Te3-based thermoelectric thin films, *J. Appl. Phys.*, (2003), **94**, 3907–3918

[36] Poudel B., Hao Q., Ma Y., Lan Y., Minnich A., Yu B., Yan X., Dresselhaus M.S., Chen G., Ren Z., High-Thermoelectric Performance of Nanostructured Bismuth Antimony Telluride Bulk Alloys, (2008), **1871**, 634–639

[37] Fitriani, Ovik R., Long B.D., Barma M.C., Riaz M., Sabri M.F.M., Said S.M., Saidur R., A review on nanostructures of high-temperature thermoelectric materials for waste heat recovery, *Renew. Sustain. Energy Rev.*, (2016), **64**, 635–659

[38] Kuznetsov V.L., Kuznetsova L.A., Kaliazin A.E., Rowe D.M., Preparation and thermoelectric properties of A8IIB16IIIB30IV clathrate compounds, *J. Appl. Phys.*, (2000), **87**, 7871–7875

[39] Dresselhaus M.S., Chen G., Tang M.Y., Yang R., Lee H., Wang D., Ren Z., Fleurial J.P., Gogna P., New directions for low-dimensional thermoelectric materials, *Adv. Mater.*, (2007), **19**, 1043–1053

[40] Hicks L.D., Dresselhaus M.S., Effect of quantum-well structures on the thermomagnetic figure of merit, *Phys. Rev. B*, (1993), **47**, 727–731

[41] Hicks L.D., Harman T.C., Sun X., Dresselhaus M.S., Experimental study of the effect of quantum-well structures on the thermoelectric figure of merit, *Phys. Rev. B*, (1996), **53**, R10493–R10496

[42] Hicks L.D., Dresselhaus M.S., Thermoelectric figure of merit of a one-dimensional conductor, *Phys. Rev. B*, (1993), **47**, 16631–16634

[43] Hicks L.D., Dresselhaus M.S., Effect of quantum-well structures on the thermoelectric figure of merit, *Phys. Rev. B*, (1993), **47**, 12727–12731

[44] Kanatzidis M.G., Nanostructured Thermoelectrics: The New Paradigm?, *Chem. Mater.*, (2010), **22**, 648–659

[45] Venkatasubramanian R., Colpitts T., Watko E., Lamvik M., El-Masry N., MOCVD of Bi2Te3, Sb2Te3 and their superlattice structures for thin-film thermoelectric applications, *J. Cryst. Growth*, (1997), **170**, 817–821

[46] Zhang G., Kirk B., Jauregui L. a, Yang H., Xu X., Chen Y.P., Wu Y., Rational synthesis of ultrathin n-type Bi2Te3 nanowires with enhanced thermoelectric properties., *Nano Lett.*, (2012), **12**, 56–60

[47] Fan S., Zhao J., Guo J., Yan Q., Ma J., Hng H.H., p-type Bi0.4Sb1.6Te3 nanocomposites with enhanced figure of merit, *Appl. Phys. Lett.*, (2010), **96**, 182104

[48] Witkoske E., Wang X., Lundstrom M., Askarpour V., Maassen J., Thermoelectric band engineering: The role of carrier scattering, *J. Appl. Phys.*, (2017), **122**, 175102

[49] Pei Y., Wang H., Snyder G.J., Band Engineering of Thermoelectric Materials, *Adv.*

Mater., (2012), **24**, 6125–6135

[50] Jaworski C.M., Kulbachinskii V., Heremans J.P., Resonant level formed by tin in ${\text{Bi}}_{2}{\text{Te}}_{3}$ and the enhancement of room-temperature thermoelectric power, *Phys. Rev. B*, (2009), **80**, 233201

[51] Zhang Q., Wang H., Liu W., Wang H., Yu B., Zhang Q., Tian Z., Ni G., Lee S., Esfarjani K., Chen G., Ren Z., Enhancement of thermoelectric figure-of-merit by resonant states of aluminium doping in lead selenide, *Energy Environ. Sci.*, (2012), **5**, 5246–5251

[52] Wiendlocha B., Resonant Levels, Vacancies, and Doping in Bi2Te3, Bi2Te2Se, and Bi2Se3 Tetradymites, *J. Electron. Mater.*, (2016), **45**, 3515–3531

[53] Zhang Z., Cao Y., Tao Q., Yan Y., Su X., Tang X., Distinct role of Sn and Ge doping on thermoelectric properties in p-type (Bi, Sb)2Te3-alloys, *J. Solid State Chem.*, (2020), **292**, 121722

[54] Properties of indium phosphite and selected compounds under irradiation with swift heavy ions, *Phys. Part. Nucl.*, (2010), **41**, 230

[55] Pei Y., LaLonde A.D., Heinz N.A., Shi X., Iwanaga S., Wang H., Chen L., Snyder G.J., Stabilizing the Optimal Carrier Concentration for High Thermoelectric Efficiency, *Adv. Mater.*, (2011), **23**, 5674–5678

[56] Wang H., Hwang J., Zhang C., Wang T., Su W., Kim H., Kim J., Zhai J., Wang X., Park H., Kim W., Wang C., Enhancement of the thermoelectric performance of bulk SnTe alloys via the synergistic effect of band structure modification and chemical bond softening, *J. Mater. Chem. A*, (2017), **5**, 14165–14173

[57] Zaitsev V.K., Fedorov M.I., Gurieva E.A., Eremin I.S., Konstantinov P.P., Samunin A.Y., Vedernikov M. V, Highly effective Mg2Si(1-x)Snx thermoelectrics, *Phys. Rev. B*, (2006), **74**, 45207

[58] Tian T., Cheng L., Zheng L., Xing J., Gu H., Bernik S., Zeng H., Ruan W., Zhao K., Li G., Defect engineering for a markedly increased electrical conductivity and power factor in doped ZnO ceramic, *Acta Mater.*, (2016), **119**, 136–144

[59] Hu L., Zhu T., Liu X., Zhao X., Point Defect Engineering of High-Performance Bismuth-Telluride-Based Thermoelectric Materials, *Adv. Funct. Mater.*, (2014), **24**, 5211–5218

[60] Mao J., Wu Y., Song S., Zhu Q., Shuai J., Liu Z., Pei Y., Ren Z., Defect Engineering for Realizing High Thermoelectric Performance in n-Type Mg3Sb2-Based Materials, *ACS Energy Lett.*, (2017), **2**, 2245–2250

[61] Tang J., Wang H.T., Lee D.H., Fardy M., Huo Z., Russell T.P., Yang P., Holey silicon as an efficient thermoelectric material, *Nano Lett.*, (2010), **10**, 4279–4283

[62] Park Y.H., Kim J., Kim H., Kim I., Lee K.Y., Seo D., Choi H.J., Kim W., Thermal conductivity of VLS-grown rough Si nanowires with various surface roughnesses and diameters, *Appl. Phys. A Mater. Sci. Process.*, (2011), **104**, 7–14

[63] Chen C., Li X., Xue W., Bai F., Huang Y., Yao H., Li S., Zhang Z., Wang X., Sui J., Liu X., Cao F., Wang Y., Zhang Q., Manipulating the intrinsic vacancies for enhanced thermoelectric performance in Eu2ZnSb2 Zintl phase, *Nano Energy*, (2020), **73**, 104771

[64] Xia K., Liu Y., Anand S., Snyder G.J., Xin J., Yu J., Zhao X., Zhu T., Enhanced

Thermoelectric Performance in 18-Electron Nb0.8CoSb Half-Heusler Compound with Intrinsic Nb Vacancies, *Adv. Funct. Mater.*, (2018), **28**, 1705845

[65] Li W., Lin S., Zhang X., Chen Z., Xu X., Pei Y., Thermoelectric Properties of Cu2SnSe4 with Intrinsic Vacancy, *Chem. Mater.*, (2016), **28**, 6227–6232

[66] Zhu B., Li D., Zhang T., Luo Y., Donelson R., Zhang T., Zheng Y., Du C., Wei L., Hng H.H., The improvement of thermoelectric property of bulk ZnO via ZnS addition: Influence of intrinsic defects, *Ceram. Int.*, (2018), **44**, 6461–6465

[67] Li Z., Xiao C., Fan S., Deng Y., Zhang W., Ye B., Xie Y., Dual Vacancies: An Effective Strategy Realizing Synergistic Optimization of Thermoelectric Property in BiCuSeO, *J. Am. Chem. Soc.*, (2015), **137**, 6587–6593

[68] Liu S., Peng N., Bai Y., Ma D., Ma F., Xu K., Fabrication of Cu-Doped Bi2Te3 Nanoplates and Their Thermoelectric Properties, *J. Electron. Mater.*, (2017), **46**, 2697–2704

[69] Cui J.L., Mao L.D., Yang W., Xu X.B., Chen D.Y., Xiu W.J., Thermoelectric properties of Cu-doped n-type (Bi2Te3)0.9–(Bi2−xCuxSe3)0.1(x=0–0.2) alloys, *J. Solid State Chem.*, (2007), **180**, 3583–3587

[70] Lognoné Q., Gascoin F., Reactivity, stability and thermoelectric properties of n-Bi2Te3 doped with different copper amounts, *J. Alloys Compd.*, (2014), **610**, 1–5

[71] Bludská J., Jakubec I., Drašar Č., Lošťák P., Horák J., Structural defects in Cu-doped Bi2Te3 single crystals, *Philos. Mag.*, (2007), **87**, 325–335

[72] Chen S., Cai K.F., Li F.Y., Shen S.Z., The Effect of Cu Addition on the System Stability and Thermoelectric Properties of Bi2Te3, *J. Electron. Mater.*, (2014), **43**, 1966–1971

[73] Lu M.-P., Liao C.-N., Huang J.-Y., Hsu H.-C., Thermoelectric Properties of Ag-Doped Bi2(Se,Te)3 Compounds: Dual Electronic Nature of Ag-Related Lattice Defects, *Inorg. Chem.*, (2015), **54**, 7438–7444

[74] Zhang Q., Ai X., Wang L., Chang Y., Luo W., Jiang W., Chen L., Improved Thermoelectric Performance of Silver Nanoparticles-Dispersed Bi2Te3 Composites Deriving from Hierarchical Two-Phased Heterostructure, *Adv. Funct. Mater.*, (2015), **25**, 966–976

[75] Singh N.K., Ramanath G., Soni A., Copper-induced majority charge carrier reversal in bismuth telluride-based nanothermoelectrics, *AIP Conf. Proc.*, (2019), **2115**, 30625

[76] Wang Y., Liu W.-D., Shi X.-L., Hong M., Wang L.-J., Li M., Wang H., Zou J., Chen Z.-G., Enhanced thermoelectric properties of nanostructured n-type Bi2Te3 by suppressing Te vacancy through non-equilibrium fast reaction, *Chem. Eng. J.*, (2020), **391**, 123513

[77] Suh J., Yu K.M., Fu D., Liu X., Yang F., Fan J., Smith D.J., Zhang Y.-H., Furdyna J.K., Dames C., Walukiewicz W., Wu J., Simultaneous Enhancement of Electrical Conductivity and Thermopower of Bi2Te3 by Multifunctionality of Native Defects, *Adv. Mater.*, (2015), **27**, 3681–3686

[78] Fu G., Zuo L., Lian J., Wang Y., Chen J., Longtin J., Xiao Z., Ion beam irradiation effect on thermoelectric properties of Bi2Te3 and Sb2Te3 thin films, *Nucl. Instruments Methods Phys. Res. Sect. B Beam Interact. with Mater. Atoms*, (2015),

358, 229–235

[79] Spark Plasma Sintering Effect on Thermoelectric Properties of Nanostructured Bismuth Telluride Synthesized by High Energy Ball Milling, *J. Nanosci. Nanotechnol.*, (2020), **20**

[80] Rawat R. ~S., Dense Plasma Focus - From Alternative Fusion Source to Versatile High Energy Density Plasma Source for Plasma Nanotechnology, In: Journal of Physics Conference Series, *(2015)*, 12021

[81] Balin K., Wojtyniak M., Weis M., Zubko M., Wilk B., Gu R., Ruello P., Szade J., Europium Doping Impact on the Properties of MBE Grown Bi2Te3 Thin Film, *Materials (Basel).*, (2020), **13**

[82] Deng Y., Xiang Y., Song Y., Template-free Synthesis and Transport Properties of Bi 2 Te 3 Ordered Nanowire Arrays via a Physical Vapor Process, *Cryst. Growth Des.*, (2009), **9**, 3079–3082

[83] Goncalves L.M., Couto C., Alpuim P., Rowe D.M., Correia J.H., Thermoelectric Properties of Bi 2 Te 3 / Sb 2 Te 3 Thin Films, *Mater. Sci. Fórum*, (2006), **516**, 156–160

[84] Guo W., Ma J., Zheng W., Bi2Te3nanoflowers assembled of defective nanosheets with enhanced thermoelectric performance, *J. Alloys Compd.*, (2016), **659**, 170–177

[85] Wu F., Song H., Gao F., Shi W., Jia J., Hu X., Effects of different morphologies of Bi2Te3 nanopowders on thermoelectric properties, *J. Electron. Mater.*, (2013), **42**, 1140–1145

[86] Sun T., Zhao X.B., Zhu T.J., Tu J.P., Aqueous chemical reduction synthesis of Bi2Te3 nanowires with surfactant assistance, *Mater. Lett.*, (2006), **60**, 2534–2537

[87] Zhu T.J., Chen X., Cao Y.Q., Zhao X.B., Controllable synthesis and shape evolution of PbTe three-dimensional hierarchical superstructures via an alkaline hydrothermal method, *J. Phys. Chem. C*, (2009), **113**, 8085–8091

[88] Ji X., Zhang B., Tritt T.M., Kolis J.W., Kumbhar A., Solution-chemical syntheses of nano-structured Bi 2Te 3 and PbTe thermoelectric materials, *J. Electron. Mater.*, (2007), **36**, 721–726

[89] Zhu H.-T., Luo J., Liang J.-K., Synthesis of highly crystalline Bi2Te3 nanotubes and their enhanced thermoelectric properties, *J. Mater. Chem. A*, (2014), **2**, 12821–12826

[90] Lu Q., Zeng H., Wang Z., Cao X., Zhang L., Design of Sb2S3 nanorod-bundles: Imperfect oriented attachment, *Nanotechnology*, (2006), **17**, 2098–2104

[91] Venkatasubramanian R., Siivola E., Colpitts T., O'Quinn B., Thin-film thermoelectric devices with high room-temperature figures of merit, *Nature*, (2001), **413**, 597–602

[92] Yamasaki I., Yamanaka R., Mikami M., Sonobe H., Mori Y., Sasaki T., Thermoelectric properties of Bi/sub 2/Te/sub 3//Sb/sub 2/Te/sub 3/ superlattice structure, In: Seventeenth International Conference on Thermoelectrics. Proceedings ICT98 (Cat. No.98TH8365), *(1998)*, 210–213

[93] Winkler M., Liu X., Schürmann U., König J.D., Kienle L., Bensch W., Böttner H., Current Status in Fabrication, Structural and Transport Property Characterization, and Theoretical Understanding of Bi2Te3 / Sb2Te3 Superlattice Systems,

Zeitschrift Für Anorg. Und Allg. Chemie, (2012), **638**, 2441–2454

[94] Park N.-W., Lee W.-Y., Yoon Y.-S., Kim G.-S., Yoon Y.-G., Lee S.-K., Achieving Out-of-Plane Thermoelectric Figure of Merit ZT = 1.44 in a p-Type Bi2Te3/Bi0.5Sb1.5Te3 Superlattice Film with Low Interfacial Resistance, *ACS Appl. Mater. Interfaces*, (2019), **11**, 38247–38254

[95] Hamdou B., Kimling J., Dorn A., Pippel E., Rostek R., Woias P., Nielsch K., Thermoelectric characterization of bismuth telluride nanowires, synthesized via catalytic growth and post-annealing, *Adv. Mater.*, (2013), **25**, 239–244

[96] Zhao X.B., Ji X.H., Zhang Y.H., Zhu T.J., Tu J.P., Zhang X.B., Bismuth telluride nanotubes and the effects on the thermoelectric properties of nanotube-containing nanocomposites, *Appl. Phys. Lett.*, (2005), **86**, 1–3

[97] Zhang Y., Hu L.P., Zhu T.J., Xie J., Zhao X.B., High Yield Bi2Te3 Single Crystal Nanosheets with Uniform Morphology via a Solvothermal Synthesis, *Cryst. Growth Des.*, (2013), **13**, 645–651

[98] Sudarshan C., Jayakumar S., Vaideki K., Sudakar C., Effect of vacuum annealing on structural, electrical and thermal properties of e-beam evaporated Bi2Te3 thin films, *Thin Solid Films*, (2017), **629**, 28–38

[99] Newbrook D.W., Richards S.P., Greenacre V.K., Hector A.L., Levason W., Reid G., de Groot C.H. (Kees), Huang R., Improved thermoelectric performance of Bi2Se3 alloyed Bi2Te3 thin films via low pressure chemical vapour deposition, *J. Alloys Compd.*, (2020), **848**, 156523

[100] Bailini A., Donati F., Zamboni M., Russo V., Passoni M., Casari C.S., Li Bassi A., Bottani C.E., Pulsed laser deposition of Bi2Te3 thermoelectric films, *Appl. Surf. Sci.*, (2007), **254**, 1249–1254

[101] Kianwimol S., Sakdanuphab R., Chanlek N., Harnwunggmoung A., Sakulkalavek A., Effect of annealing temperature on thermoelectric properties of bismuth telluride thick film deposited by DC magnetron sputtering, *Surf. Coatings Technol.*, (2020), **393**, 125808

[102] Kim D.-H., Byon E., Lee G.-H., Cho S., Effect of deposition temperature on the structural and thermoelectric properties of bismuth telluride thin films grown by co-sputtering, *Thin Solid Films*, (2006), **510**, 148–153

[103] Chang H.-C., Chen C.-H., Self-assembled bismuth telluride films with well-aligned zero- to three-dimensional nanoblocks for thermoelectric applications, *CrystEngComm*, (2011), **13**, 5956

[104] Kurokawa T., Mori R., Norimasa O., Chiba T., Eguchi R., Takashiri M., Influences of substrate types and heat treatment conditions on structural and thermoelectric properties of nanocrystalline Bi2Te3 thin films formed by DC magnetron sputtering, *Vacuum*, (2020), **179**, 109535

[105] Ahmad F., Singh S., Pundir S.K., Kumar R., Kandpal K., Kumar P., Effect of Doping and Annealing on Thermoelectric Properties of Bismuth Telluride Thin Films, *J. Electron. Mater.*, (2020), **49**, 4195–4202

[106] Li S., Soliman H.M.A., Zhou J., Toprak M.S., Muhammed M., Platzek D., Ziolkowski P., Müller E., Effects of Annealing and Doping on Nanostructured Bismuth Telluride Thick Films, *Chem. Mater.*, (2008), **20**, 4403–4410

[107] Lin J.-M., Chen Y.-C., Lin C.-P., Chien H.-C., Wen C.-Y., Chang J.-Y., Zhan Z.-Y., Annealing effects on the thermoelectric properties of silver-doped bismuth telluride thin films, *Microelectron. Eng.*, (2015), **148**, 51–54

[108] Geun Kim B., Hyun Bae S., Byeon J., Lee C., Choi S.-M., Stress-induced change of Cu-doped Bi2Te3 thin films for flexible thermoelectric applications, *Mater. Lett.*, (2020), **270**, 127697

[109] Zheng Z., Fan P., Liang G., Zhang D., Cai X., Chen T., Annealing temperature influence on electrical properties of ion beam sputtered Bi2Te3 thin films, *J. Phys. Chem. Solids*, (2010), **71**, 1713–1716

[110] Zeng Z., Yang P., Hu Z., Temperature and size effects on electrical properties and thermoelectric power of Bismuth Telluride thin films deposited by co-sputtering, *Appl. Surf. Sci.*, (2013), **268**, 472–476

[111] Nguyen T.T.T., Dang L.T., Bach G.H., Dang T.H., Nguyen K.T., Pham H.T., Nguyen-Tran T., Nguyen T.V., Nguyen T.T., Nguyen H.Q., Enhanced thermoelectricity at the ultra-thin film limit, *Appl. Phys. Lett.*, (2020), **117**, 83104

[112] Wudil Y.S., Gondal M.A., Rao S.G., Kunwar S., Alsayoud A.Q., Substrate temperature-dependent thermoelectric figure of merit of nanocrystalline Bi2Te3 and Bi2Te2.7Se0.3 prepared using pulsed laser deposition supported by DFT study, *Ceram. Int.*, (2020), **46**, 24162–24172

[113] Shupenev A.E., Korshunov I.S., Grigoryants A.G., On the Pulsed-Laser Deposition of Bismuth-Telluride Thin Films on Polyimide Substrates, *Semiconductors*, (2020), **54**, 378–382

[114] Wang K., Liang H.-W., Yao W.-T., Yu S.-H., Templating synthesis of uniform Bi2Te3 nanowires with high aspect ratio in triethylene glycol (TEG) and their thermoelectric performance, *J. Mater. Chem.*, (2011), **21**, 15057

[115] Fu J., Song S., Zhang X., Cao F., Zhou L., Li X., Zhang H., Bi2Te3 nanoplates and nanoflowers: Synthesized by hydrothermal process and their enhanced thermoelectric properties, *CrystEngComm*, (2012), **14**, 2159

[116] Zhang G., Kirk B., Jauregui L.A., Yang H., Xu X., Chen Y.P., Wu Y., Rational Synthesis of Ultrathin n-Type Bi_2Te_3 Nanowires with Enhanced Thermoelectric Properties, *Nano Lett.*, (2012), **12**, 56–60

[117] Mei Z.-Y., Guo J., Wu Y., Feng J., Ge Z.-H., Shashlik-like Te–Bi2Te3 hetero-nanostructures: one-pot synthesis{,} growth mechanism and their thermoelectric properties, *CrystEngComm*, (2019), **21**, 3694–3701

[118] Mi J.-L., Lock N., Sun T., Christensen M., Søndergaard M., Hald P., Hng H.H., Ma J., Iversen B.B., Biomolecule-assisted hydrothermal synthesis and self-assembly of Bi2Te3 nanostring-cluster hierarchical structure., *ACS Nano*, (2010), **4**, 2523–2530

[119] Fan X.A., Yang J.Y., Xie Z., Li K., Zhu W., Duan X.K., Xiao C.J., Zhang Q.Q., Bi_2Te_3 hexagonal nanoplates and thermoelectric properties of n-type Bi_2Te_3 nanocomposites, *J. Phys. D. Appl. Phys.*, (2007), **40**, 5975–5979

[120] Feng H., Wu C., Zhang P., Mi J., Dong M., Facile hydrothermal synthesis and formation mechanisms of Bi2Te3{,} Sb2Te3 and Bi2Te3–Sb2Te3 nanowires, *RSC Adv.*, (2015), **5**, 100309–100315

[121] Soni A., Shen Y., Yin M., Zhao Y., Yu L., Hu X., Dong Z., Khor K.A., Dresselhaus

M.S., Xiong Q., Interface Driven Energy Filtering of Thermoelectric Power in Spark Plasma Sintered Bi2Te2.7Se0.3 Nanoplatelet Composites, *Nano Lett.*, (2012), **12**, 4305–4310

[122] Li G., Zheng F., Tong Y., Controllable Synthesis of Bi 2 Te 3 Intermetallic Compounds with Hierarchical Nanostructures via Electrochemical Deposition Route & DESIGN 2008, *Cryst. Growth Des.*, (2008), 0–6

[123] Wang Z., Wang F., Chen H., Zhu L., Yu H., Jian X., Synthesis and characterization of Bi2Te3 nanotubes by a hydrothermal method, *J. Alloys Compd.*, (2010), **492**, L50–L53

[124] Shyni P., Pradyumnan P.P., Time-Dependent Morphological Evolution of Bi2Te3 Nanotubes: A Potential Material for Thermoelectric Applications, *{ECS} J. Solid State Sci. Technol.*, (2020), **9**, 105006

[125] Zhang Y., Xu G., Ren P., Wang Z., Ge C., Effects of Various Reductants and Surfactants on the Nanostructure of Bi2Te3 Synthesized by a Hydrothermal Process, *J. Electron. Mater.*, (2011), **40**, 835–839

[126] Morsy S., Role of Surfactants in Nanotechnology and Their Applications, *Int. J. Curr. Microbiol. App. Sci*, (2014), **3**, 237–260

[127] Dharmaiah P., Hong S.-J., Thermoelectric Properties of Bi2Te3 Nanocrystals with Diverse Morphologies Obtained via Modified Hydrothermal Method, *J. Electron. Mater.*, (2017), **46**, 3012–3019

[128] Zhang Y., Wang H., Kräemer S., Shi Y., Zhang F., Snedaker M., Ding K., Moskovits M., Snyder G.J., Stucky G.D., Surfactant-Free Synthesis of Bi2Te3−Te Micro−Nano Heterostructure with Enhanced Thermoelectric Figure of Merit, *ACS Nano*, (2011), **5**, 3158–3165

[129] Mayer J.W., Ion implantation in semiconductors, In: 1973 International Electron Devices Meeting, *(1973)*, 3–5

[130] Biersack J.P., Haggmark L.G., A Monte Carlo computer program for the transport of energetic ions in amorphous targets, *Nucl. Instruments Methods*, (1980), **174**, 257–269

[131] Toulemonde C.D. and V.K. and Y.Y.W. and Z.G.W. and F.A. and M., An attempt to apply the inelastic thermal spike model to surface modifications of CaF 2 induced by highly charged ions: comparison to swift heavy ions effects and extension to some others material, *J. Phys. Condens. Matter*, (2017), **29**, 95001

[132] Revisiting the thermal-spike concept in ion-surface interactions, *Nucl. Instruments Methods Phys. Res. Sect. B Beam Interact. with Mater. Atoms*, (1997), **122**, 458

[133] Gervais M.G. and J.P.N. and D.G. and M.T. and B., Amorphization of rare earth - cobalt intermetallic alloys by swift heavy-ion irradiation, *J. Phys. Condens. Matter*, (1996), **8**, 8191

[134] Effect of thermal spike energy created in CuFe2O4 by 150MeV Ni11+ swift heavy ion irradiation, *Nucl. Instruments Methods Phys. Res. Sect. B Beam Interact. with Mater. Atoms*, (2011), **269**, 1088

[135] Nordlund W.R. and F.D. and K., Swift heavy ion effects on DLC-nanotube-diamond thin films, *J. Phys. D. Appl. Phys.*, (2017), **50**, 355301

[136] Rana M.A., Formation of Charged Particle Tracks in Solids, *Chinese Phys. Lett.*,

(2006), **23**, 1448

[137] Thermal spike model interpretation of sputtering yield data for Bi thin films irradiated by MeV 84Kr15+ ions, *Nucl. Instruments Methods Phys. Res. Sect. B Beam Interact. with Mater. Atoms*, (2014)

[138] Goo G., Anoop G., Unithrattil S., Kim W.S., Lee H.J., Kim H. Bin, Jung M.-H., Park J., Ko H.C., Jo J.Y., Proton-Irradiation Effects on the Thermoelectric Properties of Flexible Bi2Te3/PEDOT:PSS Composite Films, *Adv. Electron. Mater.*, (2019), **5**, 1800786

[139] Wang Q., Cui K., Li J., Wu Y., Yang Y., Zhou X., Ma G., Yang Z., Lei Z., Ren S., Iron ion irradiated Bi2Te3 nanosheets with defects and regulated hydrophilicity to enhance the hydrogen evolution reaction, *Nanoscale*, (2020), **12**, 16208–16214

[140] Chien C.-H., Lee P.-C., Tsai W.-H., Lin C.-H., Lee C.-H., Chen Y.-Y., In-situ Observation of Size and Irradiation Effects on Thermoelectric Properties of Bi-Sb-Te Nanowire in FIB Trimming, *Sci. Rep.*, (2016), **6**, 23672

[141] Guerra D.B., Müller S., Oliveira M.P., Fichtner P.F.P., Papaléo R.M., Bi nanowires modified by 400 keV and 1 MeV Au ions, *AIP Adv.*, (2018), **8**, 125103

[142] Chang T., Kim J., Song M.-J., Lee W., Proton irradiation effects on the thermoelectric properties in single-crystalline Bi nanowires, *AIP Adv.*, (2015), **5**, 57101

[143] Roh J.W., Ko D.H., Kang J., Lee M.K., Lee J.H., Lee C.W., Lee K.H., Noh J.-S., Lee W., Proton irradiation effects on thermal transport in individual single-crystalline Bi nanowires, *Phys. Status Solidi*, (2013), **210**, 1438–1441

[144] Han M.-K., Jin Y., Lee D.-H., Kim S.-J., Thermoelectric Properties of Bi2Te3: CuI and the Effect of Its Doping with Pb Atoms, *Materials (Basel).*, (2017), **10**

[145] Arif F., Farooq O., Tuz Zahra F., Anis-ur-Rehman M., Structural and Thermoelectric Properties of Gd Doped Bi2Te3, *Key Eng. Mater.*, (2018), **778**, 189–194

[146] Deng Y., Nan C.W., Wei G.D., Guo L., Lin Y.H., Organic-assisted growth of bismuth telluride nanocrystals, *Chem. Phys. Lett.*, (2003), **374**, 410–415

[147] Zhang Y., Hu L.P., Zhu T.J., Xie J., Zhao X.B., Morphology via a Solvothermal Synthesis, *Cryst. Growth Des.*, (2012), 2–8

[148] Kumar V., Jaiswal M.K., Gupta R., Ram J., Sulania I., Ojha S., Sun X., Koratkar N., Kumar R., Effect of low energy (keV) ion irradiation on structural, optical and morphological properties of SnO2–TiO2 nanocomposite thin films, *J. Mater. Sci. Mater. Electron.*, (2018), **29**, 13328–13336

[149] Sander M.S., Prieto A.L., Gronsky R., Sands T., Stacy A.M., Fabrication of high-density, high aspect ratio, large-area bismuth telluride nanowire arrays by electrodeposition into porous anodic alumina templates, *Adv. Mater.*, (2002), **14**, 665–667

[150] Picht O., Müller S., Alber I., Rauber M., Lensch-Falk J., Medlin D.L., Neumann R., Toimil-Molares M.E., Tuning the geometrical and crystallographic characteristics of Bi2Te3nanowires by electrodeposition in ion-track membranes, *J. Phys. Chem. C*, (2012), **116**, 5367–5375

[151] Obara H., Higomo S., Ohta M., Yamamoto A., Ueno K., Iida T., Thermoelectric

Properties of Bi2Te3-Based Thin Films with Fine Grains Fabricated by Pulsed Laser Deposition, *Jpn. J. Appl. Phys.*, (2009), **48**, 85506

[152] Manikandan E., Moodley M.K., Sinha Ray S., Panigrahi B.K., Krishnan R., Padhy N., Nair K.G.M., Tyagi A.K., Zinc oxide epitaxial thin film deposited over carbon on various substrate by pulsed laser deposition technique., *J. Nanosci. Nanotechnol.*, (2010), **10**, 5602–5611

[153] Stabrawa I., Kubala-Kukuś A., Banaś D., Pepponi G., Braziewicz J., Pajek M., Teodorczyk M., Characterization of the morphology of titanium and titanium (IV) oxide nanolayers deposited on different substrates by application of grazing incidence X-ray diffraction and X-ray reflectometry techniques, *Thin Solid Films*, (2019), **671**, 103–110

[154] Many T., Siti K.T., Abdul M., San C., Roslan W., Evaluation of Williamson – Hall Strain and Stress Distribution in ZnO Nanowires Prepared Using Aliphatic Alcohol, *J. Nondestruct. Eval.*, (2015), 1–9

[155] Horcas I., Fernández R., Gómez-Rodríguez J.M., Colchero J., Gómez-Herrero J., Baro A.M., WSXM: A software for scanning probe microscopy and a tool for nanotechnology, *Rev. Sci. Instrum.*, (2007), **78**, 13705

[156] Shahil K.M.F., Hossain M.Z., Goyal V., Balandin A.A., Micro-Raman spectroscopy of mechanically exfoliated few-quintuple layers of Bi2Te3, Bi2Se3, and Sb2Te3 materials, *J. Appl. Phys.*, (2012), **111**, 54305

[157] Zhang J., Peng Z., Soni A., Zhao Y., Xiong Y., Peng B., Wang J., Dresselhaus M.S., Xiong Q., Raman Spectroscopy of Few-Quintuple Layer Topological Insulator Bi2Se3 Nanoplatelets, *Nano Lett.*, (2011), **11**, 2407–2414

[158] Mayer M., SIMNRA, a simulation program for the analysis of NRA, RBS and ERDA, *AIP Conf. Proc.*, (1999), **475**, 541–544

[159] Tripathi T.S., Bala M., Asokan K., Tripathi T.S., Bala M., Asokan K., An experimental setup for the simultaneous measurement of thermoelectric power of two samples from 77 K to 500 K An experimental setup for the simultaneous measurement of thermoelectric power of two samples from 77 K to 500 K, (2014), **085115**

[160] Wiese J.R., Muldawer L., Lattice constants of Bi2Te3-Bi2Se3 solid solution alloys, *J. Phys. Chem. Solids*, (1960), **15**, 13–16

[161] Park J.G., Lee Y.H., High thermoelectric performance of Bi-Te alloy: Defect engineering strategy, *Curr. Appl. Phys.*, (2016), **16**, 1202–1215

[162] Zhao Q., Wang Y.G., A facile two-step hydrothermal route for the synthesis of low-dimensional structured Bi2Te3nanocrystals with various morphologies, *J. Alloys Compd.*, (2010), **497**, 57–61

[163] Bejenari I., Kantser V., Balandin A.A., Thermoelectric properties of electrically gated bismuth telluride nanowires, (2010), 1–14

[164] Purkayastha A., Lupo F., Kim S., Borca-Tasciuc T., Ramanath G., Low-temperature, template-free synthesis of single-crystal bismuth telluride nanorods, *Adv. Mater.*, (2006), **18**, 496–500

[165] Zhang H.T., Luo X.G., Wang C.H., Xiong Y.M., Li S.Y., Chen X.H., Characterization of nanocrystalline bismuth telluride (Bi2Te3) synthesized by a

hydrothermal method, *J. Cryst. Growth*, (2004), **265**, 558–562

[166] Jiang L., Zhu Y.J., Cui J.B., Nanostructures of metal tellurides (PbTe, CdTe, CoTe2, Bi 2Te3, and Cu7Te4) with various morphologies: A general solvothermal synthesis and optical properties, *Eur. J. Inorg. Chem.*, (2010), 3005–3011

[167] Song S., Fu J., Li X., Gao W., Zhang H., Facile Synthesis and Thermoelectric Properties of Self-assembled Bi 2 Te 3 One-Dimensional Nanorod Bundles, *Chem. - A Eur. J.*, (2013), **19**, 2889–2894

[168] Rashad M.M., El-dissouky A., Soliman H.M., Ahmed M., Refaat H.M., Ebrahim A., Rashad M.M., El-dissouky A., Soliman H.M., Ahmed M., Structure evaluation of bismuth telluride (Bi 2 Te 3) nanoparticles with enhanced Seebeck coefficient and low thermal conductivity, *Mater. Res. Innov.*, (2017), **8917**, 0

[169] Kuo C.-H., Hwang C.-S., Jeng M.-S., Su W.-S., Chou Y.-W., Ku J.-R., Thermoelectric transport properties of bismuth telluride bulk materials fabricated by ball milling and spark plasma sintering, *J. Alloys Compd.*, (2010), **496**, 687–690

[170] Witting I.T., Chasapis T.C., Ricci F., Peters M., Heinz N.A., Hautier G., Snyder G.J., The Thermoelectric Properties of Bismuth Telluride, *Adv. Electron. Mater.*, (2019), **5**, 1800904

[171] Wang F., Yip S., Han N., Fok K., Lin H., Hou J.J., Dong G., Hung T., Chan K.S., Ho J.C., Surface roughness induced electron mobility degradation in InAs nanowires, *Nanotechnology*, (2013), **24**

[172] Liu Z., Mao J., Peng S., Zhou B., Gao W., Sui J., Pei Y., Ren Z., Tellurium doped n-type Zintl Zr3Ni3Sb4 thermoelectric materials: Balance between carrier-scattering mechanism and bipolar effect, *Mater. Today Phys.*, (2017), **2**, 54–61

[173] Li Y.L., Jiang J., Xu G.J., Liu F.H., Li Y., Cui P., Preparation of Bi2Te3 Nano-Powders via an Aqueous Chemical Method, *Key Eng. Mater.*, (2008), **368–372**, 541–543

[174] Zhao X.B., Ji X.H., Zhang Y.H., Lu B.H., Effect of solvent on the microstructures of nanostructured Bi2Te3prepared by solvothermal synthesis, *J. Alloys Compd.*, (2004), **368**, 349–352

[175] Zhao X.B., Ji X.H., Zhang Y.H., Cao G.S., Tu J.P., Hydrothermal synthesis and microstructure investigation of nanostructured bismuth telluride powder, *Appl. Phys. A Mater. Sci. Process.*, (2005), **80**, 1567–1571

[176] Mehta R.J., Karthik C., Singh B., Teki R., Borca-Tasciuc T., Ramanath G., Seebeck tuning in chalcogenide nanoplate assemblies by nanoscale heterostructuring, *ACS Nano*, (2010), **4**, 5055–5060

[177] Bricha M., Belmamouni Y., Essassi E.M., Ferreira J.M.F., Mabrouk K. El, Surfactant-Assisted Hydrothermal Synthesis of Hydroxyapatite Nanopowders, *J. Nanosci. Nanotechnol.*, (2012), **12**, 8042–8049

[178] Chauhan S., Sharma K., Effect of temperature and additives on the critical micelle concentration and thermodynamics of micelle formation of sodium dodecyl benzene sulfonate and dodecyltrimethylammonium bromide in aqueous solution: A conductometric study, *J. Chem. Thermodyn.*, (2014), **71**, 205–211

[179] Kato M., Ozawa S., Hayashi R., Effects of high pressure and temperature on micelle formation of sodium deoxycholate and sodium dodecylsulfate., *Lipids*,

(1997), **32**, 1229–1230

[180] Lin J.Y., Hsueh Y.L., Huang J.J., The concentration effect of capping agent for synthesis of silver nanowire by using the polyol method, *J. Solid State Chem.*, (2014), **214**, 2–6

[181] Penn R.L., Imperfect Oriented Attachment: Dislocation Generation in Defect-Free Nanocrystals, *Science*, (1998), **281**, 969–971

[182] Penn R.L., Banfield J.F., Morphology development and crystal growth in nanocrystalline aggregates under hydrothermal conditions: Insights from titania, *Geochim. Cosmochim. Acta*, (1999), **63**, 1549–1557

[183] Kim H.-B., Jang D.-J., Dislocation-driven growth of porous CdSe nanorods from CdSe·(ethylenediamine) $_{0.5}$ nanorods, *Nanoscale*, (2016), **8**, 403–410

[184] Araújo V.D., Avansi W., de Carvalho H.B., Moreira M.L., Longo E., Ribeiro C., Bernardi M.I.B., CeO $_2$ nanoparticles synthesized by a microwave-assisted hydrothermal method: evolution from nanospheres to nanorods, *CrystEngComm*, (2012), **14**, 1150–1154

[185] Tsai M.H., Chen S.Y., Shen P., Imperfect oriented attachment: Accretion and defect generation of nanosize rutile condensates, *Nano Lett.*, (2004), **4**, 1197–1201

[186] Zhao B., Zhou B., Li C.Y., Qi N., Chen Z.Q., First-Principles Calculation of Defect Formation and Positron Annihilation States in Bi₂Te₃, *Defect Diffus. Forum*, (2017), **373**, 41–45

[187] Zhu H.-T., Luo J., Liang J.-K., Synthesis of highly crystalline Bi $_2$ Te $_3$ nanotubes and their enhanced thermoelectric properties, *J. Mater. Chem. A*, (2014), **2**, 12821

[188] Saleemi M., Toprak M.S., Li S., Johnsson M., Muhammed M., Synthesis, processing, and thermoelectric properties of bulk nanostructured bismuth telluride (Bi $_2$ Te $_3$), *J. Mater. Chem.*, (2012), **22**, 725–730

[189] Feng S.-K., Li S.-M., Fu H.-Z., Probing the thermoelectric transport properties of n-type Bi 2 Te 3 close to the limit of constitutional undercooling, *Chinese Phys. B*, (2014), **23**, 117202

[190] Dirmyer M.R., Martin J., Nolas G.S., Sen A., Badding J. V., Thermal and electrical conductivity of size-tuned bismuth telluride nanoparticles, *Small*, (2009), **5**, 933–937

[191] Li Z., Xiao C., Zhu H., Xie Y., Defect Chemistry for Thermoelectric Materials, *J. Am. Chem. Soc.*, (2016), **138**

[192] Liu W.-S., Zhang B.-P., Li J.-F., Zhao L.-D., Effects of Sb compensation on microstructure, thermoelectric properties and point defect of CoSb3compound, *J. Phys. D. Appl. Phys.*, (2007), **40**, 6784–6790

[193] Guo X., Qin J., Jia X., Jiang D., Pressure-induced electrical transport properties{,} texture{,} and microstructure of the (Bi{,}Sb)2Te3 alloys, *Inorg. Chem. Front.*, (2018), **5**, 1540–1544

[194] Idnurm M., Landecker K., Changes produced in thermoelectric materials by thermal-neutron irradiation, *Br. J. Appl. Phys.*, (1967), **18**, 1209–1211

[195] Chaudhari P., Bever M.B., Defects in the Compound Bi2Te3 caused by Irradiation

with Protons, *J. Appl. Phys.*, (1967), **38**, 2417–2422

[196] Khodiri A.A., Nawar A.M., El-kader K.M.A., Effect ofX-ray Irradiation on Structural and Optical Properties of Topological Insulator Bismuth Telluride Nano-Structure Thin Film, In: *(2016)*

[197] Tripathi T.S., Bala M., Asokan K., An experimental setup for the simultaneous measurement of thermoelectric power of two samples from 77 K to 500 K, *Rev. Sci. Instrum.*, (2014), **85**

[198] Schindelin J., Arganda-Carreras I., Frise E., Kaynig V., Longair M., Pietzsch T., *et al.*, Fiji: an open-source platform for biological-image analysis, *Nat. Methods*, (2012), **9**, 676–682

[199] Tan H.H., Williams J.S., Zou J., Cockayne D.J.H., Pearton S.J., Stall R.A., Damage to epitaxial GaN layers by silicon implantation, *Appl. Phys. Lett.*, (1996), **69**, 2364–2366

[200] Kucheyev S.O., Williams J.S., Pearton S.J., Ion implantation into GaN, *Mater. Sci. Eng. R Reports*, (2001), **33**, 51–108

[201] Williams J.S., Ion implantation of semiconductors, *Mater. Sci. Eng. A*, (1998), **253**, 8–15

[202] Borschel C., Ronning C., Ion beam irradiation of nanostructures – A 3D Monte Carlo simulation code, *Nucl. Instruments Methods Phys. Res. Sect. B Beam Interact. with Mater. Atoms*, (2011), **269**, 2133–2138

[203] Dhara S., Datta A., Wu C.T., Lan Z.H., Chen K.H., Wang Y.L., Chen L.C., Hsu C.W., Lin H.M., Chen C.C., Enhanced dynamic annealing in Ga+ ion-implanted GaN nanowires, *Appl. Phys. Lett.*, (2003), **82**, 451–453

[204] Dhara S., Datta A., Wu C.T., Lan Z.H., Chen K.H., Wang Y.L., Hsu C.W., Shen C.H., Chen L.C., Chen C.C., Hexagonal-to-cubic phase transformation in GaN nanowires by Ga+ implantation, *Appl. Phys. Lett.*, (2004), **84**, 5473–5475

[205] Richter W., Becker C.R., A Raman and far-infrared investigation of phonons in the rhombohedral V2–VI3 compounds Bi2Te3, Bi2Se3, Sb2Te3 and Bi2(Te1−xSex)3 (0 < x < 1), (Bi1−ySby)2Te3 (0 < y < 1), *Phys. Status Solidi*, (1977), **84**, 619–628

[206] Zhao Y., Hughes R.W., Su Z., Zhou W., Gregory D.H., One-Step Synthesis of Bismuth Telluride Nanosheets of a Few Quintuple Layers in Thickness, *Angew. Chemie Int. Ed.*, (2011), **50**, 10397–10401

[207] Tian Y., Osterhoudt G.B., Jia S., Cava R.J., Burch K.S., Local phonon mode in thermoelectric Bi2Te2Se from charge neutral antisites, *Appl. Phys. Lett.*, (2016), **108**, 41911

[208] Keskar G.D., Podila R., Zhang L., Rao A.M., Pfefferle L.D., Synthesis and Raman Spectroscopy of Multiphasic Nanostructured Bi–Te Networks with Tailored Composition, *J. Phys. Chem. C*, (2013), **117**, 9446–9455

[209] Arora A.K., Rajalakshmi M., Ravindran T.R., Sivasubramanian V., Raman spectroscopy of optical phonon confinement in nanostructured materials, *J. Raman Spectrosc.*, (2007), **38**, 604–617

[210] Sahu G., Confinement in {MeV} Au2$\mathplus$implanted Si: a Raman scattering study, *Adv. Nat. Sci. Nanosci. Nanotechnol.*, (2013), **5**, 15002

[211] Toulemonde Z.G.W. and C.D. and E.P. and M., The S e sensitivity of metals under swift-heavy-ion irradiation: a transient thermal process, *J. Phys. Condens. Matter*, (1994), **6**, 6733

[212] Newby P.J., Canut B., Bluet J.-M., Gomès S., Isaiev M., Burbelo R., Termentzidis K., Chantrenne P., Fréchette L.G., Lysenko V., Amorphization and reduction of thermal conductivity in porous silicon by irradiation with swift heavy ions, *J. Appl. Phys.*, (2013), **114**, 14903

[213] Kabiraj S.H. and B.S. and S.O. and T.K. and D.K. and D., Structural manipulation in Ge by swift heavy ions governed by electron–phonon coupling strength, *Mater. Res. Express*, (2015), **2**, 45903

[214] Komarov F.F., Defect and track formation in solids irradiated by superhigh-energy ions, *Physics-Uspekhi*, (2003), **46**, 1253

[215] Meftah A., Brisard F., Costantini J.M., Dooryhee E., Hage-Ali M., Hervieu M., Stoquert J.P., Studer F., Toulemonde M., Track formation in ${\mathrm{SiO}}_{2}$ quartz and the thermal-spike mechanism, *Phys. Rev. B*, (1994), **49**, 12457–12463

[216] Lifshits I.M., Kaganov M.I., Tanatarov L. V, On the theory of radiation-induced changes in metals, *J. Nucl. Energy. Part A. React. Sci.*, (1960), **12**, 69–78

[217] Mavrokefalos A., Moore A.L., Pettes M.T., Shi L., Wang W., Li X., Thermoelectric and structural characterizations of individual electrodeposited bismuth telluride nanowires, *J. Appl. Phys.*, (2009), **105**, 104318

[218] Hooda S., Satpati B., Ojha S., Kumar T., Kanjilal D., Kabiraj D., Structural manipulation in Ge by swift heavy ions governed by electron{\textendash}phonon coupling strength, *Mater. Res. Express*, (2015), **2**, 45903

[219] Pan L., Mitra S., Zhao L.-D., Shen Y., Wang Y., Felser C., Berardan D., The Role of Ionized Impurity Scattering on the Thermoelectric Performances of Rock Salt AgPbmSnSe2+m, *Adv. Funct. Mater.*, (2016), **26**, 5149–5157

[220] Miura A., Zhou S., Nozaki T., Shiomi J., Crystalline–Amorphous Silicon Nanocomposites with Reduced Thermal Conductivity for Bulk Thermoelectrics, *ACS Appl. Mater. Interfaces*, (2015), **7**, 13484–13489

[221] Von Lukowicz M., Abbe E., Schmiel T., Tajmar M., Thermoelectric Generators on Satellites—An Approach for Waste Heat Recovery in Space, *Energies*, (2016), **9**

[222] Takahashi M., Kojima M., Sato S., Ohnisi N., Nishiwaki A., Wakita K., Miyuki T., Electric and thermoelectric properties of electrodeposited bismuth telluride films Electric and thermoelectric properties of electrodeposited bismuth telluride, (2008), **5582**

[223] Hsin C.-L., Wingert M., Huang C.-W., Guo H., Shih T.-J., Suh J., Wang K., Wu J., Wu W.-W., Chen R., Phase transformation and thermoelectric properties of bismuth-telluride nanowires, *Nanoscale*, (2013), **5**, 4669

[224] Chang H.-C., Chen C.-H., Kuo Y.-K., Great enhancements in the thermoelectric power factor of BiSbTe nanostructured films with well-ordered interfaces, *Nanoscale*, (2013), **5**, 7017

[225] Singh N.K., Pandey J., Acharya S., Soni A., Charge carriers modulation and thermoelectric performance of intrinsically p-type Bi2Te3 by Ge doping, *J. Alloys*

Compd., (2018), **746**, 350–355

[226] Hu L.-P., Zhu T.-J., Wang Y.-G., Xie H.-H., Xu Z.-J., Zhao X.-B., Shifting up the optimum figure of merit of p-type bismuth telluride-based thermoelectric materials for power generation by suppressing intrinsic conduction, *NPG Asia Mater.*, (2014), **6**, e88–e88

[227] Ji X.H., Zhao X.B., Zhang Y.H., Lu B.H., Ni H.L., Synthesis and properties of rare earth containing Bi2Te3 based thermoelectric alloys, *J. Alloys Compd.*, (2005), **387**, 282–286

[228] Cao X., Xin J., Wang Y., Hu J., Qu X., Sun W., Preparation of Er-doped (Bi2Te3)0.90(Sb2Te3)0.05(Sb2Se3)0.05 by mechanical alloying and its thermoelectric properties, *Mater. Sci. Eng. B*, (2014), **188**, 54–58

[229] Wu F., Wang W., Hu X., Tang M., Thermoelectric properties of I-doped n-type Bi2Te3-based material prepared by hydrothermal and subsequent hot pressing, *Prog. Nat. Sci. Mater. Int.*, (2017), **27**, 203–207

[230] Wu F., Song H., Jia J., Hu X., Effects of Ce, Y, and Sm doping on the thermoelectric properties of Bi2Te3 alloy, *Prog. Nat. Sci. Mater. Int.*, (2013), **23**, 408–412

[231] Dennard R.H., Gaensslen F.H., Rideout V.L., Bassous E., LeBlanc A.R., Design of ion-implanted MOSFET's with very small physical dimensions, *IEEE J. Solid-State Circuits*, (1974), **9**, 256–268

[232] Chen L., Zhao Q., Ruan X., Facile synthesis of ultra-small Bi 2 Te 3 nanoparticles , nanorods and nanoplates and their morphology-dependent Raman spectroscopy, *Mater. Lett.*, (2012), **82**, 112–115

[233] Medhekar N. V, Chan W.L., Shenoy V.B., Chason E., Stress-enhanced pattern formation on surfaces during low energy ion bombardment, *J. Phys. Condens. Matter*, (2009), **21**, 224021

[234] Goto M., Sasaki M., Xu Y., Zhan T., Isoda Y., Shinohara Y., Control of p-type and n-type thermoelectric properties of bismuth telluride thin films by combinatorial sputter coating technology, *Appl. Surf. Sci.*, (2017), **407**, 405–411

[235] Cheng Y.-T., Nicolet M.-A., Johnson W.L., From Cascade to Spike---a Fractal-Geometry Approach, *Phys. Rev. Lett.*, (1987), **58**, 2083–2086

[236] Cheng Y.-T., Thermodynamic and fractal geometric aspects of ion-solid interactions, *Mater. Sci. Reports*, (1990), **5**, 45–97

[237] Kaoumi D., Motta A.T., Birtcher R.C., A thermal spike model of grain growth under irradiation, *J. Appl. Phys.*, (2008), **104**, 73525

[238] Weigel C., Landwehr G., Corbett J.W., Semi-Empirical LCAO Calculations for Tellurium Crystals with Vacancies, *Phys. Status Solidi*, (1974), **65**, 339–349

[239] Otake S., Ishii Y., Matsuno N., Migration Energy of Vacancies in Bismuth, *Jpn. J. Appl. Phys.*, (1981), **20**, 1037–1040

[240] Velişa G., Wendler E., Wang L.-L., Zhang Y., Weber W.J., Ion mass dependence of irradiation-induced damage accumulation in KTaO3, *J. Mater. Sci.*, (2019), **54**, 149–158

[241] Avasthi P.R. and A.G. and V.R.R. and V.S. and D.K., Swift heavy ion induced

modification in Ti/Si system studied with sub-nanometre resolution, *J. Phys. Condens. Matter*, (2007), **19**, 36221

[242] Stettner G.S. and G.X. and P.L.G. and E.L. and R.P. and U., Determination of the electron temperature in the thermal spike of amorphous carbon, *EPL (Europhysics Lett.*, (1999), **47**, 384

[243] Extending the inelastic thermal spike model for semiconductors and insulators, *Nucl. Instruments Methods Phys. Res. Sect. B Beam Interact. with Mater. Atoms*, (2011), **269**, 1646

[244] Worsley S.O.K. and Y.M.W. and A.V.H. and M.A., Light-ion-irradiation-induced thermal spikes in nanoporous silica, *J. Phys. D. Appl. Phys.*, (2011), **44**, 85406

[245] Milosavljević M., Grce A., Peruško D., Stojanović M., Kovač J., Dražič G., Didyk A.Y., Skuratov V.A., A comparison of Ar ion implantation and swift heavy Xe ion irradiation effects on immiscible AlN/TiN multilayered nanostructures, *Mater. Chem. Phys.*, (2012), **133**, 884–892

[246] Chandramohan S., Strache T., Sarangi S.N., Sathyamoorthy R., Som T., Influence of implantation induced Ni-doping on structural, optical, and morphological properties of nanocrystalline CdS thin films, *Mater. Sci. Eng. B*, (2010), **171**, 16–19

[247] Dey S., Mardinly J., Wang Y., Valdez J.A., Holesinger T.G., Uberuaga B.P., Ditto J.J., Drazin J.W., Castro R.H.R., Irradiation-induced grain growth and defect evolution in nanocrystalline zirconia with doped grain boundaries, *Phys. Chem. Chem. Phys.*, (2016), **18**, 16921–16929

[248] Alexander D.E., Was G.S., Thermal-spike treatment of ion-induced grain growth: Theory and experimental comparison, *Phys. Rev. B*, (1993), **47**, 2983–2994

[249] Jian L., Liu J.C., Mayer J.W., Ar+ ion irradiation induced grain growth in Au and Pt thin films, *Nucl. Instruments Methods Phys. Res. Sect. B Beam Interact. with Mater. Atoms*, (1989), **36**, 306–311

[250] Chason E., Mayer T.M., Low energy ion bombardment induced roughening and smoothing of SiO2 surfaces, *Appl. Phys. Lett.*, (1993), **62**, 363–365

[251] Sahoo S.K., Mangal S., Mishra D.K., Singh U.P., Kumar P., 100 keV H+ ion irradiation of as-deposited Al-doped ZnO thin films: An interest in tailoring surface morphology for sensor applications, *Surf. Interface Anal.*, (2018), **50**, 705–712

[252] Choudhary R., Chauhan R.P., Swift heavy ion induced modifications in optical and electrical properties of cadmium selenide thin films, *Electron. Mater. Lett.*, (2017), **13**, 330–338

[253] Li A.H., Shahbazi M., Zhou S.H., Wang G.X., Zhang C., Jood P., Peleckis G., Du Y., Cheng Z.X., Wang X.L., Kuo Y.K., Electronic structure and thermoelectric properties of Bi2Te3 crystals and graphene-doped Bi2Te3, *Thin Solid Films*, (2010), **518**, e57–e60

[254] Zhao B., Zhou B., Li C.Y., Qi N., Chen Z.Q., First-Principles Calculation of Defect Formation and Positron Annihilation States in Bi2Te3, In: Positron Annihilation - ICPA-17, *Trans Tech Publications Ltd, (2017)*, 41–45

[255] Kennedy J., Murmu P.P., Kumar P., Ramanath G., Multifold enhancements in thermoelectric power factor in isovalent sulfur doped bismuth antimony telluride films, *Mater. Res. Bull.*, (2021), **142**, 111426

[256] Masarrat A., Bhogra A., Meena R., Bala M., Singh R., Barwal V., Dong C.-L., Chen C.-L., Som T., Kumar A., Niazi A., Kandasami A., Effect of Fe ion implantation on the thermoelectric properties and electronic structures of CoSb 3 thin films, *RSC Adv.*, (2019), **9**, 36113–36122

[257] Zhang Y., Liu Y., Calcabrini M., Xing C., Han X., Arbiol J., Cadavid D., Ibáñez M., Cabot A., Bismuth telluride–copper telluride nanocomposites from heterostructured building blocks, *J. Mater. Chem. C*, (2020), **8**, 14092–14099

[258] Jagadish P., Khalid M., Amin N., Hajibeigy M.T., Li L.P., Numan A., Mubarak N.M., Walvekar R., Chan A., Recycled carbon fibre/Bi2Te3 and Bi2S3 hybrid composite doped with MWCNTs for thermoelectric applications, *Compos. Part B Eng.*, (2019), **175**, 107085

[259] Kumar S., Chaudhary D., Dhawan P., Yadav R.R., Khare N., Bi 2 Te 3 -MWCNT nanocomposite: An efficient thermoelectric material, *Ceram. Int.*, (2017), **43**

[260] Li S., Fan T., Liu X., Liu F., Meng H., Liu Y., Pan F., Graphene Quantum Dots Embedded in Bi2Te3 Nanosheets To Enhance Thermoelectric Performance, *ACS Appl. Mater. Interfaces*, (2017), **9**, 3677–3685

Thesis Highlight

Name of the Student: Sinduja. M

Name of CI: Indira Gandhi Centre for Atomic Research

Enrolment No.: PHYS02 2016 04 006

Thesis Title: Investigations on the role of defects in the thermoelectric properties of nanostructured bismuth telluride

Discipline: Physical Sciences

Date: 29/7/2021

In this work, nano-structuring and defect-engineering approaches were used to improve thermoelectric (TE) characteristics of Bi_2Te_3 based TE material. Initially, the hydrothermal method growth conditions for Bi_2Te_3 nanostructures were optimized using various factors such as surfactant concentration and reaction temperature, and its effectiveness towards the thermoelectric transport characteristics were investigated. All pellets are exhibiting p-type conductivity (due to accepter type Bi_{Te} antisite defects), and thin film are demonstrating n-type conductivity (due to donor type V_{Te} defects). 100 keV He^+ ion irradiation with different ion fluences was performed on Bi_2Te_3 nanorod pellet samples.

HRTEM results showed the presence of amorphous surface layer in the Bi_2Te_3 nanorod, due to the accumulation of migrating point defects and defect clusters at the surface of the nanorod. Fig. 1 displays the evolution of Bi_2Te_3 nanorod microstructure and power factor as a function of 100 keV He^+ ion fluences. Ionized impurity dominated scattering process significantly enhances the value of power factor in the irradiated pellets.

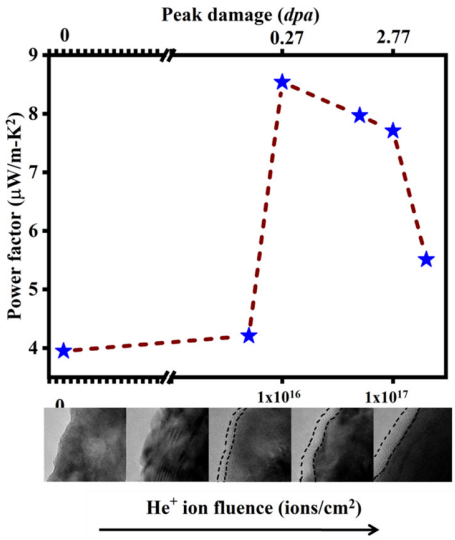

Fig.1 The evolution of Bi_2Te_3 nanorod microstructure and power factor as a function of 100 keV He^+ ion fluences

Apart from that, copper doping and inert gas ion irradiations were performed on Bi_2Te_3 thin films. The results showed the charge carrier type conversion (i.e., *n*-type to *p*-type) in He^+ ion irradiated Bi_2Te_3 thin films. Linear collision cascades are expected for He^+ ion irradiation that infuse simple type of point defects in the material. The defects appear to be mobile at room temperature through which most of them annihilate. However, stable V_{Bi} were found to increase hole density and thus expected to be responsible for the *p*-type conductivity and positive S value in He^+ ion irradiated thin films. On the other hand, at higher damage (i.e., in Ar^+ ion irradiated thin films); irradiation induced grain melting aids defect recovery, which would reduce the defect density and consequently increases the electron concentration. In case of copper doped samples, Hall-effect and Seebeck measurements showed *n*-type to *p*-type charge carrier conversion. However, Cu^+ ion implanted Bi_2Te_3 thin films after annealing exhibits *n*-type conductivity. Significance of this results show the possibility of fabricating TE micro-modules that comprises of *n*- and *p*-type semiconductors. This *n*- to *p*-type charge carrier conversion is attributed to the high density of stable defect complexes in addition to the accepter type V_{Bi} and Cu_{Bi} defects. Fig. 2 displays the variation in power factor values at room temperature as a function of peak damage and it has been observed that the maximum power factor was observed in the annealed Cu^+ ion implanted Bi_2Te_3 thin films that correspond to the value of ~106.12 μW/mK^2 at 300 K.

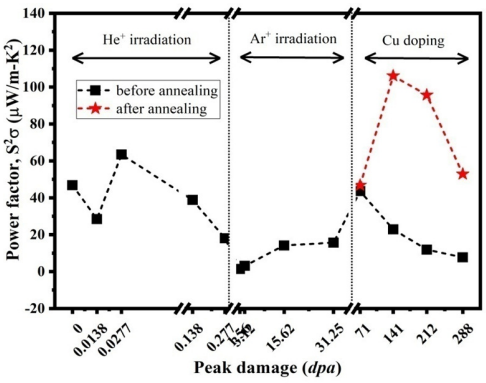

Fig.2 Variation in power factor values at room temperature for Bi_2Te_3 thin film sample as a function of peak damage values